Multi-component Elastomer Composites for Next Generation Electronics and Machines

Edward J. Barron III

Dissertation submitted to the Faculty of the
Virginia Polytechnic Institute and State University
in partial fulfillment of the requirements for the degree of

Doctor of Philosophy
in
Macromolecular Science and Engineering

Michael D. Bartlett, Chair
Michael J. Bortner
Nathan Lazarus
Alan T. Asbeck
John P. Domann

August 29, 2023
Blacksburg, Virginia

Keywords: Liquid metal, Magnetic, Composites, Elastomers, Flexible electronics, Soft machines, Robots, Multi-functional

Copyright 2023, Edward J. Barron III

Multi-component Elastomer Composites for Next Generation Electronics and Machines

Edward J. Barron III

(ABSTRACT)

Multi-component soft materials offer innovative solutions for traditional and emerging technologies by possessing unique combinations of tunable functionality and adaptive mechanical response. These materials often incorporate functional inclusions such as metals or ceramics in elastomers to create deformable composite structures with high thermal or electrical conductivities, magnetic material response, or stimuli-responsive shape and rigidity tuning. In recent years, these materials have become enabling for wearable electronics and soft machines which has led to the development of new material architectures that provide advanced functionalities while maintaining a low mechanical modulus and high extensibility. In this work, we develop methods for the fabrication and utilization of advanced material architectures which integrate room temperature liquid metals (LM), low melting point alloys (LMPA), and magnetic powders and fluids with soft elastomers to introduce multifunctionality to electronic and machine systems.

LM-elastomer composites which have high thermal and electrical conductivities are enabling for heat transfer applications and soft, extensible wiring for wearable electronics and soft robots. These materials have been utilized to create emerging devices such as electronics that are capable of improving human health and efficiency, as well as robots capable of adapting their functions based on environmental need. One possible area where LM composites could be applied is in marine environments, where wearable electronics can improve safety for divers, and soft machines could be utilized for underwater exploration. In Chapter

2, we provide the first study to quantify the effects of underwater aging in freshwater and saltwater environments on the important mechanical and functional properties of LM composites for long-term underwater use. It is found that LM composites are largely resistant to changes in their mechanical properties, as well as both thermal and electrical functionality due to long-term underwater aging. In Chapter 3, we introduce a new chemical approach for the tough bonding of LM composites to diverse substrates, which increases adhesion by up to 100x, improving the integration of these materials with rigid electronics. It is shown that the fracture energy and thermal conductivity of these materials can be tuned by controlling the size and volume loading of the LM inclusions. The utility of this method is then shown through the permanent bonding of LM composites to rigid electronics for use as thermal interface materials.

Chapter 4 introduces a multi-component shape morphing material that leverages an LMPA endoskeleton and soft LM resistive heaters to produce rapid (< 0.1 s) and reversible shape change. The morphing material utilizes a unique 'reversible plasticity' mechanism enabled by patterned kirigami cuts that allows for instantaneous shape fixing into load bearing shapes without the need for sustained power. The material properties are enabling for the creation of shape morphing robots, which we show through by integration of on board power and control to create a multi-modal morphing drone capable of land and air transport as well as through an underwater machine that can be reversibly deployed to obtain cargo.

For magnetic elastomers, the magneto-mechanical properties of state-of-the-art magnetorheological elastomers (MREs) with diverse structures are studied. These materials have long been studied for their ability to rapidly tune stiffness in the presence of a magnetic field. Chapter 5 introduces a new form of hybrid MRE material architecture which utilizes a combination of magnetic powders and fluids to achieve high magnetic permeability and low stiffness for wearable electronic applications. The zero-field magneto-mechanical properties of MREs with rigid particles, magnetic fluids, and a combination of the two are studied. The

inclusions are modeled through an Eshelby analysis which demonstrates magnetic fluids can be utilized to increase magnetic response while decreasing the stiffness of the composite material. The stiffness tuning capabilities of these material architectures are then explored in Chapter 6, where we introduce a predictive model that captures the stiffness tuning response of MREs across diverse microstructures and compositions. This model guides the creation of materials with rapid ($\sim$ 20 ms) and extreme stiffness tuning (70x) which we utilize to create a soft adaptive gripper capable of handling objects of diverse geometries.

Multi-component Elastomer Composites for Next Generation Electronics and Machines

Edward J. Barron III

(GENERAL AUDIENCE ABSTRACT)

Multi-component soft materials offer innovative solutions for traditional and emerging technologies by possessing unique combinations of tunable functionality and adaptive mechanical properties. These materials often incorporate functional inclusions such as metals or ceramics in elastomers in order to create deformable composite structures with high thermal or electrical conductivities, magnetic material response, or user-controlled shape morphing and stiffness change. In recent years, these materials have become enabling for wearable electronics and soft machines which has led to the development of new materials that provide advanced functionalities while maintaining a low stiffness and high extensibility. In this work, we develop methods for the fabrication and utilization of advanced materials that integrate room temperature liquid metals (LM), low melting point alloys (LMPA), and magnetic powders and fluids with soft elastomers to introduce multifunctionality to electronic and machine systems.

LM-elastomer composites which have high thermal and electrical conductivities are enabling for heat transfer and stretchable electronic applications for wearable electronics and soft robots. These materials have been utilized to create emerging devices such as electronics that are capable of improving human health and efficiency, as well as robots capable of adapting their functions based on environmental need. One possible area where LM composites could be applied is in marine environments, where wearable electronics can improve safety for divers, and soft robots could be utilized for underwater exploration. In Chapter

2, we provide the first study to quantify the effects of underwater aging in freshwater and saltwater environments on the important mechanical and functional properties of LM composites for long-term underwater use. It is found that LM composites are largely resistant to changes in their mechanical properties, as well as both thermal and electrical functionality due to long-term underwater aging. In Chapter 3, we introduce a new chemical approach for the tough bonding of LM composites to diverse substrates, which increases adhesion by up to 100x, improving the integration of these materials with rigid electronics. It is shown that the adhesion and thermal conductivity of these materials can be tuned by controlling the size and volume loading of the LM inclusions. The utility of this method is then shown through the permanent bonding of LM composites to rigid electronics for use as thermal interface materials.

Chapter 4 introduces a multi-component shape morphing material that leverages an LMPA endoskeleton and soft LM resistive heaters to produce rapid (< 0.1 s) and reversible shape change. The morphing material utilizes a unique 'reversible plasticity' mechanism enabled by patterned kirigami cuts that allows for instantaneous shape fixing into load bearing shapes without the need for sustained power. The material properties are enabling for the creation of shape morphing robots, which we show through by integration of on board power and control to create a multi-modal morphing drone capable of land and air transport as well as through an underwater machine that can be reversibly deployed to obtain cargo.

For magnetic elastomers, the magnetic and mechanical properties of state-of-the-art magnetorheological elastomers (MREs) with diverse structures are studied. These materials have long been studied for their ability to rapidly change stiffness in the presence of a magnetic field. Chapter 5 introduces a new form of hybrid MRE material architecture which utilizes a combination of magnetic powders and fluids to achieve exceptional magnetic properties and low stiffness for wearable electronic applications. The mechanical properties of MREs with rigid particles, magnetic fluids, and a combination of the two are studied. The inclusions are

modeled through a mechanical analysis which demonstrates magnetic fluids can be utilized to increase magnetic character while decreasing the stiffness of the composite material. The stiffness tuning capabilities of these material architectures are then explored in Chapter 6, where we introduce a predictive model that captures the stiffness tuning response of MREs across diverse microstructures and compositions. This model guides the creation of materials with rapid ($\sim$ 20 ms) and extreme stiffness tuning (70x) which we utilize to create a soft adaptive gripper capable of handling objects of diverse geometries.

Dedication

This work is dedicated to my family who have always been supportive of all my goals, and to the many generations of Edward Barron that came before me.

Acknowledgments

I would first like to thank my advisor, Professor Michael Bartlett. Mike is a professor who cares about his students' success, and does all he can to help us achieve our goals. He is the reason we have such a unique culture in our lab built upon not only personal success, but also elevating others. It has been a pleasure to work with him all these years, and I sincerely thank him for being the best mentor I could have asked for.

I would also like to thank my committee: Professors Nathan Lazarus, Michael Bortner, John Domann, and Alan Asbeck. I had the pleasure of beginning to work with Nathan early on in my graduate career, and he later became my fellowship advisor while he was with ARL. I always enjoyed the meetings I had with Nathan, and he was able to provide important insights into my work with magnetic elastomers. Nathan was a fantastic research mentor to have during my graduate career and I hope I have the opportunity to work with him in the future.

Dr. Bortner was the first professor I remember welcoming me and the other members of my lab to Virginia Tech when we made the move from our previous university. Since then, I have had the opportunity to take courses with Dr. Bortner, where he is always passionate about his teaching and shows a genuine interest in helping the students of Virginia Tech learn and succeed. He has been a profoundly positive influence on my research career, including by showing kindness at the Adhesion Society and always offering to introduce me to new people.

I'd like to thank Professors Domann and Asbeck for their thoughtful questions and feedback regarding my research.

I would also like to thank Professor Dave Dillard who taught some of my favorite courses here at Virginia Tech. He is another professor that has had a positive impact during my studies, and always had positive things to say during class or after presentations at the Adhesion Society. I also want to thank him for allowing me to visit his farm to pick fresh vegetables.

I would also like to thank Professors Al Crosby and Alex Briseno who gave me my first research opportunities in polymer science. Without them, I would not be where I am today.

I would like to thank the members of the Soft Materials and Structures Lab. When I first joined Mike we were a small group with only three graduate students including myself, but I could already tell that the lab was a special place to work with a unique culture built on helping others to succeed. Ravi and Dohgyu went out of their way to welcome me to the lab and get me up to speed with the high quality of research expected of us working with Mike. I will sincerely miss the late nights in the lab where each of us would motivate each other to accomplish our research goals. I also fondly remember us getting lunch together during the day or dinner together at the end of the week downtown to celebrate a good week's work. I would like to thank Tyler who came into our lab later on. He was a good friend to have in the lab, and a fierce worker who was able to match anyone's intensity when it came to finishing projects. One of my favorite memories with Tyler is when we stayed in the lab for nearly a week straight together refusing to get a good night's rest until the tough bonding project was finished, and I remember how thrilled we were when we were able to get the final result. I think it was there that we started the near-weekly tradition to grab dinner together after work on Fridays with Ravi which was always a great way to end the week. I would also like to thank the rest of the SMS lab who I have had the pleasure of working with, especially John and Austin who nearly always come with positive attitudes

ready to work.

Perhaps most importantly, I would like to thank the two undergraduate students who I have had the pleasure of mentoring: Ray Peterson and Ella Williams. Our lab has had amazing success with undergraduate students, and I was lucky to be able to work with these two individuals, who I think were two of the best. Ray was the first student I was able to mentor, and he was able to quickly make an impact on our magnetic elastomers paper. He always had a can-do attitude and was ready to learn new things and refine our existing methods to improve efficiency. I am proud that he decided to pursue a PhD in Macromolecular Science and Engineering, and I expect great things in his future. Ella was a student that I had the opportunity to mentor beginning in her second year of undergraduate, and I remember being immediately impressed by her work ethic and ability to learn. If given the opportunity to take a day off, she would not take it, as she was always looking towards how to finish the task at hand. I am immensely proud of her for being our lab's first undergraduate student to attend and present at the Adhesion Society, and was overjoyed that she decided to pursue her PhD in Mechanical Engineering in the SMS lab. I believe she has the potential to be the best PhD candidate that our lab has had so far.

I would also like to thank my family. First I would like to thank my father Ed, who has always made it clear that his single most important goal was the success and happiness of me and my sister. Many of the personal and leadership qualities that I try to live by, I learned from him. I would also like to thank my grandpa Ed, who always encouraged me to be a leader and an engineer and helped me foster my love for science and engineering at a young age. I would also like to thank my great-grandfather Ed who I didn't have the opportunity to know very well, but I do remember his love of family. I remember being younger and looking at the picture on the wall of the four of us together in one place, and it

is that picture that has always inspired me to try to succeed in my own way as each of you did before me.

I would also like to thank Grandpa Tony and my grandmother, PG. You two have always been immensely supportive and could not be more caring. I'd also like to thank Grandma N, who was the person who taught me to enjoy writing. I'd like to thank my grandmother Diane and my grandpa Glenn who taught me that family is the most important thing in this world. To my sister, Katie and brother, Bryce. You two have already accomplished great things, and I have the best siblings in the world.

Lastly, I would like to give thanks to my family here in Blacksburg: my fiance Anna, and my dog Stella. Anna and I met through our love of polymers during our undergraduate education, and since then we have lived in three different states in the last five years as I've traveled to get this PhD. Anna has always been my biggest supporter, and I could not be more proud of her for pursing a PhD in chemistry (working on polymers) here at Virginia Tech. My dog Stella has now traveled with us through two states and is always the first to greet me when I return home. You two are my biggest motivation, and I look forward to the many years ahead.

Contents

List of Figures **xix**

1 Soft Robotics: A Futuristic Extension of Stretchable Electronics Technology **1**

1.1 Introduction 1

1.1.1 Deterministic geometries 3

1.1.2 Intrinsically stretchable materials 4

1.1.3 Soft composite fabrication 4

1.2 Liquid metal-elastomer composites 7

1.2.1 Liquid metal 7

1.2.2 Composite processing, structure, and properties 9

1.2.3 Liquid metal elastomer composite applications 13

1.3 Low melting point alloys 14

1.3.1 Fabrication and structure of LMPA composites 16

1.3.2 LMPA composite stiffness tuning 18

1.3.3 LMPAs and soft robots 19

1.4 Magnetic elastomer composites 21

1.4.1 MRE structure 23

1.4.2 MRE properties . . . 26
1.4.3 MREs and soft robots . . . 27
1.5 Multi-component soft composites . . . 29
1.5.1 Multi-component composite architectures . . . 29
1.5.2 Multi-component composites in robots and electronics . . . 31
1.6 Research Objectives . . . 33
1.7 Acknowledgments . . . 37

2 Liquid metal-elastomer composites for water-resilient flexible electronics 38

2.1 Contributions . . . 39
2.2 Abstract . . . 40
2.3 Introduction . . . 41
2.4 Results and Discussion . . . 45
2.4.1 Underwater aging of liquid metal composites . . . 45
2.4.2 Mechanical characterization . . . 47
2.4.3 Thermal characterization . . . 49
2.4.4 Electrical characterization . . . 52
2.4.5 Water-resilient LM composite electrodes . . . 54
2.5 Conclusions . . . 56
2.6 Experimental/Methods . . . 57

2.6.1 Composite Fabrication 57
2.6.2 Underwater aging 58
2.6.3 Mechanical testing 58
2.6.4 Thermal conductivity testing 59
2.6.5 Electrical conductivity testing 59
2.6.6 Composite electrode aging 59
2.6.7 Hydrostatic testing 60
2.7 Acknowledgements 60

3 Tough bonding of liquid metal-elastomer composites for multifunctional adhesives 61

3.1 Contributions 62
3.2 Abstract 63
3.3 Introduction 64
3.4 Results and discussion 67
3.4.1 Effects of LM microstructure on fracture energy 68
3.4.2 Robust adhesion to multiple surfaces 72
3.4.3 Integration of LM composites into electronic systems 72
3.5 Conclusions 76
3.6 Experimental section 78
3.6.1 Fabrication 78

3.6.2 Characterization . . . 80

3.7 Acknowledgements . . . 82

4 Shape morphing mechanical metamaterials through reversible plasticity 83

4.1 Contributions . . . 84

4.2 Abstract . . . 85

4.3 Introduction . . . 86

4.4 Results . . . 89

4.4.1 Morphing composite design . . . 89

4.4.2 Morphing composite mechanical analysis . . . 91

4.4.3 Shape-fixing . . . 96

4.4.4 Morphing drone . . . 97

4.4.5 Morphing and deployable underwater machine . . . 98

4.5 Discussion . . . 101

4.6 Acknowledgements . . . 108

5 Mechanically cloaked multiphase magnetic elastomer soft composites for wearable wireless power transfer 110

5.1 Contributions . . . 111

5.2 Abstract . . . 112

5.3 Introduction . . . 113

5.4 Results and Discussion . . . 116
5.4.1 Composite Fabrication . . . 116
5.4.2 Microstructure . . . 117
5.4.3 Mechanical Behavior . . . 118
5.4.4 Magnetic Permeability . . . 121
5.4.5 Wireless power transfer . . . 124
5.5 Conclusions . . . 126
5.6 Experimental . . . 127
5.7 Acknowledgements . . . 129

6 A unified understanding of magnetorheological elastomers for rapid and extreme stiffness tuning 130

6.1 Contributions . . . 131
6.2 Abstract . . . 132
6.3 Introduction . . . 133
6.3.1 Results and Discussion . . . 136
6.3.2 Predicting MRE stiffness tuning . . . 136
6.3.3 MRE composition . . . 138
6.3.4 MRE characterization . . . 139
6.3.5 Active magnetorheological properties . . . 142
6.3.6 Adaptive MRE gripper . . . 145

6.4 Conclusion 146
6.5 Experimental Section 146
6.6 Acknowledgements 149

7 Conclusions **151**

7.1 Research contributions 151
7.2 Future work 157

Bibliography **159**

Appendices **223**

Appendix A Chapter 2 Supporting Information **224**

Appendix B Chapter 3 Supporting Information **230**

Appendix C Chapter 4 Supporting Information **233**

Appendix D Chapter 5 Supporting Information **242**

Appendix E Chapter 6 Supporting Information **245**

List of Figures

1.1 **Soft functional and active materials.** Multi-functional composites utilize fillers such as liquid metals, low melting point alloys, and magnetic particles and fluids to allow for deformability, thermal, electrical, and magnetic material properties, and adaptive response for electronics and machines. **Top left image:** A liquid metal elastomer composite with high thermal conductivity. Open access article.[59] **Top right image:** A low melting point alloy composite with shape morphing capabilities. Adapted from an article published in *Science Robotics*.[60] **Bottom image:** A magnetic elastomer composite with liquid metal conductive channels. Reprinted (adapted) with permission from [56]. Copyright 2020 American Chemical Society. **Center image:** A multi-component shape morphing material integrated with on-board power and control to enable a morphing drone. Adapted from an article published in *Science Robotics*.[60] 6

1.2 **Liquid metal elastomer composites.** Thermal conductivity of LM composites can be improved through micro-structure control: **a)** Change in droplet shape by mechanical deformation. Open access article.[59] **b)** Programmed properties through additive manufacturing approach. Open access article.[98] Electrical conductivity can be enabled by formation of a connected LM network: **c)** Mechanical activation can cause a percolated network of LM inclusions. Open access article.[99] **d)** Fabrication techniques can be employed to create as-prepared connected networks. Reproduced with permission. Copyright 2019 Elsevier.[100] 11

1.3 **Low melting point alloy composites.** Composites have been developed through: **a)** Fabrication of LMPA channels in elastomer. Reprinted (adapted) with permission from [132]. Copyright 2021 American Chemical Society. **b)** The creation of LMPA particles for dispersion into elastomer. **c)** 3D continuous networks of LMPA in elastomer. Reproduced with permission. Copyright 2020 Elsevier.[135] **d)** Stiffness change of LMPA composites of various microstructures, data from various sources.[54, 55, 122, 127, 136, 137] 17

1.4 **Soft robot LMPA applications.** **a)** LMPAs for shape changing multifunctional robots. Open access article.[62] 20

1.5 **Magnetorheological elastomers for functional and active materials.** **a)** Micro-structure of rigid-particle composite (RC) MREs as either isotropic or aligned as anisotropic with a magnetic field. Left image adapted from an open access article.[63] **b)** Magnetorheological fluid composite (FC) MREs can be shape programmed by additive manufacturing approaches. Reproduced with permission. Copyright 2017 Elsevier.[58] They can also be created by micro-dispersing magnetorheological fluid droplets though mixing. Reprinted (adapted) with permission from [56]. Copyright 2020 American Chemical Society. **c)** Solid/fluid hybrid composite (HC) MREs utilize a combination of particles and fluids. Reprinted (adapted) with permission from [56]. Copyright 2020 American Chemical Society. **d)** Permeability of isotropic and anisotropic MREs using data from Ref. 183. **e)** Effect of each of magnetic particles and fluids on MRE zero-field modulus. Reprinted (adapted) with permission from [56]. Copyright 2020 American Chemical Society. . . . 24

1.6 **MRE soft robot applications. a)** MREs can rapidly respond to a field for machine actuation such as in haptic feedback systems. Reprinted (adapted) with permission from [174]. Copyright 2022 American Chemical Society. **b)** Shape change can be used for reconfigurable electronic devices. Open access article.[194] **c)** The change in stiffness of MREs allows for rapidly reversible adhesion. Open access article.[185] **d)** Stiffness tuning can also be used to create adaptive robotic grippers. Open access article.[63] 29

1.7 **Multi-component soft composites. a)** Liquid metal conductive pathway integrated with magnetic elastomer composite to increase inductor efficiency. Reprinted (adapted) with permission. Copyright 2015 American Chemical Society.[42] **b)** Magnetic particles integrated with liquid metal droplets for tunable functionality. Reproduced with permission. Copyright 2020 Elsevier.[203] **c)** Low melting point alloy integrated with liquid metal-based resistive heater. Adapted from an article published in *Science Robotics*.[60] **d)** Magnetorheological fluid utilizing LMPA as a carrier fluid capable of rapid magnetorheological response and further stiffness tuning through phase change. Open access article.[204] 31

1.8 **Multi-component material systems enable next generation electroincs and machines. a)** Liquid metal heat transfer material enables robotic movement from a shape-memory alloy actuator. Open access article.[59] **b)** Magnetic elastomer backplanes improve the power transfer efficiency of LM-based wireless power transfer devices. Reprinted (adapted) with permission. Copyright 2020 American Chemical Society.[56] **c)** Liquid metal heater allows for reversibility of shape morphing material based on LMPA. Adapted from an article published in *Science Robotics*.[60] 33

2.1 **Underwater aging of liquid metal composites.** **(A)** $\phi = 40\%$ interacting with an underwater environment. **(B)** Schematic of a liquid metal composite. **(C)** Stretchable mechanical properties of Ecoflex $\phi = 40\%$. **(D)** Enhanced thermal conductivity through the inclusion of liquid metal in elastomer. When heat is applied via a heat gun, the LM composite shows improved heat transfer to an underlying metal plate. **(E)** Electrical conductivity of Sylgard $\phi = 80\%$ composite enables circuits. **(F)** Environmental aging chamber with water filtration, circulation, and heating. 44

2.2 **Morphological and chemical analysis.** **(A-D)** SEM images of Ecoflex ($\phi = 80\%$) composites showing distribution of Ga, In, Na, and Cl for different aging conditions. **(E)** Weight fraction of O_2, Na, and Cl on the surface of aged samples determined from EDS. **(F)** Mass change of Ecoflex ($\phi = 0\%$). Error Bars represent standard deviation for n = 3. 46

2.3 **Mechanical analysis.** **(A)** Microscopy of liquid metal composites. **(B)** Measured and predicted moduli for liquid metal composites. Tensile moduli of **(C)** Ecoflex and **(D)** Sylgard composites throughout underwater aging. Error bars represent standard deviation for n = 3. 48

2.4 **Thermal conductivity analysis.** **(A)** Schematic of the transient hot wire embedded samples. **(B)** Measured and predicted values for thermal conductivity as a function of LM loading. Thermal conductivity of **(C)** ambient **(D)** freshwater **(E)** saltwater and **(F)** concentrated saltwater aged samples. Error bars represent standard deviation. See Table A.1 for more information. 50

2.5 **Electrical conductivity analysis.** **(A)** Electrical activation method. **(B)** Micrographs of samples before and after activation. **(C)** Representative measurements used to calculate conductivity. Conductivity in samples aged in **(D)** ambient, **(E)** freshwater **(F)** saltwater and **(G)** concentrated saltwater environments. Error bars represent standard deviation. See Table A.2 for more information. 53

2.6 **Aging Liquid metal composite and copper electrodes.** **(A)** Aging setup for the demonstration samples. **(B)** Images showing the progression of aging of the LM composite and copper samples. **(C)** Copper and **(D)** Sylgard composite ($\phi = 80\%$) electrodes after 18 days of aging in a CS environment. **i)** Observations of visual changes in the electrodes after aging. **ii)** An LED is integrated with the electrodes and their ability to function as a circuit is evaluated. The copper electrodes fail due to degradation while the Sylgard composite electrode is able to function after aging. 55

3.1 **Strong bonding of liquid metal composite.** **a)** Schematic representation of liquid metal composite adhesion without (left) and with (right) chemical anchoring. **b)** Fracture energy (G_c) versus displacement of representative LM composites ($\phi = 20\%$, $d = 2$ µm) undergoing peeling. **c)** Fracture energies of untreated and chemically anchored samples ($\phi = 20\%$, $d = 2$ µm). Error bars represent the standard deviation for n = 3. **d)** Strong LM composite adhesive supporting bricks of total mass 6.8 kg from a 15 mm wide, pre-cracked peel specimen. 66

3.2 **LM composite adhesion. a)** Adhesive and cohesive failures of LM composite sample ($\phi = 20\%$, $d = 2$ µm) in T-peel without and with APTES surface treatment **b)** Macrophotograph image of the crack front of an LM adhesive ($\phi = 20\%$, $d = 60$ µm) undergoing cohesive fracture with **c, d)** showing the corresponding micrographs. **e)** Schematic representation of liquid metal droplet elongation at the crack front. 68

3.3 **Adhesion and property characterization of LM composites. a)** Fracture energies of LM composites in T-peel. **b)** Comparison of LM composite fracture energy and elastic modulus. **c)** Comparison of LM composite fracture energy and thermal conductivity. **d)** Fracture energy of LM composite on varied surfaces in 90° peel for $\phi = 40\%$, $d = 15$ µm. **e)** Macrophotograph of the cohesive failure of a 90° peel sample on copper. Error bars represent the standard deviation for n = 3. 70

3.4 **Integration and heat dissipation of electronics with LM composites. a)** Temperature measured by the GPU thermocouple during idle and benchmark tests. **b)** Performance of the graphics card with the stock configuration and with LM composite and Ecoflex as replacements for the thermal interface material. **c)** Suspension of both the heatsink (66 grams) and an additional 50 grams from a chemically anchored LM composite. 73

3.5 **Stretchable circuits through tough LM composite adhesives. a)** Schematic representation of an integrated LM composite device. **b)** Thermal profiles of Ecoflex and LM composite samples after 80 s. **c)** Ecoflex sample timelapse, showing thermal failure of the LED (ii) and adhesive failure at the bottom copper contact (iii). **d)** LM composite sample timelapse, showing high stretchability and heat dissipation and eventual fracture through the bottom neck (v-vi) at ∼310% global applied strain. **e)** LM composite thin film with (from left to right) chemically anchored to an LED and supporting acrylic substrate, hand-stretching, torsion, and stress applied directly to the LED while pulling with tweezers. 75

4.1 **Multimaterial kirigami composite with instantaneous complex shape-fixing and reversibility.** (**A**) Schematic showing the layers of a kirigami-inspired multilayered composite. (**B**) A top down schematic showing the kirigami incisions, endoskeleton, and elastomer in an undeformed state with the deformed state in the inset. (**C**) Image sequence showing the composite morphing into the programmed shape of an inflating elastomeric membrane underneath and can support 240 g in the reconfigured state after the membrane is deflated. By activating embedded heaters (inset shows IR images), the morphed composite undergoes a phase change and returns to the flat, initial state and can then be actuated repeatedly. Scale bar = 50 mm. (**D**) Gaussian curvature map of the deployed kirigami composite showing the complex shape. 90

4.2 **Mechanical performance of kirigami composites with uni-axial endoskeleton structures.** (**A**) Kirigami composite at zero and 100 % strain. Scale bar = 20 mm. (**B**) Load versus applied tensile strain for different kirigami composites (l_{LMPA}= 20 mm, width w_{LMPA} = 1.9 mm, and thickness t_{LMPA} = 1,000 µm). (**C**) FEA results showing the development of plastic hinges at different applied strains. (**D**) Kirigami composite stiffness for different endoskeleton states. Error bars represent the standard deviation for n = 10. (**E**) Effective stiffness versus kirigami beam geometry w_{LMPA}/l_{LMPA} for kirigami composites with 12 different endoskeleton geometries. Inset: Composite schematic showing geometric parameters. Error bars represent the standard deviation for n = 3. (**F**) Normalized stiffness as a function of the number of cycles for a LMPA-embedded kirigami composite. Inset: a cross-section of the composite. Scale bar = 1 mm. 93

4.3 **Shape-fixing at rapid time scales with complex shapes.** (**A**) Load versus strain shape-fixing curves for two specimens with different kirigami stiffness and a sample without an endoskeleton. The inset presents a schematic of the measurement of a shape fixity ratio (R_f). (**B**) Shape fixity ratio R_f as a function of ε_{appl} from Fig. 4.3A. Error bars represent the standard deviation for $n = 3$. (**C**) A kirigami composite undergoes substantial out-of-plane deformation through the impact of a metal ball which causes rapid reconfiguration and shape-fixing into the deformed shape in ~ 70 ms. The second to last image shows the structure inverted against gravity where it maintains the reconfigured shape and the last image shows reversibility of the shape through activation of the embedded heater. Scale bar = 50 mm. (**D**) Photographs of a tri-axial kirigami composite that morphs onto objects with complex curvatures reversibly. Insets shows the representative Gaussian curvature of the objects. Scale bar = 50 mm. 95

4.4 **Multifunctional autonomously morphing drone.** (**A, B**) Photographs of the two distinct functional states of the soft robotic morphing drone and its integrated rigid electronics. State 1 is a land transport machine. State 2 is a fully functional quadrotor air vehicle. Scale bar = 60 mm. (**C**) Video frame sequence showing the morphing drone driving in State 1, transforming into the flying state, then taking flight in State 2. Scale bar = 100 mm. (**D**) Image sequence showing the transformation from State 1 to State 2, top row shows images the bottom row shows IR images. Scale bar = 60 mm. 98

4.5 **Morphing and deployable underwater machine.** (**A**) Photographs of the distinct functional states of the underwater morphing machine with a schematic showing the machine cross section. State 1 is a compact, retracted configuration for storage. State 2 is a functional deployed machine for underwater locomotion and cargo collection. Scale bar = 20 mm. (**B**) Image sequence showing the independent morphing, shape-fixing, and reversibility of the top and bottom sides on the machine. (**C**) Images showing multifunctionality of the machine which can deploy through instantaneous shape-morphing and fixing, propel through water jetting, and reverse to a retracted state through integrated heaters. Scale bar = 20 mm. (**D**) Demonstration of the multifunctional underwater morphing robot which is deployed, locomotes through water propulsion and buoyancy control, obtains cargo, and is retrieved (tubing is cropped out for clarity beyond the first image). (**E**) After retrieval, the cargo is emptied and the machine is connected to a power source to activate reversibility to return to the original, retracted state. 100

5.1 a) Schematics of rigid particle composites, b) suspension composites, and c) hybrid composites. d) Mechanical and magnetic comparison of surveyed materials [368, 370, 371] and materials used in this paper. e) Deformed stretchable planar inductor with magnetic backplane. 116

5.2 Micrographs of a) hematite rigid particle composite, b) hematite suspension composite, and c) hematite hybrid composite. Scalebars represent the same length for Figures a-c. d) Representative Sendust stress-strain data for rigid particle (R.C.), suspension (S.C.), and hybrid (H.C.) composites. e) Tensile modulus vs rigid particle volume loading comparing the three classes of magnetic elastomers produced in this work. Symbols are experiment data points while the dotted and dashed lines are predictions from Equation 1. 119

5.3 a) Measured relative permeability of suspension and hybrid composites for a given $\Omega_{composite}$. b) Soft inductor fabrication schematic. c) Cyclical power transfer testing of coupled stretchable inductors. d) Strain vs time for cyclical power transfer test. Maximum strain is increased by 10 % for each cycle. . . 123

5.4 a) Wireless power transfer between soft transmitter and rigid receiver. b) Locations of wearable devices produced for this work. c) Rigid receiver coil and integrated LED. d) Wireless power demonstration of athletic armband. e) Wireless power transfer and reliability demonstration of wireless power transfer glove. 125

6.1 **Material structure and properties. a)** Schematics of rigid particle composite (RC), **b)** magnetorheological fluid composite (FC), and **c)** hybid composite (HC) material architectures. **d)** Effect of zero-field modulus on the relative MR effect of the materials tested in this work (E_{mag} = 530 kPa for Equation 2). **e)** Change in stiffness of an RC MRE with no field applied and with a magnetic flux density of 0.75 T. f) Image of a hybrid composite magnetorheological elastomer utilizing magnetorheological stiffness tuning to realize a shape memory effect. **g)** SEM image of hybrid composite MRE. The image is artificially colored red for the magnetic elastomer phase and blue for the MR fluid phase. An unaltered image can be found in Figure E.2. 135

6.2 **Magnetorheological elastomer characterization. a)** Schematic of the magnetic compression fixture used to determine magnetorheological properties in this work. **b)** FEA analysis for RC and HC MREs to determine the magnetic flux density and uniformity throughout the compression specimen. **c)** Compressive stress-strain curves of Ecoflex RC, **d)** FC, and **e)** HC MRE with 0 and 280 kA m^{-1} applied fields. **f)** Tunability of zero-field modulus with respect to material architecture for constant elastomer matrix modulus. **g)** Tunability of zero-field modulus with respect to matrix modulus with constant material architecture. 140

6.3 **Magnetorheological stiffness tuning. a)** Range of achievable moduli of MREs as a function of their zero-field modulus. The bottom of the floating bars indicate the zero-field modulus of the sample, while the top of the bars correspond to the measured modulus with an applied field of 280 kA m^{-1}. **b)** Maximum measured magnetorheological enhancement ratio as a function of zero-field modulus for the materials tested in this work as well as literature data (E_{mag} = 530 kPa for Equation 1).[57, 158, 178, 425, 428] 141

6.4 **Adaptive MRE gripper. a)** Schematic of an adaptive gripper consisting of an HC MRE membrane and an incorporated air pocket and test fixture. **b)** Images of the adaptive gripper grasping a tomato, **c)** a Lego brick, **d)** a marker, and **e)** a cluster of grapes. 144

A.1 Micrographs and associated particle size distributions for a) Ecoflex ϕ = 40% (n = 42 droplets) b) Ecoflex ϕ = 80% (n = 35) c) Sylgard ϕ = 40% (n = 38) and d) Sylgard ϕ = 80% samples (n = 49). 226

A.2 Energy disperse X-ray spectroscopy spectra of Ecoflex ϕ = 80% aged for two weeks in **a)** ambient, **b)** freshwater, **c)** saltwater, **d)** concentrated saltwater environments. 227

A.3 Strain at break of Ecoflex LM composites and d-f) Sylgard composites. Error bars represent standard deviation for n = 3. 228

A.4 Pressure pot setup for hydrostatic testing. 228

A.5 ϕ = 40% remains nonconductive after 1 hour at 3 atm in a pressure pot. . . 229

A.6 ϕ = 80% remains nonconductive after 1 hour at 3 atm in a pressure pot. . . 229

B.1 **Liquid metal droplet micrographs.** Rows show different LM volume loadings (ϕ = 20, 40, 60%) and columns show different LM droplet sizes (d = 2, 15, 60 µm). Scale bar is 50 µm. 231

B.2 **LM composite particle analysis.** From top to bottom: Analyzed SEM image of composite with smallest particles (ϕ = 20%), analyzed micrograph of composite with medium-sized particles (ϕ = 60%), analyzed micrograph of composite with large particles (ϕ = 60%), with associated major droplet diameter histograms with Gauss and lognormal fits. All scale bars are 50 µm. 232

C.1 **Modeled and fabricated samples.** CAD models and fabricated sample images of three different kirigami configurations including uni-axial, bi-axial, and tri-axial designs. 234

C.2 **Self-healing evaluation through cyclic fracture/healing testing.** (**A**) Normalized stiffness as a function of cycle number. The average normalized stiffness value of three composites is included for each cycle. We intentionally break then heal the endoskeleton by vacuum-assisted thermal healing before each cycle. Error bars represent the standard deviation for n = 3. (**B**) Microscopic images of a fractured then healed point before cycle 4, (**C**) before cycle 7, and (**D**) before cycle 10. 235

C.3 **Cyclic loading test of unpressurized kirigami composite.** The normalized effective stiffness of an unpressurized kirigami composite as a function of loading cycle. 236

C.4 **Poor crack healing of an unpressurized system.** Optical micrographs of a LMPA endoskeleton beam in an unpressurized kirigami composite (**a**) before and (**b**) after thermal healing. The composite is tested under uni-axial loading 10 cycles before taking micrographs. The large void is created due to interfacial phenomena (*e.g.*, oxide formation). 237

C.5 **Excellent crack healing of a pressurized system.** Optical micrographs of two LMPA endoskeleton beams in a pressurized kirigami composite. The composite is tested under uni-axial loading 10 cycles and shown to have no substantial fractures and voids. (**a-b**) We intentionally fracture two beams and characterized thermal healing capability. (**c-d**) After the thermal healing process, the cracks are effectively recovered. (**e-f**) Through a vacuum-assisted thermal healing process, the cracks are fully recovered. 238

C.6 **Tensile loading test.** Plot of load as a function of applied strain. After $\varepsilon_{appl} = 50$ % is applied to the composite, the sample is unloaded at different rates $\dot{\delta}_{UL} = 0.005$, 0.01, 0.05, 0.1, 0.325, 0.55, 0.775, and 1 mm s^{-1}. 239

C.7 **Shape-fixing capability.** Plot of shape-fixity ratio as a function of unloading rates for $\varepsilon_{appl} = 50$ %. The data is obtained from Fig. C.6, and the fixity ratio is calculated using Equation 2. Error bars represent the standard deviation for $n = 3$. 240

C.8 **Material calibration of elastomer.** Comparison of experimental and FE model of elastomeric material of kirigami in (a) engineering and (b) true stress-strain frameworks. 241

D.1 Micrograph of a 33 % by volume propylene glycol in Ecoflex composite demonstrating immiscibility. 243

D.2 Magnetic comparison between rigid particle composites (R.C.) and suspension composites (S.C.) at the same $\Omega_{composite}$ = 15 %. The rigid particle and suspension composites were found to have similar permeabilities at the same rigid particle volume fractions of $\Omega_{composite}$ = 15 %. 244

E.1 **MRE response time. a)** Schematic of magneto-response testing fixture. Hall effect circuit activates LED in response to a magnetic field from the electromagnet. **b)** Measured response of MRE to applied magnetic field. MRE begins to respond within 21 ms of magnetic field activation. Full actuation of the MRE is measured to be 322 ms. 246

E.2 **Hybrid composite MRE microstructure.** Scanning electron microscopy (SEM) of hybrid composite MRE cross-section. **a)** Uncolored SEM. **b)** Artificially colored hybrid composite MRE from Figure 1g. The magnetorheological fluid droplets are determined as the regions where elastomer is not visible on the surface. 247

E.3 **MREs with diverse microstructure.** SEM images of RC, FC, and HC MREs at different depths of the material (magnification = 1500x). 248

E.4 **Microstructural imaging at lower magnification.** SEM images of RC, FC, and HC MREs at different depths of the material (magnification = 250x). 249

E.5 **Magnetic flux density through MRE samples. a)** Finite element analysis of MRE testing fixture. **b)** Average magnetic flux density through compression testing specimens. 250

Chapter 1

Soft Robotics: A Futuristic Extension of Stretchable Electronics Technology

Modified from a manuscript in preparation.

Edward J. Barron III[1,2] and Michael D. Bartlett.[1,2] Soft Robotics: A Futuristic Extension of Stretchable Electronics Technology. *In preparation*, 2023.

1. Macromolecules Innovation Institute, Virginia Tech, Blacksburg, VA 24061, USA.
2. Mechanical Engineering, Soft Materials and Structures Lab, Virginia Tech, Blacksburg, VA 24061, USA.

1.1 Introduction

Stretchable electronics have been a topic of interest for decades, with much work being done to determine how to create devices that can be mechanically deformed while accomplishing tasks capable by modern devices such as sensors, computers, and smart phones. In contrast to traditional rigid electronics, stretchable electronics allow for greater freedom of application in human-machine interfacing, such as the ability to place sensors on high deformation regions of the human body, or in sensitive regions for medical applications.[1, 2] The development of stretchable electronic devices requires the ability to create multi-functional material systems

capable of achieving functional properties such as electrical and thermal conductivity while maintaining a low mechanical stiffness and high strain limit. Research into these materials has been successful in recent years, which has not only advanced understanding of stretchable electronics technology, but has also enabled emerging technologies such as soft robots. Soft robotics has been an area of study that has proceeded largely in tandem with soft electronics, and these machines maintain unique contrasts with traditional robots, with many examples allowing for bio-inspired functions, safer human-machine interaction, and the ability to adapt their properties and function to accomplish diverse tasks.[3, 4, 5, 6] As soft robotic research began, the difference between soft and conventional machines was relatively minimal, largely due to the lack of soft functional materials technology available at the time.[7] However, with the evolution of stretchable electronics came the rise of soft multi-functional materials which have allowed for significant advances in robots such as self-healing,[8, 9, 10] high deformability,[11] and passive adaptivity,[12] which has given rise to an emphasis of research into soft machines.[13]

To understand the evolution of soft robots, it is useful to understand the research behind stretchable and flexible electronics and the innovations in soft functional materials. Traditional electronics require functional components such as wiring to transfer power to electronic devices, heat transfer components such as heat sinks that prevent overheating, and often times magnetic materials which improve the efficiency of electromagnetic components. However, the materials that possess the most outstanding electrical, thermal, and magnetic properties are rigid metals and ceramics, which are useful for traditional electronics but are a limiting factor in the development of stretchable electronics and soft robots. The ability to produce deformable electronics has largely occurred through the creation of material systems through three techniques: 1) deterministic geometries, such as the patterning of rigid functional materials to globally deform to relatively high strain rates without catastrophic

local deformation, 2) intrinsically stretchable materials, such as the chemical synthesis of intrinsically soft and conductive polymers, and 3) soft composites, including the fabrication of composites that utilize functional fillers in highly extensible polymers.[14, 15]

1.1.1 Deterministic geometries

Through deterministic geometries, rigid electronic materials are architectured to take advantage of the comparatively low strains in bending to create stretchable systems.[11, 16, 17, 18] Examples of this technique include wrinkled or buckled structures, where thin rigid materials undergo out of plane bending to realize large global deformations. These techniques often use thin (< 1 µm) functional materials such as single crystal semiconductors integrated with soft elastomer substrates, allowing the material system to undergo substantial global deformation while maintaining local strains of less than < 1 % in the functional material.[19, 20] Rigid materials can be added to a pristine flexible substrate for material systems with high degrees of bending, or added to a pre-strained substrate to allow for further axial deformation by leveraging material buckling.[21, 22] In addition to wrinkled geometries, other patterns include the creation of serpentine structures and fractal patterns which allow for tensile stretching and twisting.[23, 24, 25] A recent engineering technique used to create deformable electronics has evolved from kirigami, or the art of paper cutting.[26, 27] The technique of applying engineered cuts is scalable, works on a diverse number of materials, and can be applied to rigid functional materials to enable extensibility for flexible electronic components.[26, 27, 28, 29] In addition to electronics, kirigami has been utilized to create muti-functional materials capable of improving soft robots, such as through improving actuation and shape change.[30, 31, 32]

1.1.2 Intrinsically stretchable materials

Intrinsically soft and functional polymers have been synthesized for electronics applications. These polymers are typically semiconducting or electrically conductive and are largely synthesized as π-conjugated polymers, often leading to semi-crystalline morphologies.[33, 34] These intrinsically stretchable materials are often less deformable than other approaches, but this can be improved by integrating with an elastic substrate or through approaches like confinement which give more molecular mobility.[34, 35, 36] Another form of conductive polymers are ionic hydrogels and ionogels which utilize electrolytic solutions or ionic liquids.[37, 38] These polymers can be highly elastic, soft, and are capable of the deformation needed for many stretchable electronics applications, however, these intrinsically functional soft polymers often struggle to approach the conductivity of rigid conductors ($\sim 10^{-1}$ Ωm), with their strength instead focused on speed of signal transmission ($\sim 10^{-8}$ s).[37, 39]

1.1.3 Soft composite fabrication

Composites have also been used to create soft functional materials. These composites often rigid functional fillers such as metallic or ceramic nano and micro-inclusions including particles,[40] flakes,[41, 42] wires,[43] or nanotubes as inclusions to soft extensible polymers such as gels and elastomers.[44] These materials can be made thermally conductive for heat transfer applications such as thermal pads and interface materials.[45, 46] Electrically conductive soft composites can be created by utilizing a sufficiently high volume fraction of conductive filler to reach the percolation threshold, where a continuous electrical pathway is created by the rigid inclusions.[47, 48, 49] One downside to this approach is that there is a fundamental trade-off between the mechanical and functional properties of soft composites, where the high volume fractions of functional inclusions often necessary to achieve

desirable properties lead to a significant stiffening of the composite and a decrease in the strain limit of the material.[50] Additionally, the functional properties can vary or, in the case of electrical conductivity, become eliminated with high deformation due to the strain-dependent microstructure. One recent method utilized to overcome some of these problems has been through the use of functional liquid inclusions. By utilizing fluids instead of rigid particles, soft functional composites can be highly loaded with filler while still maintaining low stiffness and high extensibility.[51] The creation of these solid-fluid composites requires the utilization of fluids with sufficient functionality which has been carried out with room temperature liquid metals and low melting point alloys that have high thermal and electrical conductivities,[9, 52, 53, 54, 55] as well as with magnetic fluids to impart magnetic response.[56, 57, 58]

The evolution of soft robots and machines has occurred in tandem with advancements in soft functional composites. Recent soft machines have shown incredible properties, such as the ability to self heal after damage events,[9, 60, 61] reconfigure shapes to adapt to different tasks,[60, 62] and passively grasp objects of a variety of shapes.[63, 64] Many of these abilities rely on the materials science advances of functional composite materials which allow for functional and adaptive response on the material level. The precursors to soft robots were actuators which generally used a combination of rigid components and selectively placed compliant regions rather than being developed entirely by soft materials.[7, 65] As research into active soft systems evolved, actuators and artificial muscles began to become more commonly researched, with many made out of nearly entirely soft systems such as by utilizing pneumatic devices to activate rubber-based actuators.[66, 67, 68, 69] With the advancement soft composite materials, there is more flexibility in the creation of state of the art soft robots and machines. Pneumatic systems are still heavily utilized in soft robots,[70, 71] but in addition to these devices there have been composites that can accomplish material level shape

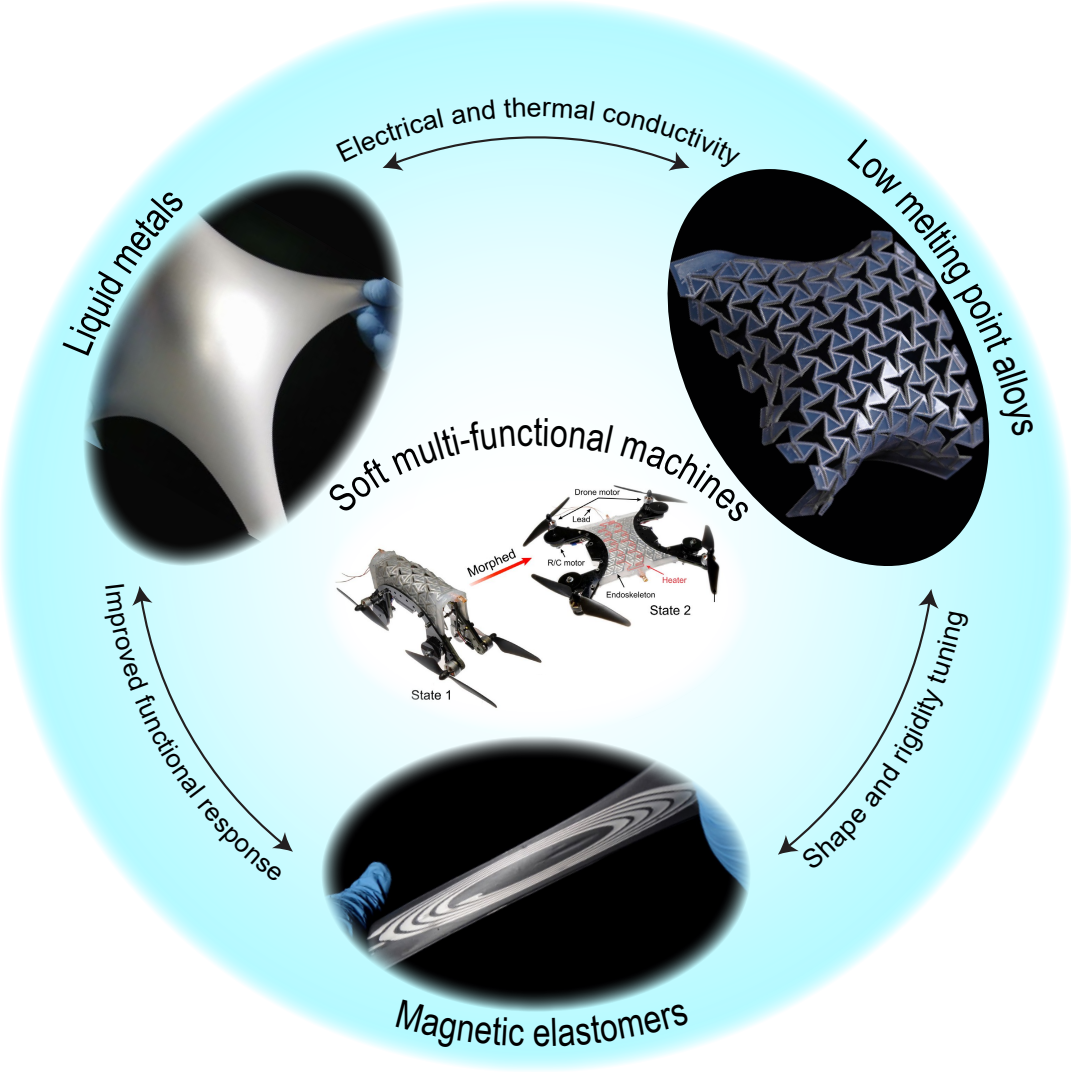


Figure 1.1: **Soft functional and active materials.** Multi-functional composites utilize fillers such as liquid metals, low melting point alloys, and magnetic particles and fluids to allow for deformability, thermal, electrical, and magnetic material properties, and adaptive response for electronics and machines. **Top left image:** A liquid metal elastomer composite with high thermal conductivity. Open access article.[59] **Top right image:** A low melting point alloy composite with shape morphing capabilities. Adapted from an article published in *Science Robotics*.[60] **Bottom image:** A magnetic elastomer composite with liquid metal conductive channels. Reprinted (adapted) with permission from [56]. Copyright 2020 American Chemical Society. **Center image:** A multi-component shape morphing material integrated with on-board power and control to enable a morphing drone. Adapted from an article published in *Science Robotics*.[60]

change, stiffness tuning, and actuation via electrical, thermal, and magnetic stimuli.[72, 73, 74] The integration of these materials together into multi-component systems significantly increases the potential of machine design, and opens pathways for the intelligent design of the next generation of robots with unique properties not capable of being accomplished with traditional robotic systems.

In this chapter, we will discuss the fabrication, microstructure, and properties of composite materials that enable soft robots and machines. First there will be a discussion of elastomer composites that utilize room temperature liquid metals for high thermal and electrical conductivities in soft and extensible systems for deformable wiring and efficient heat transfer in soft robots. We will then discuss composites with low melting point alloys (LMPAs), which are defined as solids at room temperature with melting points slightly above room temperature. These materials allow for similar increases to functional properties seen in liquid metals, while also allowing for adaptivity in rigidity and shape. We will then discuss magnetic elastomer composites which utilize magnetic fillers to control magnetic circuits and enable adaptive properties such as rapid shape change and stiffness tuning. To finish, multi-component composites which utilize a combination of several functional materials in a single system will be discussed, which allow for diverse capabilities for soft machines.

1.2 Liquid metal-elastomer composites

1.2.1 Liquid metal

Metals have long been used in engineering because of their mechanical strength which lends well to structural applications, as well as their functional properties in electronics, such as copper's use in traditional wiring, and aluminum's use as heat sinks for electronics. However,

not all metals exist solely as solids at room temperature. Elements such as mercury (T_m = -38.8 °C), francium (T_m = 27 °C), cesium (T_m = 28.5 °C), gallium (T_m = 29.8 °C), and rubidium (T_m = 39 °C) are metals that exist as liquids at or near room temperature.[75, 76, 77] While liquid-metals offer intriguing possibilities for soft functional composites, many of these materials have inherent problems. Francium is radioactive and chemically unstable, with a half-life of $\sim$ 20 min, while cesium and rubidium are explosively reactive which limits their use.[78] Mercury is perhaps the most well known of these materials due to its heavy usage in past devices and materials such as thermometers and dental amalgam.[79, 80]. However, mercury's toxicity render it unfeasible for many modern and emerging devices such as wearable and bio-electronics.

Gallium is an intriguing alternative material that liquefies near room temperature, has the low toxicity necessary to be used as contrast agents and in pharmaceuticals, and produces desirable functional properties.[81] Of particular importance for soft systems is gallium's ability to readily alloy with a wide variety of metals which can be utilized to reduce its melting point.[78] Two increasingly studied gallium alloys are Eutectic Gallium-Indium (EGaIn) and Galinstan, which are both liquids at room temperature. These liquid metals (LMs) maintain low toxicity, and have near zero vapor pressure.[78] These alloys have been used for cooling of electronic components in replacement of thermal pastes, and have been proposed for medical and pharmaceutical applications. EGaIn (T_m = 15.7 °C) is a an alloy of gallium (75 wt %) and indium (25 wt %) with an electrical conductivity only an order of magnitude below copper ($\sigma = 3.4 \times 10^6$ S m^{-1}) and a thermal conductivity of (k = 26.4 W m^{-1} K^{-1}).[82, 83] Galinstan is composed of gallium, indium, and tin and can have various mixing ratios that can change its melting behavior with a typical composition of 68.5 wt % Ga, 21.5 wt % In, and 10 wt % Sn.[82] Galinstan often possesses a lower melting point (T_m = -19 to 10 °C), a similar electrical conductivity ($\sigma = 3.5 \times 10^6$ S m^{-1}), and a relatively high thermal

conductivity (k = 16.5 W m^{-1} K^{-1}) when compared to EGaIn but also posesses a lower boiling point ($T_b \simeq$ = 1300 °C).[82, 84]

EGaIn and Galinstan possess interesting mechanical properties that allow for a variety of use cases. Both EGaIn and Galinstan have low viscosities at about twice that of water (2.0×10^{-3} and 2.4×10^{-3} Pa s respectively) which allows for them to be processed similarly to many fluids.[82] However, in contrast to many traditional liquids, these LMs also rapidly form a solid oxide skin on their surface in the presence of oxygen, with a thickness on the order of nanometers.[78, 85] This oxide skin can provide a unique mechanical stability to the liquid that allows for further avenues of processing. LM can be spray-coated onto surfaces utilizing similar methods to airbrushing with paints, which allows for thin layers of the material to be patterned into conductive circuits.[86] The LMs can also be injected into channels that are patterned into a material utilizing methods such as applying positive pressure through a syringe, or utilizing vacuum assisted filling.[87, 88] There are also direct printing techniques that can be utilized to print 3d structures that have free-standing mechanical stability because of the oxide skin of the material.[89] While LMs can be processed independently, it has become increasingly common to utilize these functional fluids as inclusions in elastomers for soft electronic devices and robots, which allow for a combination of LM functionality while providing solid-state stability and containment for the LM.

1.2.2 Composite processing, structure, and properties

The combination of LM functionality and distinct mechanical response allows for unique processing and microstructure-dependent properties for LM-elastomer composites. One common method for the fabrication of LM composites is through shear mixing of liquid metals into an elastomer to produced micro-dispersed composite architectures.[90, 91, 92, 93] During

shear mixing, bulk LM breaks up into smaller droplets, where the final composite will be composed of discrete micro-droplets within the elastomer matrix. The average diameter of LM droplets can be controlled by the mixing speed, where higher rates of mixing allow for smaller mean droplets.[53, 93, 94] Through shear mixing alone, LM droplets are often in the range of 1 to several hundred micrometers, however other processing techniques can be used to further decrease particle size.[53, 93, 94] Nano-scale LM droplets can be fabricated prior to mixing into the elastomer by methods such as sonication which provide high intensity energy for further droplet break-up.[93, 94, 95]

Micro-dispersed LM composites can be created with exceptional functionality because of their ability to achieve high inclusion volume fractions of up to 90 %.[96] The LM in micro-dispersed samples exist as discrete droplet domains with insulating elastomer existing between each droplet leading to samples that can achieve enhanced thermal conductivities ($k \sim 1.5$ W m^{-1} K^{-1}),[59, 97] however these samples can remain electrically insulating (relative permittivity, $\epsilon_r \sim 1$ - 100) due to a lack of continuous electrical pathway which is particularly enabling for heat transfer in electronics devices.[59, 93]

The thermal conductivity and dielectric constant of these materials can be increased by elongation of the inclusions to create anisotropic samples, with high aspect ratio inclusions being responsible for some of the highest thermal conductivities reported in literature for soft, electrically insulating systems ($k \sim 13$ W m^{-1} K^{-1}).[52] Utilizing LMs allows for several unique opportunities to control inclusion shape. For example, the shape of micro-dispersed LM inclusions can be tuned through mechanical deformation (Figure 1.2a) where the droplets elongate in the direction of strain. [59] This allows for strain-dependent heat transfer characteristics that can be enabling for tunable electronics. However, in traditional thermoset elastomer composites the material will return approximately to its original state upon the release of stress. One method for producing these highly elongated LM inclusions in a stress-

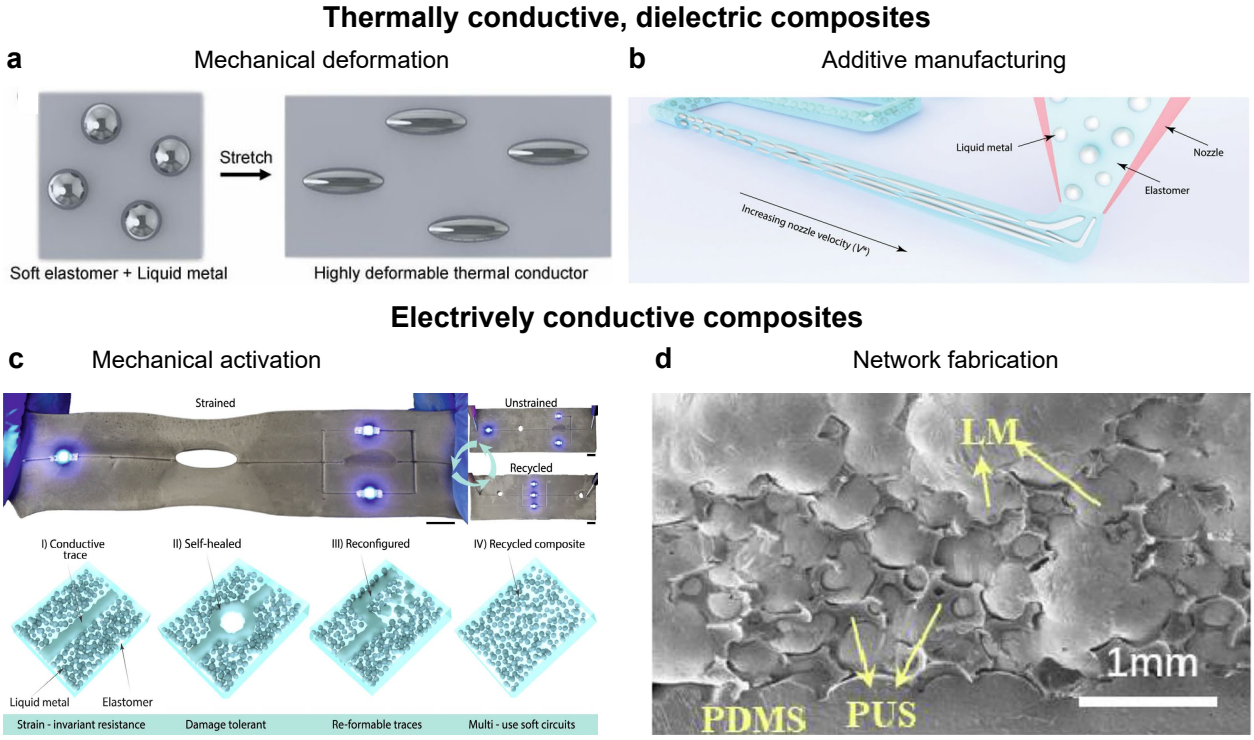


Figure 1.2: **Liquid metal elastomer composites.** Thermal conductivity of LM composites can be improved through micro-structure control: **a)** Change in droplet shape by mechanical deformation. Open access article.[59] **b)** Programmed properties through additive manufacturing approach. Open access article.[98] Electrical conductivity can be enabled by formation of a connected LM network: **c)** Mechanical activation can cause a percolated network of LM inclusions. Open access article.[99] **d)** Fabrication techniques can be employed to create as-prepared connected networks. Reproduced with permission. Copyright 2019 Elsevier.[100]

free state is through the use of thermoplastic elastomers. These materials can be processed to contain highly elongated droplets in a stress-free state by deforming the sample to produced elongated inclusions, followed by annealing the thermoplastic elastomer to eliminate residual stress.[52] Additionally, the shearing of the uncured LM-polymer emulsion can elongate the droplets, while the rapid formation of gallium oxide imparts mechanical stability to the individual droplets which is believed to inhibit the ability of surface tension to rapidly return the droplet to its spherical shape. Upon curing the elastomer the LM droplets are fixed into shape. This method is especially useful as it can be used with additive manufacturing

methods such as through direct ink-write printing (Figure 1.2b) which allows for spatially programmable thermal properties by controlling print parameters.[98]

Although as cast LM composites are typically electrically insulating, these materials can be made electrically conducting through post-processing. This type of electrical activation process was initially accomplished with LM droplets on a surface (not embedded in a composite) through a method referred to as mechanical sintering, where pressure is applied to cause rupture of the LM droplets which form a percolated conductive network.[101, 102, 103] LM composites can also be mechanically activated.[9] The activation pressure is dependent on the stiffness of the elastomer, the volume fraction of LM,[53] and the size of the dispersed droplets.[101] Softer LM composites have generally been shown to be more challenging to activate, as they resist rupture of the LM inclusions,[104] where low volume fractions can be challenging to activate and decreased droplet size increase the activation pressure required. LM composites can also be created to activate upon the application of strain, realizing 10^8-fold increases in conductivity after activation strains of 50%.[102] Techniques such as embossing which utilize stamps to selectively apply pressure to the composite can be utilized, to create circuits with local conductive patterns by activation pressure (Figure 1.2c).[99] Similarly, local activation can be achieved through writing techniques that apply sufficient surface pressure to hand-sinter.[105] Interestingly, these materials can also be self healing, with damage events causing further percolation of droplets allowing for instantaneous healing of conductivity.[8, 9, 99]

LM composites can also be fabricated as electrically conductive materials through fabrication techniques that create a continuous LM network. One method to accomplish this is to utilize porous materials such as sugar which can intake LM or elastomer into their pores under vacuum. If LM is used to infiltrate the pores of the sugar, a subsequent step can be used where the LM is solidified below its melting temperature to hold shape and the sugar

can then be dissolved in water.[106] The LM can then be penetrated and encapsulated with elastomer. If elastomer is used to infiltrate the pores of the sugar, the elastomer can be cured to hold shape, and LM can then be pulled into the elastomer.[107] Polymeric materials with 3D interconnected networks such as a polyurethane sponge (PUS) can also be purchased and infiltrated with LMs through vacuum to form a continuous network (Figure 1.2d).[100] Additionally, multiphase systems can create electrically conducive composites as fabricated. This includes approaches where Ag flakes and LM are used together, the Ag flakes bridge between the LM droplets and are electrically conductive.[108]

1.2.3 Liquid metal elastomer composite applications

The functional properties of LM composites are enabling for soft electronic and robotic applications.[14, 109, 110] Thermally conductive LM-elastomer composites are capable of more efficient heat transfer than traditional elastomers, which can be utilized to improve the efficiency of soft machines.[50, 52, 92, 111, 112, 113] These materials are utilized to keep electronics such as high-powered LEDs cool and prevent overheating which can cause failure of the electronics.[52, 97] These materials have also been utilized to transfer heat away from heat-activated artificial muscles, keeping them cooler to enhance comfort for body-integrated devices as well as to speed up actuation cycles.[52, 59] Electrically conductive LM composites can be used to create mechanically compliant circuits capable of being interfaced with the human body.[1, 114, 115, 116] In one example, conductive composites were utilized to create a body-worn triboelectric nanogenerator, where EGaIn was allowed to preferentially settle onto one side of the composite to create a conductive region and a dielectric region.[117] The triboelectric generator uses the EGaIn-rich side of the composite and human skin as electrodes separated by the layer of dielectric silicone elastomer. Deformation by the human body is then used to generate current capable of powering wearable devices.[117] LM can also

be utilized for shape change and actuation by taking advantage of its solidification at low temperatures.[118] In this work, anisotropic composites that utilize an EGaIn-rich phase and an elastomer-rich phase can be utilized to create shape morphing materials. The material can be pre-stretched and then frozen to solidify the LM, which causes the material to fix into place. Phase change in the LM can be caused by either heating or utilizing a laser on the composite, which causes the composite to change shape.[118] Electrically conductive soft composites can also be used to create self healing robots and electronics,[8, 99, 119, 120] such as where a soft robot was created by utilizing the LM composite as conductive wiring and integrating the robot with soft actuators and on-board control.[9] Upon damage events to the soft wiring, percollation of the LM inclusions occur, instantaneously repairing the conductive pathway without external intervention and allowing the robot to continue functioning.[9]

1.3 Low melting point alloys

Low melting point alloys (LMPAs) are similar materials to liquid metals, and can be used to impart conductivity to soft composites as well as to allow for adaptive responses such as changes in stiffness and shape through phase change. LMPAs are generally considered to be metals with melting points bellow 300 °C,[41] however for this work we will distinguish LMPAs from LMs by focusing on alloys with melting points bellow 100 °C that are solids above room temperature (25 °C). As such, we will not discuss LM alloys that are a liquid at room temperature such as EGaIn and Galinstan.

Gallium is a solid at room temperature,[121] but its melting point of 29.8 °C is often too low for robotic applications, as the material may experience an undesireable transition due to the heat from electronics components or weather. Bismuth-based LMPAs are strong options for soft robotic systems, as there are several candidates with melting points between 60 and

150 °C.[121] A preferred LMPA used for stiffness tuning materials is known as Field's metal which is an alloy of 32.5% bismuth, 51% indium, and 16.5% tin by weight.[91, 122, 123] Field's metal is a desirable choice as it achieves a melting temperature of 62.5 °C,[122] which is low enough that a transition can be accomplished at relatively small timescales with on-board heaters while high enough to withstand environmental temperatures without unplanned phase transition.

Much like LMs, LMPAs can possess desirable functional properties with Field's metal producing high thermal ($k \sim 19.2$ W m^{-1} K^{-1}) and electrical ($\sigma = 1.92 \times 10^6$ S m^{-1}) conductivities at room temperature.[121] The high thermal conductivity and phase change behavior of Field's metal has made it an attractive candidate for heat transfer in electronics and larger systems. LMPAs can also be utilized as thermal buffers for electronics which can absorb or release heat during phase change.[124] The low melting point and high electrical conductivity has also made Field's metal a desirable candidate for non-toxic, lead-free solder.[125] Similarly, Field's metal has been studied for its ability to be used as electrical contacts through 3D printing methods. While electrodes on traditional electronics such as solar cells are often deposited through thermal evaporation, Field's metal has been shown to be printable through direct ink-write printing to produce electronics with similar performance to the state of the art counterparts.[126] The emergence of soft electronics and robots has created new opportunities for LMPAs which have enabling properties for these systems, and has resulted in the use of LMPAs for soft composites. Solid-state LMPAs are particularly enabling for soft robots as they can be transitioned from solid to liquid state with the input of thermal energy. By utilizing these materials as inclusions to elastomer composites, the solid-liquid phase transition can be leveraged to tune stiffness and create reconfigurable materials that can lock into different shapes.[121, 122, 127, 128, 129, 130, 131]

1.3.1 Fabrication and structure of LMPA composites

The integration of LMPAs into elastomers allows for an increase in thermal and electrical conductivity of the composite as well as large magnitude stiffness change, where the elastomer gives containment to the LMPA during its liquid state. The fabrication strategies of LMPAs are diverse, owing to its ability to be processed as in either their solid or liquid form. One method for creating these composites is through encapsulation of the LMPA, where the LMPA is solidified and elastomer is placed around the solid-state LMPA.[127] The LMPA can be fabricated into complex shapes by molding of the LMPA in its liquid state, followed by subsequent cooling. Another method of fabricating these composites is by introducing the LMPA into pre-patterned elastomer channels (Figure 1.3a) which can be accomplished through several methods.[132] One method is by patterning an elastomer with channels that contain both an inlet and outlet hole.[133, 134] The LMPA can be melted over the inlet chamber and positive pressure can force the LMPA through the channel which can then be cooled and sealed.[54] Another method is to create channels with a single access port.[60] LMPA can be placed on the access port and melted in a vacuum oven, which will pull air from the channels that are then filled with LMPA. Another method is to utilize a heated syringe. By outfitting a resistive heater onto a syringe, the LMPA can be melted and injected into channels in its liquid state.

Recently, composites have also been made by utilizing LMPA micro-particles (Figure 1.3b) that are dispersed throughout a polymer matrix. LMPAs can be processed into particles through several methods including shear mixing and sonication. One method utilizes a combination of an overhead mixer and homogenizer. Fields metal is added to a container with heated water kept at 90 °C from an oil bath. The homogenizer is utilized to shear the bulk material into smaller particles while the overhead mixer is utilized to keep particles suspended and will mixed to ensure passage through the homogenizer. The particles are allowed to cool

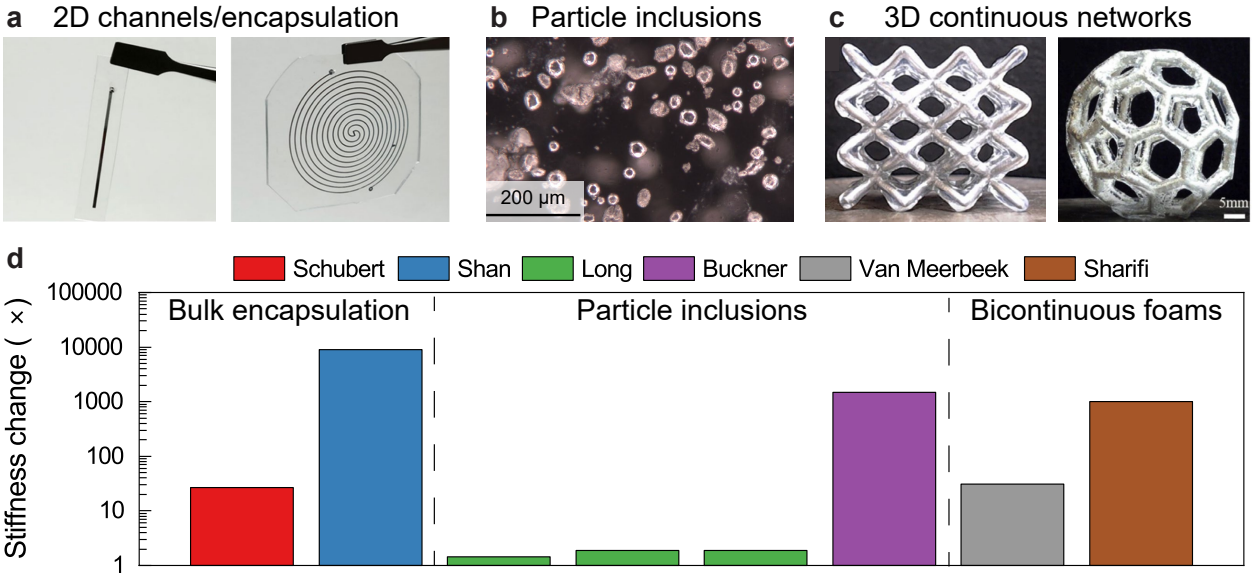


Figure 1.3: **Low melting point alloy composites.** Composites have been developed through: **a)** Fabrication of LMPA channels in elastomer. Reprinted (adapted) with permission from [132]. Copyright 2021 American Chemical Society. **b)** The creation of LMPA particles for dispersion into elastomer. **c)** 3D continuous networks of LMPA in elastomer. Reproduced with permission. Copyright 2020 Elsevier.[135] **d)** Stiffness change of LMPA composites of various microstructures, data from various sources.[54, 55, 122, 127, 136, 137]

during overhead mixing. This method produced particles with a large size distribution from 10 to 800 µm.[122] Field's metal micro-particles have been also been fabricated by a technique known as shearing liquids into complex particles (SLICE).[138] Field's metal was added to a 5 % aqueous acetic acid solution and heated to 95 °C before being shear mixed to produce particles with average diameters of 12.6 ± 8.9 µm. Another way of producing Fields metal particles is through sonication. Fields metal can be added to water at 70 °C, and an ultrasonicator can be used to break up the droplets. This has been utilized to produce Field's metal droplets with average diameter of 1.19 µm.[139] A similar method utilizing a large viscosity continuous phase (polyalphaolefin) instead of water has been used to create fields metal nano-particles with average diameters as low as 15 nm.[140] After creating the LMPA particles, they can then be dispersed through the elastomer by mixing, where the composite can then be set into a desired shape through molding.[122] In addition

to molding, the shape of these LMPA micro-particle composites can be created through additive manufacturing techniques such as direct ink-write printing.[136]

LMPA-elastomer composites have also been created in unique structures such as 3D continuous networks (Figure 1.3c).[135] These can be created through a multi-step process where first a sacrificial lattice structure is 3D printed and an investment mold is cast around the part. Next, the sacrificial lattice can be burnt out of the mold, and the mold can be infiltrated with LMPA at elevated temperature. Lastly, the investment mold can be removed from the LMPA, and the LMPA can be coated with elastomer.[135] In addition to macro-scale geometries, 3D continuous networks can also be formed at the micro-scale in the form of bi-continuous foams.[55, 137] Making these foams is a multi-step process, where open-cell foams can be created by mixing uncured elastomer precursor with grains of salt. The elastomer can then be immersed in water to dissolve the salt inclusions and leave pores.[137] The LMPA is then heated into its liquid state, and the elastomer foam is submerged in the LMPA under vacuum to draw the LMPA into the material. By controlling pore size, the mechanical properties of the composite can be tuned, where larger porosity can result in a greater dependence on the modulus of the LMPA and a lower dependence on the modulus of the elastomer. The opposite processing technique can also be used, where salt can be added to the LMPA to produce an LMPA foam which can then be infiltrated with liquid elastomer precursor prior to curing.[55] This technique produces a more continuous LMPA structure.

1.3.2 LMPA composite stiffness tuning

LMPA composites possess some of the highest magnitudes of stiffness tuning among active materials due to their ability to tune from liquid-state inclusions with low storage modulus to solid state inclusions on the order of GPa.[74, 121, 131] The response time of LMPA

composites is generally dependent on the melting point of the LMPA used, the mass of LMPA in the composite, and the heating mechanism utlized to drive the phase transformation, and has been reported to be as fast as 0.5 s or as slow as ∼10 min.[54, 60] The response time to cool the composite from liquid to solid state can also be on the order of minutes. The stiffness tuning capability of LMPA composites can be up to 10,0000x for encapsulated systems (Figure 1.3d).[54, 55, 122, 127, 136, 137] Dispersed particle composites and other forms of LMPA structure have also shown large changes in stiffness of greater than 1000x.[55] One additional approach has been to create soft composites from undercooled Field's metal particles, which are metastable at room temperature. This traps the particles in a liquid state at room temperature, and upon mechanical perturbation the particles rapidly solidify which results in a 300% increase in Young's modulus.[141]

1.3.3 LMPAs and soft robots

LMPA composites are particularly enabling for soft robots that must undergo changes in shape for multifunctional use cases or require stiffening for changes in mechanical stability. Variable stiffness fibers have been fabricated that utilize LMPA as a core that is encapsulated with elastomer and heating elements to allow for shape change of robotic systems.[62, 142] These fibers can also show a shape memory effect where the rigid LMPA allows for shape retention, while elastic restoration by the polymer can allow for shape reversibility upon melting of the LMPA.[142] These fibers can be used as joints in shape morphing robotic systems that change shape to allow for different modes of transport such as flying or driving (Figure 1.4a).[62] Low melting point alloys can also be utilized to create soft robotic manipulators.[143] In this case, a syringe pump is attached to an elastomer manipulator, with both the elastomer and syringe wrapped in resistive heating wires. The actuation is pressure driven by utilizing the LMPA in its liquid state, and the deflection of the manip-

ulator can be controlled by the amount of liquid LMPA provided from the syringe. The LMPA can also be solidified to increase its stiffness to allow for higher forces of deflection. LMPA-elastomer composites can also be utilized to affect adhesion in order to create soft robotic grippers, where the gripping force can be reversibly controlled through stiffness tuning.[144, 145] LMPA bi-continuous foams can also be used to create soft actuators capable of both high degrees of bending and shape-locking effects.[137] By integrating the LMPA foam with a pneumatically driven-elastomer, the actuator can change shape and rigidity. The LMPA foam can decrease its stiffness by heating which allows the pneumatic actuator to change shape with pressure, and the actuator can then solidify into shape by allowing the LMPA foam to cool, which allows for a greater ability to manipulate objects.[137] By utilizing LMPA composites as the main body of robots, large scale shape change can be accomplished which enables deployable machines and multi-modal robots.[60] In addition to stiffness tuning effects, stretchable electronics have been produced by the 3D printing of Field's metal onto soft substrates, where it can be deposited into patterns that allow for stretchability in its solid-state.[146]

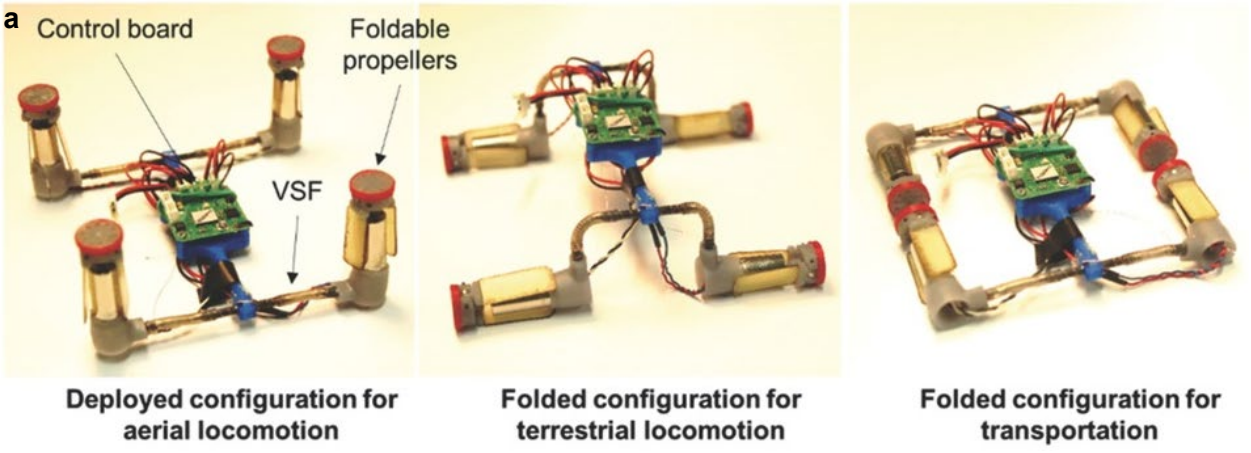


Figure 1.4: **Soft robot LMPA applications.** **a)** LMPAs for shape changing multi-functional robots. Open access article.[62]

1.4 Magnetic elastomer composites

Magnetic materials play an important role in traditional electronic devices and robots for functions like power transfer and actuation. To create mechanically soft magnetic materials for soft systems, magnetic fluids or magnetic particles in elastomers are often utilized. Magnetorheological fluids (MRFs) are a class of adaptive fluid created by dispersing magnetic powders into a non-magnetic carrier fluid, and have been studied for their field dependent rheology such as tunable viscosity and yield stress for their use in variable damping and energy dissipation systems.[147, 148, 149, 150, 151] The tunable properties of MRFs are enabled by the magnetic particle response to a magnetic field. When a magnetic field is applied, the particles translate within the carrier fluid and largely align in the direction of the field forming a network structure of particles. This network structure resists deformation from an applied load, and the mechanical response portrays an initial linear region of stress and strain up until the yield stress of the MRF.[147, 148] After reaching the yield stress, the magnetic particles begin to slip past each other and flow of the MRF is observed, although there is still an increase in the resistance to flow, and therefore viscosity, when compared to a non-activated sample due to the continued particle interaction with the applied field.[147, 152, 153] MRFs are particularly enabling for machine systems because of not only their tunable rheology, but also because of their rapid response time ($\sim$ 10 - 100 ms).[148, 149]

Magnetic elastomers or magnetorheological elastomers (MREs) are a class of adaptive solids created by dispersing magnetic powders into a non-magnetic elastomer. Magnetic elastomers can introduce both functional characteristics and an adaptive mechanical response. For magnetic functionality, the addition of magnetic material to an elastomer provides increased magnetic permeability which allows for control over magnetic field magnitude and direction, which is important for the development of magnetic circuits.[42, 154] Magnetic elastomers

also possess unique magneto-mechanical properties such as magnetostriction: the change in length or volume in response to a magnetic field, and a magnetorheological effect which leads to tunable mechanical properties in response to a magnetic field.[155, 156, 157, 158] MREs have been similarly studied for their use as adaptive materials for applications such as actuators and automotive components capable of variable damping properties through their magnetorheological response.[159, 160, 161, 162] These composite materials are the solid analog to MRFs, and have traditionally been made as rigid particle composites, with micron-scale magnetic powders dispersed throughout an elastomer matrix.[163] MREs overcome many limitations observed in MRFs, as the elastomer provides structural stability to the particles, which allows for material usage without the need for a containment vessel, and eliminates the time-dependent settling of particles than can be seen in their fluid counterpart. When a magnetic field is applied to these materials, they rapidly undergo changes to their mechanical response such as through storage and loss modulus, making them ideal for tunable stiffness and energy dissipation materials.[164, 165] The mechanism behind this tunability is similar to that seen in MRFs with some key differences. Upon an application application of a magnetic field, the embedded particles attempt to align in the direction of the field, however in contrast to MRFs, the particles are embedded in a solid state matrix, which limits their ability to fully align. However, the magnetic response of these particles provides an adaptive material response in the form of magnetostriction,[155] as well as a change in stiffness because of the resistance to deformation of the embedded inclusions.[166] These materials have been shown to have some of the fastest response times ($<$ 10 ms) among adaptive materials, allowing for rapid response and tuning of their mechanical properties.[167, 168] In this section we will discuss the fabrication and microstructure of MREs, as well as the implications towards magnetic functional response and adaptive mechanical response. The applications of these materials towards soft electronics and robots will then be explored.

1.4.1 MRE structure

To allow for a controllable and useful response, MREs should possess a higher magnetic permeability which allows for a large magnetic response, a high saturation magnetization which allows for the material to adapt its response over a large range of applied fields, and a low remnant magnetization which governs the material's ability to rapidly reverse its response in the absence of a magnetic field.[169] For these reasons, iron is often chosen as the magnetic filler due to its high permeability, highest saturation magnetization among elements, and low remnant magnetization, as well as its relative cost when compared to other engineered magnetic powders.[169, 170]

MREs are often measured by their change in modulus under an applied field, called the MR effect, which can either be measured as an absolute (ΔE_c) or relative (i.e. $\frac{\Delta E_c}{E_{c,B=0}} \times 100\%$) value, where $E_{c,B=0}$ is the composite modulus in the absense of a magnetic field. In order to improve the MR effect, MREs can be optimized through the material structure, which is often done through magnetic particle size,[171, 172, 173, 174] shape,[155, 165, 175] volume fraction,[158, 176, 177, 178] and the microstructure distribution throughout the MRE.[56, 157] The particle size for most MRE systems is on the order of microns, however recent work has shown MR effects utilizing nano-particles as well.[174] The volume fraction of magnetic particles has a significant effect on the magnetic response of MREs, where higher volume fractions of particles lead to higher relative permeability and higher activated modulus.[154, 158] However, larger particle volume fractions also increase the zero-field modulus of the MRE, which can lead to a lower relative MR effect.[158]

Rigid particle composite (RC) MREs are often made by evenly distributing the particles throughout the elastomer,[179] however one way of improving MRE properties is through the development of anisotropic composites (Figure 1.5a). Anisotropic MREs can be made by

curing the sample in the presence of a magnetic field, which preferentially aligns the particles prior to curing.[169] This results in samples with higher relative permeability in the direction of the field and a larger magnetorheological effect.[180, 181] The degree of anisotropy is larger in lower loaded particle systems, where lower volume fractions show significant anisotropy and differences when compared to isotropic systems. However, at high volume (> 30 %) fractions the particles will form a more complex network structure similar to those seen in isotropic MREs or activated MRFs.[158, 182]

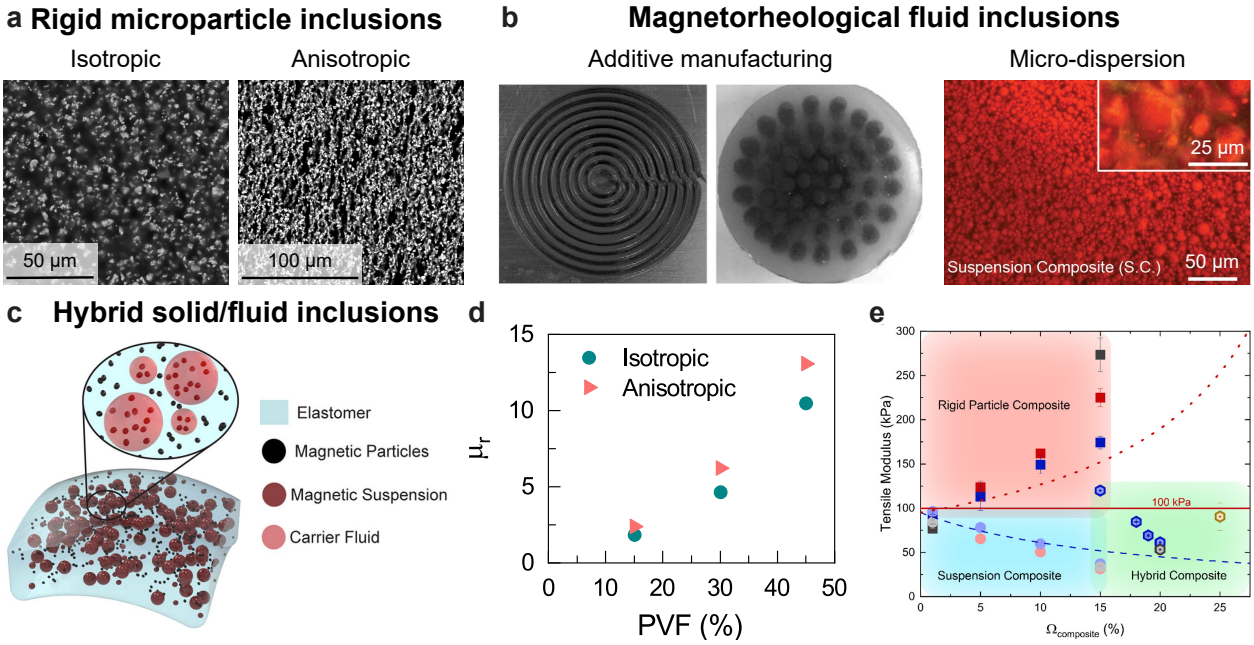


Figure 1.5: **Magnetorheological elastomers for functional and active materials.** **a)** Micro-structure of rigid-particle composite (RC) MREs as either isotropic or aligned as anisotropic with a magnetic field. Left image adapted from an open access article.[63] **b)** Magnetorheological fluid composite (FC) MREs can be shape programmed by additive manufacturing approaches. Reproduced with permission. Copyright 2017 Elsevier.[58] They can also be created by micro-dispersing magnetorheological fluid droplets though mixing. Reprinted (adapted) with permission from [56]. Copyright 2020 American Chemical Society. **c)** Solid/fluid hybrid composite (HC) MREs utilize a combination of particles and fluids. Reprinted (adapted) with permission from [56]. Copyright 2020 American Chemical Society. **d)** Permeability of isotropic and anisotropic MREs using data from Ref. 183. **e)** Effect of each of magnetic particles and fluids on MRE zero-field modulus. Reprinted (adapted) with permission from [56]. Copyright 2020 American Chemical Society.

In addition to magnetic particles, magnetorheological fluids have recently been used as inclusions in elastomers to increase their MR effect. These magnetorheological fluid composite (FC) MREs have demonstrated some of the largest relative MR effects seen in in MRE systems.[57, 58, 184, 185] FC MREs have been made through several methods including bulk encapsulation in an elastomer,[184] additive manufacturing approaches to selectively place shape-controlled millimeter scale fluid domains into desired positions,[58] and recently micro-dispersed MRFs have been added to elastomers (Figure 1.5b).[56, 57, 63, 185] For bulk encapsulation, MR fluid is filled into an elastomer mold, which is than sealed with elastomer. The elastomer provides a structural component to the MRE, while the mechanical response is tuned with the bulk the fluid phase. This material showed higher tunability in mechanical response when compared to traditional RC MREs.[184] To provide further microstructural control, additive manufacturing approaches have also been used to create FC MREs, where millimeter-scale fluid domains can be selectively added to desired positions within an elastomer matrix. By utilizing 3D printing, the shape and position of MRF domains can be prescribed, allowing for spatial tuning of magnetorheological properties, as well as adding anisotropy and complex domain shapes to MREs. The control over size and shape were shown to have a strong influence on the adaptive properties of the MRE.[58] In addition to these approaches, micro-dispersed FC MRE composites have recently been produced. These materials are made by mixing MRF into uncured polymer prior to curing, and have shown some of the highest changes in stiffness of MRE materials (up to 30x).[56, 57, 63] Additionally, the microstructure of these materials was observed under x-ray tomography, which showed alignment of individual MRF domains in response to a field, providing insight into the response of MRF inclusions. Other advances have been the addition of both solid and fluid magnetic fillers into elastomers which have resulted in hybrid composite MREs (Figure 1.5c) with stiffness changes of up to 50 times their zero-field modulus.[56, 63]

1.4.2 MRE properties

The mechanical and functional properties of MREs are influenced by the material structure. For isotropic composites with spherical inclusions, the effective relative permeability (μ_{eff}) of magnetic elastomer composites is effected by the magnetic permeability of the embedded particles (μ_i), the magnetic permeability of the elastomer (μ_e), and the volume fraction (f) of magnetic particles.[186] The effect of relative permeability can be estimated by models such as the Maxwell Garnett equation (Equation 1) which assumes evenly distributed particles with only weak interaction between particles.[187] This model works well for composites of lower volume fractions, but begins to under-predict the permeability as the volume fraction increases and more inter-particle interactions are observed.[183]

$$\mu_{eff} = \mu_e + 2\mu_e \frac{\mu_i - \mu_e}{\mu_i + \mu_e - f(\mu_i - mu_e)} \tag{1}$$

As previously discussed, the magnetic permeability of composites can be increased by utilizing a magnetic field to impart anisotropic alignment of particles through the elastomer, especially if anisotropic particle geometries are incorporated. Preferential alignment of magnetic particles allows for magnetic shorting of the elastomer matrix between particles resulting in higher magnetic field strength arising from higher effective permeability.[154] Figure 1.5d demonstrates the difference in relative permeability as volume fraction is increased for both isotropic and anisotropic composites.[183] In this case, the relative permeability of the composite increases by 25% when the magnetic particles are aligned with a magnetic field. For isotropic MREs, the relative permeability has not been shown to be dependent on whether the composite is made with rigid particles, magnetic fluids, or a combination of the two, and is instead dependent on the total volume fraction of magnetic content in the material.[56]

The zero-field mechanical properties of MREs are also heavily dependent on the volume fraction of magnetic inclusions as well as the type of magnetic material used (Figure 1.5e).[56] As previously discussed, MREs have traditionally been made as rigid particle composites, and recently as magnetorheological fluid composites as well as hybrid composite material architectures. The composite modulus (E_c) of MREs can generally be predicted by an Eshelby model (Equation 1), where E_i is the modulus of the magnetic inclusions, E is the modulus of the elastomer, and ϕ is volume fraction of the inclusions.[188]

$$E_c = E\frac{1+\frac{2E_i}{3E}}{(\frac{2}{3}-\frac{5\phi}{3})\frac{E_i}{E}+(1+\frac{5\phi}{3})} \tag{2}$$

For rigid particle composites, ϕ is equal to the volume fraction of magnetic particles ($\Omega_{composite}$), and E_i is equal to the elastic modulus of the particles. For magnetorheological fluid composites, ϕ is equal to Ψ, the volume fraction of magnetorheological fluid. For FC MREs, E_i has been shown to be equal to zero, indicating that the magnetic particles in the MRF can remain encapsulated in the dispersed microdroplets, and decrease the modulus of the composite.[56] For RC MREs, the composite modulus increases as the volume fraction of solid increases. Different powder geometries can also have an effect on the composite modulus, such as flake-like geometries which can further increase the stiffness of the composite at lower volume fractions than spherical powders.[42, 56]

1.4.3 MREs and soft robots

The rapid magnetorheological and shape change response of MREs is enabling for soft electronics and adaptive machines.[73, 189] For example, the shape translation through magnetic interaction can be used for soft actuation and movement,[159, 190, 191, 192] and for the de-

velopment of reconfigurable electronics and robots.[193, 194] MREs have been used for haptic feedback systems which can be spatially actuated with a magnetic field to produce indentation and stiffness change at desired locations (Figure 1.6a).[174] In this case, the material was made as an Arduino-controlled interface capable of deforming six buttons at different positions on the surface of the device, where the buttons were activated with a magnet to spell letters in braille. Reconfigurable electronics can be made by utilizing MREs with a conductive pathway that acts as a switch when magnetically actuated (Figure 1.6b).[194] The MRE is utilized with a conductive composite created with silver-coated nickel micro-particles on one side. Upon activating with a magnet, the material can actuate towards an LED circuit to complete the conductive pathway and switch the LED on. The stiffening material response of MREs can also be utilize to rapidly tune adhesion for switchable adhesives,[195, 196, 197] where in many cases the on state of the adhesive is the magnetically actuated state, and the off state realizes a decrease in adhesion and stiffness (Figure 1.6c).[185] Magnetic elastomers can also be used for soft robotic grippers that can adapt to the shape of fragile objects and then firmly grasp the objects upon the application of a magnetic field.[63, 198, 199] In Figure 1.6d a magnetic elastomer gripper was integrated with an electromagnet to create a gripper that can passively conform to a variety of object geometries while soft, but can then rapidly ($\sim$ 20 ms) increase its stiffness by up to 50x to grasp the object upon application of a magnetic field.[63] Additionally, recent research has used hard magnetic powders as inclusions which can be utilized for greater control over material motion which can be used for locomotion and actuation of miniature soft robots.[200, 201, 202] A miniature robot has been created using hard magnetic powders that achieves multiple modes of motion, allowing it to crawl, walk, roll, swim, and even grasp objects depending on the direction and strength of the field.[200]

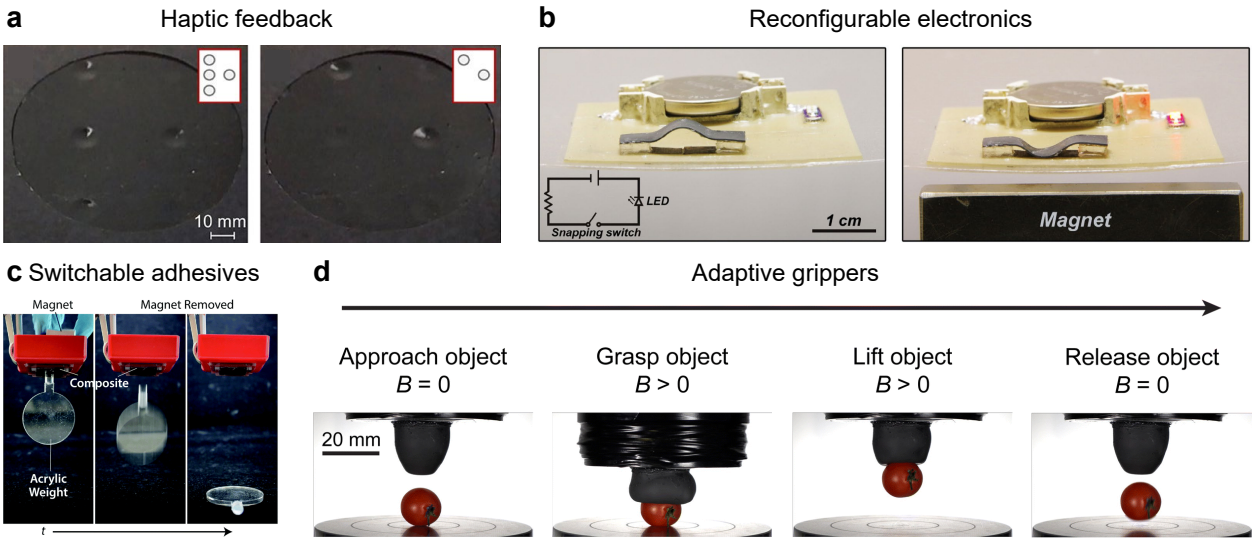


Figure 1.6: **MRE soft robot applications. a)** MREs can rapidly respond to a field for machine actuation such as in haptic feedback systems. Reprinted (adapted) with permission from [174]. Copyright 2022 American Chemical Society. **b)** Shape change can be used for reconfigurable electronic devices. Open access article.[194] **c)** The change in stiffness of MREs allows for rapidly reversible adhesion. Open access article.[185] **d)** Stiffness tuning can also be used to create adaptive robotic grippers. Open access article.[63]

1.5 Multi-component soft composites

Multifunctional composites enable notable advances for soft robotic applications including soft wiring, heat transfer, and adaptive shape and mechanical response. While the advancement of each individual property is important, soft robots often utilize combinations of functional and active properties which can be enhanced through the creation of multi-component material systems.

1.5.1 Multi-component composite architectures

Liquid metal can be utilized to create soft wiring for electronic components, however some electronics can be enhanced with the addition of integrated functional materials. Inductive power transmitters feature a coil-shaped electrical pathway which transmits a magnetic field

to an inductive receiver. Traditional wireless power devices feature a copper coil as well as backplane made of magnetic material which increases the efficiency of power transfer. Stretchable inductors can be made by utilizing a multi-component system which utilizes a liquid metal inductor coil integrated with a high permeability magnetic elastomer backplane. (Figure 1.7a).[42] Multi-component materials can also be used to tune material response, such as when magnetic particles are used in addition to liquid metals. An anisotropic liquid metal magnetorheological elastomer was developed which utilizes magnetic alignment to enhance the properties of the liquid metal composite. Alignment both significantly increases the undeformed electrical conductivity of the composite in all directions as well as introduces positive and both negative piezoconductivity where the conductivity can increase or decrease with applied strain depending on the direction of electrical measurement (Figure 1.7b).[203]

Another Multi-component elastomer strategy is to utilize both liquid metals and low melting point alloys. Continuous liquid metal channels can be utilized as resistive heaters for low melting point alloys, allowing for a compliant on-board heater capable of large deformations. By combining LMs and LMPAs in a multi-layered system, shape and stiffness tuning materials can be made that allow for reconfigurability in soft robots. (Figure 1.7c).[60]

For stiffness tuning materials, MREs show some of the fastest response times among stiffness tuning materials, however other material systems such as LMPAs often show a larger magnitude response. One material system utilizes liquid-state LMPA as the carrier fluid for a magnetorheological fluid which can also change phase to become a solid.[204] By utilizing a combination of LMPA and magnetic particles, rapid response time can by achieved in stiffness tuning materials while also allowing for higher magnitudes of change in elastic modulus by solidifying the LMPA (Figure 1.7d).

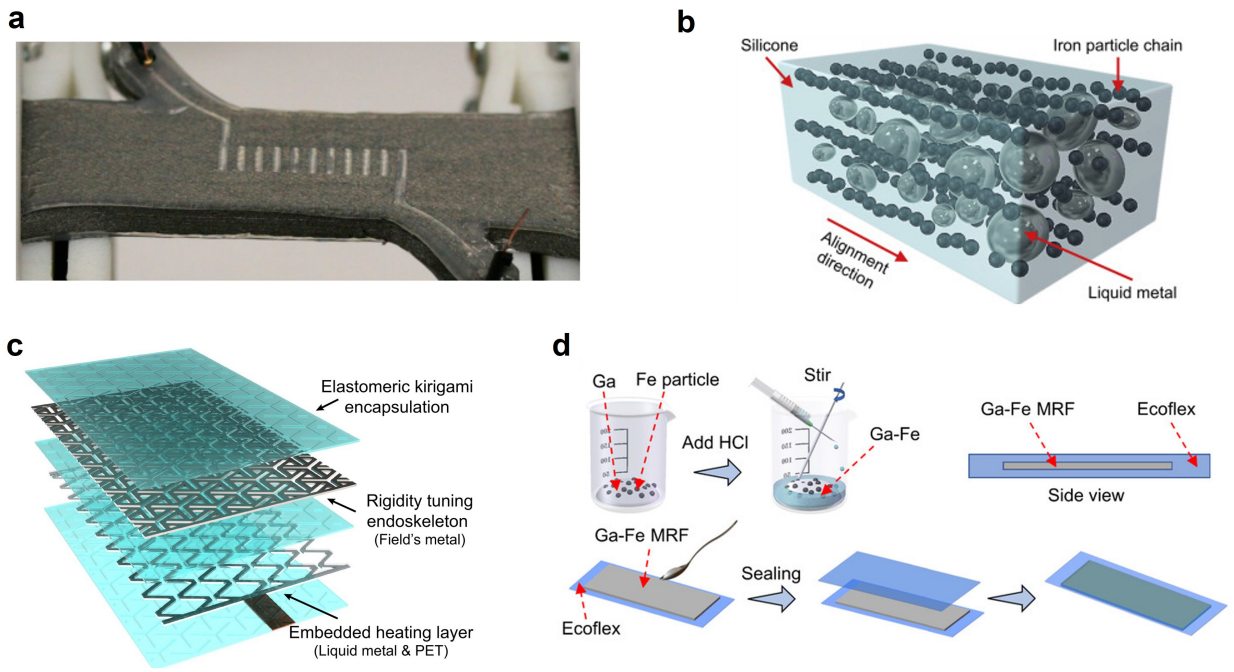


Figure 1.7: **Multi-component soft composites. a)** Liquid metal conductive pathway integrated with magnetic elastomer composite to increase inductor efficiency. Reprinted (adapted) with permission. Copyright 2015 American Chemical Society.[42] **b)** Magnetic particles integrated with liquid metal droplets for tunable functionality. Reproduced with permission. Copyright 2020 Elsevier.[203] **c)** Low melting point alloy integrated with liquid metal-based resistive heater. Adapted from an article published in *Science Robotics*.[60] **d)** Magnetorheological fluid utilizing LMPA as a carrier fluid capable of rapid magnetorheological response and further stiffness tuning through phase change. Open access article.[204]

1.5.2 Multi-component composites in robots and electronics

Multi-component materials allow for unique combinations of properties for new forms of soft electronic devices and robots. For example, shape memory alloys (SMAs) are an active material that can change between crystalline phases in response to heat. This can give rise to an actuation effect, where the material will deform in response to heat and return to its original configuration in response to cooling. However, the ability to rapidly cycle SMA actuation requires a method to cool the SMA. Liquid metal elastomers with high thermal conductivity have been utilized as heat dissipating layers for SMAs that are com-

pliant enough for actuation while removing heat to improve actuation. Figure 1.8a shows the capability of high thermal conductivity LM composites to increase the functionality of a shape memory alloy actuator on a soft robotic fish.[59] Further, robotic fabrics can be created through LMPA filaments and SMA wires for load bearing structures that morph into different configurations.[205] These types of robotic skins can also be applied to tensegrity robotics.[206, 207]

Utilizing multi-phase magnetic composites in addition to liquid metal wiring allows for soft and conformal inductors capable of wireless power transfer. Liquid metal coils can be added to elastomers to create inductors capable of wirelessly transmitting and receiving power. Magnetic elastomers that utilize iron particles as inclusions can act as a magnetic backplane, which improves power transfer efficiency of these devices. By incorporating liquid metal coils into magnetic backplanes, wireless power transfer systems can be created. These all soft transmitted and receiver systems can transfer power up to 100 % strain. These can be utilized in high deformation regions of the human body, such as the palm of a human hand. Figure 1.8b shows the ability of LM-magnetic elastomer inductors to be used for wearable wireless power transfer to rigid wireless receivers.[56] Additionally, magnetoactive phase change materials with magnetic particles embedded in liquid metal can reversibly switch between solid and liquid states. The composite can also morph by changing shape, splitting, or merging by controlling the composite magnetically in the liquid state.[208]

Liquid metal and low melting point alloy multi-layer composites allow for rabid and reversible shape morphing in soft robot systems. These can be enabling for the creation of deployable machines, which can start in a flat and compact shape before transforming into a functional shape. These machines can interact with their environment such as through obtaining cargo, and reverse back into their compact shape after use. Figure 1.8c shows a deployable underwater machine diving underwater and obtaining cargo before being retrieved and reversed

to its original shape.[60]

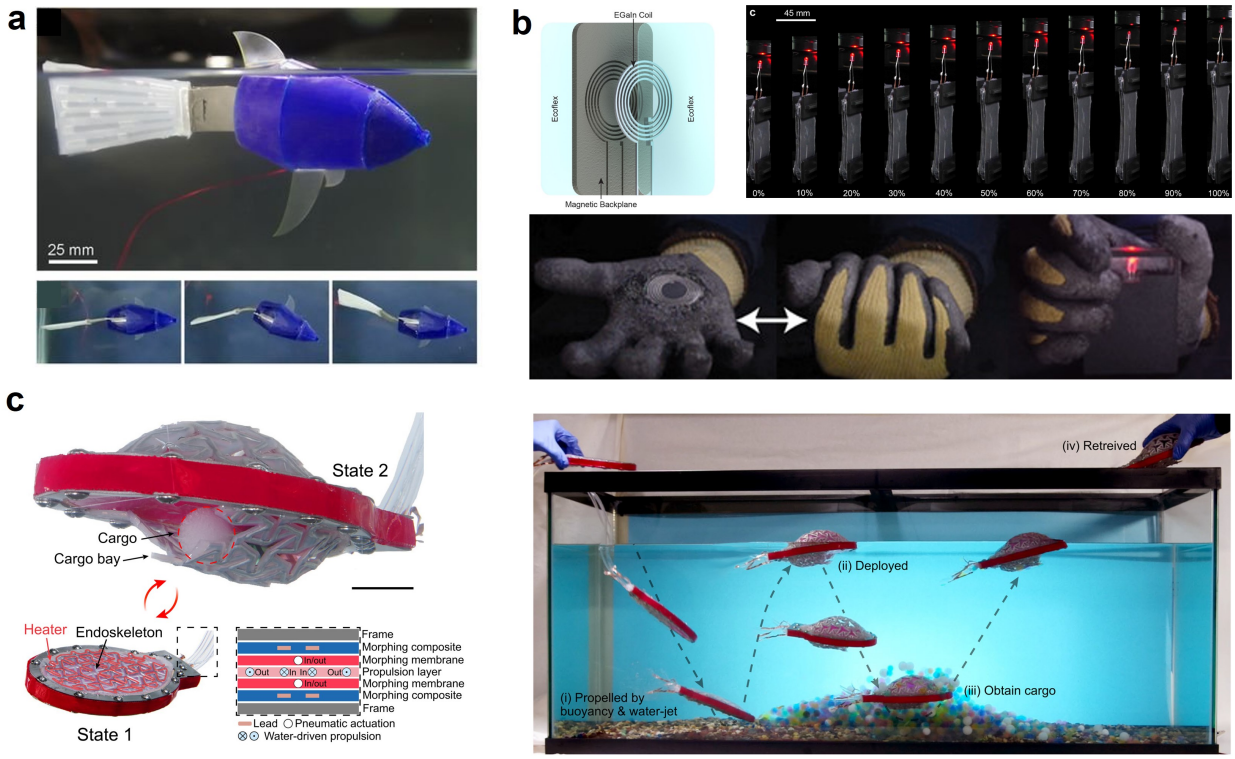


Figure 1.8: **Multi-component material systems enable next generation electroincs and machines. a)** Liquid metal heat transfer material enables robotic movement from a shape-memory alloy actuator. Open access article.[59] **b)** Magnetic elastomer backplanes improve the power transfer efficiency of LM-based wireless power transfer devices. Reprinted (adapted) with permission. Copyright 2020 American Chemical Society.[56] **c)** Liquid metal heater allows for reversibility of shape morphing material based on LMPA. Adapted from an article published in *Science Robotics*.[60]

1.6 Research Objectives

Soft functional composites are essential components for emerging soft robots. Soft functional materials such as liquid metal composites and magnetic elastomers allow for high thermal, electric, and magnetic properties in a compliant and deformable material. Additionally, the study of soft functional devices has lead to the development of adaptive materials that can

change their properties and shape in response to engineering stimuli. Magnetorheological elastomers and low melting point alloys can be utilized to allow for tunable stiffness and reconfigurability in soft machines. By combining multifunctional materials in multi-component systems, properties from several forms of soft functional composite can be combined, which opens intriguing opportunities for material properties and soft robot applications, such as tunable material properties including conductivity and piezoresistivity, increased efficiency of wearable devices such as wireless chargers, and further degrees of stiffness tuning by combining LMPAs and magnetic materials.

In this work, we undertake a multi-disciplinary approach that combines materials design, composite processing, polymer mechanics, and adhesion to accomplish our central goal of creating multi-functional materials with enabling characteristics for next generation electronics and machines. We achieve this goal through the completion of five research objectives: 1. Quantification of underwater environments on LM composite properties, 2. Development of a tough bonding strategy for LM composite integration, 3. Creation of multi-functional adaptive machines with material-level shape change, 4. Processing of multi-phase magnetic elastomers with low stiffness and large magnetic response, and 5. Quantification and prediction of stiffness tuning response of multi-phase magnetic elastomers.

Research objective 1: Quantify effect of underwater environments on LM composite properties

LM-elastomer composites have shown strong potential for multi-functional electronics applications owing to their soft mechanical response and large thermal and electrical conductivities. These material properties make LM composites feasible candidates for underwater exploration applications including for wearable sensing and health monitoring and for bio-inspired underwater robots. However, the effect of underwater environments during long-term aging on the mechanical and functional properties of these materials has not been studied. In order to understand how underwater aging affects these material properties,

silicone-elastomer composites with varied LM volume fractions (0 to 80%) will be tested for their elastic modulus, thermal conductivity, and electrical conductivity. Freshwater and saltwater aging chambers will then be used to quantify the change in these properties during the course of up to one month of underwater submersion. We will then determine the utility of these materials by comparing LM composite electrodes with traditional copper electrodes that have undergone underwater aging.

Research objective 2: Development of a tough bonding strategy for LM composite integration

While LM composites are enabling for soft electronics and robotics due to their unique combination of low rigidity, high strain limit, and metal-like thermal and electrical conductivities, the integration of LM composites with diverse components remains a challenge. Silicone-based LM composites face challenges with adhesion to low surface energy substrates including many polymers and metals, which limits their ability to be incorporated into polymer-based clothing, and to be integrated with rigid electronic materials. In order to improve adhesion between LM composites and diverse substrates, a chemical anchoring methodology that consists of the surface treatment of desired substrates utilizing (3-Aminopropyl)triethoxysilane (APTES) will be developed. The effect of LM composite microstructure on the material's adhesive properties will be determined by systematically testing the fracture energy of silicone elastomer composites with LM volume fractions of 0 - 60% and mean droplet diameters of 2 - 60 µm. The utility of these materials will be shown by creating soft electronics systems that utilize the adhesion mechanism to integrate LM composites with LEDs.

Research objective 3: Creation of multi-functional adaptive machines with material-level shape change

Soft materials have shown potential for the creation of shape and rigidity tuning materials for multi-functional robots. However, soft machines face challenges simultaneously achiev-

ing three important properties: deformation into complex geometries, rapid morphing into load-bearing structures without the need for sustained power, and the ability to reverse deformation back to its original shape. In order to demonstrate the utility of multi-component elastomer composites as material-level shape and rigidity tuning components for adaptive machines, we will integrate an elastomeric kirigami-inspired morphing material that utilizes an unconventional reversible plasticity mechanism in LMPAs to rapidly and reversibly morph into load-bearing geometries. The material will be tested to for its ability to rapidly morph to extreme deformations while still being able to be reversed to its original shape through phase change of the LMPA by its integrated LM heater. We will then demonstrate the material's use case by integrating it with onboard power and control to create a multi-modal soft robot capable of both land and air transport through shape change, and a deployable underwater machine capable of interacting with its environment to obtain cargo.

Research objective 4: Processing of multi-phase magnetic elastomers with low stiffness and large magnetic response

In addition to LMs and LMPAs, magnetic inclusions to elastomers have been utilized to create wearable electronics devices. Functional liquid fillers such as LMs have shown strong promise for creating soft functional materials. The processing of magnetic fluids to create soft composites with low stiffness and high magnetic permeability could be especially enabling for soft electronic devices such as wireless power transmitters and receivers. In order to understand how magnetic fluids affect the mechanical and magnetic response of elastomer composites, we will develop a processing method to disperse magnetic fluids as discrete droplets within an elastomer. The role of microstructure on material properties will then be studied by creating magnetic composites consisting of rigid particle inclusions, magnetic fluid inclusions, and a combination of the two. The elastic modulus and magnetic permeability with respect to each of these structures will be studied. The utility of the materials will

then be shown by creating soft power transfer systems that utilize the magnetic elastomers as magnetic backplanes for soft inductors.

Research objective 5: Quantification and prediction of stiffness tuning response of multi-phase magnetic elastomers

Magnetic elastomers can also adapt their mechanical properties such as their shape and stiffness in response to an applied field, which is useful for automotive applications, shape morphing robots, and soft adaptive grippers. In order to understand the stiffness tuning response of multi-phase magnetic elastomers, we will quantify the relationship between microstructure and stiffness change of these materials. The materials, made with rigid particle inclusions, magnetic fluid inclusions, and a combination of the two, will have their elastic modulus tested in compression both with and without an applied field. In addition to microstructure, the stiffness tuning effect will also be quantified with respect to the initial (zero-field) mechanical properties of the material. The utility of the material will then be shown by creating a soft robotic gripper capable of grasping a variety of objects.

1.7 Acknowledgments

We acknowledge support from the Office of Naval Research Young Investigator Program (YIP) (N000142112699) and NSF (No. CMMI-2054409).

Chapter 2

Liquid metal-elastomer composites for water-resilient flexible electronics

Modified from a manuscript accepted for publication in *Journal of Polymer Science*.

Edward J. Barron III,[1,2†] Ella T. Williams,[1†] Brittan T. Wilcox,[1] Dong Hae Ho,[1] and Michael D. Bartlett.[1,2*] Liquid metal-elastomer composites for water-resilient flexible electronics. *Journal of Polymer Science*, 2023.

1. Mechanical Engineering, Soft Materials and Structures Lab, Virginia Tech, Blacksburg, VA 24061, USA.

2. Macromolecules Innovation Institute, Virginia Tech, Blacksburg, VA 24061, USA.

† These authors contributed equally to this work.

∗ To whom correspondence should be addressed: mbartlett@vt.edu

2.1 Contributions

For the work titled "**Liquid metal-elastomer composites for water-resilient flexible electronics**" the dissertation author Edward J. Barron III contributed the following:

- Was an equal contributor (along with E.T.W.) in conducting all experiments presented in the main text of this work.
- Analyzed all data shown and discussed in the main figures of this work.
- Created all figures shown in the main text of this work.
- Was the primary contributor responsible for writing this work.

2.2 Abstract

Liquid metal-elastomer composites have immense potential for emerging electronic applications due to their exceptional mechanical and functional properties. Underwater exploration is one area of interest for these composites, where divers or robots could benefit from wearable sensing, health monitoring, and energy harvesting. However, the influence of water submersion on liquid metal composites is not well understood. Here, the effect of underwater environments on the mechanical, thermal, and electrical properties of liquid metal composites exposed to month-long aging is quantified. Under most conditions, liquid metal composites maintain their initial properties over the course of aging. However, for composites with high volume loadings of liquid metal ($\phi = 80$ %) exposed to saltwater conditions, a decrease up to 70 % in tensile modulus and up to 44 % in thermal conductivity can occur. The aging environments were not shown to have an effect on the electrical conductivity of the composites. Liquid metal composites are then shown to outperform traditional copper electrodes after saltwater aging, demonstrating these soft, multifunctional composites as strong candidates for wearable, water-resistant devices and machines.

2.3 Introduction

Soft electronics can be worn or integrated into clothing to create functionalities such as health and body monitoring,[209, 210, 211, 212, 213] environmental sensing,[214, 215] and seamless power storage and transfer.[216, 217, 218] In contrast to traditional electronics, wearable systems require careful consideration of their mechanical properties and body placement to ensure that the wearer is not limited in mobility. One approach to creating body-compliant systems is through the creation of elastomer-based electronics which can provide the necessary functions for useful human augmentation while maintaining the low modulus and high extensibility desired for comfortable wear.[219, 220] While elastomer-based electronics systems have shown significant progress and advantages at the research level, widespread application and consumer adoption will rely on the ability to provide reliable, long-lasting, integrated systems that can withstand exposure to various environments. One area of interest are the working environments of marine divers, who can benefit from body-integrated cameras and displays,[221] lighting,[222, 223, 224] and vital sensing electronics.[225, 226, 227] For underwater applications, traditional sensors and electronics composed of rigid materials often need rigid pressure chambers to survive the hydrostatic pressure present underwater.[228] However, soft electronics hold the promise to survive without external rigid pressure chambers due to their incompressiblity,[229] which can enhance flexibility and stretchability for various underwater electronics, sensors, and robotics. Divers experience freshwater and saltwater environments which can have significant effects on the durability of elastomer-based electronics.

Soft electronic devices have become increasingly enabled by unique material designs and novel processing methods to create soft and flexible composites with desirable functional properties.[230, 231, 232] An intriguing material candidate for these devices that has recently emerged are liquid metal-elastomer composites that utilize room temperature liquid

metals as inclusions in elastomers to create mechanically compliant materials with highly tunable thermal or electrical conductivities.[91, 233] In contrast to traditional rigid fillers, liquid metals such as eutectic Gallium-Indium (EGaIn) possess high thermal ($K = 26.4$ W m^{-1} K^{-1}) and electrical conductivity ($\sigma = 3.4 \times 10^6$ S m^{-1}) while maintaining a liquid-like mechanical response. This enables multifunctional elastomers without a substantial increase in rigidity.[82, 83, 90] Further, the utilization of liquids as fillers enables unique processing methods to optimize material properties, such as through aerosol spray deposition of soft conductive traces,[234] utilization of liquid metals to fill microchannels,[235, 236, 237, 238] or additive manufactured materials with spatially tunable properties through real-time microstructural patterning of inclusion shape.[98] One common method to create these composites is by dispersing liquid metals as discrete droplets throughout an elastomer matrix, where the size of the inclusions can be controlled through mixing parameters.[93] By dispersing these materials as discrete droplets, composites can be made that are ultra-soft and extensible, posses metal-like thermal conductivity (up to 13 W m^{-1} K^{-1}),[52] yet can remain dielectric when advantageous for electronics applications.[59, 239, 240] These composites can also be made electrically conductive by creating a continuous network structure through methods such as pressure induced sintering,[9, 99, 101, 241] which allows for a heat-free approach to circuit creation.

The combination of advanced properties and innovative processing approaches has led liquid metal composites to be utilized for wearable electronics devices and soft robots capable of exploring underwater environments and adapting to different tasks.[60, 242, 243, 244] The material composition of liquid metal composites has the potential to be used for underwater electronics, as elastomers such as silicone rubber are hydrophobic which often leads to good environmental resistance.[245] However, continued exposure to water has been shown to cause changes in the mechanical properties of silicone-based adhesives,[246] elastomers,[245, 247]

and sealants.[248, 249] Further, the interaction between underwater environments and the functional properties of liquid metal-elastomer composites has not been studied.

Here we determine the effect of freshwater and saltwater environments on the properties of liquid metal (LM) composites through underwater aging experiments (Figure 2.1A). The LM composites are fabricated by dispersing EGaIn with volume fractions of $\phi = 0, 40$, and 80% throughout commonly-used silicones (Ecoflex 00-30 and Sylgard 184). This forms dispersions of discrete LM droplets (Figure 2.1B) that can remain thermally conductive and electrically insulating or be mechanically activated to be electrically conductive through pressure induced activation (embossing). The essential properties of LM composites for wearable electronics such as their mechanical response (Figure 2.1C), thermal conductivity (Figure 2.1D), and electrical conductivity (Figure 2.1E) are characterized, and their properties are quantified with respect to their aging time in underwater environments. To understand their response to underwater environments, we design environmental aging chambers integrated with water filtration, circulation and heating (Figure 2.1F). We then fill these chambers with freshwater (FW), saltwater (SW) with a salt concentration of 35,000 ppm to simulate an ocean environment, and concentrated saltwater (CS) that has a salt concentration of 70,000 ppm to act as an aging accelerant. The mechanical and functional properties of the LM composites are investigated during and after environmental aging, and we find the composites to be exceptional candidates for underwater electronics as they experience little change in their mechanical and functional properties under most conditions.

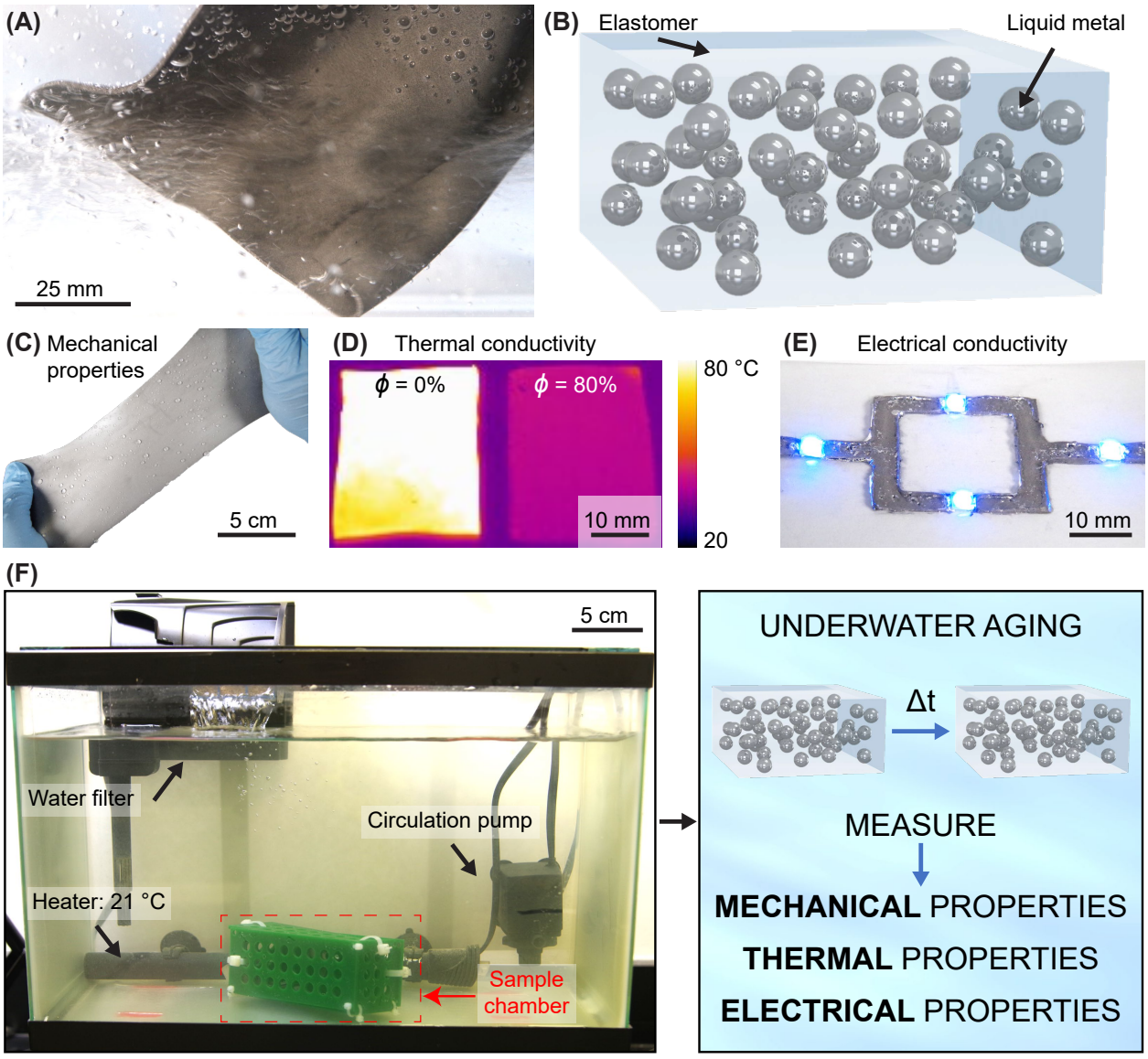


Figure 2.1: **Underwater aging of liquid metal composites.** **(A)** $\phi = 40\%$ interacting with an underwater environment. **(B)** Schematic of a liquid metal composite. **(C)** Stretchable mechanical properties of Ecoflex $\phi = 40\%$. **(D)** Enhanced thermal conductivity through the inclusion of liquid metal in elastomer. When heat is applied via a heat gun, the LM composite shows improved heat transfer to an underlying metal plate. **(E)** Electrical conductivity of Sylgard $\phi = 80\%$ composite enables circuits. **(F)** Environmental aging chamber with water filtration, circulation, and heating.

2.4 Results and Discussion

2.4.1 Underwater aging of liquid metal composites

To determine the effect of underwater aging on material structure, composites utilizing Ecoflex silicone rubber and LM volume fractions of $\phi = 0$, 40, and 80% are submerged in FW, SW, and CS for a period of two weeks. By controlling the mixing parameters LM droplets are maintained at a similar average size of ∼45 µm (Figure A.1). In addition to these conditions, control samples are left in ambient room conditions. During this time, the samples are periodically removed from their aging environments and the their mass is measured. At the end of two weeks, the samples are removed, and their structures are analyzed with scanning electron microscopy (SEM) which provides a clear view of the LM inclusions located in the elastomer matrix. Energy disperse X-ray spectroscopy (EDS) is performed to analyze the change in chemical composition throughout aging.

Figure 2.2A-D shows SEM images with EDS overlay for Ecoflex composites with $\phi = 80\%$. Here, EDS is used to determine the location of both liquid metal and impurities that may occur as a result of underwater aging. The liquid metal is observed by mapping the location of Gallium and Indium which are shown as dark blue and light blue respectively. Sodium and Chlorine are shown as red and orange respectively. We then utilize the EDS data to determine the change in weight fraction of the impurities. Figure 2.2A and B show the microstructure and chemical composition of samples aged in ambient and FW environments. These samples show the expected result of a large amount of Ga and In due to the LM inclusions, and no large indication of Na or Cl. Analysis of the samples aged in SW and CS environments are shown to contain salt on the surface (Figure 2.2C and D). To quantify the change in material composition with aging, the weight fractions of oxygen (O) and the sum of sodium and chlorine (Na + Cl) are determined from EDS over the surface analyzed for

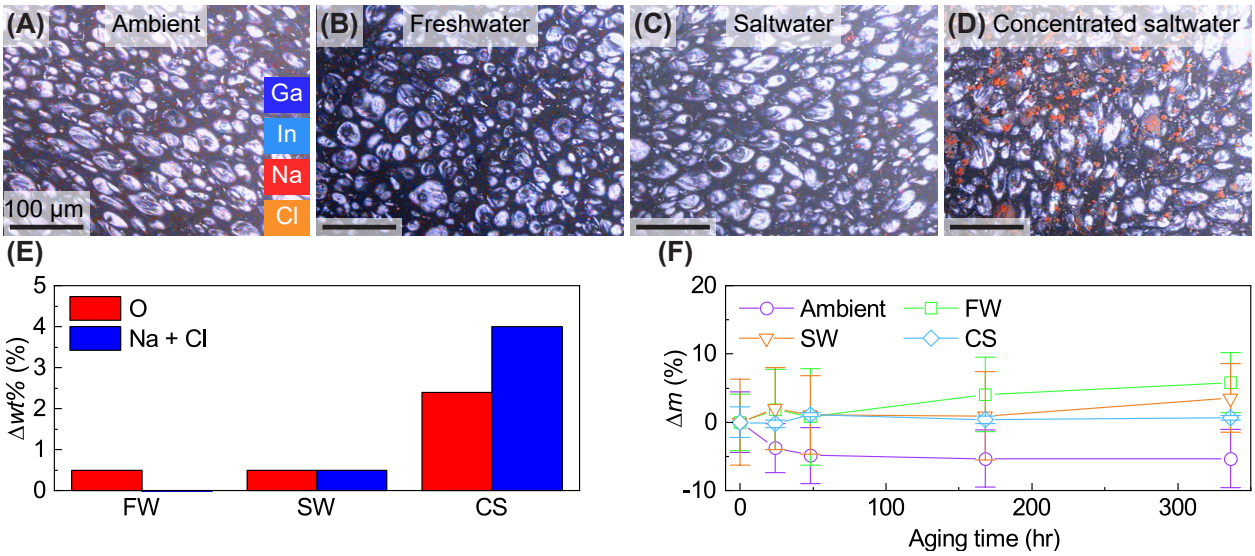


Figure 2.2: **Morphological and chemical analysis. (A-D)** SEM images of Ecoflex ($\phi = 80\%$) composites showing distribution of Ga, In, Na, and Cl for different aging conditions. **(E)** Weight fraction of O_2, Na, and Cl on the surface of aged samples determined from EDS. **(F)** Mass change of Ecoflex ($\phi = 0\%$). Error Bars represent standard deviation for n = 3.

each of the four samples (Figure 2.2E, Figure A.2). All three of the water-aged samples show increases in oxygen levels when compared to the ambient condition. As previous research has shown that both water and dissolved oxygen in water can permeate into silicone membranes, we attribute this increase in oxygen as either permeated oxygen due to water exposure or as water intake.[250, 251] The SW and CS-aged samples also show an increase in salt concentration of up to 4.1 wt%. This is attributed to salt deposition on the surface or salt ion diffusion which has been shown in previous work.[252] Figure 2.2F presents the mass gain of the composites after two weeks of aging. The samples present mass gains of 5.8, 3.5, and 0.6% for the FW, SW, and CS-aged samples respectively. The difference in mass gain is likely due to the salt present in the SW and CS environments, which has been shown to impede the water uptake of silicones.[246] In contrast, the samples aged at ambient conditions present a mass loss of 5.3%. This may be attributed to a loss of silicone oils which are frequently used to soften silicone elastomers and can migrate to the surface over time.[253]

2.4.2 Mechanical characterization

The mechanical properties of liquid metal-elastomers are essential to their performance as soft electronic components, which require low stiffness and extensibility to conform to complex surfaces. To determine the effect of underwater aging on the mechanical response of liquid metal composites with matrix materials of different mechanical properties, we fabricate these materials using both Ecoflex and Sylgard silicone elastomers (Figure 2.3A). The liquid metal inclusions contain a liquid core with a solid gallium oxide shell with a typical thickness of between 0.5 and 5 nm that spontaneously forms in the presence of oxygen.[85] This oxide layer can give the liquid metal inclusions both solid and liquid character.[254] One method to understand the effect of LM inclusions is through the use of an Eshelby analysis (Equation 1), which predicts the elastic modulus of the composite (E_c) as a function of ϕ, the elastic modulus of the polymer matrix (E_m), and the effective modulus of the inclusions (E_i):[51, 188]

$$E_c = E_m \frac{1 + \frac{2E_i}{3E_m}}{(\frac{2}{3} - \frac{5\phi}{3})\frac{E_i}{E_m} + (1 + \frac{5\phi}{3})} \tag{1}$$

Figure 2.3B shows E_c for the Ecoflex and Sylgard LM composites as a function of ϕ. The Sylgard LM composites (E_m = 1800 kPa) demonstrate a decrease in E_c of over 60% as the volume fraction of LM increases to 80%. However, for Ecoflex composites (E_m = 50 kPa), the tensile modulus increases by over 2.5x as ϕ increases from 0 to 80%. To understand the mechanical contribution of the LM inclusions, Equation 1 is fit to the tensile data utilizing the measured E_m of Sylgard and Ecoflex while utilizing E_i as a fitting parameter. The prediction of E_c through Equation 1 with E_i = 111 kPa is plotted alongside the experimental data. As the liquid metal has a thin oxide shell ($\sim$ nm thick) it gives a non-zero effective inclusion modulus E_i.[254] Therefore, soft matrix materials will result in stiffer composites if $E_i > E_m$

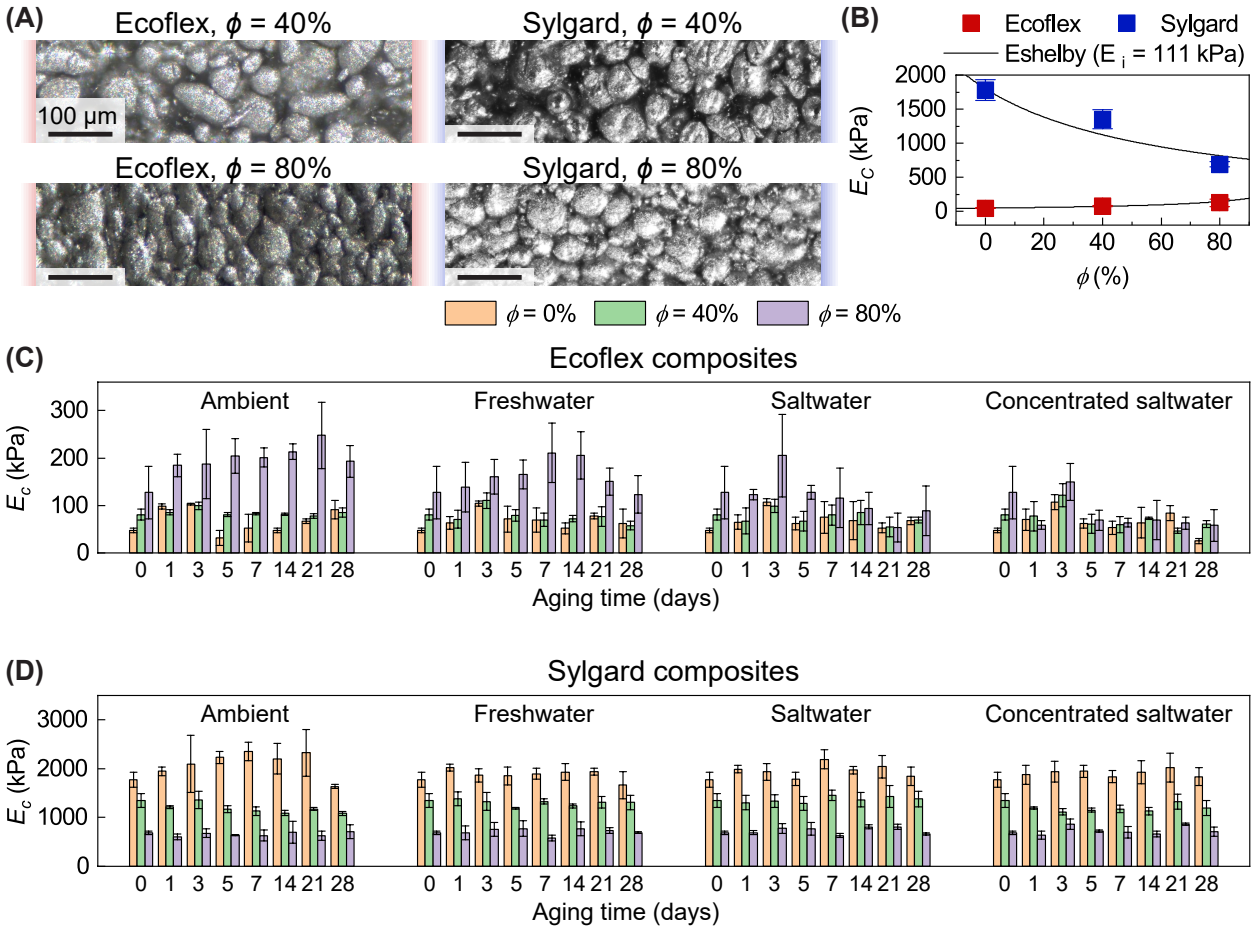


Figure 2.3: **Mechanical analysis.** **(A)** Microscopy of liquid metal composites. **(B)** Measured and predicted moduli for liquid metal composites. Tensile moduli of **(C)** Ecoflex and **(D)** Sylgard composites throughout underwater aging. Error bars represent standard deviation for n = 3.

and stiffer matrix materials will soften if $E_i < E_m$. The prediction from the Eshelby analysis shows agreement with the data, accurately estimating the decrease in E_c observed in the Sylgard composites and the increase in stiffness observed in the Ecoflex composites.

Figure 2.3C and 2.3D present the measured values of tensile modulus over four weeks of aging for Ecoflex and Sylgard LM composites respectively. Most of the composite samples show no noticeable change in E_c between the ambient environment and underwater aged samples throughout the total duration of aging and maintain their high elongation of up

to 860% for Ecoflex and 150% for Sylgard (Figure A.3). However, some of the composites realize an increase in tensile modulus over the first week of aging. This may be attributed to further crosslinking of the elastomer, which can be exacerbated in underwater environments due to an increase in chain mobility,[248, 249] or from a loss of silicone oils for the ambient samples. The Ecoflex LM composites with $\phi = 80\%$ do show an apparent difference in tensile modulus throughout the duration of testing, where the material shows up to a 70% decrease in E_c between the ambient and CS-aged samples after four weeks, and the ambient-aged samples show a higher modulus than all underwater aged samples. Previous work has shown that the modulus of the silicones will decrease after long term aging due to plasticization from increased moisture content, as well as chain scission.[246, 248, 249] Salt water may also present its own effects on mechanical properties due to its more aggressive chemical nature.[245] This extreme change in mechanical properties may be occurring due to the low volume fraction of elastomer and low E_m, where plasticization and salt water effects on chain scission may be amplified.

2.4.3 Thermal characterization

LM elastomer composites have demonstrated promise as thermal interface materials and heat sinks capable of transferring heat away from electronics to improve device performance and user comfort for wearable applications.[97, 255] An important feature of these materials is high thermal conductivity (k) in extensible materials while maintaining electrical insulation at high volume fractions of LM.[59, 93] To understand the effect of environmental aging on LM composite thermal conductivity, we create custom testing fixtures based on a transient hot-wire (THW) approach that are capable of monitoring k for each of the samples during aging (Figure 2.4A). The LM composite is located inside of a 3D-printed mechanical support structure, while an embedded resistive Platinum wire allows for thermal measurements.

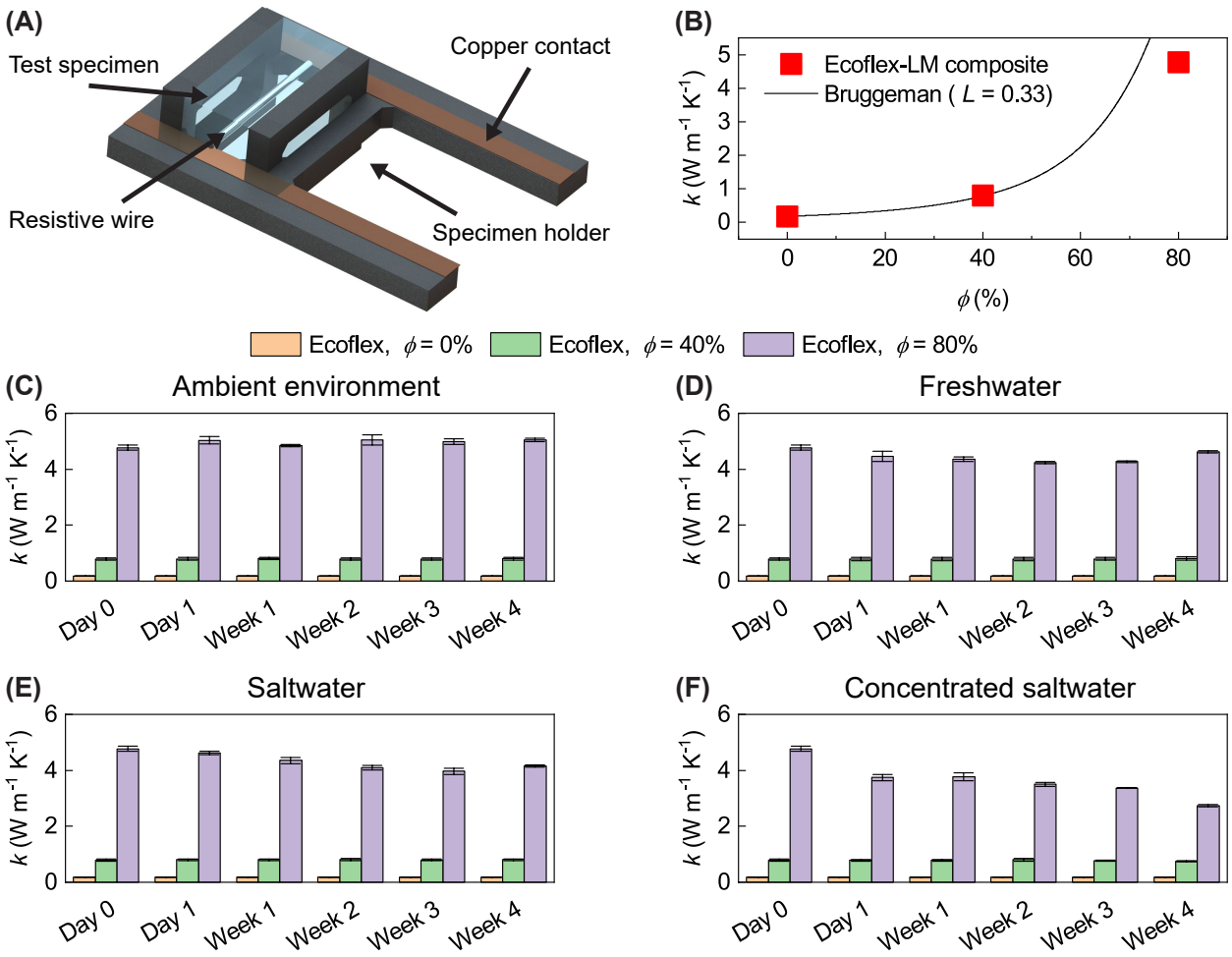


Figure 2.4: **Thermal conductivity analysis.** **(A)** Schematic of the transient hot wire embedded samples. **(B)** Measured and predicted values for thermal conductivity as a function of LM loading. Thermal conductivity of **(C)** ambient **(D)** freshwater **(E)** saltwater and **(F)** concentrated saltwater aged samples. Error bars represent standard deviation. See Table A.1 for more information.

Ecoflex was chosen as a representative silicone elastomer for thermal characterization and composite samples were fabricated consisting of an Ecoflex matrix with $\phi = 0, 40$, and 80% LM inclusions.

The thermal conductivity of LM composites is largely dependent on both ϕ and the shape of the LM inclusions, with elongated droplets allowing for an increase in k in the direction of alignment.[52] The thermal conductivity of LM composites has been shown to be predicted

through a Bruggeman effective medium theory (Equation 2).[50, 59] Here, k_c is the thermal conductivity of the composite, k_i is the thermal conductivity of the inclusions, and k_m is the thermal conductivity of the matrix. L is the depolarization factor, which can be modified to predict k_c as a function of inclusion shape. For the composites tested in this work, it is expected that $L_c \simeq \frac{1}{3}$, which is the depolarization factor for spherical particles.[59]

$$\left(\frac{k_i - k_c}{k_i - k_m}\right)\left(\frac{k_m}{k_c}\right)^L = 1 - \phi \tag{2}$$

Figure 2.4B presents the thermal conductivity of the composites with respect to volume loading of LM. Under ambient conditions, as ϕ is increased from 0 to 80%, E_c realizes a 27x increase up to 4.8 W m^{-1} K^{-1}. To understand how the structure of the LM inclusions affects thermal conductivity, the predicted values of k_c from Equation 2 are plotted using L as a fitting parameter, the measured value of k_m (0.18 W m^{-1} K^{-1}) and the previously reported thermal conductivity value for EGaIn (k_i = 26.4 W m^{-1} K^{-1}).[83] Equation 2 fits the data with a value of $L = 0.33$, indicating the LM functions as close to spherical inclusion geometries as expected from the results in Figure 2.2A-D and Figure 2.3A.

For aging, the LM composites and testing fixtures are subjected to ambient, FW, SW, and CS environments for a period of four weeks to determine how underwater aging effects k_c (Figure 2.4C-F). For the composites undergoing ambient and FW aging, no observable change in k_c is apparent after four weeks. Similarly, the samples with $\phi = 0$ and 40% experience no change after aging in the SW and CS conditions. However, for the samples with ϕ = 80%, the SW and CS environments do appear to have an effect on k_c, showing a decrease by 15 and 44% respectively. The decrease in thermal conductivity in salt environments is not expected, and further experiments are required to determine the mechanism. However,

the lack of change in k_c under most other aging conditions is promising for the use of LM composites for underwater heat transfer applications. While in most cases, ϕ may be chosen to optimize cost and thermal conductivity, a higher ϕ will provide enhanced performance at an increased cost relative to a lower filled composite.

2.4.4 Electrical characterization

In addition to heat transfer, LM composites are also of interest for soft electronics, which require both extensibility and high electrical conductivity. As previously discussed, LM composites that utilize discrete spherical inclusions are often dielectric, however these materials can become electrically conductive by applying localized pressure to connect the LM droplets. Here, Sylgard LM composites with $\phi = 40$ and 80% are compressed between two plates to electrically activate the materials (Figure 2.5A). Upon application of sufficient pressure, the morphology of the composite changes, as the discrete droplets merge to form continuous domains throughout the polymer matrix (Figure 2.5B). Due to Ecoflex's extremely soft mechanical characteristics (modulus $<$ 100 kPa) electrical activation is inconsistent. For this reason, we selected Sylgard as the representative polymer matrix for electrical characterization. The electrical properties are measured through a four-point probe analysis. Here, the increase in resistance is measured as a function of length (Figure 2.5C) from 10 to 30 mm. The electrical conductivity (σ) is then determined from the slope (m) of R vs l for each of the specimens tested, where $\sigma = \frac{1}{mA}$, and A is the cross sectional area of the conductor. As the composites are relatively thin at 0.3 mm, and microscopy confirms morphological change over the entirety of the width, we take the cross sectional area of the conductor to be equal to the cross sectional area of the sample. The average electrical conductivity of the LM composites with $\phi = 40$ and 80% are determined to be 2.8×10^4 and 1.4×10^5 S m^{-1} respectively. Figure 2.5D-G contain the data for the LM composite samples over four weeks of aging in

ht!]

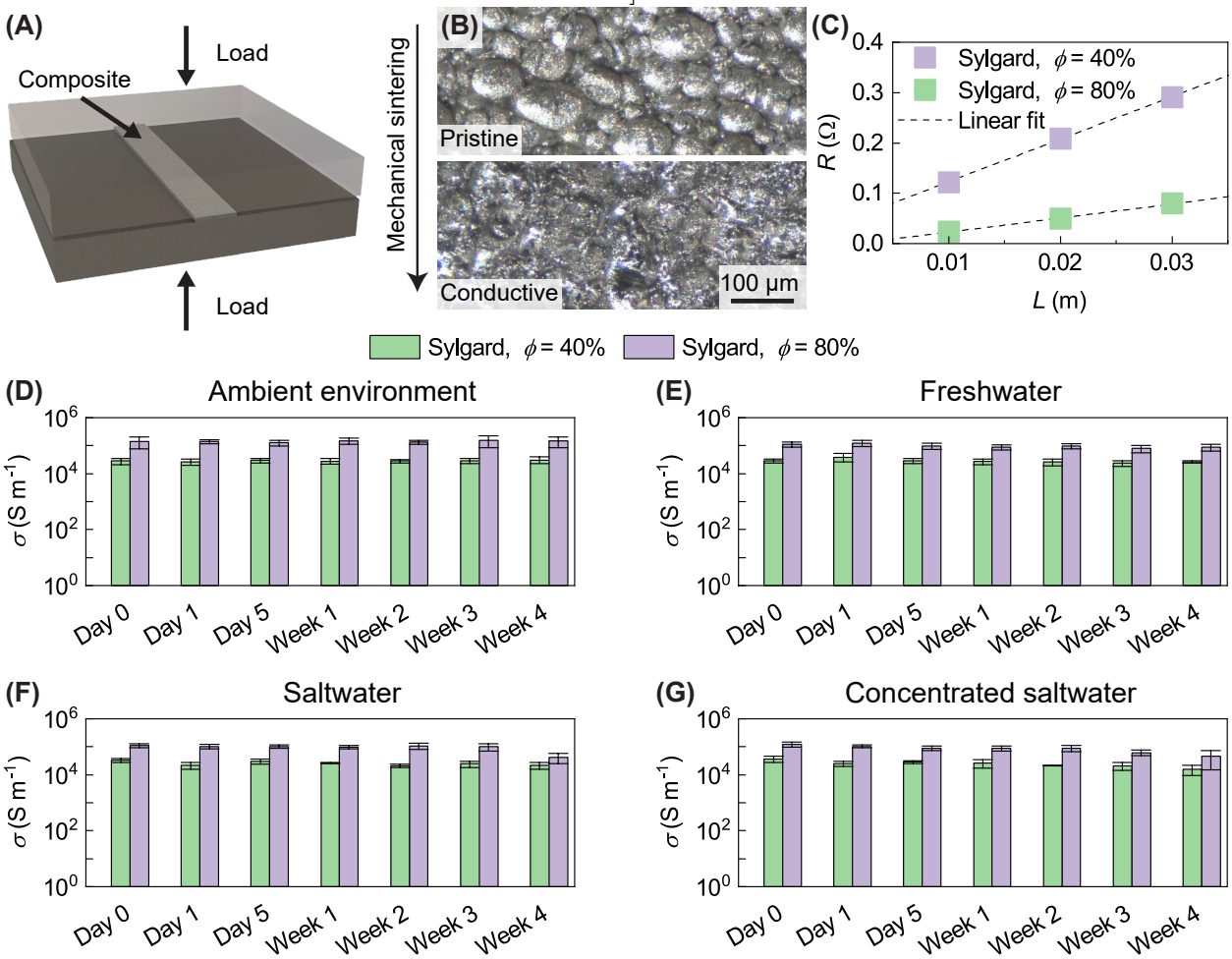


Figure 2.5: **Electrical conductivity analysis.** **(A)** Electrical activation method. **(B)** Micrographs of samples before and after activation. **(C)** Representative measurements used to calculate conductivity. Conductivity in samples aged in **(D)** ambient, **(E)** freshwater **(F)** saltwater and **(G)** concentrated saltwater environments. Error bars represent standard deviation. See Table A.2 for more information.

ambient, FW, SW, and CS environments. No substantial change is realized throughout the aging process which suggests LM composites may be a useful conductor for electronic devices due to its inherent resistance to underwater aging. Additionally, the high conductivity of the $\phi = 40\%$ composite demonstrates that EGaIn may be fabricated at $\phi = 40\%$ rather than $\phi = 80\%$ to create a more economical electrode. Traditional conductors such as aluminum, silver, and copper all undergo corrosion in the presence of saltwater environments which often occurs due to oxidation of the metal followed by reaction with chlorine anions that are present due to the inclusion of salt.[256, 257, 258] Notably, when the composites were submerged in 35,000 ppm saltwater for one hour they did not become electrically conductive at 3 atm of hydrostatic pressure for the $\phi = 40\%$ or $\phi = 80$ % samples. Based on this result, these soft electronic circuits would not undergo inadvertent electrical conductivity even at depths of approximately 30 m, enabling underwater use of these LM composite electronics (Figure A.4, A.5 and, A.6). The ability to use LM composites as water-resilient conductors has the potential to impact not only soft or flexible electronics, but could be utilized in traditional rigid underwater electronics.

2.4.5 Water-resilient LM composite electrodes

LM composites show strong potential for use as water-resilient soft electronic materials due to their soft mechanical response, high electrical and thermal conductivities, and their resilience to property change under harsh underwater environments. To demonstrate the utility of LM composites for water-resistant flexible devices and their advantage over traditional conductors such as copper during long-term seawater exposure, LM composite (Sylgard, $\phi = 60\%$) and copper electrodes of equal thickness ($t \simeq 100$ µm) are mounted on polyethylene terephthalate (PET) and suspended in the middle of a water tank. Figure 2.6A shows the experimental testing setup, which includes temperature control, filtration, and circula-

tion.

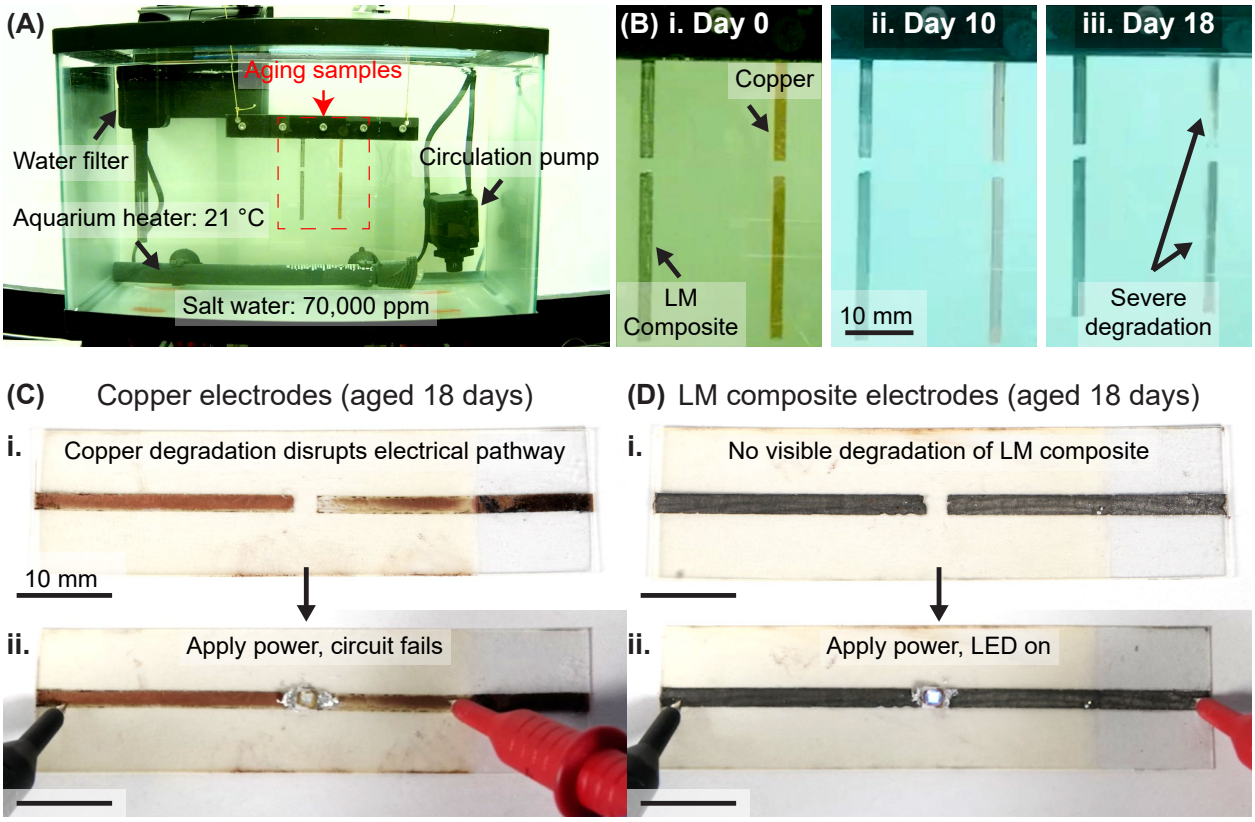


Figure 2.6: **Aging Liquid metal composite and copper electrodes.** **(A)** Aging setup for the demonstration samples. **(B)** Images showing the progression of aging of the LM composite and copper samples. **(C)** Copper and **(D)** Sylgard composite ($\phi = 80\%$) electrodes after 18 days of aging in a CS environment. **i)** Observations of visual changes in the electrodes after aging. **ii)** An LED is integrated with the electrodes and their ability to function as a circuit is evaluated. The copper electrodes fail due to degradation while the Sylgard composite electrode is able to function after aging.

Figure 2.6B shows the evolution of the electrodes over 18 days of aging in a CS environment. At day 0 (Figure 2.6B(i)), the composite and copper electrodes appear pristine with defined edges and uniform color. After 10 days of aging (Figure 2.6B(ii)), the copper electrodes begin to turn dark at the edges and the water begins to turn green-blue. From day 10 to day 18 (Figure 2.6B(iii)) the copper begins to noticeably degrade and break away from the PET sheet. The degradation of copper in saltwater can be explained by the anodic dissolution of

copper which happens through a multi-step process.[258] Agitation or flow of water has also been shown to enhance the dissolution of the copper.[259, 260] Additionally, the reaction of copper with the saltwater environment predicts the color change observed on the copper electrodes and in the aqueous environment, where copper(I) oxide is a dark brown color, and the copper(II) chloride appears green.[259] As opposed to the copper electrodes, the LM composite electrodes show no visible degradation.

After 18 days of aging, the composite and copper electrodes are removed from water and their ability to function in an electrical circuit is tested (Figure 2.6C and D). Figure 2.6C(i) shows the copper electrode after 18 days of aging, where degradation of the copper by the CS environment has caused disruptions in the continuous pathway of copper. An LED is added to the copper electrodes and copper paste is added to facilitate contact between the copper and LED contacts. Upon application of power, the circuit fails due to degradation of the copper (Figure 2.6C(ii)), and the LED does not turn on. In contrast to the copper, the LM composite electrodes show no visible sign of degradation (Figure 2.6D(i)), and the electrical conductivity is expected to be maintained as shown in the aging studies from Figure 2.5. The LED is then integrated with the LM composite electrodes, and the circuit functions upon application of power (Figure 2.6D(ii)) demonstrating the utility of LM composites as water-resilient materials for underwater electronics.

2.5 Conclusions

In this work, the effect of underwater aging on the mechanical and functional properties of LM-elastomer composites is quantified. The materials are shown to undergo changes in their material compositions through the diffusion of water and salt as confirmed through mass measurements and EDS. The mechanical response of the materials is largely unchanged over

the aging period, with notable exceptions occurring at volume fractions of 80%, where the CS-aged Ecoflex samples show a 70% decrease in modulus when compared to the ambient samples. The Ecoflex LM-composites with LM volume fractions of 80% show a decrease of 15 and 44% in thermal conductivity after aging in SW and CS environments respectively, however the rest of the aging conditions do not present a noticeable change. The electrical conductivity of Sylgard LM-composites was also tested, and showed no appreciable change after four weeks of aging. While this study quantifies the effect of underwater aging on LM composites, future aging studies could focus on the corrosion effects of LM composite-rigid electronic interfaces, which may face alternative methods of degradation such as galvanic corrosion. Furthermore, the effect on thermal and electrical conductivities under mechanical loading (such as hydrostatic pressure or tension) and underwater aging could provide further information on underwater resilience. Nonetheless, the understanding provided in this work facilitates the design of LM technologies for different applications, including their use for wearable devices to improve human health and safety in underwater environments, and for the integration of these materials into robotic systems for underwater exploration.

2.6 Experimental/Methods

2.6.1 Composite Fabrication

Sylgard 184 (Dow) is mixed with a 10:1 weight ratio of base to curing agent using a dual asymmetric centrifugal (DAC) mixer (FlackTek) for 1.5 min at mixing speeds of up to 1800 rpm under vacuum. Ecoflex-30 (Smooth-On) is a two-part platinum catalyzed silicone that is mixed with a 1:1 ratio of part A to part B using the DAC mixer for 2 min at mixing speeds up to 1600 rpm under vacuum. The LM droplet size was set by incorporating $\phi =$

80% into the matrix polymer at 800 rpm for two minutes under vacuum. $\phi = 40\%$ samples were fabricated by diluting the initial mixture with additional elastomer at 800 rpm for one minute under vacuum. The samples are then cured in a convection oven with a set temperature of 80 °C.

2.6.2 Underwater aging

Three underwater testing chambers were created with different Instant Ocean brand salt concentrations of 0, 35,000, and 70,000 ppm respectively (Figure 2.1A). The first two salt concentrations mimic the approximate conditions of freshwater and marine salt water respectively, while the 70,000 ppm concentration is made to accelerate the effect of salt water on silicone aging. As of 2015, Instant Ocean contained (Cl^-, Na^+, SO_4^{2-}, Mg^{2+}, Ca^{2+}, K^+, HCO_3^-, B^{3+}, Sr^{2+}) [261] The testing chambers were outfitted with aquarium heaters to maintain a constant temperature of 21 °C. Circulation pumps were integrated to promote even mixing and heat transfer, and filtration systems were added to prevent algae growth and remove impurities. The samples are placed into immersion chambers made from 1.6 mm thick acrylic with laser cut 6 mm diameter -holes to ensure proper contact with the underwater environments (Figure 2.1B).

2.6.3 Mechanical testing

Mechanical samples were initially drawn out as thin sheets of approximately 300 µm thickness after curing. Samples were then cut with a dogbone-geometry die to a width of 3 mm and a gauge length of 30 mm. Each sample is removed from the tanks and tested via uniaxial extension at a rate of 60 mm min^{-1} until failure. Three specimens are measured for each aging data point.

2.6.4 Thermal conductivity testing

Transient hot wire (THW) analysis was used to evaluate the thermal conductivity of Ecoflex composites with $\phi = 0$, 40, and 80% volume LM. Platinum wire with a length of 20 mm and a diameter of 0.0254 mm was soldered between copper tape contacts integrated with a printed resin support structure. The elastomer was then cast as a 20 mm x 15 mm x 17 mm geometry that encapsulated the support structure. For the LM composites with $\phi = 80\%$, hexanes were added to the uncured mixture to reduce the viscosity and improve the molding process. The hexanes were then removed through application of negative pressure from a vacuum pump prior to curing in a convection oven set to 80 °C. The THW experiment was carried out using a Kiethley 2461 Sourcemeter utilizing the same procedure as Tutika *et al.*[50]

2.6.5 Electrical conductivity testing

Sylgard LM composites with $\phi = 40$ and 80% were cast at a thickness of 0.3 mm and cut into 60 mm x 10 mm rectangular geometries. The samples were then mechanically sintered across the entire surface by placing the sample between two steel plates and applying compressive force. The resistance was tested using the 4 point ohmmeter setting on a Kiethley 2461 Sourcemeter over a distance of 10, 20, and 30 mm.

2.6.6 Composite electrode aging

The LM composite electrodes were fabricated by a multi-step process. First 150 µm thick PET is subjected to O_2 plasma treatment for 2 min to facilitate adhesion of the elastomer to the substrate. A masking layer is then used to cast the Sylgard LM composites ($\phi = 80\%$)

electrodes in geometries of 2 mm x 40 mm with a casting thickness of 100 µm separated by a distance of 2.5 mm for application of the LED. The copper electrodes are fabricated adhering copper tape (t = 100 µm) with a width and length of 2 mm x 40 mm respectively to 150 µm thick PET. The electrodes are then hung in the middle of the tank filled with a 70,000 ppm saltwater solution and aged for a period of 18 days prior to testing with an integrated LED.

2.6.7 Hydrostatic testing

Sylgard ϕ = 40% and 80% samples were immersed in 35,000 ppm saltwater within the chamber of a pressure pot. The pressure was raised to 3 atm and the samples were left for an hour. The samples were then removed from the pressure pot and tested for electrical conductivity with a multimeter (Figure A.4, A.5 and, A.6).

2.7 Acknowledgements

We acknowledge support from the Office of Naval Research Young Investigator Program (YIP) (N000142112699). This work was performed in part at the Nanoscale Characterization and Fabrication Laboratory, which is supported by the Virginia Tech National Center for Earth and Environmental Nanotechnology Infrastructure (NanoEarth), a member of the National Nanotechnology Coordinated Infrastructure (NNCI), supported by NSF (ECCS 1542100 and ECCS 2025151).

Chapter 3

Tough bonding of liquid metal-elastomer composites for multifunctional adhesives

Modified from a manuscript published in *Small*.

Tyler A. Pozarycki,[1†] Dohgyu Hwang,[1,2†] Edward J. Barron III,[1,2†] Brittan T. Wilcox,[1] Ravi Tutika,[1,2] and Michael D. Bartlett.[1,2*] Tough Bonding of Liquid Metal-Elastomer Composites for Multifunctional Adhesives. *Small*, 2022, 18(41), 2203700.

1. Mechanical Engineering, Soft Materials and Structures Lab, Virginia Tech, Blacksburg, VA 24061, USA.

2. Macromolecules Innovation Institute, Virginia Tech, Blacksburg, VA 24061, USA.

† These authors contributed equally to this work.

∗ To whom correspondence should be addressed: mbartlett@vt.edu

3.1 Contributions

For the work titled "**Tough bonding of liquid metal-elastomer composites for multifunctional adhesives**" the dissertation author Edward J. Barron III contributed the following:

- Refined and co-developed the method described in this work that utilizes (3-Aminopropyl)triethoxysila (APTES) to chemically anchor LM composites to diverse substrates.
- Carried out the majority of adhesive characterization used in this work and analyzed all adhesion data utilized in Figure 3.1, and Figure 3.3a-c.
- Was an equal contributor (along with T.A.P.) in the design, integration, and fulfillment of the demonstrations shown Figure 3.5.
- Was the primary creator and editor of Figure 3.3 and Figure 3.5, and was an editor of Figure 3.1.
- Was a primary contributor in the writing of this work.

3.2 Abstract

Liquid metal (LM) composites, which consist of LM droplets dispersed in highly deformable elastomers, have recently gained interest as a multifunctional material for soft robotics and electronics. The incorporation of LM into elastic solids allows for unique combinations of material properties such as high stretchability with thermal and electrical conductivity comparable to metals. However, it is currently a challenge to incorporate LM composites into integrated systems consisting of diverse materials and components due to a lack of adhesion control. Here we present a chemical anchoring methodology to increase adhesion of LM composites on diverse substrates. The fracture energy increases up to 100x relative to untreated surfaces, with values reaching up to 7800 J m^{-2}. Furthermore, the fracture energy, tensile modulus, and thermal conductivity can be tuned together by controlling the microstructure of LM composites. Finally, the bonding technique is used to integrate LM composites with functional electronic components without encapsulation or clamping, allowing for extreme deformations while maintaining exceptional thermal and electrical conductivity. These findings can accelerate the adoption of LM composites into complex soft robotics and electronics systems where strong, reliable bonding between diverse materials and components is required.

3.3 Introduction

Soft materials with high stretchability, conformability, and thermal and electrical conductivity are critical for emerging applications in soft robotics and electronics systems.[10, 16, 56, 60, 62, 262, 263, 264] Recently, soft composites consisting of liquid metal (LM) droplets dispersed in highly deformable elastomers have gained particular interest, as these materials are soft and stretchable yet display exceptional mechanical, thermal, and electrical properties.[9, 14, 52, 59, 99, 233, 265, 266, 267, 268, 269] For example, LM composites can act as soft wiring for wearable devices, yet be flexible enough to seamlessly interface with the contours of human tissue.[241, 270, 271, 272, 273] Liquid metal and LM composites are also useful as thermal interface materials (TIMs) for electronic components to improve heat dissipation. [52, 92, 274, 275, 276] To fully utilize LM composites for applications in soft robotics, wearable computing, and reconfigurable systems, they must be integrated with and attached to different components and interfaces. However, current integration strategies rely primarily on physical attachment, clamping, and encapsulation,[9, 59, 117, 277] and strategies to strongly bond LM composites to diverse materials are lacking.

Bonding LM composites to substrates, particularly polymers, is challenging due to their low surface energy and lack of functional groups.[253, 278, 279, 280] One method is to utilize substrates with fibrous or porous structures to allow for mechanical interlocking between the elastomer and substrate.[281, 282] However, in many cases, bonding to smooth substrates is desired. Another approach is to perform plasma treatment on the materials for surface cleaning and activation. Plasma bonding is a common technique for adhering silicone elastomers such as PDMS to various surfaces,[283, 284] yet there are limitations to the effectiveness of the technique when used with silicones of high plasticizer content. For example, commercial silicones such as Ecoflex are widely used for LM composites and other applications in soft electronics and soft robotics, but their high content of silicone oils leads to chal-

lenges with plasma bonding[253]. Silicone surfaces treated with oxygen plasma experience hydrophobic recovery over time due to surface fouling with contaminants and diffusion of unreacted oligomer to the surface, both of which decrease bonding capabilities shortly after treatment.[278] One way to overcome limited work time is to incorporate chemical treatment across interfaces. For example, substrates can be coated with chemical primers such as cyanoacrylates to allow for strong bonding with other materials.[285, 286, 287] However, hardened cyanoacrylates can generate a mechanical compliance mismatch with deformable materials, resulting in significant stress concentrations and interfacial failures. One promising approach to solve this problem is to treat desired surfaces with functional silanes before bonding.[288] Silane treatment of a material alters its surface chemistry, thus avoiding compliance mismatches generated by the addition of adhesive materials at interfaces. The organosilane (3-aminopropyl)triethoxysilane (APTES) has demonstrated the ability to create stable siloxane bonds between silicones and hydroxylated substrates.[289, 290, 291] However, there is limited work on bonding LM composites through surface treatments and to silane-functionalized surfaces.

Here we show an approach to generate tough, permanent adhesion of LM composites to diverse substrates. Strong bonding is achieved by chemically anchoring LM composites to various materials through a surface treatment process that uses oxygen plasma and APTES (Figure 3.1a). This approach increases the fracture energy (G_c) of peel specimens by up to 100x relative to specimens with no treatment (Figure 3.1b, c), with maximum values around 7800 J m^{-2}. Furthermore, the adhesives can bear heavy loads, as demonstrated by suspending three bricks (total mass 6.8 kg) from a pre-cracked peel specimen with a width of 15 mm (Figure 3.1d). It is found that by varying LM droplet size from 2 - 60 µm and volume loading from 20 - 60%, the fracture energy can be tuned with tensile modulus and thermal conductivity. These results show that the smallest droplets lead to the highest values of G_c

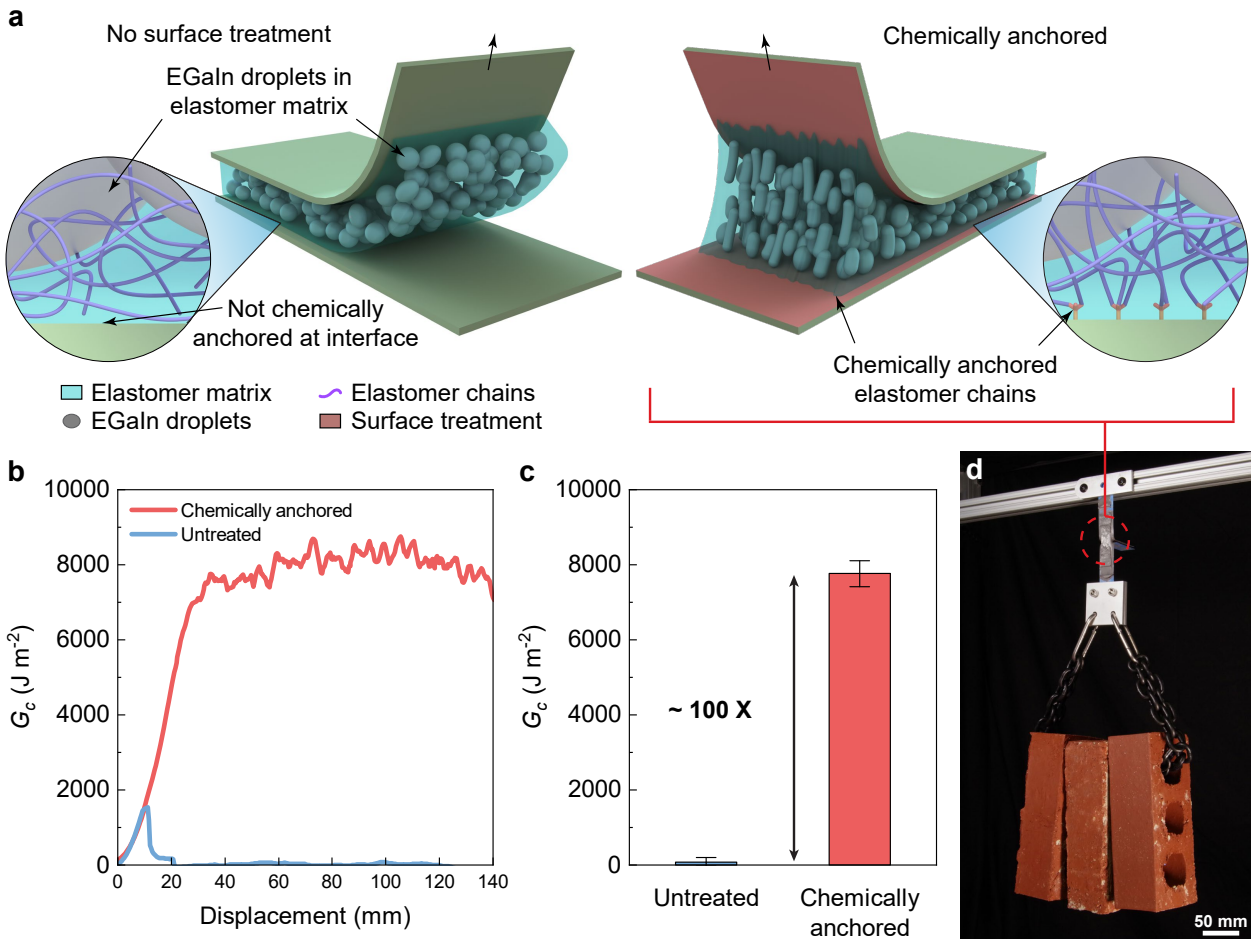


Figure 3.1: **Strong bonding of liquid metal composite. a)** Schematic representation of liquid metal composite adhesion without (left) and with (right) chemical anchoring. **b)** Fracture energy (G_c) versus displacement of representative LM composites ($\phi = 20\%$, $d = 2$ µm) undergoing peeling. **c)** Fracture energies of untreated and chemically anchored samples ($\phi = 20\%$, $d = 2$ µm). Error bars represent the standard deviation for n = 3. **d)** Strong LM composite adhesive supporting bricks of total mass 6.8 kg from a 15 mm wide, pre-cracked peel specimen.

and modulus, while thermal conductivity is similar over different size droplets, thus demonstrating control of toughness and thermal properties. Finally, we demonstrate potential applications of this tough bonding approach in soft robotics and electronics by chemically anchoring rigid materials and electronic components to LM composite to create robust soft electronics systems. These systems are developed without encapsulation or clamping of the LM composite, thus simplifying integration while maintaining extreme deformability and

exceptional thermal and electrical performance.

3.4 Results and discussion

The LM composites consist of Ecoflex silicone elastomer with dispersed droplets of eutectic gallium-indium (EGaIn). The volume fraction of LM was varied from $0 \leq \phi \leq 60\%$ with droplet sizes ranging from $2 \leq d \leq 60$ μm based on particle analysis (see Figure B.1 and Figure B.2). To create chemically anchored samples, substrates were treated with oxygen plasma, submerged into a 0.1 vol% APTES in ethanol solution, and allowed to dry at room temperature. Then, liquid-state LM composite was cast onto the surface and cured. Untreated samples were prepared using a similar procedure except oxygen plasma and APTES solution were not utilized (see experimental section for more details). The APTES creates an abundance of functional amine groups on a material surface. Additionally, pretreating with plasma increases the amount of active sites for APTES to attach compared to a pristine material.[292, 293] Upon casting liquid-state LM composite onto the treated surface, chemical anchoring of elastomer chains occurs through interfacial compatibilization of the silane treatment and the silicone elastomer, which can occur through the formation of an interpenetrating polymer network (IPN) between polymer chains and the silane molecules (Figure 3.1a).[294]

Adhesion performance was analyzed by conducting T-peel tests in which LM composite was cast between two flexible polyethylene terephthalate (PET) adherends (Figure 3.2a). The untreated samples experienced adhesive failure at the composite-PET interface. In contrast, the chemically anchored composites did not debond from the adherends. Instead, the crack propagated cohesively through the composite, as material fracture was more energetically favorable than breaking the interfacial bonds. To investigate LM composite fracture on the

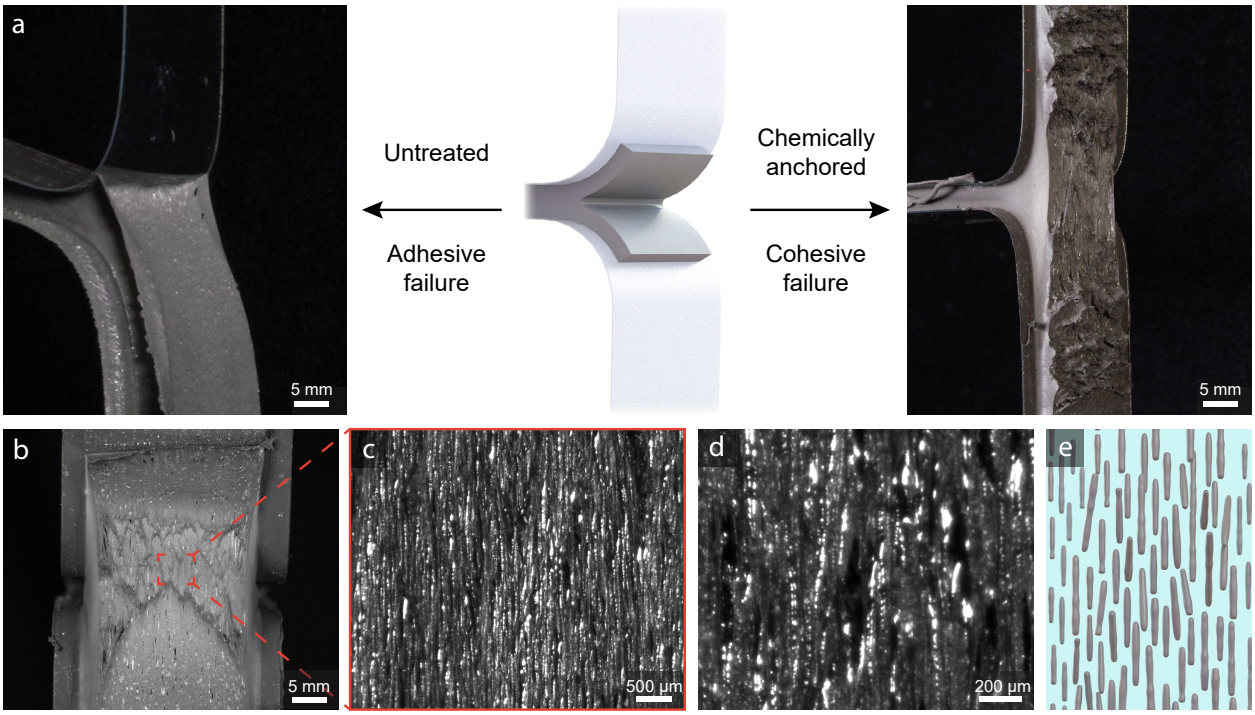


Figure 3.2: **LM composite adhesion. a)** Adhesive and cohesive failures of LM composite sample ($\phi = 20\%$, $d = 2$ µm) in T-peel without and with APTES surface treatment **b)** Macrophotograph image of the crack front of an LM adhesive ($\phi = 20\%$, $d = 60$ µm) undergoing cohesive fracture with **c, d)** showing the corresponding micrographs. **e)** Schematic representation of liquid metal droplet elongation at the crack front.

microscale, the crack front of a chemically anchored sample was monitored during peeling (Figure 3.2b-d). We observed significant deformation which resulted in the LM inclusions elongating in the damage region. This behavior is represented schematically in Figure 3.2e and highlights the reconfigurable nature of the LM droplets under deformation.

3.4.1 Effects of LM microstructure on fracture energy

To investigate the effect of microstructure on fracture energy, nine distinct compositions of chemically anchored composites were tested under T-peel, including three LM volume loadings ($\phi = 20, 40, 60\%$) each with three mean droplet diameters ($d = 2, 15, 60$ μm).

Unloaded Ecoflex samples were also fabricated ($\phi = 0\%$). For each sample, the fracture energy G_c is obtained by normalizing the measured plateau peel force F by the composite width w, $G_c = 2F/w$.[295, 296] A decrease in volume fraction and mean droplet diameter is observed to lead to an increase in fracture energy (Figure 3.3a). The largest G_c is obtained with $\phi = 20\%$, $d = 2$ µm, which is similar to that of the unfilled elastomer. Although G_c decreases with increasing ϕ, a significant G_c value of 2880 ± 150 J m^{-2} is achieved for $\phi = 60\%$. Previous work by Kazem et al. has shown that higher LM volume fractions in soft elastomers result in an extreme toughening effect;[297] however, the work presented here shows a contrasting trend which is attributed to differences in the crack propagation mechanism. Kazem et al. showed that extreme toughening is a result of crack redirection due to elongation of LM inclusions perpendicular to the propagating crack. In this work, chemically anchored specimens tended to fracture in a serrated or sawtooth pattern, where the pronouncement of the pattern has been shown to depend on parameters such as loading conditions, sample thickness, and adherend thickness.[298, 299] This characteristic serrated morphology likely results in the crack moving back and forth along the direction of loading, not directly through the centerline of the crack front. This would reduce the crack deflection effectiveness of the LM droplets, allowing the crack to propagate along the inclusions, not through the inclusions where deflection could occur. Next, with regard to LM droplet size, smaller LM droplets tend to act as stiffer inclusions.[254] This has been shown through elastocapillary arguments as well as the existence of a stiff, solid oxide layer on the surface of LM particles.[51] As LM droplet size decreases, the ratio of outer solid surface area to inner liquid volume increases, resulting in a higher effective stiffness. This trend is similar to elastocapillarity, which states that the surface tension of liquid inclusions will stiffen a composite when the inclusion size is sufficiently small. This increased composite stiffness tends to toughen the LM composites for the same ϕ as observed in Figure 3.3a.

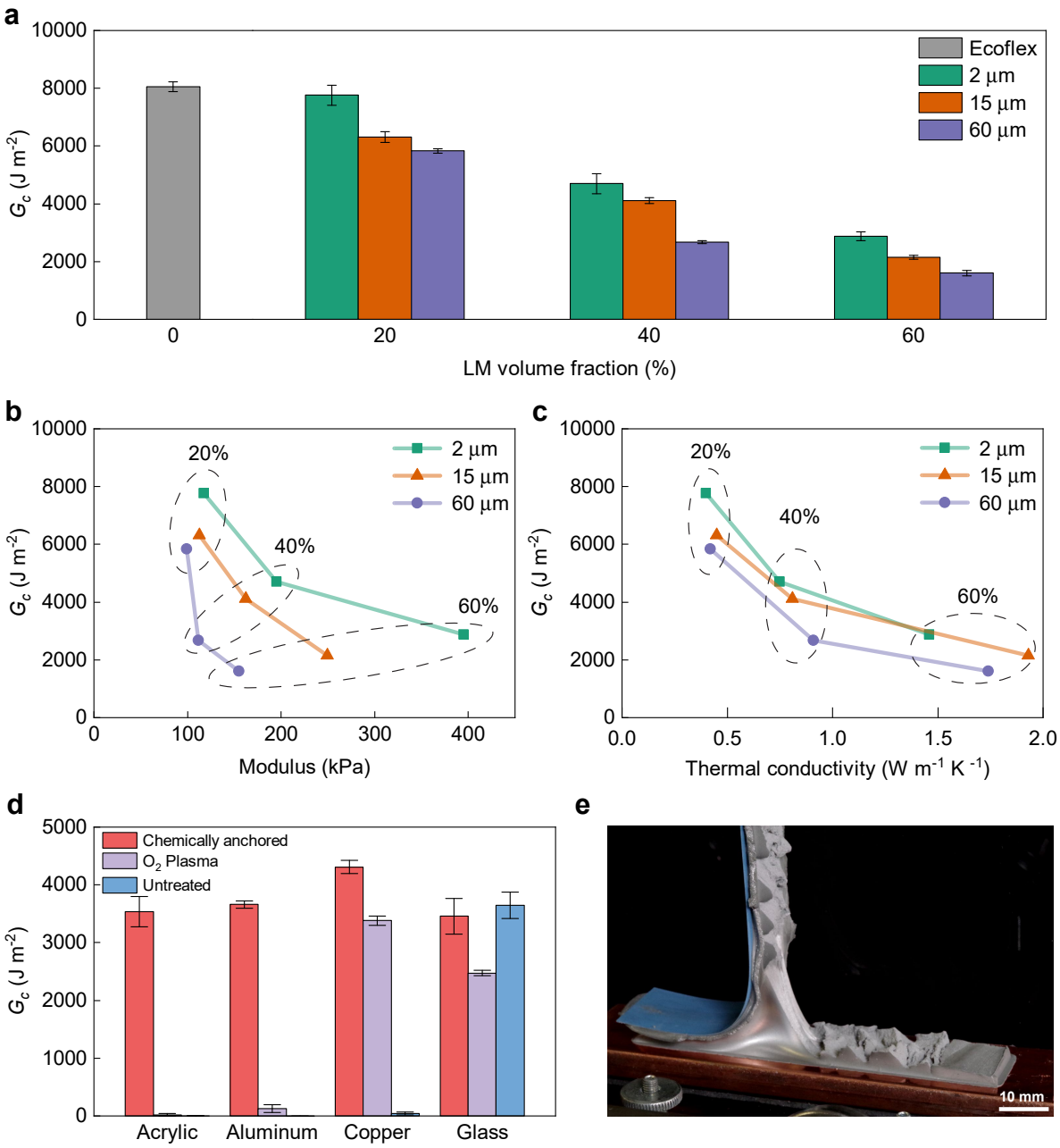


Figure 3.3: **Adhesion and property characterization of LM composites. a)** Fracture energies of LM composites in T-peel. **b)** Comparison of LM composite fracture energy and elastic modulus. **c)** Comparison of LM composite fracture energy and thermal conductivity. **d)** Fracture energy of LM composite on varied surfaces in 90° peel for $\phi = 40\%$, $d = 15$ µm. **e)** Macrophotograph of the cohesive failure of a 90° peel sample on copper. Error bars represent the standard deviation for n = 3.

The effect of LM droplets on composite modulus and thermal conductivity are important areas of research for soft matter systems. [233] Previous work has focused on understanding the effect of LM droplets on the mechanical response of soft composites. [265] Additionally, significant research has been performed to create LM composites with exceptional thermal conductivities (k), which can be achieved through high liquid metal content for isotropic composites (k = 2 - 6.7 W m^{-1} K^{-1}),[50, 300] or by droplet elongation to increase functionality in the direction of alignment (k = 3.8 - 13.0 W m^{-1} K^{-1}).[52, 59, 92] These materials can benefit from simplified integration through tough bonding; however, the relationship between fracture energy with thermal conductivity and tensile modulus has not been explored.

In this work, we show LM composites with desirable thermal and mechanical properties while also achieving tough adhesion to various substrates. Figure 3.3b shows the relationship between G_c and composite modulus. By controlling the volume loading and mean LM droplet diameter, composites with prescribed combinations of toughness and modulus can be created. For example, by maintaining an LM volume fraction of 20% and changing the mean droplet diameter from 2 to 60 µm, the fracture energy can be tuned by ∼2000 J m^{-2} with a slight change in modulus of less than 20 kPa. In contrast, at higher LM volume fractions, the mean LM droplet diameter is shown to have a greater effect on modulus than on toughness. At a volume fraction of 60%, a change in modulus of over 240 kPa results in a change in G_c of 1275 J m^{-2} as mean droplet diameter is changed from 2 to 60 µm.

The thermal conductivity of these composites can also be tuned while controlling the fracture energy. Figure 3.3c shows the relationship between G_c and k, where G_c generally decreases with increasing composite thermal conductivity. The thermal conductivity does not display a pronounced dependence on LM droplet diameter, and instead is dependent on volume fraction. In contrast, changes in droplet size have a noticeable effect on fracture energy. These findings are enabling for the development of LM composite adhesives with desired

combinations of thermal conductivity and fracture energy, which can be controlled by LM volume fraction and droplet size respectively.

3.4.2 Robust adhesion to multiple surfaces

Strong bonding to diverse substrates is required for a variety of applications. In order to show the broad application of the chemical anchoring technique, one composition of LM composite (ϕ = 40%, d = 15 µm) is bonded to several rigid, non-porous substrates. The fracture energy is then measured via 90 ° peel test, for which $G_c = F/w$ (Figure 3.3d). All untreated samples, except for glass, experience adhesive failure at the composite-substrate interface. This results in very low adhesion ($<$ 10 J m^{-2} for acrylic and aluminum and $<$ 50 J m^{-2} for copper), as is commonly observed with silicones and LM composites. Oxygen plasma treatment without APTES was also performed, where only select substrates showed strong adhesion such as copper and glass, while acrylic and aluminum showed low adhesion. In contrast, all chemically anchored samples that utilize both oxygen plasma and APTES treatment fracture through the composite thickness with G_c values over 3000 J m^{-2}. It is observed that the cohesive fracture energy measured in 90° peel for the chosen sample composition is similar to that measured in T-peel. Furthermore, samples tested in 90° peel also display a serrated or sawtooth appearance of the fracture surface (Figure 3.3e). Given these results, the chemical anchoring technique is promising for the incorporation of LM composites into larger systems consisting of diverse materials.

3.4.3 Integration of LM composites into electronic systems

The high thermal conductivity of LM composite gives rise to its potential use as a thermal interface material (TIM) in modern electronics.[52, 275, 301] Furthermore, an electrically

insulating matrix such as Ecoflex lessens the risk of electrical shorting, mitigates the corrosive effect of gallium[92, 302], and allows for chemical anchoring techniques to be leveraged. To demonstrate, computer graphics benchmark tests are conducted using the as-received thermal compound between the graphics processing unit (GPU) and a passive heatsink. The compound is then replaced with chemically anchored LM composite (ϕ = 60%, d = 60 µm) and unfilled Ecoflex. It is found that the GPU temperature and performance with LM composite is similar to the stock thermal compound (Figure 3.4a, b). However, Ecoflex performs notably worse, as the GPU reaches much higher temperatures. Finally, to demonstrate strong adhesion from chemical anchoring, the screws holding the heatsink (66 grams) in place on the GPU circuit board are removed and an additional 50 g mass is suspended near the 7.6 x 9 mm area containing the chemically anchored LM composite (Figure 3.4c). The strong adhesion and thermal control of the LM composite could be leveraged for future integrated systems within rigid electronics applications.

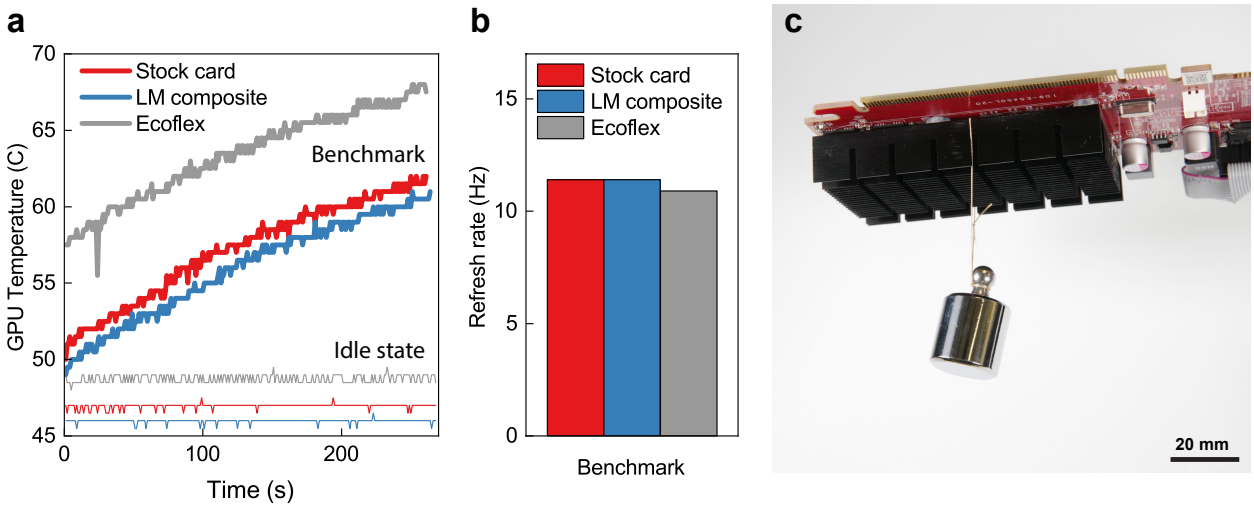


Figure 3.4: **Integration and heat dissipation of electronics with LM composites.** **a)** Temperature measured by the GPU thermocouple during idle and benchmark tests. **b)** Performance of the graphics card with the stock configuration and with LM composite and Ecoflex as replacements for the thermal interface material. **c)** Suspension of both the heatsink (66 grams) and an additional 50 grams from a chemically anchored LM composite.

Along with its high thermal conductivity, LM composite demonstrates exceptional stretchability and toughness, and these properties are especially important to the emerging field of stretchable electronics. To demonstrate a stretchable electronics system which leverages all three properties, a LM composite sample is created in which electronic components and external leads are directly integrated without encapsulation or clamping. Here, a high-power LED (Cree Extreme High Power (XHP)) and external copper contacts are chemically anchored to a LM composite sample ($\phi = 60\%$, $d = 60$ µm). A pristine Ecoflex sample is also created with untreated copper contacts (Figure 3.5a). On both samples, LM traces are spray coated from the copper to the LED contacts to complete an electrically conductive network. The LEDs are supplied with a current of 0.6 A while the samples remain unstretched, resulting in a power output of ∼3 W with a high brightness. After 80 s, the LED anchored to the Ecoflex sample reaches a temperature over 135 °C, leading to thermal failure (Figure 3.5b, c, i-ii). The LED anchored to the composite reaches a temperature of approximately 85 °C and remains on after the same amount of time (Figure 3.5b, d, i-ii). At this point, both the samples are stretched and at ∼35% global strain, the Ecoflex sample completely detaches from the untreated bottom copper contact and the top grip continues to rise (Figure 3.5c, iii-vi). In comparison, the LM composite remains anchored to its treated copper contacts until ∼310% global strain, at which the sample fractures at the bottom neck, breaking the LED circuit (Figure 3.5d, iii-vi). Thus, chemical anchoring prevents failure due to debonding between components and instead allows for system design based on the mechanical properties of the composite material. Furthermore, LM composite allows for more efficient thermal dissipation, while the pristine polymer demonstrates poor thermal properties.

The use of chemically anchored LM composites in stretchable electronics systems is further demonstrated through the robust attachment of a circular membrane film (750 µm) to an LED and a supporting acrylic substrate, without encapsulation or mechanical clamping

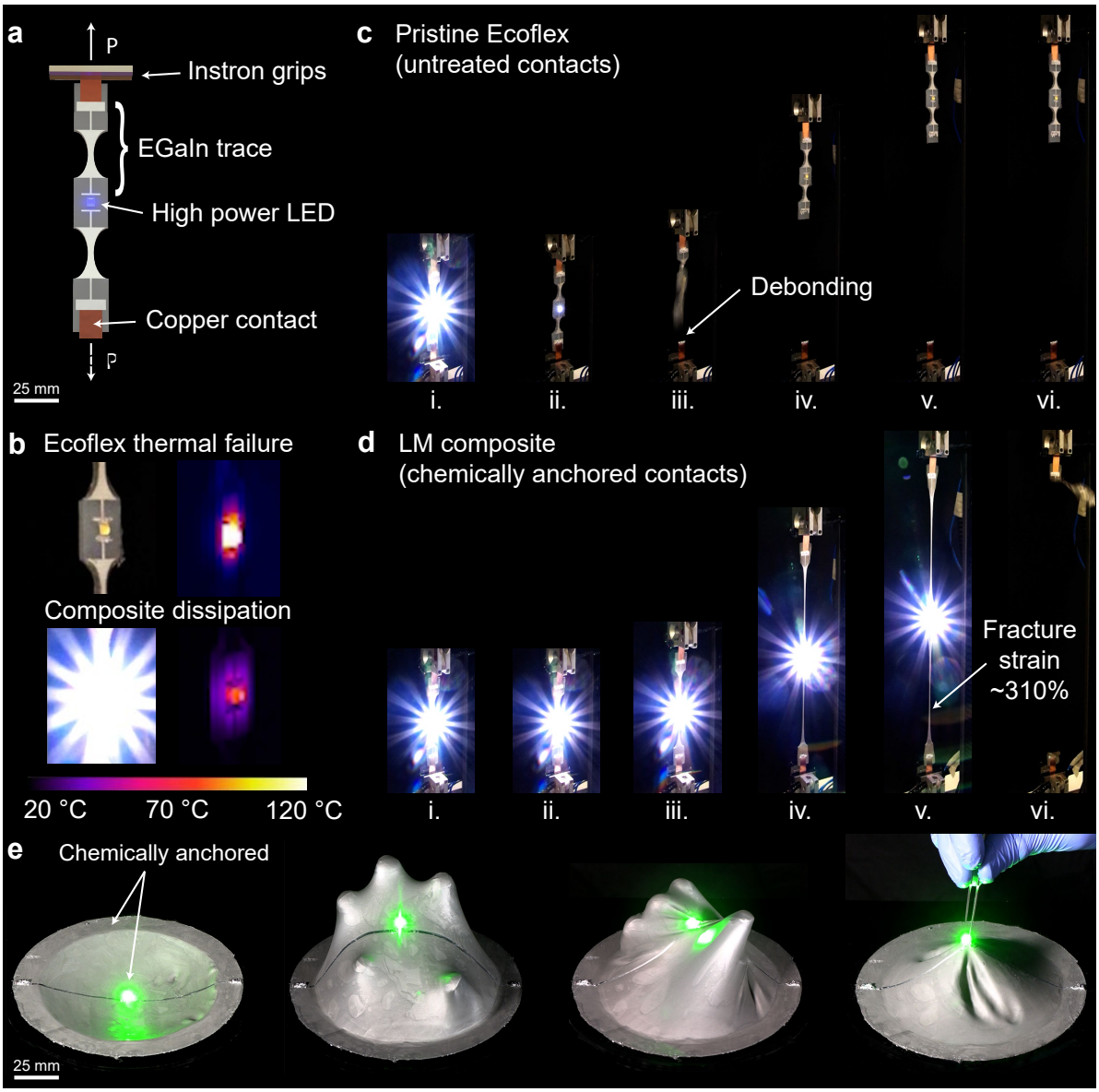


Figure 3.5: **Stretchable circuits through tough LM composite adhesives.** **a)** Schematic representation of an integrated LM composite device. **b)** Thermal profiles of Ecoflex and LM composite samples after 80 s. **c)** Ecoflex sample timelapse, showing thermal failure of the LED (ii) and adhesive failure at the bottom copper contact (iii). **d)** LM composite sample timelapse, showing high stretchability and heat dissipation and eventual fracture through the bottom neck (v-vi) at ∼310% global applied strain. **e)** LM composite thin film with (from left to right) chemically anchored to an LED and supporting acrylic substrate, hand-stretching, torsion, and stress applied directly to the LED while pulling with tweezers.

(Figure 3.5e, i). After supplying the LED with 0.05 A current, the system is subjected to tensile and torsional stresses. During each stress scenario, the film remains bonded to the acrylic substrate and the LED remains on (Figure 3.5e, ii-iii). Additionally, the LED does not detach from the composite even when stress concentration occurs across the small interfacial area by pulling the LED with tweezers (Figure 3.5e, iv). These characteristics demonstrate the exceptional toughness of the chemically anchored interfaces as well as the ability to leverage the functional properties of LM composites for the creation of robust, stretchable systems.

3.5 Conclusions

In this work, we present a method to permanently adhere LM composites to a variety of materials. Tough adhesion is achieved through the functionalization of surfaces with oxygen plasma and APTES, which allows for chemical anchoring of elastomer chains to a desired material. Chemical anchoring leads to steady-state crack propagation in the composite layer, resulting in an increase in fracture energy of up to 100x relative to samples with untreated adherends. The fracture energy is controlled by LM composite microstructural parameters such as droplet size and volume loading. Additionally, G_c demonstrates paired tunability with other functional properties such as modulus and thermal conductivity. Notably, the fracture energy of the toughest composite system ($\phi = 20\%$, $d = 2$ µm) is similar to that of the pristine elastomer ($\phi = 0\%$). Given that smaller values of both ϕ and d tend to translate to higher values of G_c, the fabrication of composites with nanoparticles, volume fractions less than 20%, or a combination thereof may provide opportunities for creating a composite system in which the fracture energy is superior to that of the pristine elastomer. However, the balance of properties such as thermal conductivity and modulus may also need

to be considered, allowing for future optimization of desired properties by controlling particle size, LM loading, elastomer choice, and distribution and shape of droplets. These properties are particularly useful for applications in soft electronics and robotics since tough, stretchable, and thermally conductive materials are often desired in these areas. The utility of the bonding method is demonstrated by successfully integrating various materials with LM composites to create robust, highly stretchable, and thermally conductive soft electronics systems. These results could inspire the development of more complex soft matter systems not otherwise possible without reliable bonding, thus creating more seamless integration between soft functional materials and rigid electronic components for robust, hybrid electronic and robotic systems.

3.6 Experimental section

3.6.1 Fabrication

Liquid metal composite fabrication- LM particles are fabricated using an in-situ technique where the bulk LM is first added to uncured elastomer (Ecoflex 00-30, Smooth-On, Inc.) and mixed with a stirring rod for 2 min. To achieve particle diameters of 80 and 20 µm, solutions containing 66 vol% LM in elastomer are shear mixed in a dual asymmetric centrifuge (DAC 1200-500 VAC, FlackTek) at 1200 and 1700 RPM, respectively. To fabricate particles with a 2 µm diameter, separate solutions containing 70 vol% LM in prepolymer and LM in curing agent are mixed using an overhead mixer (6015 Ultra Speed, Caframo) at 6000 RPM. Emulsions containing the desired particle sizes are then diluted with uncured elastomer to set the volume loading[50]. In the case of 2 µm particle size, the separate 70 vol% solutions are combined 1:1 and subsequently diluted. The final composites are cast into molds to prepare the samples for testing.

T-peel fabrication- PET adherends are laser cut into 125 mm x 20 mm strips from stock sheets of 125 µm-thick PET. After cleaning with isopropyl alcohol, the strips are treated with oxygen plasma (3 min, 300 mTorr oxygen, 400 W, PE-75 Series, Plasma Etch, Inc.) to functionalize the surface in preparation for APTES treatment. The plasma-treated PET strips are then dip coated in a 0.1 vol% APTES in ethanol solution and placed onto a glass plate to dry for 5 h. Ecoflex and LM composite samples are cast directly onto an APTES-treated PET adherend placed underneath a 75 mm x 15 mm x 3.2 mm acrylic mold. A second APTES-treated PET adherend is laid on top of the uncured sample. The completed T-peel specimen is cured at 80°C for at least 12 h. Viscous composites such as $\phi = 60\%$, $d =$ 2 µm are cured at room temperature for 12-15 h and then at 80°C for 3 hours. After curing, the mold is removed and a 10 mm pre-crack is cut through the midplane of the thickness

and along the sample length using a razor blade.

90° peel fabrication- Substrates are cleaned with isopropyl alcohol, treated with oxygen plasma, submerged into a 0.1 vol% APTES in ethanol solution, and left to dry. An acrylic mold is secured on top of the treated substrate and the LM composite is cast onto the substrate surface. Finally, an APTES-treated PET adherend is placed on top of the uncured sample and the specimen is left to cure at room temperature for at least 12 hours. Following room temperature curing, the mold is removed and the sample is cured at 80°C for 3 hours. 90° peel specimens are also given a 10 mm pre-crack prior to testing.

Stretchable electronics LED sample fabrication- Copper strips 60 mm in length (Basic Copper) and LEDs (Cree XLAMP XHP50 GEN 3, Digi-Key Electronics) are cleaned with isopropyl alcohol, treated with oxygen plasma, submerged into a 0.1 vol% APTES in ethanol solution, and left to dry. Two strips are then secured with VHB tape at 25 mm along the length on each side of a 170 mm x 40 mm acrylic backing layer, and the sample mold is then secured on top of this assembly with electrical tape. The sample is cast into the mold and cured at 80°C for 60-90 min. After curing, the sample is removed from the mold and LM traces are spray coated onto the sample using a stencil made from laser patterned orange mask (Blazer Orange Laser Mask, Johnson Plastics Plus). The LED heat sink is dabbed with uncured sample, placed onto the center of the specimen, and cured at 40°C for 1 h. After curing, an electrically conductive network is completed by using EGaIn-copper paste to connect the LM traces to the edges of the copper strips and LED leads.

Stretchable electronics circular thin film fabrication- An acrylic ring of 155 mm outer diameter and 135 mm inner diameter is laser cut from an acrylic sheet of 3.2 mm thickness. The ring and LED (Luxeon Rebel 530NM SMD, Digi-Key Electronics) are chemically treated using the same process described above. LM composite (ϕ = 60%, d = 60 µm) is cast onto an acrylic slide coated with mold release (Ease Release 200, Reynolds Advanced Materials) and

the thickness is set using a thin film applicator (Zua 2000, Proceq). The film is cured at 80°C for 30 min. After curing, a circle of 140 mm diameter is laser patterned into the thin film. The acrylic ring is coated with uncured LM composite and placed over top of the circular thin film. This assembly is cured at 80°C for 12 h. Following this cure, the circular thin film with the chemically anchored ring is removed from the acrylic slide. LM traces are spray coated and the LED is connected to the center of the film using uncured sample. The final assembly is cured at 40°C for 1 h.

3.6.2 Characterization

Peel specimens- T-peel samples are tested under uniaxial tension and 90° peel samples are tested using a wire cable actuated test apparatus on an Instron 5944 universal testing system. T-peel and 90° peel tests are performed at an extension rate of 254 and 60 mm/min, respectively. Fracture energy is calculated from the plateau region of the load-displacement curve.

Tension tests- Mechanical properties are measured under uniaxial tension. Dogbone specimens are die-cut according to 50% dimensions of ASTM D412-C specimens. The test is performed at an extension rate of 1 mm/s using an Instron 5944 universal testing system. Tensile modulus is calculated from the stress-strain curve up to 5 % strain.

Thermal imaging- IR images are captured with a FLIR E54sc infrared camera at a frame rate of 30 frames per second with emissivity = 0.9 and reflection temperature of 20°C.

Optical microscopy- Optical micrographs are obtained using a Zeiss Axio Zoom v16 stereo microscope.

Scanning electron microscopy- SEM images are obtained on a FEI Quanta 600 FEG-SEM in back-scattered electron (BSE) mode at a spot size of 5.5 and an accelerating voltage of

30 kV. The cross-sections of samples were sputter coated with a Pt-Pd layer of ∼10 nm thickness prior to SEM analysis.

Particle analysis- Fiji software is used to perform particle analysis in which the area of a particle is calculated from a binary image and an ellipse of that area is fit on the particle. The mean particle size and standard deviation are calculated from plotting a histogram of the major diameters of the ellipses and utilizing Gaussian and lognormal fits on the data. Micrographs with ellipses fits and corresponding particle size histograms can be referenced in the Supplementary Information.

Thermal conductivity measurement- Thermal conductivity is measured using a transient hot wire (THW) measurement detailed in previous work.[50]

Graphics card performance benchmarking- The performance of a Visiontek Radeon 5450 graphics card is evaluated by measuring idle temperatures and running Unigine Heaven 4.0 as a benchmark program. The computer is a Dell Precision 5820 Tower X-series with an i9-10900X CPU and 32 GB of RAM. All tests are conducted with the side panel of the computer removed. To measure GPU temperature, the TechPowerup GPU-Z program is used, and "GPU Temp #1" is recorded. To measure the idle temperature, the computer is turned on and GPU-Z tool measures the temperature after steady-state is achieved for at least ten minutes. To record the refresh rate, MSI Afterburner with Rivatuner Statistics Server is used. During benchmark testing, the rendered resolution is 1280x720 in DirectX 11 mode, and all settings are set to low with tessellation, stereo 3D, multi-monitor, and anti-aliasing disabled. No other processes are conducted on the computer for the duration of the benchmark. After a benchmark run is conducted, the computer is left unused until the GPU temperature returns to its idle state before starting another benchmark run.

3.7 Acknowledgements

We appreciate discussions with Vince Baranauskas. We acknowledge support from the Office of Naval Research Young Investigator Program (YIP) (N000142112699), the Defense Advanced Research Projects Agency Young Faculty Award (DARPA YFA) (D18AP00041), and the Institute for Critical Technology and Applied Science (ICTAS) at Virginia Tech. This work was performed in part at the Nanoscale Characterization and Fabrication Laboratory, which is supported by the Virginia Tech National Center for Earth and Environmental Nanotechnology Infrastructure (NanoEarth), a member of the National Nanotechnology Coordinated Infrastructure (NNCI), supported by NSF (ECCS 1542100 and ECCS 2025151).

Chapter 4

Shape morphing mechanical metamaterials through reversible plasticity

Modified from a manuscript published in *Science Robotics*.

Dohgyu Hwang,[1,2†] Edward J. Barron III,[1,2†] A.B.M Tahidul Haque,[1] and Michael D. Bartlett.[1,2*] Shape morphing mechanical metamaterials through reversible plasticity. *Science Robotics*, 2022, 7(63), eabg2171.

1. Macromolecules Innovation Institute, Virginia Tech, Blacksburg, VA 24061, USA.

2. Mechanical Engineering, Soft Materials and Structures Lab, Virginia Tech, Blacksburg, VA 24061, USA.

† These authors contributed equally to this work.

∗ To whom correspondence should be addressed: mbartlett@vt.edu

4.1 Contributions

For the work titled "**Shape morphing mechanical metamaterials through reversible plasticity**" the dissertation author Edward J. Barron III contributed the following:

- Aided in the development of the morphing material for integration with multifunctional machines.
- Was an equal contributor (along with D.H.) in the development and and fulfilment of the demonstration in Figure 4.3C.
- Was the primary contributor in the design, integration, and fulfilment of the multifunctional autonomously morphing drone demonstration shown in Figure 4.4.
- Was the primary contributor in the design, integration, and fulfilment of the morphing and deployable underwater machine demonstration shown in Figure 4.5.
- Contributed to the writing and figure making in this work.

4.2 Abstract

Biological organisms such as the octopus can reconfigure their shape and properties to perform diverse tasks. However, soft machines struggle to achieve complex configurations, morph into shape to support loads, and go between multiple states reversibly. Here we introduce a multifunctional shape morphing material with reversible and rapid polymorphic reconfigurability. We couple elastomeric kirigami with an unconventional reversible plasticity mechanism in metal alloys to rapidly (< 0.1 seconds) morph flat sheets into complex, load bearing shapes, with reversibility and self-healing through phase-change. This kirigami composite overcomes trade-offs in deformability and load bearing capacity and eliminates power requirements to sustain reconfigured shapes. We demonstrate this material through integration with onboard control, motors, and power, to create a soft robotic morphing drone which autonomously transforms from a ground to air vehicle and an underwater morphing machine which can be reversibly deployed to collect cargo.

4.3 Introduction

Shape morphing materials with tunable rigidity are key components for emerging technologies ranging from stretchable electronics and soft robotics to reconfigurable structures and multimodal vehicles [303, 304, 305, 306]. Key to these systems is the ability to occupy complex configurations, maintain shape without consuming power, and to go between multiple states reversibly. However, such attributes are uncommon in a single material system. One promising approach to create morphing systems is to utilize initially flat sheets that contain designed geometric features. For example, by incorporating cuts (kirigami) or folds (origami) into materials, prescribed 3D output shapes can be obtained under deformation [307, 308, 309, 310]. This class of materials, often referred to as mechanical metamaterials, allows for a high degree of freedom and high extensibility [311, 312]. These systems are particularly appealing for shape morphing due to the energetically favorable bending modes driven by the slender structures in kirigami networks, compared with continuous membranes whose deformation is dominated by stretching modes which can cause structural collapse [313]. However, the reconfigurability and reversibility of such systems can be limited, as the structures are often bistable [314, 315], require applied loads to maintain configurations due to elastic restoring forces [316], or utilize permanent deformation to change shapes [317, 318]. Bistable metamaterials can successfully go between different stable states, but achievable shapes are often dictated pre-fabrication by prescribed designs and specific loading conditions, which can limit field reconfigurability or multifunctionality during use [319, 320]. Further, the intrinsic trade-off between load bearing capacity and high deformability in homogeneous sheets is limiting for soft matter engineering applications that require dramatic shape change and structural strength [321].

Another approach to create morphing systems is to control material properties across a sheet. This is often achieved by tuning deformations through heterogeneous material stiffness or

placing responsive materials at prescribed locations [322, 323, 324]. For example, stiffness gradients or swelling regions can allow for expansion at different locations for prescribed, reversible shapes. This can be driven through stimuli such as differential growth or swelling [325, 326], pneumatics [324, 327], heat [328], electric fields [329], and magnetic fields [330]. However, morphing with these mechanisms cannot be obtained without constantly applied stimuli or energy inputs (*e.g.*, pressure, specific solvent/temperatures, magnetic field), as the reconfigured shape is maintained by a specific condition or applied field. One way to overcome limited shape reconfigurability is to leverage variable stiffness materials, such as those driven through phase change, or shape memory materials [306, 331, 332, 333, 334, 335, 336]. However, continuous membrane geometries can limit shape fixity, and reconfiguration through melting and subsequent cooling to maintain different configurations is intrinsically slow due to thermal diffusion [337].

Here we introduce shape and rigidity morphing materials with reversible and rapid polymorphic three-dimensional reconfigurability and programmable stiffness (Fig. 4.1). The material rapidly morphs (< 0.1 s) into load bearing configurations, yet reconfigures and self-heals through a phase transition for shape and stiffness reconfigurability. To achieve this, we create a kirigami composite metamaterial sheet which synergistically combines shape morphing by nonlinear deformations of elastomeric kirigami architectures, shape-fixing by nonlinear material response through plasticity and phase change of an embedded low melting point alloy (LMPA), and reversibility with an integrated heater to trigger a phase change in the LMPA to elastically recover plastic deformation.

The elastomeric kirigami architecture undergoes extreme deformations, achieves complex shapes, and displays non-linear force-extension characteristics, which allows for minimal restoring forces at high extensibility, enabling high shape retention during shape-fixing in different configurations. The LMPA (Field's metal) displays material non-linearities for shape

morphing, which we introduce through an unconventional reversible-plasticity mechanism. Although plasticity (a non-reversible change of shape in response to applied force) is typically associated with material failure, we now utilize this mechanism to introduce advanced functionality: the rapid reconfiguration of shapes in soft materials that become instantly load bearing. The LMPA intrinsically deforms plastically at low strains, which we leverage to immediately morph the material into load bearing shapes (< 0.1 s). Mechanical deformation induces plasticity which sustains the shape without any electrical energy consumption or time limitations due to mass or thermal transport. Yet, the shape is reversible by utilizing the embedded heaters to melt the LMPA, which then allows the elastomeric kirigami to elastically reverse the plasticity and enable reconfigurability and self-healing over numerous cycles. By patterning the elastomer and embedded LMPA with kirigami patterns, complex shapes are achievable and can display combinations of negative, zero, and positive Gaussian curvature. Thus, by combining kirigami structures, LMPA, and embedded heaters, our multimaterial system displays extreme deformations and reversible-plasticity. This approach achieves rapid shape-fixing into complex configurations and maintains reversibility and load bearing capacity. This approach overcomes limitations in morphing material systems and trade-offs between extensibility and load bearing capacity in reconfigurable soft systems. These materials are integrated with onboard power, control, motors, and embedded heaters to create a functional morphing drone with multiple remotely controlled locomotion modes enabled by an autonomous morphing from a ground to air vehicle configuration. We further show a morphing underwater machine that can be reversibly deployed to collect cargo through integrated water propulsion and buoyancy control.

4.4 Results

4.4.1 Morphing composite design

The composite consists of a rigidity tuning endoskeleton made of a LMPA, an embedded heating layer, and elastomeric kirigami encapsulation (Fig. 4.1A). The LMPA is Field's metal, which is a eutectic alloy of bismuth, indium, and tin, and transitions from a high elastic modulus (> 3 GPa) solid to a flowable liquid at relatively low melting temperatures (melting point of 62°C) [331]. The sample is fabricated by first creating the endoskeleton through a vacuum-assisted replica molding process which enables arbitrary continuous geometries. This design flexibility can create common kirigami designs such as uni-axial, bi-axial, and tri-axial cut patterns (see Fig. C.1). The endoskeleton and heating layers are then embedded in elastomer, and kirigami incisions are laser cut throughout the sample to define the kirigami geometry (Fig. 4.1B). To demonstrate the rapid shape morphing capability and reversibility, a relaxed tri-axial kirigami composite in the solid state is deformed through an inflated pneumatic membrane (Fig. 4.1C). This film rapidly morphs into a doubly-curved surface with complex curvature as demonstrated by a curvature map showing the positive and negative Gaussian curvatures (Fig. 4.1D). Upon deflating the underlying membrane, the free-standing kirigami film is reconfigured into the programmed shape through plasticity. Due to the rigidity of the solid endoskeleton, the structure immediately achieves load bearing capacity and supports a disk-shaped weight (240 g). However, by electrically activating the embedded heater through Joule heating, the endoskeleton undergoes a phase transition to a liquid phase, and the elasticity of the elastomer returns the structure into a relaxed, liquid state. This phase change coupled with the elasticity of the elastomer enables reversible plasticity. The structure can be morphed in the liquid state to become highly compliant. By holding the deformed state and undergoing a phase transition back to a solid state, the kirigami

film becomes rigid to regain a load bearing configuration. This process can be repeated by activating the heater to return the film to a relaxed, solid state.

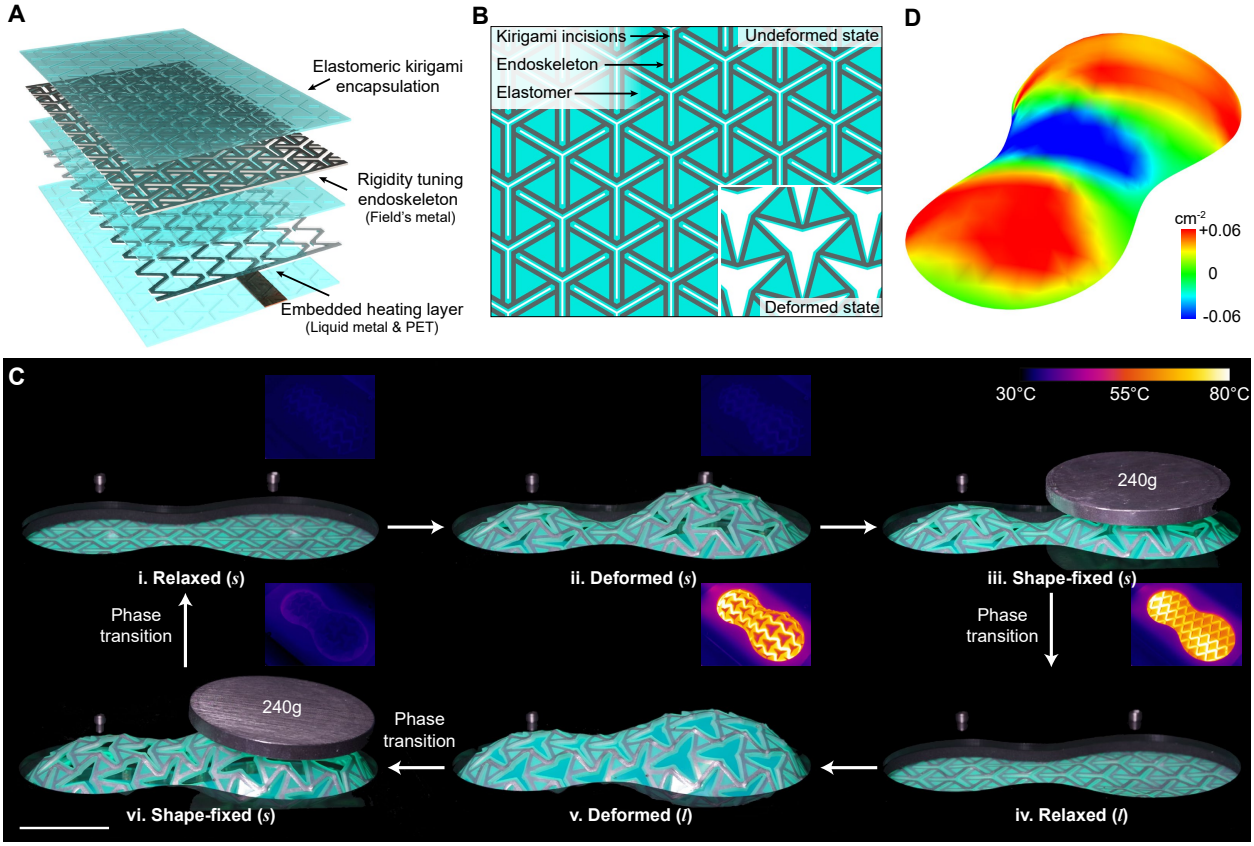


Figure 4.1: **Multimaterial kirigami composite with instantaneous complex shape-fixing and reversibility.** (**A**) Schematic showing the layers of a kirigami-inspired multi-layered composite. (**B**) A top down schematic showing the kirigami incisions, endoskeleton, and elastomer in an undeformed state with the deformed state in the inset. (**C**) Image sequence showing the composite morphing into the programmed shape of an inflating elastomeric membrane underneath and can support 240 g in the reconfigured state after the membrane is deflated. By activating embedded heaters (inset shows IR images), the morphed composite undergoes a phase change and returns to the flat, initial state and can then be actuated repeatedly. Scale bar = 50 mm. (**D**) Gaussian curvature map of the deployed kirigami composite showing the complex shape.

4.4.2 Morphing composite mechanical analysis

The kirigami composite is mechanically analyzed under uni-axial loading for different endoskeleton states and geometries of the LMPA endoskeletons (Fig. 4.2A). Fig. 4.2B shows representative load P versus applied strain ε_{appl} curves for kirigami composites in either a solid state, a liquid state, or elastomer without a LMPA endoskeleton. Each composite is cyclically loaded three times to 100 % strain and then returned to zero strain, with the unloading step performed in the liquid endoskeleton state. The solid-state composite is shown to be rigid (effective stiffness, $K_{eff} = 8480 \pm 770$ N/m) in the initial loading ($\varepsilon_{appl} \leq 10$ %), however once localized plastic deformation is observed, the load-displacement response becomes non-linear. At this point, substantial softening and a slight negative stiffness is observed where the structure extends with minimal additional strain energy. This load plateau after initial loading is critical as this allows for high degrees of shape reconfigurability as discussed below. In contrast, the liquid-state composite exhibits a soft response with a negligible effective stiffness ($K_{eff} = 65 \pm 10$ N/m), which is ~ 130 times softer than the solid state (Fig. 4.2D), and softer than the elastomeric kirigami alone.

We determine the underlying elasto-plastic morphing mechanism of the endoskeleton in the solid-state using finite element analysis (FEA). We follow the multilayered kirigami composite of Fig. 4.2A to develop the layered composite section for the FE model. The LMPA is simulated with elasto-plastic material behavior, and the elastomeric layers are modeled by a hyperelastic formulation. The Materials and Methods section for FEA describes materials and elements in more detail. The FEA accurately captures the experimental load-strain characteristics for the solid phase kirigami composite in Fig. 4.2B. Furthermore, the FEA gives insight into the plastic deformation process at a material level. In Fig. 4.2C, FEA results illustrate the plastic hinge formation at the joints of kirigami beams at different stages of global strain $\varepsilon_{appl} = 0$ %, 10 %, and 100 %. The kirigami joints remain primarily elastic until

reaching $\varepsilon_{appl} = 10$ % where most of the plastic hinges are formed. Thereafter, the plastic zone intensifies around kirigami joints, and the kirigami structure deforms without any notable resistance to the applied strain ε_{appl}. Stress concentrations are common in kirigami structures near the vicinity of the cut, which enhances the generation of plasticity in these regions [338]. This local plastic deformation contributes to the soft structural response of the solid-state kirigami between $\varepsilon_{appl} = 10 - 100$ % in Fig. 4.2B and allows for the composite to be morphed into different stable configurations.

The effective stiffness of the structure (K_{eff}) can also be tuned by controlling the kirigami geometry, where the stiffness K_{eff} can be calculated as

$$K_{eff} = \beta \frac{E w^3 t}{l^3} \tag{1}$$

where β depends on boundary conditions and system size and t, w, l are beam thickness, width, and length, respectively [312]. We investigate various compositions of LMPA beams such as length ($l_{LMPA} = 20$ mm, 30 mm), width ($w_{LMPA} = 1.1$ mm, 1.5 mm, and 1.9 mm), and thickness (t_{LMPA} ranging from 300 µm to 1,000 µm) with constant encapsulating layer geometry. In Fig. 4.2E, the upper line predicts stiffness of kirigami structures that include ~ 1 mm-thick endoskeletons with varying slenderness, and the lower line predicts that with ~ 0.3 mm-thick endoskeletons, with the shaded region indicating intermediate thickness and showing the large tunability through kirigami structure. The experimental data is well captured by the analytical solution and numerical analyses. The composite is also robust under cyclic loading (Fig. 4.2F). Here, the kirigami composite is deformed in the solid state to 100 % strain where after the first cycle the rigidity is stable for the remaining cycles (10 cycles are run). During this process, no fracture in the endoskeleton is observed. Robustness is further investigated by intentionally breaking the endoskeleton at multiple points, melting

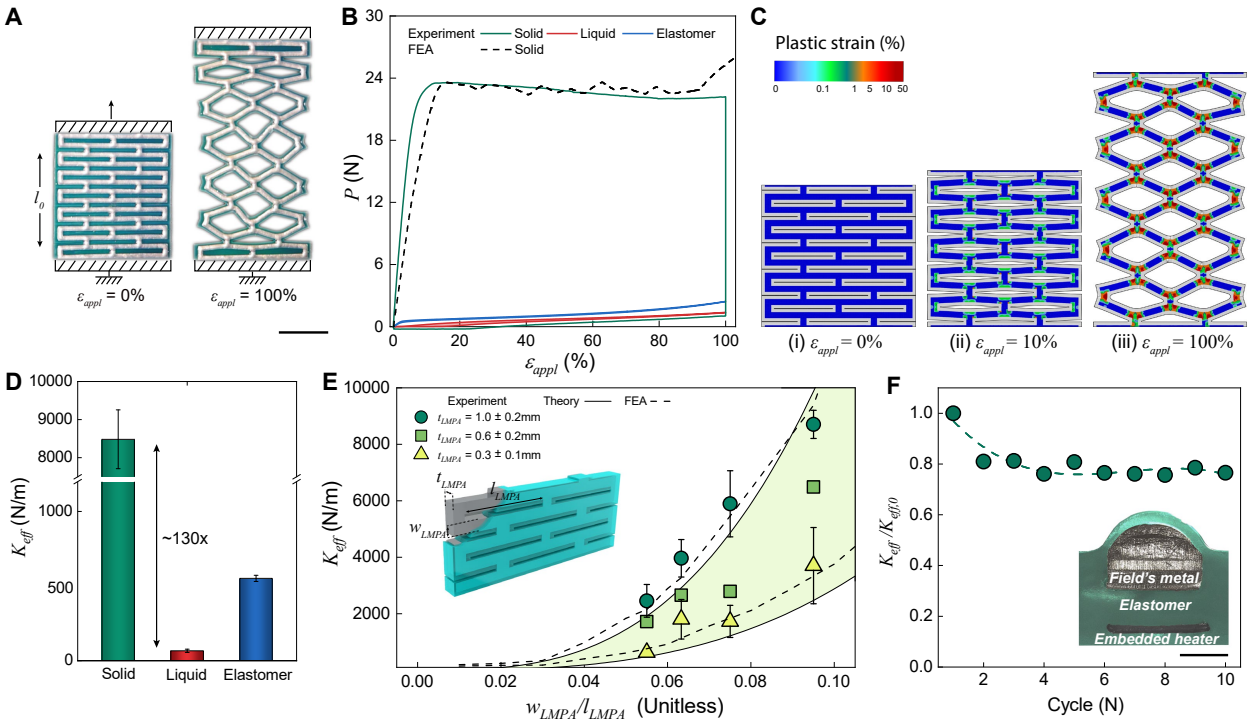


Figure 4.2: **Mechanical performance of kirigami composites with uni-axial endoskeleton structures.** (**A**) Kirigami composite at zero and 100 % strain. Scale bar = 20 mm. (**B**) Load versus applied tensile strain for different kirigami composites (l_{LMPA}= 20 mm, width w_{LMPA} = 1.9 mm, and thickness t_{LMPA} = 1,000 µm). (**C**) FEA results showing the development of plastic hinges at different applied strains. (**D**) Kirigami composite stiffness for different endoskeleton states. Error bars represent the standard deviation for $n = 10$. (**E**) Effective stiffness versus kirigami beam geometry w_{LMPA}/l_{LMPA} for kirigami composites with 12 different endoskeleton geometries. Inset: Composite schematic showing geometric parameters. Error bars represent the standard deviation for $n = 3$. (**F**) Normalized stiffness as a function of the number of cycles for a LMPA-embedded kirigami composite. Inset: a cross-section of the composite. Scale bar = 1 mm.

the composite endoskeleton, and then resolidifying at room temperature to heal the structure. The self-healing efficiency is then quantified by measuring the stiffness for 10 fracture/healing cycles. The stiffness of the healed sample is consistent with the pristine sample and shows no degradation over the 10 cycles, demonstrating excellent healing efficiency (Fig. C.2). Critical to this behavior is the over pressurization of the LMPA during fabrication (see Fig. C.3, C.4, and C.5). This enables the material to flow back in contact and resolidify into a

monolithic structure.

We quantify the shape-fixing capability of the kirigami composite through uni-axial cyclic experiments (Fig. 4.3A). Here we apply strains of $\varepsilon_{appl} = 10$ to 50 % and then unload under quasi-static conditions, until the load drops to zero (loading and unloading rate of 1 mm/s and 0.01 mm/s, respectively). The strain at zero load is the plastic strain (ε_p) and represents the amount of deformation that remains after morphing. We define the shape-fixity ratio R_f as:

$$R_f = \frac{\varepsilon_p}{\varepsilon_{appl}} \tag{2}$$

We evaluate R_f as a function of ε_{appl} for two kirigami films with endoskeletons in the solid state (the stiffest and least stiff from Fig. 4.2E), an endoskeleton loaded in the liquid state and solidified at ε_{appl}, and a kirigami elastomer control without an endoskeleton (Fig. 4.3B). When the elastomer control (endoskeleton-free material) is deformed, nearly no shape retention occurs regardless of ε_{appl} due to the elastomer elasticity which restores the structure to the undeformed state. For the smallest stiffness solid endoskeleton, we observe $10 < R_f < 30$ where the low values of R_f are attributed to the restoring force of the elastomeric layers, which dominates over the endoskeleton. In contrast, the sample with the largest stiffness shows $R_f \sim 30$ % for small ε_{appl} (2.5 %) and reaches $R_f \sim 85$ % for larger ε_{appl} (50 %). Recall from Fig. 4.2B that the development of full plasticity in the kirigami endoskeleton requires $\varepsilon_{appl} > 10$ %. Therefore, modest R_f for low ε_{appl} is attributed to a low degree of plastic deformation in the kirigami endoskeleton. High shape-fixity ratio (≈ 100 %) can be obtained by loading the sample at $T > T_m$ and holding it until the LMPA solidifies (see data points for Loaded in liquid in Fig. 4.3B). However, in this case, heating and cooling are required, and the morphing process can take minutes [337]. In contrast, when loaded in

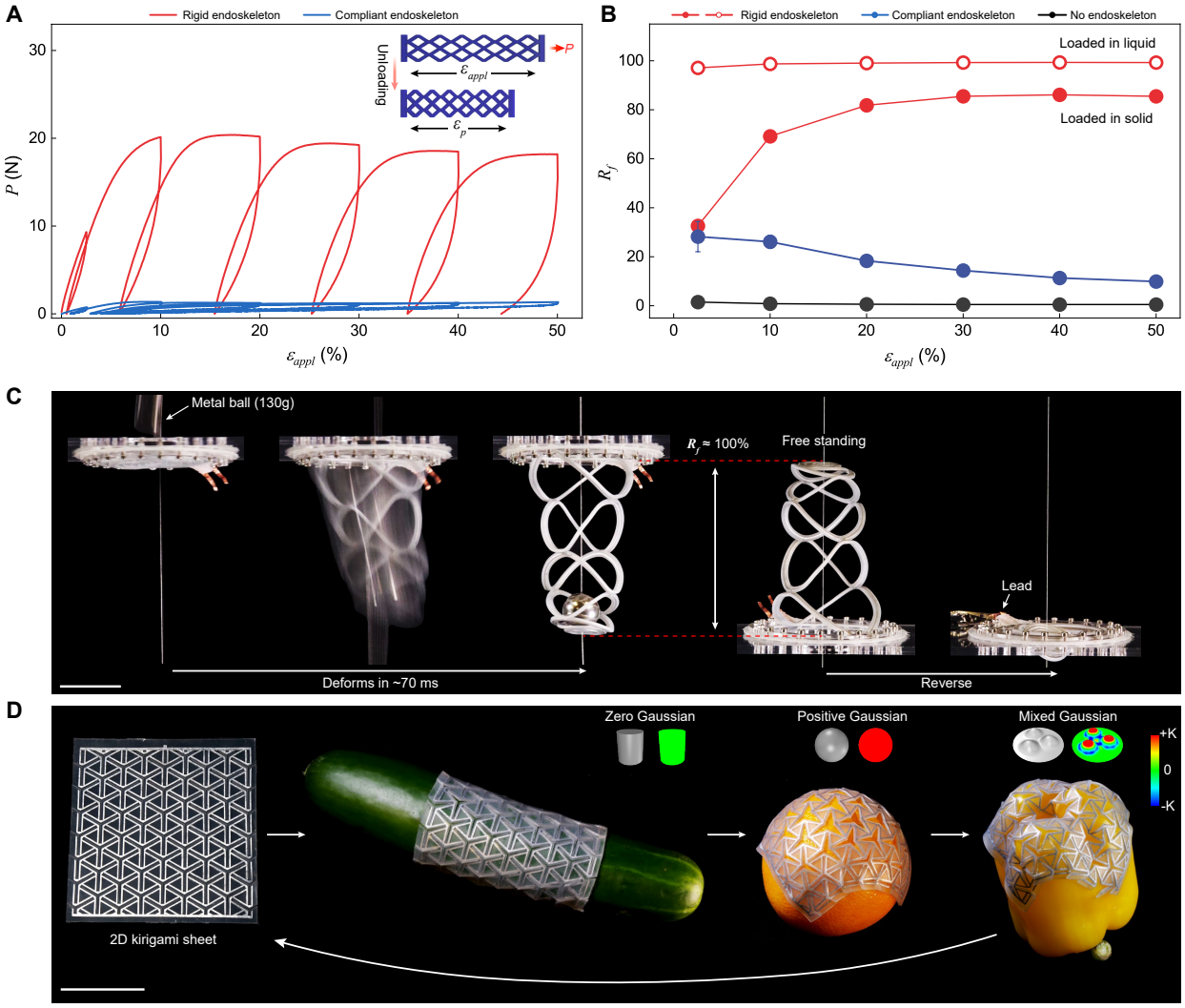


Figure 4.3: **Shape-fixing at rapid time scales with complex shapes.** (**A**) Load versus strain shape-fixing curves for two specimens with different kirigami stiffness and a sample without an endoskeleton. The inset presents a schematic of the measurement of a shape fixity ratio (R_f). (**B**) Shape fixity ratio R_f as a function of ε_{appl} from Fig. 4.3A. Error bars represent the standard deviation for $n = 3$. (**C**) A kirigami composite undergoes substantial out-of-plane deformation through the impact of a metal ball which causes rapid reconfiguration and shape-fixing into the deformed shape in $\sim$ 70 ms. The second to last image shows the structure inverted against gravity where it maintains the reconfigured shape and the last image shows reversibility of the shape through activation of the embedded heater. Scale bar = 50 mm. (**D**) Photographs of a tri-axial kirigami composite that morphs onto objects with complex curvatures reversibly. Insets shows the representative Gaussian curvature of the objects. Scale bar = 50 mm.

the solid state, the material is instantaneously load bearing and does not require electrical energy input to maintain its reconfigured shape. We also vary the unloading rate to determine the time dependence of shape fixity for $\varepsilon_{appl} = 50$ %, and find that when varying the unloading rate by over 2-orders of magnitude (from 0.005 mm/s to 1 mm/s) R_f varies by less than 7 % (See Fig. C.6 and C.7) and is always higher than 83%.

4.4.3 Shape-fixing

Kirigami architectures and material plasticity enable very rapid, large dynamic reconfigurability, and stable shape fixity without a continuous input of energy. To demonstrate the rapid shape-fixing behavior, we create a kirigami composite with a spiral cut pattern and then impact a metal ball (130 g) into the center of the composite (Fig. 4.3C). Upon impact of the metal ball, extreme deformation occurs in $\sim$ 70 ms by dissipating the kinetic energy through large plastic deformation of the kirigami composite. After removal of the metal ball and inversion of the structure, the deformed shape is maintained with an excellent shape fixity ($R_f \sim 100$ %). The embedded heater is then activated to melt the LMPA endoskeleton, which allows the elastomer to elastically reverse the plasticity and transform the structure back to its initial configuration. This demonstrates the ability to achieve substantial deformation and shape-fixing at rapid time scales through plasticity coupled with the ability to restore the initial configuration through heating and elastic recovery. To further demonstrate the shape-morphing capability of the kirigami composite, a single kirigami composite sheet with triangular cut patterns morphs into various objects that exhibit positive (an spherical orange), zero (a cylindrical cucumber), and mixed Gaussian curvature (bottom of a bell pepper) shapes (Fig. 4.3D). The same sheet is reconfigured through heating to conform to the three different objects, demonstrating reversibility. The tri-axial pattern enables planar

expansions due to negative Poisson's ratio, ensuring good replication of the different complex shapes in three dimensions. This is characteristic of the non-linear structural response of the system, where localized rotations or bending enable a minimal rise in force with increasing deformation. This low restoring force allows for shape-fixing capabilities in different, complex configurations.

4.4.4 Morphing drone

Morphing materials that can support load and reconfigure shape without continuous energy input can enable highly adaptable and mobile machines. To demonstrate these enabling characteristics, the kirigami composite is utilized as a reconfigurable body to create a multifunctional, bi-modal morphing soft robotic drone (Fig. 4.4A,B). The kirigami-drone body consists of LMPA endoskeletons embedded in an elastomer to provide shape morphing, and an embedded heating layer to enable phase transition of the endoskeleton. By integrating onboard power, control, antennas, and motors, the drone can be remotely driven in state 1 on the ground, autonomously morphed from a ground to air vehicle configuration, and then be flown in state 2 (Fig. 4.4C). The embedded heater is localized at specific morphing points to enable the autonomous transformation from an upright driving state, to the flat flying state (Fig. 4.4D). The shape transformation is initiated upon contact between copper wires on the drone and liquid metal layers deposited on a power transfer station (see Experimental), which enables transformation to occur with no external intervention. To measure the power for Joule heating, we normalize the power input by the interfacial area between the liquid metal channels and LMPA regions and the value is measured to be 9.3 mW/mm^2. By going beyond manual reconfiguration or morphing demonstrations that lack integration of functional components, our morphing material-based drone achieves locomotion in multiple distinct configurations. The load bearing capacity coupled with the ability to dramatically

transform configurations is critical to the locomotion modes, and highlights the potential of our morphing kirigami composites to enable future applications in multifunctional systems for reconfigurable robotics and electronics.

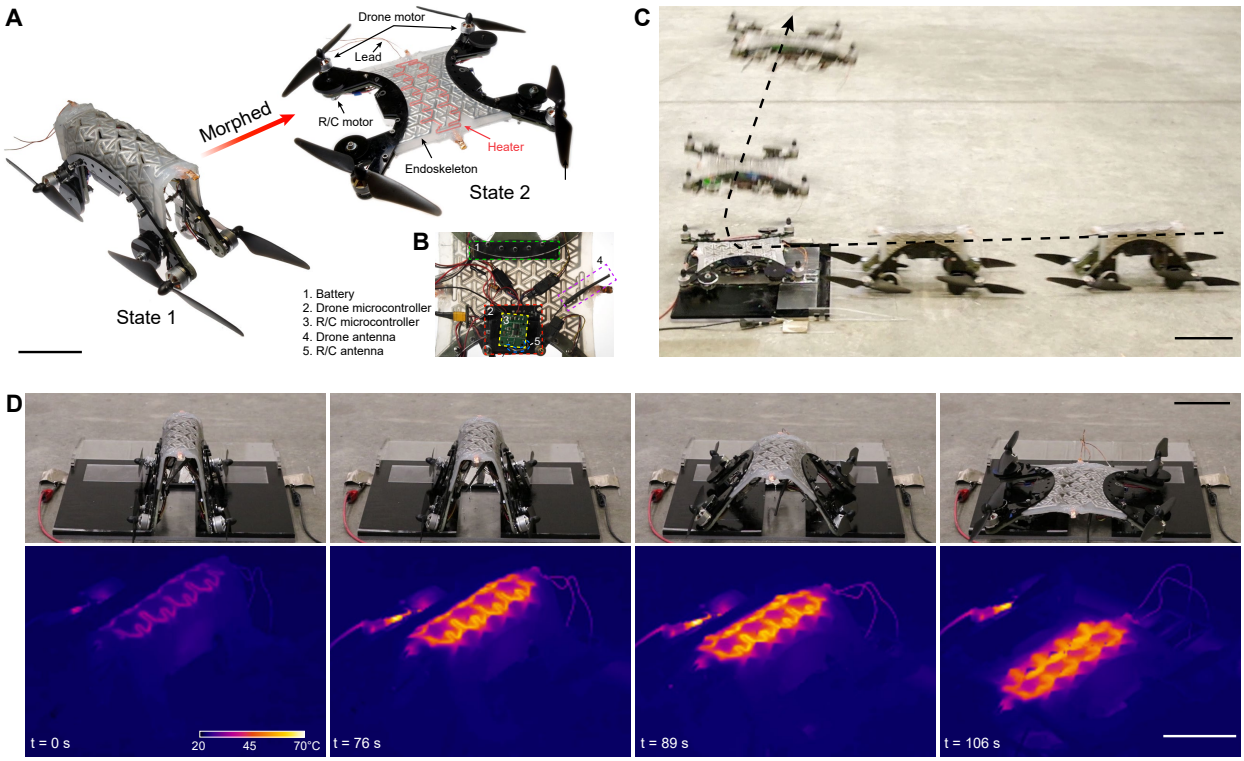


Figure 4.4: **Multifunctional autonomously morphing drone.** (**A, B**) Photographs of the two distinct functional states of the soft robotic morphing drone and its integrated rigid electronics. State 1 is a land transport machine. State 2 is a fully functional quadrotor air vehicle. Scale bar = 60 mm. (**C**) Video frame sequence showing the morphing drone driving in State 1, transforming into the flying state, then taking flight in State 2. Scale bar = 100 mm. (**D**) Image sequence showing the transformation from State 1 to State 2, top row shows images the bottom row shows IR images. Scale bar = 60 mm.

4.4.5 Morphing and deployable underwater machine

The morphing kirigami composites presented in this work rapidly and reversibly morph into complex, load bearing geometries without the need for continuous energy input. This com-

bination of properties is enabling for deployable robots, which must exist in a slim, easily transportable form factor prior to being deployed to perform tasks. Morphing mechanisms can allow underwater machines to achieve advanced functions and deploy from a packed state [339, 340]. Different approaches to create underwater morphing robots have been shown, however morphing has been predominantly utilized for locomotion [340, 341, 342, 343]. Creating a reversibly deployable machine with locomotion and sufficient mechanical stability to perform functions and practically interact with the environment remains a challenge [344, 345, 346, 347]. Motivated by this, we utilize kirigami composites to develop a deployable underwater machine capable of starting in a flat, transportable geometry (State 1) which is then sequentially morphed into a swimming state with features that interact with the environment to collect cargo (State 2), and then morph back to the retracted configuration (State 1) (Fig. 4.5A). The underwater machine consists of multiple stacked layers, including morphing kirigami composites with embedded liquid metal heaters, inflatable pneumatic membranes, and water propulsion channels. The pneumatic membranes on each side of the machine are individually controllable, which allows for independent morphing of the top and bottom layers and offers buoyancy control. Fig. 4.5B illustrates the different states of the underwater machine. The machine is deployed by actuating the pneumatic membranes which expand to morph the composite layers. The morphed kirigami composites instantaneously become fixed into the deformed shapes and maintain their desired structure after the pneumatic membranes are deflated without consuming power. Upon completion of its task, the machine can be reversed to its original, retracted shape using the embedded liquid metal heaters. This underwater morphing machine is capable of reversible deployment by morphing between the retracted state and deployed state, moving by water jet propulsion with buoyancy control, and interacting with the environment with rigid functional structures to collect cargo (Fig. 4.5C).

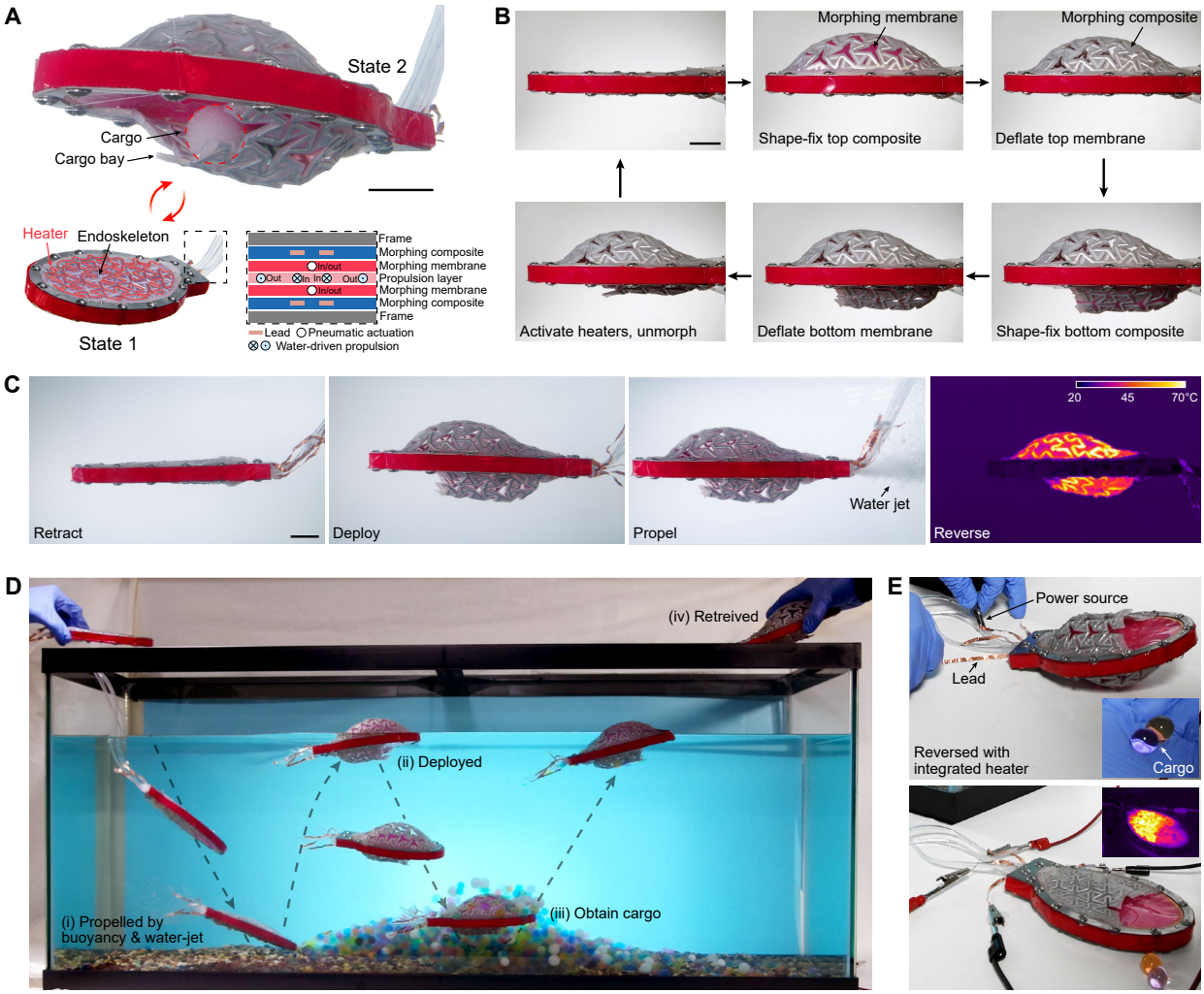


Figure 4.5: **Morphing and deployable underwater machine.** (**A**) Photographs of the distinct functional states of the underwater morphing machine with a schematic showing the machine cross section. State 1 is a compact, retracted configuration for storage. State 2 is a functional deployed machine for underwater locomotion and cargo collection. Scale bar = 20 mm. (**B**) Image sequence showing the independent morphing, shape-fixing, and reversibility of the top and bottom sides on the machine. (**C**) Images showing multifunctionality of the machine which can deploy through instantaneous shape-morphing and fixing, propel through water jetting, and reverse to a retracted state through integrated heaters. Scale bar = 20 mm. (**D**) Demonstration of the multifunctional underwater morphing robot which is deployed, locomotes through water propulsion and buoyancy control, obtains cargo, and is retrieved (tubing is cropped out for clarity beyond the first image). (**E**) After retrieval, the cargo is emptied and the machine is connected to a power source to activate reversibility to return to the original, retracted state.

The morphing layers are multifunctional, providing structural shape, buoyancy control, protection of the soft pneumatic membrane, and allowing for environmental interaction. The bottom layer is designed to morph to collect cargo, enabling the machine to collect materials during deployment, and the top layer morphs and controls buoyancy for locomotion. The functionality of the underwater machine is demonstrated in Fig. 4.5D. The underwater machine is dropped into the water in Fig. 4.5D(*i*) and is immediately morphed and deployed to simultaneously achieve flotation and its functional form factor in Fig. 4.5D(*ii*). The bottom membrane is then deflated, producing an empty cargo bay with size and shape controlled by the bottom morphing composite layer. Next, air is removed from the top membrane to reduce the buoyancy of the underwater machine, causing it to descend. The water jets propel the machine quickly towards the desired cargo at a speed greater than 210 mm s^{-1} (1.3 body lengths per second). The machine then collects spherical, hydrogel beads as cargo. The top membrane is inflated and the machine resurfaces by propelling forward in Fig. 4.5D(*iii*). The underwater machine is then retrieved in Fig. 4.5D(*iv*) and its cargo is emptied (Fig. 4.5E). Lastly, the machine is connected to an electrical power source, supplying power of 1.9 mW/mm^2 and 2.5 mW/mm^2 to the top and bottom heaters respectively, where it reverses to its original, easily transportable shape. This implementation highlights the reversible deployability of morphing kirigami sheets, providing a platform for underwater robots that can morph into different functional shapes while moving through water to perform tasks such as sampling and transporting cargo.

4.5 Discussion

We have introduced a composite material system that can morph into diverse 3D shapes through kirigami-inspired structures, become instantaneously load bearing through plastic

deformation of the LMPA endoskeleton, and recover the initial shape through an unconventional reversible plasticity mechanism driven by the thermally-induced phase transition of the LMPA. The combination of material plasticity and structural deformation provides a platform to simultaneously achieve reversible morphing and shape-fixing mechanisms at rapid time scales. Although plasticity is typically associated with permanent, irrecoverable deformation, by utilizing LMPA we can induce plasticity and then 'elastically' recover the deformation to reverse the plasticity. This recovery is achieved by activating the heaters, which causes the LMPA endoskeleton to melt, allowing the kirigami elastomer to both encapsulate the liquid and also elastically recover and guide the system back to the undeformed state. When the endoskeleton resolidifies morphing can be performed again and a different shape can be achieved, where this reconfiguration process can be repeated over multiple cycles. Therefore, plasticity or deformation while the endoskeleton is in the solid state can be thought to switch on the shape shifting and melting the endoskeleton with elastic recovery driven by the elastomeric kirigami can switch off the shape shifting. If the endoskeleton fractures, the composite can also self-heal by melting the LMPA to repair the broken endoskeleton.

As the LMPA endoskeleton is embedded in kirigami-inspired architectures, large deformations can be achieved with high degrees of shape fixity combined with the ability to conform to complex geometries defined by non-zero Gaussian curvatures. Although LMPA fibers/sheets and kirigami approaches have been independently demonstrated, by introducing an LMPA endoskeleton embedded into kirigami structures, our integrated composite enables unique possibilities for advanced morphing systems. Our composite introduces a reversible plasticity mechanism in LMPAs to leverage material non-linearities (plasticity and phase change), combined with kirigami structures that leverage non-linear mechanical response, which allows for unique force-displacement relationships for efficient morphing to large de-

formations. This allows us to synergistically combine material and structural non-linearities to achieve unique functionality such as rapid shape morphing into complex shapes that are immediately load bearing. Additionally, we show that our composite morphs reversibly and does not consume power to hold the reconfigured state. Taken together, this represents an enabling combination of properties for integrated morphing systems.

The reversible plasticity mechanism enables nearly instant load bearing capacity and high rigidity even after large deformations. One of the limitations in our current approach is the necessity to couple the shape morphing composites with external actuation mechanisms. For the case of the multifunctional morphing drone, we do not use external actuation but rely on gravity to morph the vehicle in one direction, where further reconfiguration after the initial morphing step currently requires manual intervention. In the morphing membrane in Figure 1 and in the morphing and deployable underwater machine in Figure 5, we couple the morphing composite with integrated pneumatic actuators. This allows for controlled transitions between multiple stable states through the reversible plasticity mechanism without external intervention. Therefore, the incorporation of actuation schemes is key to cyclic morphing behavior. In addition to the pneumatic actuators that we have used, other actuation schemes offer intriguing opportunities for integration into the shape morphing composites presented in this work. These can include using soft active materials like liquid crystal elastomer (LCE) actuators [348, 349], artificial muscles like shape memory alloy (SMA) wires or carbon nanotube (CNT) fibers [59, 350], or tendon driven actuation with electromechanical motors [351]. Materials like LCEs could replace the currently passive elastomer layer where the LCE could be programmed to deform to different shapes [352]. Artificial muscles and pneumatic actuation can also be directly incorporated into the elastomer layer or as a supporting layer [9]. Electromechanical motors could be deployed into supporting structures, as has been done in foldable drones [353], or could be leveraged with fiber driven actuation

throughout the film [354]. These different actuation approaches will require co-design with the shape morphing composites through geometric and material selections to ensure optimal shape morphing and performance.

Our kirigami composite sheet allows us to achieve complex curvatures across the entire sheet, without having to pre-program specific deformations. Instantaneous load-bearing is achieved through plasticity or phase-change to reconfigure into different, complex shapes. Although bistable systems can display different load bearing configurations, creating multiple stable states often requires pre-programming or tiling sub-units together, which can increase complexity and result in a restricted set of achievable morphologies. The kirigami composite sheet does not need pre-programming to achieve diverse configurations, which can be an advantage for reconfigurable or multifunctional applications. Further, the materials and processes to make the kirigami composite sheets can be adapted to other kirigami or origami metamaterial approaches and geometries, which we anticipate could open further possibilities for deployable, architectured, or mechanical logic applications.

The materials presented in this work enable complex reconfigurations, load bearing, and incorporation of functional components including controllers, motors, and batteries that can lead to dynamic functionalities in robotic systems. As the reconfigured state is maintained without continuous energy supply, mobile and deployable machines can be reconfigured in the field for multiple tasks that require load bearing capability. Although complex shapes have been achieved, optimization of kirigami layouts with embedded reversible-plasticity could potentially enhance load bearing capabilities. This could allow for additional functionalities such as field reconfigurable materials to rapidly support injuries or multi-purpose robotics for gripping, carrying, or delivering supplies.

Materials and Methods

Endoskeleton Fabrication: We fabricate kirigami endoskeletons made of low-melting point alloys (Field's metal, 32.5 wt% Bismuth, 16.5 wt% Tin, and 51 wt% Indium; Roto metals) through replica molding and vacuum-assisted injection of liquid metals. A replica mold of polydimethylsiloxane (PDMS) elastomer (Sylgard 184 with a 20:1 base-to-curing agent ratio; Dow Corning) with the kirigami pattern is cleaned with isopropyl alcohol to remove all residue and is brought into contact with clean glass. Liquid Field's metal is placed on an inlet of the replica mold and is placed under vacuum for $\sim$ 15 min (for the fabrication of LMPA skeleton in the drone demonstration, the vacuum time extends to 3 hr due to its larger scale). When the vacuum is released, the atmospheric air pressure pushes the liquid metal into the microchannels. After the channels are completely filled, the sample is removed from the oven to cool, and the metal skeleton is removed.

Embedded heating layer Fabrication: PET films ($E = 2.6 \pm 0.1$ GPa, $t = 75$, 125 µm, Grainger) are patterned using a laser machine (Epilog Laser Fusion M2, 75 w), and then copper tapes (3M Inc.) are attached to both ends of the heater. The prepared sample is spray coated across the entire sheet with liquid metal (eutectic gallium-indium (EGaIn)) and then sealed inside elastomeric sheets during the composite fabrication process.

Composite Fabrication: Kirigami composites are composed of LMPA endoskeletons, embedded heating layers, and encapsulating elastomers. For all composites presented here, stacks of single-sided adhesive layers (t of single layer = 160 µm, Blazer Orange Laser Mask, IKONICS Imaging) are used to pattern bulk materials and control the thickness of each layer. First, a thin Dragon Skin layer (Dragon Skin 00-30, Smooth-on) is formed on a substrate within a stack of mask layers ($t = 320$ µm) using a thin-film applicator (ZUA 2000, Zehntner) and then cured at 80 °C for 5 min. The liquid metal-coated side of the prepared

heating layer is placed onto the cured Dragon Skin layer. Another stack of mask layers (t = 480 µm) is attached, and a batch of Dragon Skin is formed within the frame (cured at 80 °C for 5 min). The substrate is then cooled and a LMPA endoskeleton is placed on the substrate in alignment with the heating layer underneath (cured at 80 °C for 10 min). A last stack of mask layers (t = 960 µm) are attached and the top Dragon Skin layer is formed (cured at 80 °C for 10 min). The fabricated composite is then laser machined to create kirigami films. In order to pressurize the LMPA endoskeleton channels, we place the patterned composite on a hot plate (80 °C) and inject excess liquid-state LMPA into the channels. The inlet is sealed back with glue (Sil-Poxy, Smooth-On). Embedded heaters are pressurized with liquid metal EGaIn with a syringe and needle. After filling, the injected hole is sealed with Sil-Poxy and cured for 12 hr.

Mechanical Testing: Tests are conducted under uni-axial loading on an Instron 5944 mechanical testing machine with a 50 kN load cell at a loading rate of 1mm/s and at various unloading rates. All mechanical data are analyzed with custom MATLAB code to measure stiffness and plastic strain at each step of each cycle. Copper leads are connected to a DC power supply to provide current when melting LMPA skeleton.

Morphing drone: The soft robot body is a kirigami composite composed of a single LMPA endoskeleton located between two embedded heaters connected in series and encapsulated in an elastomer. Drone components are harvested from a quadrotor drone (Drocon Bugs 3). The body is outfitted with a fiberglass and acrylic frame for integration of rigid electronics and machinery. We place 6 mm thick acrylic wheels at the four inner protrusions of the frame. The 4.5 cm diameter rear wheels are adhered to 200 rpm brushed motors (Greartisan DC 6 V) and the 4 cm diameter front wheels are attached to screws and allowed to freely rotate. The soft robot is powered by a lithium polymer battery (Tenergy 7.4 V 1,000 mAh) connected in parallel to the drone and R/C car (Jeypod 2.4 GHz Racing Car) microcontrollers. Two 17

cm long 20 AWG copper wires are connected to either end of the embedded heaters to allow for contact with the power transfer station. At the supplied power input of 9.3 mW/mm^2 the morphing drone changes shape from State 1 to State 2 in $\sim$ 1 minute and 30 seconds with an active transformation time of $\sim$ 2 seconds. Power is then turned off, and the morphing drone is cooled at room temperature for $\sim$ 7 minutes before the drone takes flight.

Underwater machine fabrication: The kirigami composite for both upper and bottom layer is composed of a LMPA endoskeleton and a liquid metal heater, which is encapsulated by the elastomeric layer. A 1/16" solid acrylic layer is adhered between the top and bottom pneumatic systems with Sil-Poxy adhesive (Smooth-On) to allow for independent control of the membranes. The top system is comprised of a 7/64" thick acrylic sheet with cut channels to allow for insertion of a 3/32" outer diameter pneumatic tube for inflation of the membrane. The 7/64" acrylic sheet is adhered with Sil-Poxy to a 700 µm thick dragon skin membrane. The bottom system is comprised of a 3/16" acrylic layer with cut channels to allow for a 3/32" outer diameter pneumatic tube as well as two 5/32" outer diameter water propulsion tubes. A 700 µm thick dragon skin membrane is adhered to the acrylic layer. 125 µm thick PET sheets are added to both the top and bottom dragon skin membranes to control the inflated shape. 1/32" stainless steel frames are placed on the outside of the kirigami composites. The layers are bolted together with #6-32 stainless steel binding barrels and screws. Water propulsion is controlled by a diaphragm pump (Hooshing 12V 60W diaphragm water pump).

Mechanical and Finite Element Analysis (FEA): The analytical calculations are performed by considering only the geometry and material properties of LMPA endoskeleton, as its modulus and thickness are substantially higher than the elastomeric encapsulation and embedded heating layer. The kirigami structure is simulated using non-linear finite element program ABAQUS (SIMULIA, Providence, RI) in the framework of three-dimensional (3D)

coordinate system. The 3D deformable shell objects are modeled using 4-node reduced integration shell element with enhanced hourglass control. The composite layout feature of ABAQUS is employed to develop the five layered rigidity tuning endoskeleton where the solid LMPA and heating layer are defined using elasto-plastic behavior of Field's metal and PET, respectively. The elastomeric kirigami encapsulation of this endoskeleton is modelled by a hyperelastic model. We use an elastic modulus of $E = 4.0$ GPa and yield stress of $E = 30.0$ MPa to capture the LMPA behavior. The stress-strain relation of the elastomer is calibrated using non-linear Yeoh hyperelastic model [355] by fitting to a strain energy function:

$$U = \sum_{j=1}^{3} \left[C_{j0}[\bar{I}_1 - 3]^j + \frac{1}{D_j}[J-1]^{2j} \right] \tag{3}$$

where, $J = det(\mathbf{F})$, $\bar{I}_1 = J^{-\frac{2}{3}tr(\mathbf{F}^T\mathbf{F})}$, and $\mathbf{F}$ represent volumetric deformation, first invariant, and deformation gradient, respectively. The material coefficients $C_{10} = 0.16$ MPa, $C_{20} = 0.002$ MPa, $C_{30} = 0$, and $D_1 = D_2 = D_3 = 0$ are used to incorporate the elastomers in the FE model. The material calibration parameters of elastomer (Dragon skin) is curve-fitted to simulate the experimental stress-strain relation (See Fig. C.8). All these materials and section definitions are incorporated into the FEA simulation to validate the experimental elasto-plastic character shown in Fig. 4.2B. Furthermore, the study on geometric configuration of LMPA beam composition is also simulated for various combinations of lengths (l_{LMPA}) and widths (w_{LMPA}).

4.6 Acknowledgements

We thank S.T. Frey for assistance with sample fabrication. The authors acknowledge support through Defense Advanced Research Projects Agency Young Faculty Award (DARPA YFA)

(D18AP00041).

Chapter 5

Mechanically cloaked multiphase magnetic elastomer soft composites for wearable wireless power transfer

Modified from a manuscript published in *ACS Applied Materials & Interfaces*.

Edward J. Barron III,[1,2†] Ray S. Peterson,[3] Nathan Lazarus,[4] and Michael D. Bartlett.[1,2*]

Mechanically cloaked multiphase magnetic elastomer soft composites for wearable wireless power transfer. *ACS Applied Materials & Interfaces*, 2020, 12(45), 50909-17.

1. Macromolecules Innovation Institute, Virginia Tech, Blacksburg, VA 24061, USA.

2. Mechanical Engineering, Soft Materials and Structures Lab, Virginia Tech, Blacksburg, VA 24061, USA.

3. Department of Materials Science and Engineering, Iowa State University, Ames, Iowa 50011, USA

4. Sensors and Electron Devices Directorate, U.S. Army Research Laboratory, Adelphi, Maryland 20783, USA

∗ To whom correspondence should be addressed: nathan.lazarus2.civ@mail.mil, mbartlett@vt.edu

5.1 Contributions

For the work titled "**Mechanically cloaked multiphase magnetic elastomer soft composites for wearable wireless power transfer**" the dissertation author Edward J. Barron III contributed the following:

- Conducted all experiments presented in this work.
- Analyzed all data shown and discussed in this work.
- Created all figures shown in this work.
- Was the primary contributor responsible for writing this work.

5.2 Abstract

Wearable electronics allow for new and immersive experiences between technology and the human body, but conventional devices are made from rigid functional components that lack the necessary compliance to safely interact with human tissue. Recently, liquid inclusions have been incorporated into elastomer composites to produce functional materials with high extensibility and ultra-soft mechanical responses. While these materials have shown high thermal and electrical conductivity, there has been an absence of research into compliant magnetic materials through the incorporation of magnetic fluids. Compliant magnetic materials are important for applications in soft matter engineering including sensing, actuation, and power transfer for soft electronics and robotics. In this work, we establish a new class of highly functional soft materials with advanced magnetic and mechanical properties by dispersing magnetic colloidal suspensions as compliant fluid inclusions into soft elastomers. Significantly, the rigid magnetic particles are encapsulated by the fluid. This mechanically cloaks the solid particles and enables a fluid-like mechanical response while imparting high magnetic permeability to the composite. This microstructure reduces the modulus of the composite below that of the initial elastomer to < 40 kPa while increasing the permeability by over 100% to greater than 2. We demonstrate the functionality of these materials through conformable magnetic backplanes which enables a completely soft, coupled inductor system capable of transferring power up to 100 % strain and wearable devices for wireless power transfer.

5.3 Introduction

Wearable electronics have the potential to reinvent the relationship between technology and the wearer by providing a seamless and useful augmentation of the human body.[16] However, conventional electronics have been designed with functional materials that display desirable thermal, electrical, and magnetic properties, but lack the necessary mechanical compliance of human tissue. The next generation of wearable devices require the development of materials that can match the low elastic modulus of human skin (< 100 kPa), while providing the necessary performance characteristics for usable devices. Several methods of achieving mechanically soft functional materials have been demonstrated including synthesis of functional soft polymers,[356] patterning of rigid functional materials,[357, 358, 359, 360, 361] and fabrication of elastomer composites with functional inclusions.

In the case of elastomer composites, rigid functional inclusions typically impart increased thermal [362, 363, 364, 365] and electrical conductivity, [366, 367] as well as enhanced magnetic permeability. [368, 369, 370, 371, 372, 373] However, as the functionality of these materials increases, a trade-off in mechanical response arises due to the increased rigid particle loading. [362, 364, 374, 375] More recently, this problem has been addressed by using functional liquid inclusions rather than rigid particles.[376] For example, liquid metal composites have realized unprecedented thermal and electrical conductivity while maintaining a soft mechanical response,[203, 374, 377, 378, 379, 380, 381, 382, 383, 384] and high permittivity liquid doping inclusions have been used in elastomers for the creation of flexible triboelectric generators.[385]

Magnetic materials provide essential functions to electronics and security such as memory storage,[386, 387] sensing,[388, 389] actuation,[390] and power transfer.[371, 372, 391, 392, 393] Wearable wireless chargers will allow for seamless charging of portable devices. As smart

devices become more necessary to carry out essential tasks, it is critical for these devices to remain charged and ready for use. Inductive wireless charging can be improved through the use of high magnetic permeability backplanes which improve power transfer efficiency and coupling coefficient by creating a pathway of least reluctance for the magnetic circuit.[372, 391, 392] Previous work has shown the addition of a magnetic elastomer backplane can improve the maximum power transfer efficiency of a wireless charging system from 81 % to 90 %. [372] Therefore, the improvement of wearable wireless charging systems requires the development of materials with high magnetic permeability, while remaining soft and deformable enough for integration with the human body.

Magnetorheological elastomers (MREs), which consist of rigid magnetic powders dispersed in an elastomer, have been extensively studied due to their ability to change their elastic modulus under an applied magnetic field.[394, 395, 396, 397, 398, 399, 400, 401] To obtain high magnetorheological (MR) performance, however, these materials contain high volume fractions of magnetic powders, which significantly increase the stiffness of the composite. Ferrogels have been similarly studied due to their low elastic modulus and high MR effect, [373] but are often too brittle for use as backplanes in wearable systems and soft robots. Magnetic liquids such as ferrofluids and magnetorheological fluids have recently been incorporated in elastomer systems.[402, 403, 404, 405, 406] Continuous-phase MR fluids were encapsulated in elastomer and studied for their potential damping properties.[402, 404, 405] These MR fluid elastomer systems were shown to have better damping properties than their MRE counterparts.[404] More dispersed millimeter-scale MR fluid inclusion elastomers were created via 3D printing,[403] but were similarly only studied for their damping and magnetorheological behavior. Recently, a dispersed MR fluid composite was created that showed over a 30 fold change in modulus and was studied for its shape-memory effect.[406] MR fluid dispersed elastomers have strong potential for use in wearable and robotic systems, but the

mechanical and functional tradeoffs of these functional suspension inclusions have not been studied.

Here we demonstrate magnetic colloidal suspensions as compliant fluid inclusions in an elastomer matrix leading to exceptional magneto-mechanical properties for use in wearable wireless power transfer systems. Three different categories of magnetic composites are examined: i) Rigid particle composites consisting of magnetic micropowders dispersed in an elastomer (Figure 5.1a), ii) Suspension composites consisting of stable magnetic colloidal suspension droplets dispersed within the elastomer (Figure 5.1b), and iii) Hybrid composites consisting of both rigid and suspension inclusions (Figure 5.1c). The magnetic colloidal suspensions present a unique mechanical behavior in which the functional suspension acts as a fluid inclusion. This shows a noticeable decrease in the tensile modulus of the composite as the functional particle volume fraction is increased. Figure 5.1d presents the mechanical compliance (inverse modulus) vs relative permeability of the tested composites. We find that the carrier fluid of the colloidal suspension mechanically cloaks the rigid particulate, creating exceptionally compliant composites while demonstrating comparable relative permeabilities to rigid particle composites found in other work.[368, 370, 371] Previous work has shown magnetic rigid particle composites with relative permeabilities approaching 3, but lacking the mechanical compliance to interact seamlessly with human skin (< 0.01 kPa^{-1}). In this work, hybrid composites are shown to approach the volume loadings and relative permeabilities of previously studied magnetic elastomers, while achieving mechanical compliance softer than that of human skin. We demonstrate these composites for applications in wearable electronics by creating soft, magnetic backplanes for stretchable inductors (Figure 5.1e), which enables wireless power transfer to be built into consumer clothing.

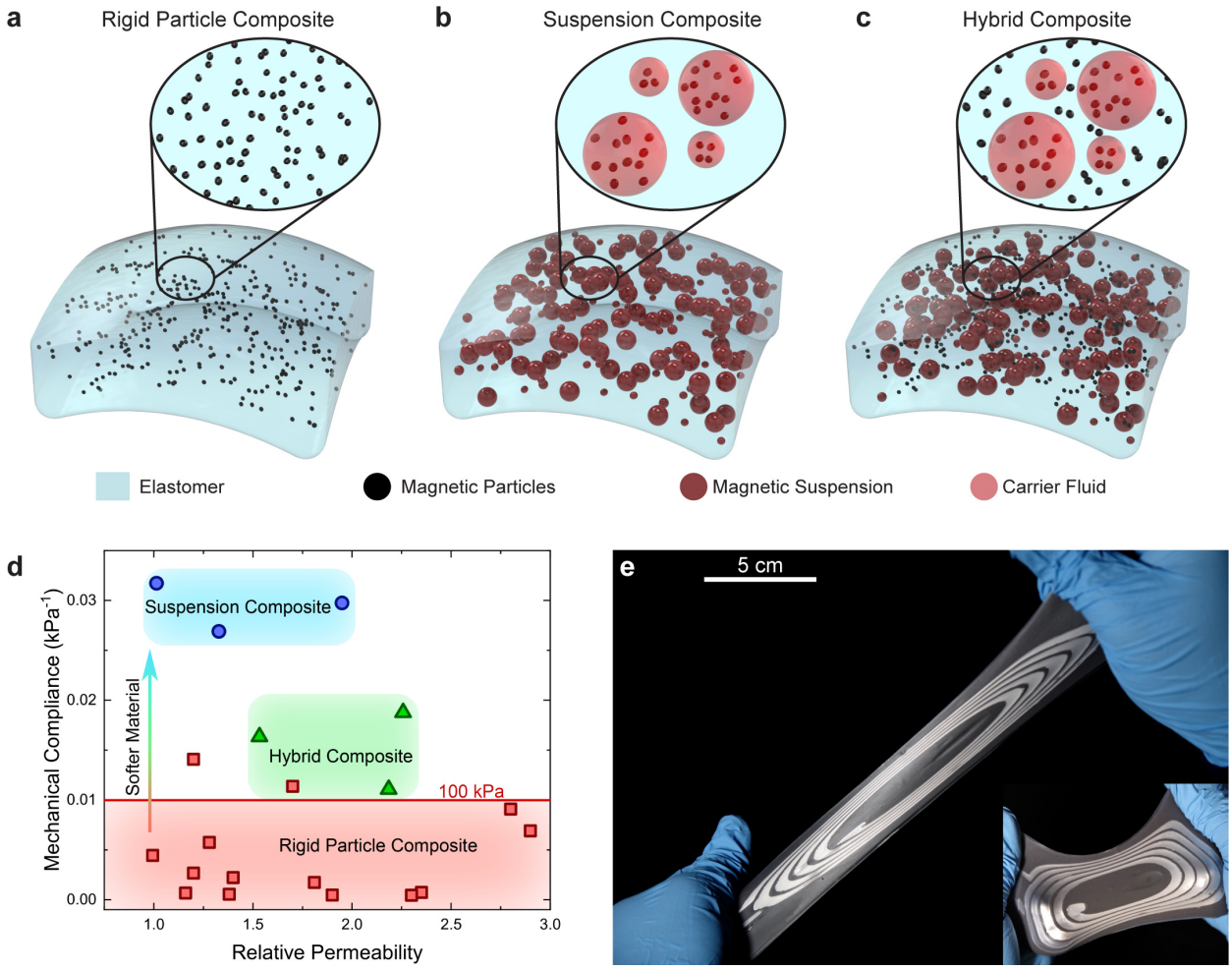


Figure 5.1: a) Schematics of rigid particle composites, b) suspension composites, and c) hybrid composites. d) Mechanical and magnetic comparison of surveyed materials [368, 370, 371] and materials used in this paper. e) Deformed stretchable planar inductor with magnetic backplane.

5.4 Results and Discussion

5.4.1 Composite Fabrication

The three classes of composites are created to compare the mechanical and functional effects of rigid and complex fluid inclusions on the composite. Each consists of an Ecoflex 00-30 silicone elastomer matrix with different microstructures of dispersed magnetic particles

including hematite, magnetite, iron powder, and Sendust. For suspension and hybrid composites, the carrier fluid is propylene glycol due to its immiscibility with silicone (Figure D.1). Hematite ($\alpha - Fe_2O_3$) is a red powder with low initial relative permeability ($\mu_i \sim 1.11$) [407] that provides a clear picture of the microstructure. Magnetite (Fe_3O_4) is a magnetic oxide with a higher permeability than hematite ($\mu_i \sim 75$). [408, 409] Iron powder ($\mu_i \sim 1{,}150$) [410] and Sendust ($\mu_i \sim 16{,}000$) [411] are the highest permeability magnetic particles used in this work. Sendust is an alloy consisting of 85 % Fe, 9 % Si, and 6 % Al.

Rigid particle composites are made through a single mixing step consisting of mixing the magnetic particles into liquid elastomer. Suspension composites are fabricated through a multi-step process consisting of 1) creating a magnetic suspension by mixing magnetic particles into a carrier fluid, and then 2) dispersing the magnetic suspension throughout the elastomer. Hybrid composites are made by 1) creating a magnetic suspension by mixing particles into a carrier fluid, then 2) mixing rigid particles into liquid elastomer, and then 3) dispersing a magnetic suspension throughout the mixture. Rigid particle composites and suspension composites are fabricated at similar volume loadings to directly compare their magnetic and mechanical properties. Due to challenges in processing rigid and suspension composites at high particle loadings, hybrid composites are created which have a higher volume fraction of functional particles due to the rigid particles being mixed into the elastomer (matrix phase) and into the dispersed fluid (magnetic suspension). This allows for greater magnetic permeability in the hybrid composites.

5.4.2 Microstructure

Optical microscopy is used to determine the microstructure of the composites. Hematite presents the clearest picture for the comparison of the composites due to its bright red color,

but similar structures are observed for all four functional materials tested for the same class of composite. We define the particle volume fraction as $\Omega_{composite} = \frac{vol(rigid\ particles)}{vol(elastomer+total\ inclusions)}$, which represents the total magnetic content in the composite. For the images in Figure 1.2, the rigid particle and suspension composites show $\Omega_{composite} = 15$ % while $\Omega_{composite} = 20$ % for the hybrid sample. The rigid particle composite micrographs show uniformly dispersed particles throughout the elastomer matrix (Figure 5.2a). The suspension composite micrograph displays droplet dispersion within the elastomer matrix. The droplets appear uniformly dispersed throughout the matrix, and are larger ($\sim$ 10 - 50 µm) than the inclusions observed in the rigid particle composite. Significantly, the rigid particles remain in the fluid during processing (Figure 5.2b), which enables a unique microstructure where the mechanical properties of the rigid particles are cloaked by the propylene glycol, enabling the solid particles to act as a fluid. The hybrid sample (Figure 5.2c) shows a combination of complex fluid and rigid inclusions.

5.4.3 Mechanical Behavior

Samples are measured under uniaxial extension to compare the tensile modulus of the three classes of composites. While the dynamic mechanical response of materials is also important to some wearable devices, the deformation frequency of human skin during normal cyclical movement (1 - 4 Hz) is relatively low,[412] and Ecoflex-based materials have been used successfully for wearable sensing devices during dynamic movement on several parts of the human body.[378, 413] The difference in mechanical response is clearly observed in Figure 5.2d, where representative stress-strain curves are shown for each of the three classes of Sendust composites. The rigid particle, suspension, and hybrid samples have volume fractions of $\Omega_{composite} = 15$ %, 15 %, and 20 % respectively. The results show the rigid particle composite to have a much more rigid mechanical response than the suspension and hybrid

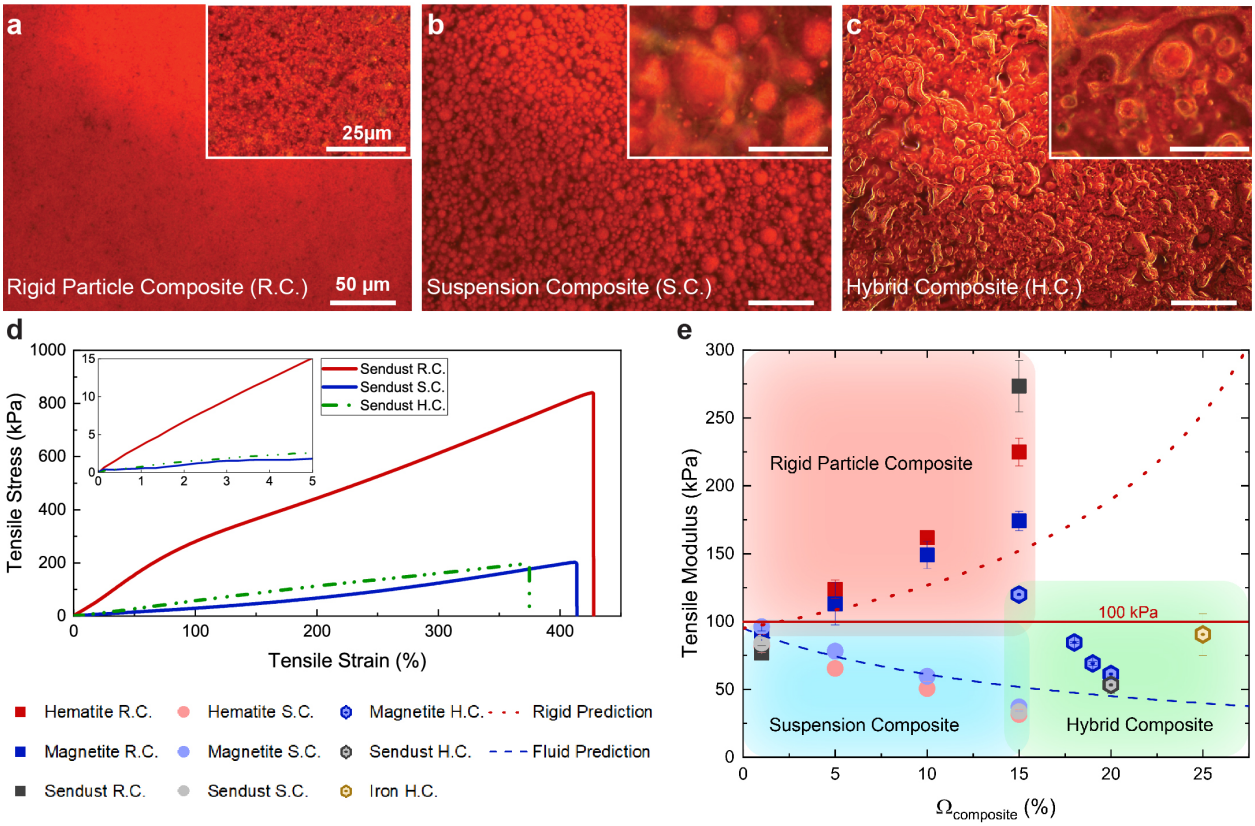


Figure 5.2: Micrographs of a) hematite rigid particle composite, b) hematite suspension composite, and c) hematite hybrid composite. Scalebars represent the same length for Figures a-c. d) Representative Sendust stress-strain data for rigid particle (R.C.), suspension (S.C.), and hybrid (H.C.) composites. e) Tensile modulus vs rigid particle volume loading comparing the three classes of magnetic elastomers produced in this work. Symbols are experiment data points while the dotted and dashed lines are predictions from Equation 1.

composites, while the hybrid composite has a particle loading 33 % greater than that of the rigid particle composite. Additionally, the strain at break remains over 350 % for all three composites.

The elastic modulus of the composites are modeled using an Eshelby analysis where E_c is the composite modulus, E is the modulus of the matrix, E_i is the modulus of the inclusions, and ϕ is the inclusion volume fraction, such that:[375]

$$E_c = E\frac{1+\frac{2E_i}{3E}}{(\frac{2}{3}-\frac{5\phi}{3})\frac{E_i}{E}+(1+\frac{5\phi}{3})} \quad (1)$$

Rigid inclusions ($E_i \sim 200$ GPa) are predicted to increase E_c significantly as particle loading increases. Liquid inclusions ($E_i \sim 0$ Pa) are predicted to decrease E_c as ϕ increases. Figure 5.2e presents the mechanical data taken for the rigid particle, suspension, and hybrid samples as a function of $\Omega_{composite}$. The red dotted line represents Eshelby's prediction (Eq. 1) for rigid inclusions ($E_i = 200$ GPa), while the blue dashed line shows Eshelby's prediction for the suspension composites, modeled with liquid inclusions ($E_i = 0$ Pa). For the case of the rigid particle composites, $\phi = \Omega_{composite}$, while for the suspension composite ϕ is equal to the functional suspension volume fraction ψ, where $\psi = \frac{vol(rigid\ particles\ +\ propylene\ glycol)}{vol(elastomer+total\ inclusions)}$. For suspension composites, $\Omega_{composite}$ is a function of the amount of magnetic particles added to the magnetic suspension ($\Omega_{suspension} = \frac{vol(rigid\ particles)}{vol(rigid\ particles\ +\ propylene\ glycol)}$) and ψ, the amount of magnetic suspension added to the composite. ψ can be related to $\Omega_{composite}$ through $\Omega_{composite} = \psi\ \Omega_{suspension}$ to compare the magnetic particle loading between rigid particle and suspension composites.

E_c for rigid particle composites increases significantly and follows with Eshelby's model at low volume fraction, but begins to deviate as $\Omega_{composite}$ approaches 15 %. Additionally, Sendust has a flake-like geometry which typically leads to a higher tensile modulus at the same volume fraction as spherical inclusions.[371] This can be observed at $\Omega_{composite}$ =15 % for the rigid composite samples. In contrast, the suspension composites demonstrate a dramatic decrease in E_c as $\Omega_{composite}$ increases. Additionally, E_c appears to be independent of particle geometry. The suspension composites follow very closely to Eshelby's model for a fluid inclusion, which suggests that the propylene glycol encapsulates the rigid particles.

We call this mechanical cloaking, as the mechanical signature of the rigid particles is hidden by the fluid inclusions. This behavior is further evidence that the rigid particles stay stable within the fluid phase of the composites.

The hybrid composites consist of a magnetic suspension phase dispersed in a rigid particle elastomer (matrix phase). The matrix phase increases the rigidity of the composite, while the magnetic suspension phase decreases the rigidity of the composite. The magnetite and Sendust samples are made by mixing magnetic particles into liquid elastomer at a matrix phase volume fraction of $\Omega_{matrix} = 10$ % ($\Omega_{matrix} = \frac{vol(rigid\ particles)}{vol(elastomer\ +\ rigid\ particles)}$). A suspension with volume fraction of $\Omega_{suspension} = 30$ % is then added to the matrix phase until the desired $\Omega_{composite}$ is reached. As the ratio of the magnetic suspension phase to the matrix phase increases, $\Omega_{composite}$ increases, and the tensile modulus E_c decreases. This behavior can be observed by the magnetite hybrid samples in Figure 5.2e. The iron samples are made with $\Omega_{matrix} = 15$ % and $\Omega_{suspension} = 35$ %. These samples show a higher tensile modulus than the Sendust and magnetite hybrids due to a higher volume fraction in the matrix phase.

5.4.4 Magnetic Permeability

For an inductor backplane, the magnetic permeability of the composite is important for limiting the stray magnetic fields, which improves power transfer. The magnetic permeability can be measured by encapsulating a rigid inductor in the selected material and measuring its inductance. Since the inductance of a solenoid is dependent on its geometry and the permeability of its core, the general equation of a solenoid inductor can be rearranged to obtain the relative permeability of the encapsulating material.

$$\mu_r = \frac{Ll}{N^2 A \mu_0} \tag{2}$$

The equation solves for the relative permeability of the core μ_r in terms of its length (l), number of turns (N), cross sectional area (A), inductance (L), and the permeability of free space μ_0. To measure the magnetic permeability of the composites we embed solenoids of the same geometry in rigid particle, suspension, and hybrid composites. Rigid particle and suspension composites have a magnetic particle volume fraction of $\Omega_{composite} = 15$ %, while hybrid samples were able to reach higher particle loadings of $\Omega_{composite} = 20$ % for magnetite and Sendust, and up to $\Omega_{composite} = 25$ % for iron. The relative permeability of the encapsulating material can then be found by taking a reference sample of known relative permeability, measuring inductance, and normalizing the magnetic elastomer samples by that reference material. Air was chosen as the reference sample which has a relative permeability of 1. The inductance was measured at a frequency sweep of 1 Hz to 1 MHz, and averaged for all phase angles approaching the expected 90 °of an inductor. The relative permeabilities of the samples are presented in Figure 5.3a. The rigid particle and suspension composites measure an almost identical permeability at the same loadings (Figure D.2).

The relative permeabilities of the tested suspension and hybrid composites are compiled in Figure 5.3a. The hematite suspension composite showed a negligible increase in relative permeability of about 1 %, while the Sendust suspension composite showed a significant increase in relative permeability to 2.02, which is over 100 % greater than the initial elastomer. The hybrid composites increased the particle loading to $\Omega_{composite} = 20$ % for the magnetite and Sendust composites, and $\Omega_{composite} = 25$ % for the iron composites. The increased particle loading yielded an increased relative permeability. The Sendust hybrid showed a relative

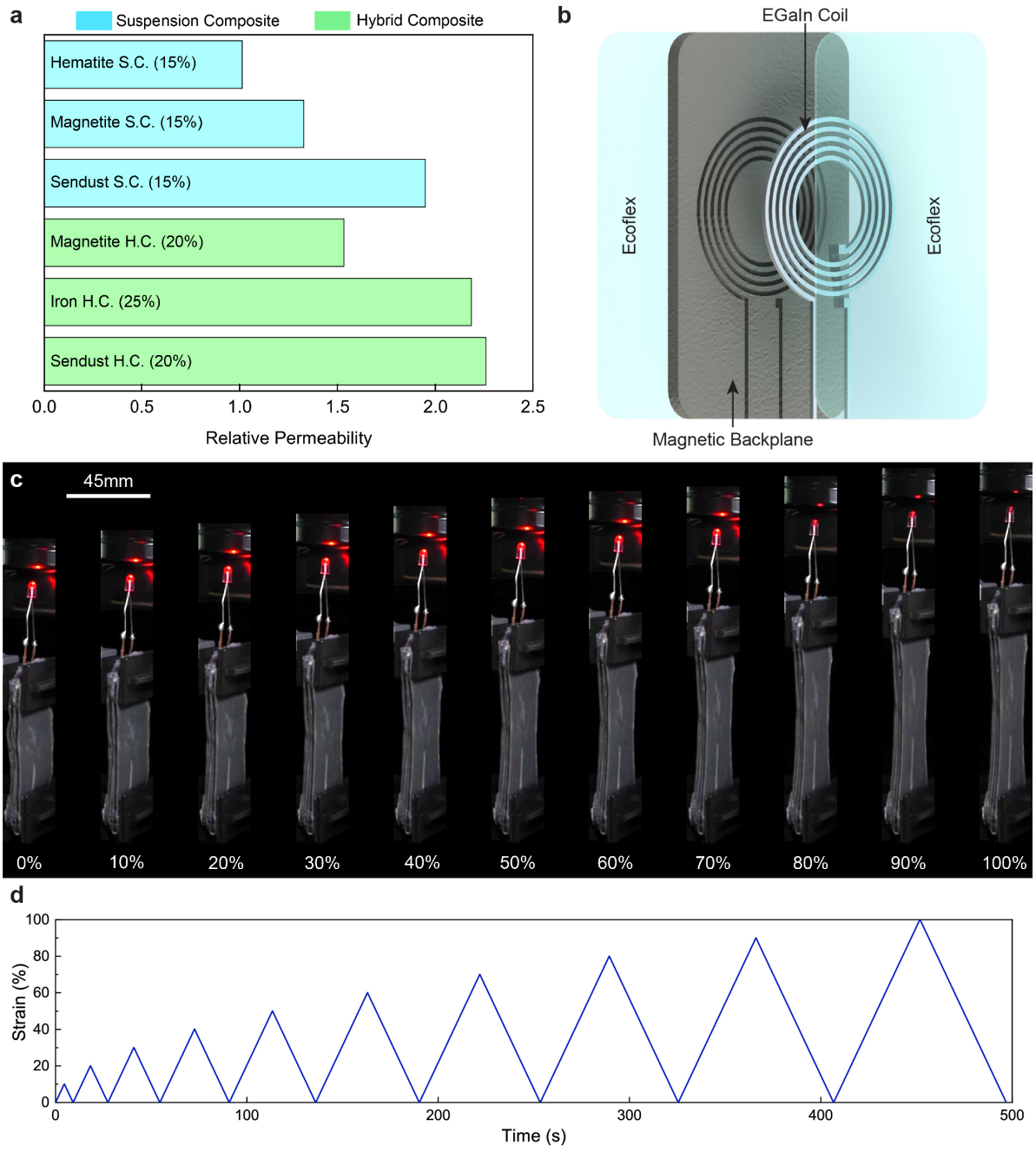


Figure 5.3: a) Measured relative permeability of suspension and hybrid composites for a given $\Omega_{composite}$. b) Soft inductor fabrication schematic. c) Cyclical power transfer testing of coupled stretchable inductors. d) Strain vs time for cyclical power transfer test. Maximum strain is increased by 10 % for each cycle.

permeability 225 % of the initial elastomer, while the $\Omega_{composite}$ = 25 % hybrid iron composite showed a similarly high relative permeability of 2.19, while being easier to process than the Sendust hybrid samples. Due to the similarity in magnetic permeability ($\sim$ 3 % difference), and easier manufacturing of the iron composites, we chose to focus on the iron hybrid composites for fabrication of stretchable inductors.

5.4.5 Wireless power transfer

Stretchable inductors (Figure 5.3b) are made to show the viability of the hybrid composites as deformable backplanes, and to introduce the concept of a completely soft power transfer component. A 3 mm thick iron-hybrid composite is molded into a backplane with 1 mm thick channels. Eutectic gallium-indium (EGaIn) is injected into the channels as a soft alternative to traditional rigid copper wiring. Ecoflex 00-30 layers of 0.5 mm thickness are added to either side as a sealing layer for the EGaIn channels. To demonstrate the performance and stretchability of the inductors, a completely soft wireless power transfer system is created. Two soft inductors are placed into close contact with each other. One inductor acts as the receiver and is soldered to an LED light, while the soft transmitter is connected to a function generator supplying a peak-to-peak potential of 20 V at a square wave frequency of 3 MHz. The inductors are then cycled step-wise from 0 % to 100 % engineering strain, increasing by 10% with each cycle (Figure 5.3c-d). Despite the large change in aspect ratio of the coil, power is transmitted to the LED to approximately 100% strain, where an inductor fails due to delamination of the encapsulating elastomer layer from the magnetic backplane.

To demonstrate the soft inductors for wearable, wireless charging a soft inductor transmitter is integrated into clothing, while a rigid reciever coil is connected to an LED (Figure 5.4a). The inductor is integrated into a glove and athletic armband (Figure 5.4b) to show the

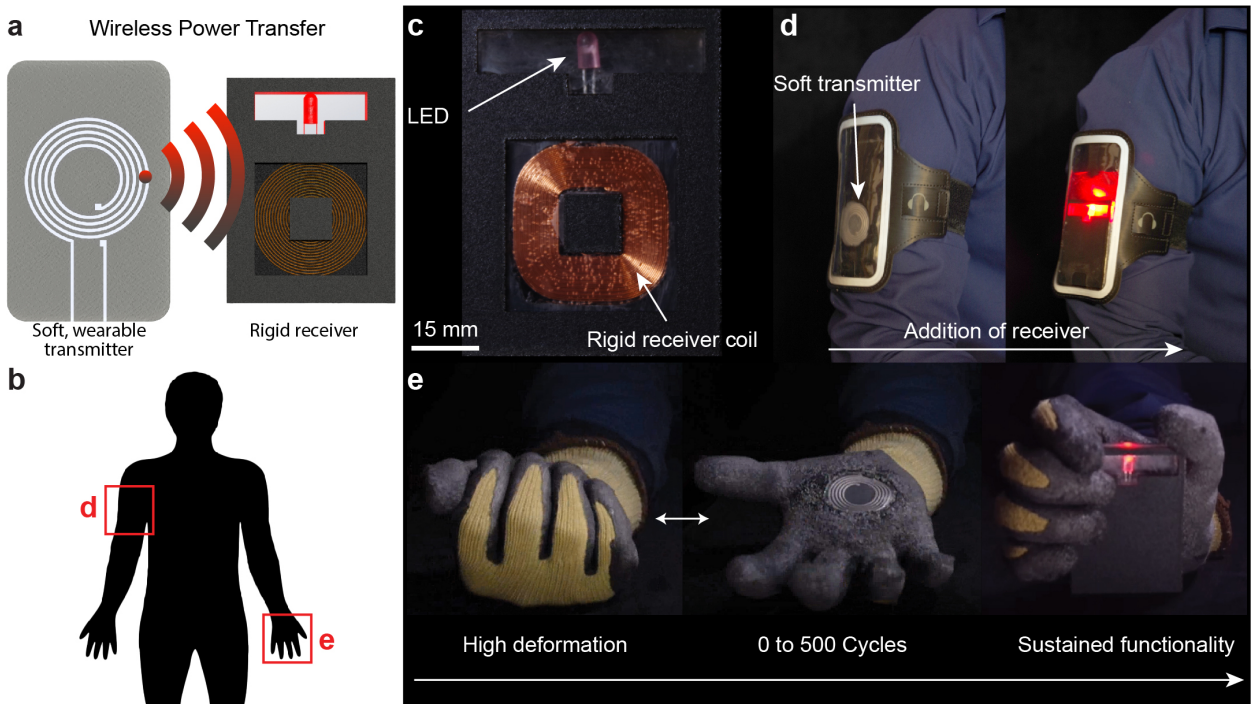


Figure 5.4: a) Wireless power transfer between soft transmitter and rigid receiver. b) Locations of wearable devices produced for this work. c) Rigid receiver coil and integrated LED. d) Wireless power demonstration of athletic armband. e) Wireless power transfer and reliability demonstration of wireless power transfer glove.

applications towards wearable wireless charging. The soft inductor is connected to a function generator, and a rigid receiver coil is connected to an LED and placed into an acrylic housing to simulate the receiver found in smart devices (Figure 5.4c). As the rigid receiver approaches the soft transmitter, power is transferred between the two coils and the LED turns on. Figure 5.4d shows the transmitter integrated into an athletic armband. The entire armband is compliant with the skin, offering superior conformability and mobility when compared to a rigid transmitter. When the receiver is added to the armband, power transfer occurs. Figure 5.4e showcases the composite's ability to conform to high deformation regions on the body such as the palm of a glove. When the receiver is picked up by the glove, the LED turns on. The reliability of the material is tested by cyclical opening, creating a closed fist, and opening again. The inductor continues to wirelessly transmit power over 500 cycles. These

demonstrations exemplify the functionality of the material for wearable applications, where the combination of soft mechanical response with magnetic properties can enable stretchable, flexible, wireless charging.

5.5 Conclusions

We introduce an approach to cloak rigid particles in fluid inclusions to enable soft composites with exceptional magnetic properties. Mechanical data shows the suspension composites to decrease in stiffness by up to 60 % as $\Omega_{composite}$ increases from 1 % to 15 %, and to be nearly 90 % softer than their rigid composite counterparts at $\Omega_{composite} = 15$ %. The magnetic permeabilities were measured to be nearly identical between the rigid composite and suspension composite samples at the same composite volume fraction. Hybrid samples enabled functional particle loadings of up to $\Omega_{composite} = 25$ %, while demonstrating an ultra compliant mechanical response softer than human skin. The hybrid samples allowed for an increase in permeability, while still achieving the necessary mechanical response for interaction with the human body, leading them to be excellent candidates for use in wearable inductor backplanes for wireless power transfer. Ultra compliant wearable chargers will allow for increased safety and efficiency by keeping essential equipment powered, while allowing for superior conformability and mobility compared with rigid power transfer devices. We further anticipate that the suspension dispersion process can be leveraged to create a variety of soft functional materials by creating complex fluid inclusions with unique mechanical, magnetic, thermal, and electrical properties.

5.6 Experimental

Rigid Particle Composites: Rigid particle composites are fabricated by mixing a 1:1 ratio by mass of two component Ecoflex 00-30 in a dual asymmetric centrifugal (DAC) mixer under vacuum. Rigid microparticles are then added to the elastomer and mixed at 800 rpm for 1 minute under vacuum. Hematite, magnetite, or iron powder are added directly to the elastomer. Sendust is first placed into a ball mill at 250 rpm for 20 hours to decrease particle size before being added to the elastomer. The resulting mixture is poured into a mold and placed into a convection oven at 40 °C for at least 15 hours.

Functional Colloidal Suspensions: Hematite, magnetite, and Sendust (20 hour milled) were mixed by hand with propylene glycol at solid volume fractions of $\Omega_{suspension} = 30$ %, while the iron powder suspension was fabricated at $\Omega_{suspension} = 35$ %.

Suspension Composites: A 1:1 ratio by mass of two component Ecoflex 00-30 is mixed in the DAC under vacuum. The colloidal suspensions are then added to the liquid elastomer until the desired $\Omega_{composite}$ is reached, and then mixed at 800 rpm for 3 minutes under vacuum. The resulting mixture is then poured into a mold and heated at 40 °C for at least 15 hours.

Hybrid Composites: The magnetic matrix is created by first mixing the two component elastomer under vacuum in the DAC. Hexane is then added to the elastomer in a 1:4 ratio by weight and mixed in the DAC under atmospheric pressure. The microparticles are then added at a volume fraction of $\Omega_{matrix} = 10$ % for hematite, magnetite, and Sendust. Iron samples were made with a volume fraction of $\Omega_{matrix} = 15$ % to test the effect of increased loadings. The rigid particles are mixed into the elastomer at 800 rpm for 1 minute. The resulting magnetic matrix is hand mixed with the colloidal suspension to the desired $\Omega_{composite}$. The resulting mixture is poured into a mold, placed into a desiccator, and vacuum pumped for

5 minutes to remove hexanes and air. The sample is then removed from the desiccator and cured at 40 °C for at least 15 hours.

Mechanical Testing Samples

Rigid particle composites are measured from $\Omega_{composite}$ = 1 - 15 % for hematite, magnetite, and Sendust. Suspension composites are similarly measured at $\Omega_{composite}$ = 1 - 15 % at constant $\Omega_{suspension}$ = 30 % for hematite, magnetite, and Sendust. Magnetite hybrid composites were measured from $\Omega_{composite}$ = 15 - 20 % at constant $\Omega_{suspension}$ = 30 % and Ω_{matrix} = 10 %. Sendust hybrid samples are measured at $\Omega_{composite}$ = 20 %, $\Omega_{suspension}$ = 30 %, and Ω_{matrix} = 10 %. The iron powder hybrids were the highest particle loading samples measured. Iron samples were measured at $\Omega_{composite}$ = 25 %, $\Omega_{suspension}$ = 35 % Ω_{matrix} = 15 %.

Soft Inductor Fabrication

An $\Omega_{composite}$ = 25 % iron hybrid composite is processed and poured into an inductor mold. The composite is cured at 40 °C for at least 15 hours. Ecoflex 00-30 is mixed in the DAC under vacuum, and poured onto a lubricated glass plate, where a thin film applicator is used to make a 0.5 mm thick layer. The elastomer is then partially cured for approximately 30 minutes. The font side of the molded inductor is then placed onto the partially cured elastomer and heated at 40 °C for at least one hour. Another 0.5 mm thick elastomer is then made, and partially cured. The back side of the inductor is then placed onto the elastomer and heated at 40 °C for at least 15 hours. After, curing EGaIn is injected into the channel using a syringe, 18 AWG copper wire is inserted into the channel ports, and the channels are then sealed with Silpoxy silicone adhesive. The sample is then allowed to cure at room temperature for at least 5 hours before use.

Rigid Inductor Housing A commercial receiver coil (STMicroelectronics STEVAL-ISB042V1) is soldered directly to the two contacts of an LED. The receiver and LED are then placed

into a laser-cut acrylic housing.

5.7 Acknowledgements

Research was sponsored by the Army Research Laboratory and was accomplished under Cooperative Agreement Number W911NF-20-2-0039. The views and conclusions contained in this document are those of the authors and should not be interpreted as representing the official policies, either expressed or implied, of the Army Research Laboratory or the U.S. Government. The U.S. Government is authorized to reproduce and distribute reprints for Government purposes notwithstanding any copyright notation herein.

Chapter 6

A unified understanding of magnetorheological elastomers for rapid and extreme stiffness tuning

Modified from a manuscript published in *RSC Applied Polymers*.

Edward J. Barron III,[1,2] Ella T. WIlliams,[2] Ravi Tutika,[1,2] Nathan Lazarus,[3] and Michael D. Bartlett.[1,2*] A unified understanding of magnetorheological elastomers for rapid and extreme stiffness tuning. *RSC Applied Polymers*, 2023.

1. Macromolecules Innovation Institute, Virginia Tech, Blacksburg, VA 24061, USA.

2. Mechanical Engineering, Soft Materials and Structures Lab, Virginia Tech, Blacksburg, VA 24061, USA.

3. Electrical and Computer Engineering Department, University of Delaware, Newark DE 19716, USA.

∗ To whom correspondence should be addressed: mbartlett@vt.edu

6.1 Contributions

For the work titled "**A unified understanding of magnetorheological elastomers for rapid and extreme stiffness tuning**" the dissertation author Edward J. Barron III contributed the following:

- Conducted the majority of all experiments presented in this work.
- Analyzed all data shown and discussed in this work.
- Created all figures shown in this work.
- Was the primary contributor responsible for writing this work.

6.2 Abstract

Magnetorheological elastomers (MREs), which adapt their mechanical properties in response to a magnetic field, can enable changes in stiffness and shape for applications ranging from vibration isolators to shape morphing robots and soft adaptive grippers. Here, a unified design approach is introduced to create MRE materials for extreme stiffness tuning, up to 70x, with rapid ($\sim$ 20 ms) and reversible shape change. This guides the creation of a hybrid MRE composite architecture that incorporates a combination of magnetic particles and magnetic fluids into elastomers. The role of both solid and fluid inclusions on magnetorheological response is systematically investigated and a predictive model is developed that captures the stiffness tuning response of MREs across diverse material microstructures and compositions. This general understanding enables MRE materials with programmable response and greatly enhanced stiffness tuning and rapid response times compared to many MRE, granular jamming, and phase change approaches. This insight is utilized to optimize composites for a soft adaptive gripper which grasps and releases objects of diverse geometries.

6.3 Introduction

Adaptive materials which change their stiffness and shape in response to engineering stimuli have emerged as important components for emerging applications such as reconfigurable and adaptive robots and machines.[60, 103, 201, 414, 415, 416, 417, 418, 419, 420] One essential feature of these materials is the ability to rapidly undergo extreme changes in stiffness to enable multifunctional components. Stiffness tuning can be accomplished at the material level by utilizing mechanisms such as phase change,[54, 122, 421] granular jamming,[422, 423, 424] or magnetic material response.[425, 426] The stiffness tuning capability of a material is typically an experimentally measured quantity for several performance parameters including the magnitude of stiffness, the stiffness tuning ratio, and the response time.[74] For example, materials utilizing low melting point alloys and polymers have demonstrated large changes in stiffness by taking advantage of their solid-liquid phase transition in response to heat.[54, 60, 127, 421] Granular media rapidly responds to negative pressure with a transition between a fluid-like granular state, where particles freely move past each other, to a jammed state, where the jammed particles form a solid-like mechanical response.[422, 423, 424, 427] Magnetically active materials such as magnetorheological elastomers (MREs) have some of the fastest response times among stiffness tuning materials (< 0.01 s),[167, 168] however, the stiffness change of traditional MRE systems ($\sim$ 10x) is typically lower than that of other stiffness tuning materials.[167, 428] Improvement of the stiffness tuning effect of MREs offers the possibility to create adaptive materials with both rapid response and extreme stiffness tuning that enable the next generation of adaptive machines.

Magnetic elastomer composites have traditionally been created by incorporating magnetic particles into soft elastomers such as silicones or polyurethanes,[429] to provide a combination of soft mechanical response and magnetic functionality for applications including stretchable and adaptive electronics and sensing,[42, 56, 174, 194, 430, 431] automotive

components,[166, 432, 433] and soft robotic grippers.[40, 195, 198, 434, 435] A key feature that has lead to substantial research of MREs is their magnetorheological effect, which leads to magnetic field-driven tunable stiffness,[425, 426] variable energy dissipation and damping,[436, 437] and shape-memory effects.[57] To improve the stiffness tuning effect (often called the MR effect or MR ratio) of these materials, MREs have been created with varied parameters such as elastomer matrix material,[170, 171, 173, 176, 438, 439, 440, 441] magnetic particle size,[171, 172, 173, 174] shape,[155, 175, 442] and volume fraction,[158, 176, 177, 178] and recently through the introduction of magnetic fluids as functional content.[56, 57, 58] Magnetorheological fluids, which are magnetic fluids that rapidly change viscosity and yield stress when subjected to a magnetic field,[148, 149] have recently been used as inclusions for MREs. These fluid inclusions are incorporated as millimeter-scale droplets into elastomers through 3D printing or by micro-dispersing magnetorheological fluid droplets through mixing, and provide unique opportunities to achieve large stiffness tuning with highly deformable and adaptive properties.[56, 57, 58, 185] However, how stiffness tuning and response in these diverse MREs depends on material composition and microstructure is not well understood, which limits performance and programming of desired properties.

Here we determine a predictive model for the understanding and enhancement of MRE properties to optimize magnetic elastomers with rapid material response and extreme stiffness tuning. The model is validated through MREs with diverse material architectures, which includes traditional rigid particle composites (RCs), state-of-the-art magnetorheological fluid composites (FCs), and a new form of hybrid composite (HC) MRE which contains both rigid particles and magnetorheological fluids as discrete domains (Figure 6.1a-c). We systematically investigate the effects of material structure and zero-field mechanical response on the MR effect of MREs, and find that our model unifies the stiffness tuning effect for each of the three investigated microstructures under a single predictive equation (Figure 6.1d). This

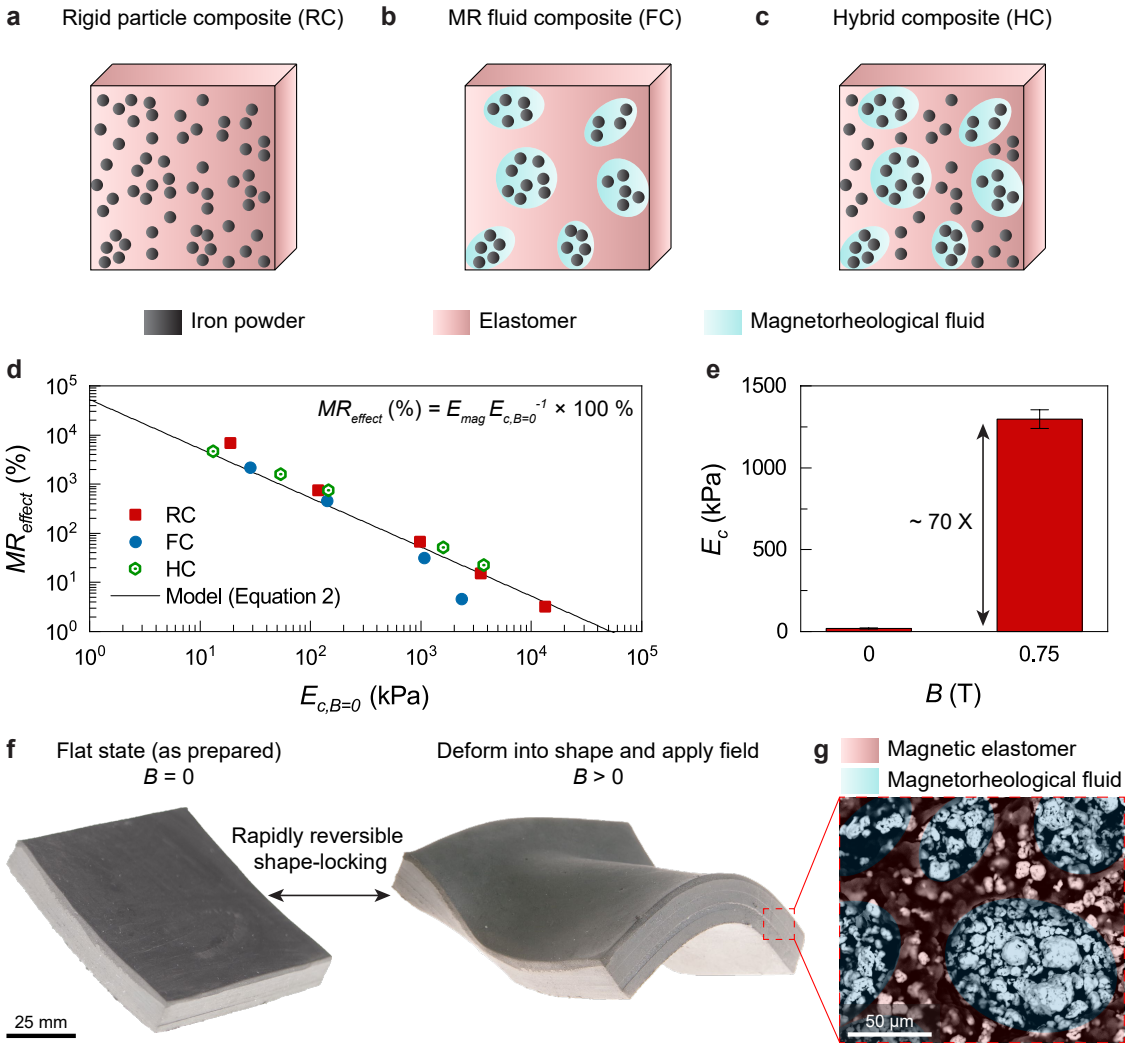


Figure 6.1: **Material structure and properties. a)** Schematics of rigid particle composite (RC), **b)** magnetorheological fluid composite (FC), and **c)** hybid composite (HC) material architectures. **d)** Effect of zero-field modulus on the relative MR effect of the materials tested in this work (E_{mag} = 530 kPa for Equation 2). **e)** Change in stiffness of an RC MRE with no field applied and with a magnetic flux density of 0.75 T. f) Image of a hybrid composite magnetorheological elastomer utilizing magnetorheological stiffness tuning to realize a shape memory effect. **g)** SEM image of hybrid composite MRE. The image is artificially colored red for the magnetic elastomer phase and blue for the MR fluid phase. An unaltered image can be found in Figure E.2.

quantitative understanding of the relationship between zero-field modulus and MR effect allows for the optimization of MRE performance, which we show through the creation of MRE materials with unprecedented changes in stiffness (70x) (Figure 6.1e) and rapid magnetic

response times of $\sim$ 20 ms (Figure E.1). The magnetorheological response of these materials gives rise to a rapidly reversible shape-locking and stiffness tuning effect (Figure 6.1f), which we utilize through our multi-phase HC MRE (Figure 6.1g) to create adaptive grippers for controlled manipulation of diverse objects.

6.3.1 Results and Discussion

6.3.2 Predicting MRE stiffness tuning

To predict the stiffness tuning of magnetically active composite materials, we consider a material effect from the composite zero-field modulus ($E_{c,B=0}$) and a magnetic contribution (E_{mag}). When subjected to a magnetic field, we assume that the material and magnetic forces are additive (i.e. a parallel arrangement of springs) which yields a composite modulus, E_c, such that $E_c = E_{c,B=0} + E_{mag}$. We then normalize this equation by $E_{c,B=0}$ to understand how the tunability of the magnetic composite depends upon both the material contribution and the effective magnetic contribution:

$$\frac{E_c}{E_{c,B=0}} = E_{mag}E_{c,B=0}^{-1} + 1 \tag{1}$$

Equation 1 gives an analytical expression for the MR enhancement factor ($\frac{E_c}{E_{c,B=0}}$), which is the ratio between the composite modulus under a magnetic field (i.e. activated) and the zero-field modulus of the composite (i.e. unactivated), where large values indicate high stiffness tunability. When the MR enhancement factor approaches a value of 1, the composite modulus does not increase when subjected to a magnetic field, which occurs as $E_{mag} \ll E_{c,B=0}$. This provides a lower, physical limit to rigidity tuning when magnetic interactions are low or when the initial composite modulus is high. Equation 1 provides a clear design paradigm

where maximum rigidity tuning is achieved when magnetic interactions are increased or when initial composite modulus is lowered. From a materials design perspective, this requires an approach to achieve significant magnetic material loading to increase the magnetic effect, while still maintaining a soft composite response. Through this general guidance, we will show how composite microstructure and composition can be used to achieve high degrees of stiffness tuning and programmable composite modulus.

We can also rearrange this relationship to predict a parameter that is commonly used to quantify stiffness tuning for MREs: the MR effect (MR_{effect}), or the relative change in modulus of the sample. By utilizing the relationship between parallel springs and solving for MR_{effect}, the MR effect can be modeled as a function of $E_{c,B=0}$ and E_{mag}:

$$MR_{effect} = E_{mag}E_{c,B=0}^{-1} \times 100\% \tag{2}$$

These simple yet robust relationships provide an accurate fit to the data acquired in this work across RC, FC, and HC composite architectures over several orders of magnitude in zero-field modulus of the composites, where E_{mag} is used as a fitting parameter (Figure 1.1d). We consider $E_{c,B=0}$ a primary factor in determining the magnetorheological response, as previous work has shown that stiffness tuning becomes limited as the zero-field modulus of the composite increases.[443] This is consistent with our results and prediction, where $MR_{effect} \propto E_{c,B=0}^{-1}$, demonstrating that as $E_{c,B=0}$ increases MR_{effect} decreases.

We note that Equation 1 and Equation 2 are not simply the equations for the MR effect, which is typically an experimentally measured quantity relating the modulus of the material under a magnetic field (E_c) relative to the same material without a magnetic field ($E_{c,B=0}$), i.e. ($\frac{E_c - E_{c,B=0}}{E_{c,B=0}} \times 100\%$). Equation 1 and Equation 2 instead give insight into the stiffness tuning contributions from the inherent stiffness of the composite material ($E_{c,B=0}$) and the

effective stiffness imparted to the material through an applied magnetic field (E_{mag}).

6.3.3 MRE composition

To determine the effect of microstructure on the magnetorheological response, as guided by Equations 1 and 2, we fabricate MREs of three different material architectures and mechanically quantify their stiffness tuning properties. RC MREs are fabricated with a volume fraction of 25% iron powder within the elastomer matrix. This volume fraction was chosen as it allowed for a low enough viscosity to be easily processed into testing geometries, while also imparting a significant magnetic response. FC MREs incorporate an iron based MRF that contains a volume fraction of 35% iron powder in a propylene glycol carrier fluid that is immiscible with the silicone matrix and processed to be contained as discrete microdroplets within the elastomer. The volume fraction of MRF in the FC MREs is 50%, leading to a total iron powder volume fraction of 17.5%. Above an MRF volume fraction of 50 % large-scale phase separation occurred and evenly dispersing the MRF as microdroplets was a challenge. This volume fraction of MRF is higher than that reported in previous work for FC MREs which showed MRF volume fractions of 30 - 40 %.[57, 185] HC MREs are fabricated with a volume fraction of 50% MRF, as well as 15% iron powder located in the elastomer matrix for a total iron particle volume fraction of 25%, which is equivalent to the volume fraction of magnetic content in the RC MREs. Scanning electron microscopy of the RC, FC, and HC material architectures can be found in Figures E.3 and E.4. In addition to investigating microstructure, the elastic modulus of the silicone matrix (E_m) is varied to study the effect of zero-field modulus on the stiffness tuning capabilities for each of the MRE material architectures. E_m is controlled by changing the crosslinking density of the silicone matrix, or by creating blends of two silicone elastomers with different matrix moduli (details in the experimental section).

6.3.4 MRE characterization

The MR effect of the magnetic elastomer composites is measured through a custom magnetorheological compression fixture (Figure 6.2a). The MRE testing fixture consists of a copper electromagnetic coil integrated with a 1020 steel bottom compression plate and an outer steel housing (top compression plate). Compression tests are run on each material using the electromagnet with average magnetic field strengths of H = 0-280 kA m^{-1}. Finite element analysis (FEA) is used to determine the average magnetic flux density through the samples (Figure 6.2b), which is determined to be up to 0.75 T for the RC and HC MREs and up to 0.58 T for the FC MREs (Figure E.5). The difference in flux density arises from the difference in magnetic content between the material architectures.

Representative compression curves for RC, FC and HC MREs with constant E_m = 200 kPa are shown in Figure 6.2c-e respectively, with the solid lines representing the zero-field mechanical response and the dashed lines indicating the mechanical response with an applied field of 280 kA m^{-1}. For the same matrix modulus, RC MREs demonstrate a more rigid zero-field mechanical response than the FC and HC MREs. This is attributed to the incorporation of MRF in both the FC and HC MREs, which mechanically cloaks the rigid character of the solid particle inclusions and create a softer composite mechanical response. The RC MRE also shows shows a substantially smaller change in mechanical properties under the influence of a 280 kA m^{-1} field. From our understanding introduced in Figure 6.1d we attribute this to the larger zero-field modulus of the RC MREs. Thus, to program the magnitude of the magnetorheological stiffness effect, it becomes necessary to control the zero-field modulus of the composite ($E_{c,B=0}$).

Control over $E_{c,B=0}$ is demonstrated through two material design strategies: the microstructure of the MREs can be changed to either increase or decrease the modulus of the composite

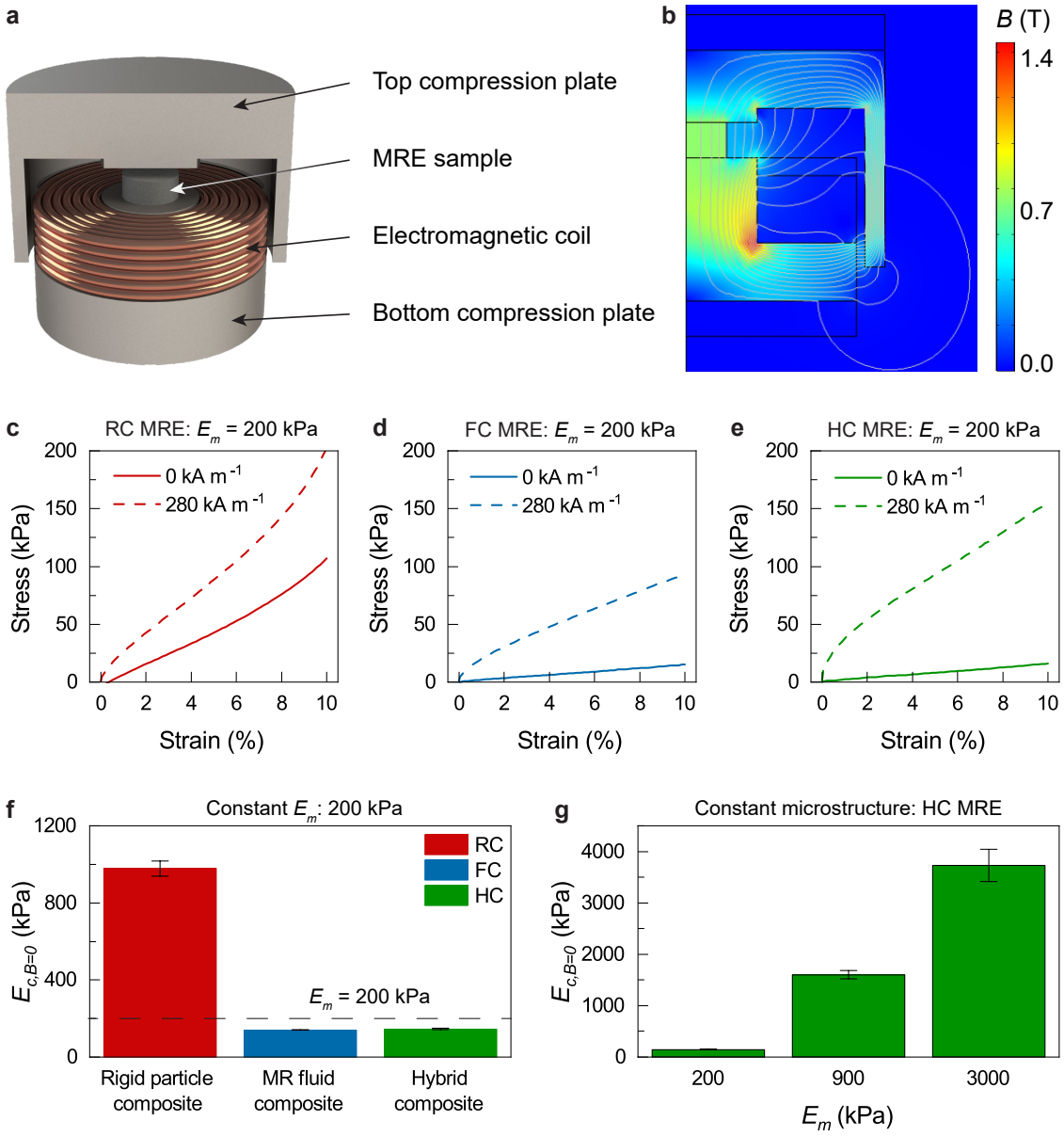


Figure 6.2: **Magnetorheological elastomer characterization. a)** Schematic of the magnetic compression fixture used to determine magnetorheological properties in this work. **b)** FEA analysis for RC and HC MREs to determine the magnetic flux density and uniformity throughout the compression specimen. **c)** Compressive stress-strain curves of Ecoflex RC, **d)** FC, and **e)** HC MRE with 0 and 280 kA m^{-1} applied fields. **f)** Tunability of zero-field modulus with respect to material architecture for constant elastomer matrix modulus. **g)** Tunability of zero-field modulus with respect to matrix modulus with constant material architecture.

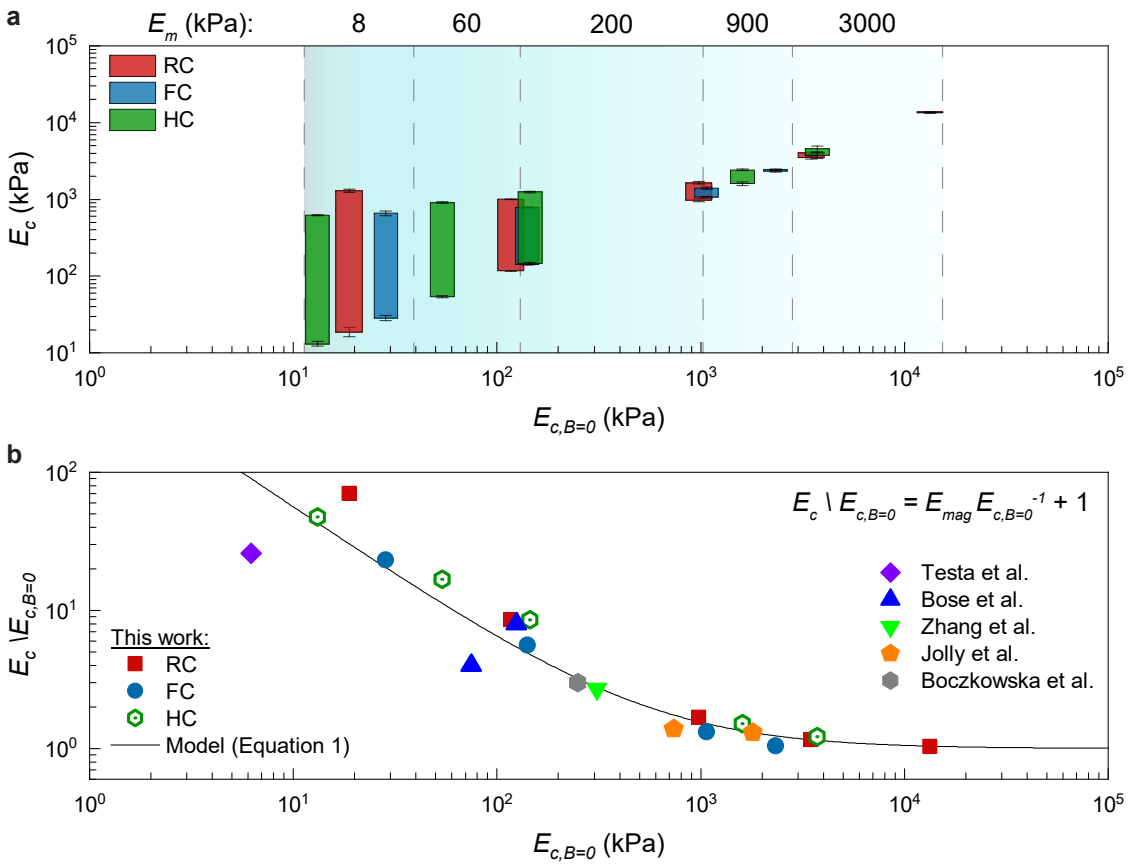


Figure 6.3: **Magnetorheological stiffness tuning. a)** Range of achievable moduli of MREs as a function of their zero-field modulus. The bottom of the floating bars indicate the zero-field modulus of the sample, while the top of the bars correspond to the measured modulus with an applied field of 280 kA m^{-1}. **b)** Maximum measured magnetorheological enhancement ratio as a function of zero-field modulus for the materials tested in this work as well as literature data (E_{mag} = 530 kPa for Equation 1).[57, 158, 178, 425, 428]

by utilizing rigid particle or MRF inclusions, or E_m can be varied through changes in elastomer crosslinking which has a strong influence on the composite modulus. These two design strategies allow for diversity of fabrication in the event that an application is limited by either the choice of elastomer or the magnetic inclusions. Figure 6.2f shows the change in zero-field modulus with respect to each of the material architectures with a constant E_m of 200 kPa. The compressive moduli are determined from the linear portion of the of the stress versus strain curves (details in experimental). The addition of solid filler increases the

zero-field modulus of the composite, while the addition of the MRF decreases the modulus of the composite. Figure 6.2g shows the alternative method of controlling the zero-field modulus for a constant material architecture of HC MRE by varying the elastomer modulus, E_m. Controlling the zero-field modulus of the composite by either of these two methods has a strong influence on the magnetorheological effect.

6.3.5 Active magnetorheological properties

For MREs to be utilized for active property tuning, it is essential to understand how the MRE material properties relate to the active stiffness tuning response. We determine that the zero-field modulus, $E_{c,B=0}$, is the controlling factor in determining the stiffness tuning capabilities of MREs. Figure 6.3a shows the range of achievable modulus of MREs as a function of zero-field modulus. The lowest point on each bar represents the lowest achievable modulus ($E_{c,B=0}$) of the sample, while the highest point of each bar is the modulus under an applied field of H = 280 kA m^{-1}. The softest MREs in this work were fabricated with $E_{c,B=0}$ on the order of 10 kPa, and demonstrate changes of stiffness of up to 70x their zero-field modulus. As the zero-field modulus is increased up to 13 MPa the relative tunability of the composite modulus decreases to only $\sim$ 3%. This decrease in mechanical tunability with respect to $E_{c,B=0}$ is a fundamental trade-off in these material systems that is attributed to stiffer material resisting the distortion of the composite by the magnetic inclusions,[443, 444] creating a large effect of $E_{c,B=0}$ relative to E_{mag}.

Figure 6.3b shows the maximum measured MR enhancement factor as a function of $E_{c,B=0}$ for the materials tested in this work as well as literature data. [57, 158, 178, 425, 428] Here, we focus only on the maximum achievable stiffness tuning effect to understand the factors governing the creation of extreme stiffness tuning MREs. We find that Equation

1 accurately predicts the stiffness tuning effect of not only the MREs in this work, but of those reported in previous research as well by fitting the data to a single value of E_{mag}. The data is fit with a value of E_{mag} = 530 kPa, which remains accurate across the wide range of $E_{c,B=0}$, is independent of the investigated microstructures, and fits a wide variety of iron particle volume fractions ranging from 17-30 %, and MRF volume fractions from 40-50 %. The MR enhancement factor is shown to approach a value of 1, indicating a negligible change in modulus as $E_{c,B=0}$ is increased above 1 MPa, which quantifies the fundamental tradeoff between MRE active properties and their zero-field modulus. This is consistent with the prediction that when $E_{mag} \ll E_{c,B=0}$ the MR enhancement factor approaches 1. This finding is an essential result for the optimization of MREs, in that it provides evidence that the maximum magnetic contribution to the modulus is not drastically changed by any of the three material structures. E_{mag} is instead likely primarily a factor of the magnetic properties of the inclusions, where iron is most commonly chosen because of its high permeability, high saturation, and low remnant magnetization.[169, 170] For materials with the same magnetic inclusions, the ability to tune E_{mag}, even across relatively large changes in volume fraction, does not have as great of an effect on the maximum stiffness tuning effect as $E_{c,B=0}$. By understanding that zero-field modulus is a dominant factor in determining the stiffness tunability of these material systems, we can now program the MR effect through their zero-field response by utilizing either E_m or material structure as discussed in Figures 6.2f-g.

MREs have long been known to have rapid response times, however the stiffness tunability has been lacking when compared to other active material systems.[167] By creating MREs with a sufficiently low zero-field modulus, we can produce materials with extreme stiffness tuning effects (MR_{effect} = 7000%) that are greater than many granular jamming and low melting point systems,[54, 416, 421, 427] while showing faster response times on the order

of ~ 20 ms. The results of this work produce a clear design framework for MREs of diverse structures that allows for the optimization of MRE materials with extreme stiffness tuning capabilities and rapid response, overcoming trade-offs in MRE and phase change based stiffness tuning materials.

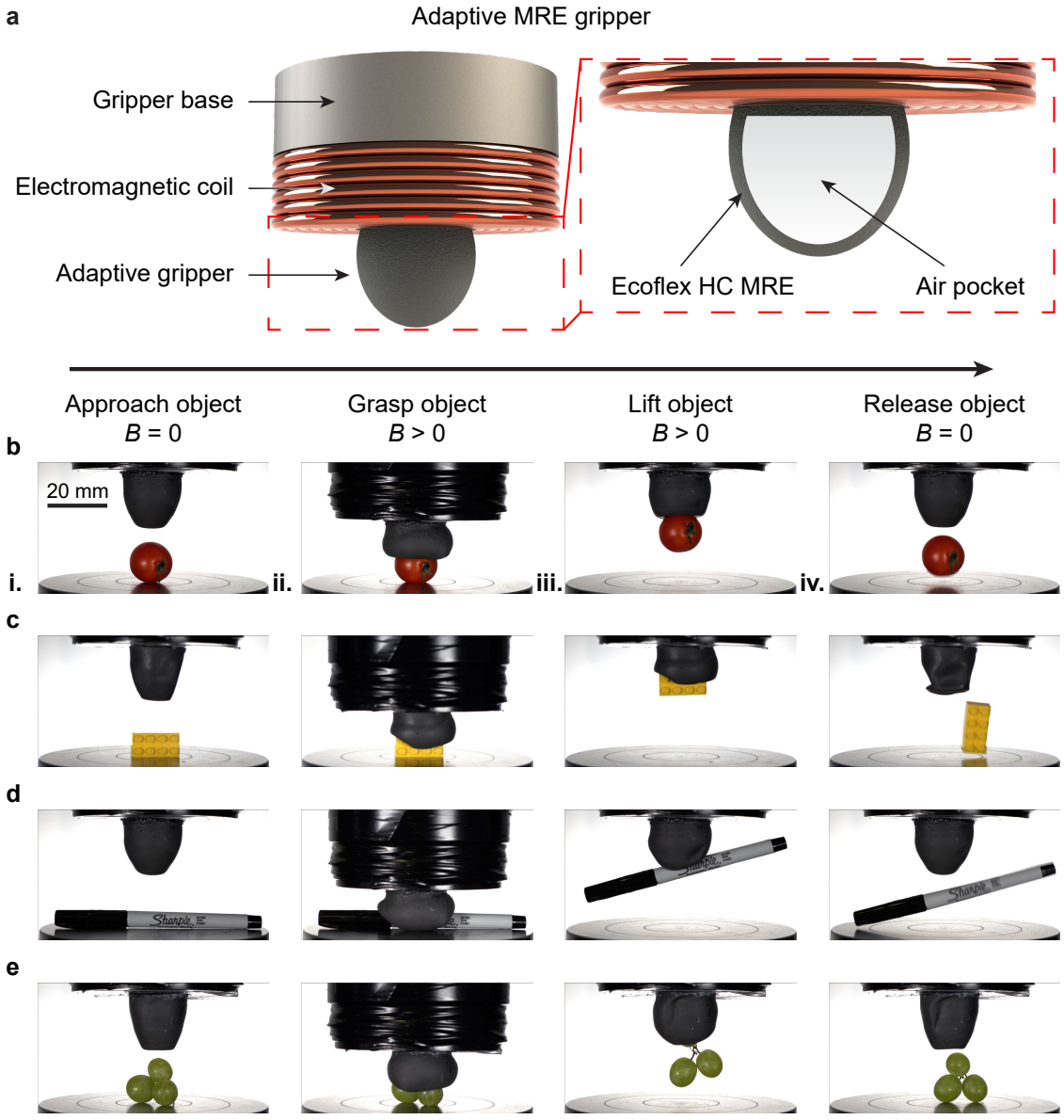


Figure 6.4: **Adaptive MRE gripper. a)** Schematic of an adaptive gripper consisting of an HC MRE membrane and an incorporated air pocket and test fixture. **b)** Images of the adaptive gripper grasping a tomato, **c)** a Lego brick, **d)** a marker, and **e)** a cluster of grapes.

6.3.6 Adaptive MRE gripper

The magnetorheological response of the HC MREs leads to a shape-locking effect with a rapid material response to a magnetic field. Here we show a soft adaptive gripper capable of rapidly gripping and releasing delicate and rigid objects with diverse geometries (Figure 1.5). The gripper consists of an HC MRE ($E_m = 200$ kPa) membrane which becomes rigid and locked into shape through a magnetic field, integrated with an inflated air pocket which allows for rapid reversibility to drop the object upon reduction of the field. The MRE gripper is adhered to the center of the electromagnet (Figure 6.4a), where the magnetic field is controlled electronically.

The gripper is able to passively conform around delicate objects without damage, and then grasp upon the application of an applied magnetic field, which increases the stiffness of the MRE membrane and locks in the conformed shape. Figure 6.4b demonstrates the grasping of a tomato, where i) the gripper begins to approach the object, ii) the gripper conforms around the object and the magnetic field is applied, iii) the gripper is retracted while grasping the object, and iv) after holding the object for 10 seconds at its original position, the magnetic field is turned off and the object rapidly drops from the gripper in less than 0.07 s. The adaptive gripper is also able to adapt to objects of complex geometry, which is shown through the grasping of a lego brick (Figure 6.4c), objects of small cross-sectional area such as a marker (Figure 6.4d), and complex, multipart shapes such as a cluster of grapes (Figure 6.4e). This HC MRE composite gripper is enabling for areas such as robotic manipulation and manufacturing which may require diverse grasping capabilities.

6.4 Conclusion

A unified MRE stiffness tuning model is demonstrated which accurately predicts the stiffness tuning effect of diverse MRE architectures. As a result of this model, the fundamental trade-off between MR effect and zero field modulus is quantified, and materials above $E_{c,B=0} = 1$ MPa are shown to have a drastically reduced MR enhancement factor approaching 1. This fundamental understanding of MRE active properties is utilized to create MREs with unprecedented MR effects of up to 7000 % that can respond on the order of 20 ms. The large mechanical adaptability and rapid response of the MREs shown in this work are expected to have applicability towards stiffness tuning elements for applications in robotics, transportation, and active technologies such as human-machine interfaces. Further, the improved understanding of the microstructure and magnetorheological response of soft composites is expected to have impacts on the development of active and programmable material systems for future advancements in functionality.

6.5 Experimental Section

Silicone elastomer fabrication and mechanical property control

The silicone elastomers in this work utilize Sylgard 184 poly(dimethylsiloxane) (PDMS) silicone elastomer (Dow Silicones) which is a two part silicone elastomer, Ecoflex 00-30 (Smooth-On) which is a two-part platinum-catalyzed silicone elastomer, or a combination of the two silicone elastomers to vary E_m. The elastomers are prepared prior to the introduction of magnetic content. The silicone matrix with $E_m = 8$ kPa is made utilizing PDMS. The PDMS is mixed with a 60:1 ratio of base to curing agent in a dual asymmetric centrifugal (DAC) mixer under vacuum (FlackTek) at 1800 RPM for 100 s. For the silicone with $E_m =$

60 kPa, the PDMS is mixed with a 45:1 ratio of base to curing agent at 1800 RPM for 100 s under vacuum. The silicone matrix with $E_m = 200$ kPa is made utilizing Ecoflex 00-30. Ecoflex is mixed with equal parts by weight of part A and part B. The uncured elastomer is mixed for 270 s at 2000 RPM under a vacuum. The silicone matrix with $E_m = 900$ kPa is made utilizing a combination of PDMS and Ecoflex 00-30. Ecoflex is mixed with equal parts by weight of part A and part B for 270 s at 2000 RPM under a vacuum. PDMS is mixed with a 10:1 ratio of base to curing agent at 1800 RPM for 100 s. The two uncured elastomers are combined in a 1 to 1 ratio by weight. The mixture is then mixed for 270 s at 2000 RPM under a vacuum. The silicone matrix with $E_m = 3000$ kPa is made utilizing PDMS. The PDMS is mixed with a 10:1 ratio of base to curing agent at 1800 RPM for 100 s under vacuum. Further information about the composition of these silicones can be found in Table E.1.

Composite fabrication

RC MREs are fabricated with iron powder (mean particle diameter: 5 µm, US Research Nanomaterials) with a particle volume fraction of $\Omega_{composite} = 25\%$. A 35% volume fraction of iron powder in propylene glycol is used to create the MRF used for both the FC and HC MREs ($\Omega_{MRF} = 35\%$). FC MREs are fabricated with an MRF volume fraction of $\Psi = 50\%$. The HC MRE consists of an MRF volume fraction $\Psi = 50\%$ and a magnetic elastomer phase with $\Omega_{matrix} = 15\%$. The total iron powder volume fraction for FC and HC MREs can be determined by $\Omega_{composite,FC} = \Psi\Omega_{MRF}$ and $\Omega_{composite,HC} = \Psi\Omega_{MRF} + (1 - \Psi)\Omega_{matrix}$, giving values of $\Omega_{composite,FC} = 17.5\%$ and $\Omega_{composite,HC} = 25\%$ respectively. Further information about the composition of these materials can be found in Table E.2.

RC MREs are fabricated by adding the 25% by volume iron powder to the uncured silicone elastomer and then mixing at 800 RPM for 120 s under vacuum in a FlackTek SpeedMixer.

The molded samples were then cured in a convection oven for at least 12 hours at 40 °C.

FC MREs are fabricated by adding the magneteorhelogical fluid to the uncured elastomer in a 50% mixture by volume. The composite is then mixed for 120 s at 800 RPM under vacuum in the SpeedMixer. The samples are cured by convection oven for at least 12 hours at 40 °C.

HC MREs are fabricated by adding 15% iron powder by volume to the uncured elastomer. Hexanes are added in a 1:4 proportion to the uncured elastomer by weight to reduce the viscosity for ease-of-processing. The composite is then mixed for 120 s at 800 RPM at atmospheric pressure in the SpeedMixer. The magnetorheological fluid is then added to the mixture in a 1:1 ratio of MRF to elastomer and iron powder by volume. The mixture is then hand mixed. The material is poured into molds, placed under vacuum to remove residual hexanes, then cured for at least 12 hours in a convection oven at 40 °C.

Magnetorheological testing fixture

A two part magnetic compression testing fixture was machined out of 1020 steel. The bottom half of the fixture is a compression plate, and the top half is a steel housing to increase the magnetic flux density through the material. 500 turns of 18 AWG copper of wire are integrated with the bottom compression plate to provide the magnetic field. Currents of 0 - 7 A are supplied to the electromagnet resulting in average magnetic field strengths of $H =$ 0-280 kA m^{-1}.

Magnetorheological compression tests

Compression samples were cured in 28.6 mm diameter, 12.5 mm deep molds. Samples are tested via a multi-step process with the MRE loaded in the magnetic compression testing fixture. Because the test fixture itself is subject to a force when a magnetic field is applied to

the system, a series of reference tests are used to determine what proportion of the measured load was applied as a stress to the sample. First, reference data is taken by measuring the load exerted by the magnetic field on the sample at several static displacements and all applied currents. A power law curve is fit to the reference data for each sample to model the load exerted by the magnetic field during sample testing. Compression tests with three loading and unloading cycles are then carried out on the sample with currents from 0-7 A applied to the electromagnet. The load from the power law model is then subtracted from the compression test load data to determine the material response to the magnetic field. Tests were performed at a rate of 12 mm min^{-1} and the compressive modulus was calculated by determining the slope of a linear fit of the stress versus strain data from 2.5 – 7.5% strain.

Adaptive gripper fabrication

The gripper is made from an HC MRE (E_m = 200 kPa) cast into into a 30 mL high form crucible. The uncured composite is placed under vacuum to remove residual hexanes. The material is then poured into the crucible and then checked for air inclusions. Then the bulk of the material is poured out leaving a thin coating (similarly to a slipcasting process). The crucible is then immediately set upside down on the glass plate, which allows the excess material to flow down onto the plate creating a sealed bottom. The mold is then placed in a 40 °C oven and allowed to fully cure for at least 45 min.

6.6 Acknowledgements

We acknowledge support from the Office of Naval Research Young Investigator Program (YIP) (N000142112699) and by the Army Research Laboratory under Cooperative Agreement Number W911NF-20-2-0039. The views and conclusions contained in this document

are those of the authors and should not be interpreted as representing the official policies, either expressed or implied, of the Army Research Laboratory or the U.S. Government. The U.S. Government is authorized to reproduce and distribute reprints for Government purposes notwithstanding any copyright notation herein. This work was performed in part at the Nanoscale Characterization and Fabrication Laboratory, which is supported by the Virginia Tech National Center for Earth and Environmental Nanotechnology Infrastructure (NanoEarth), a member of the National Nanotechnology Coordinated Infrastructure (NNCI), supported by NSF (ECCS 1542100 and ECCS 2025151).

Chapter 7

Conclusions

In this work, functional materials such as room temperature liquid metals, low melting point alloys, and magnetic powders and fluids are integrated into elastomers to produce multifunctional materials for soft electronics and machines. Concerning LM elastomer composites, we introduce the first systematic study characterizing the effects of underwater aging on LM composite properties. We also introduce a new method to increase the adhesion of LM composites with high thermal conductivity to improve integration with rigid electronic components. We utilize both LM and LMPA to engineer a multi-layer morphing material capable of rapidly and reversibly morphing into load bearing structures. We also introduce a new process to disperse magnetic fluids as discrete droplets in elastomers and systematically study the zero-field and active mechanical response of magnetorheological elastomers with several diverse material architectures.

7.1 Research contributions

1. *Liquid metal-elastomer composites for water resilient flexible electronics*

The goals described in *Research objective 1* were achieved by quantifying the effect of underwater environments on LM material properties. LM-elastomer composites made with two commonly used silicone elastomer composites are created with LM volume fractions of up to 80%. The materials are aged in four environments: including an ambient environment, a

freshwater environment, and two saltwater environments with salt concentrations of 35,000 and 70,000 ppm. The changes to material morphology, elastic modulus, thermal conductivity, and electrical conductivity are observed over the course of up to four weeks of aging in each of the four conditions. We find that LM composites possess intrinsic water resistance for many of their properties which makes them strong candidates for underwater electronics applications.

My specific contributions include:

- Provided the first systematic study to quantify the effect of underwater aging on the mechanical and functional properties of LM-elastomer composites.
- Found for high volume fraction LM composites ($\phi = 80$ %) salt water was shown to decrease the tensile modulus by up to 70 %. Salt water was also shown to decrease the thermal conductivity of $\phi = 80$ % LM composites by up to 44 %. However, the majority of samples did not show a pronounced change in mechanical or functional properties from underwater aging.
- Determined the electrical conductivity remained consistent for all samples during aging, showing no observable change after underwater aging in freshwater or salt water environments. LM composites were shown to outperform traditional copper electrodes because of their inherent water resistance.

2. *Tough bonding of liquid metal-elastomer composites for multifunctional adhesives*

The goals described in *Research objective 2* were achieved by developing a tough bonding strategy for the integration of LM composites with desirable substrates. The strategy consists of O_2 plasma of tough-to-bond substrates followed by surface treatment with an organosilane, APTES, which is shown to increase adhesion to diverse substrates when compared

to untreated surfaces or surfaces treated with O_2 plasma only. The effects of composite microstructure on fracture energy is observed by evaluating composites with LM volume fractions of up to 60% and mean droplet diameters of between 2 and 60 µm. The tough bonding method is useful for the integration of LM composites with rigid electronic components which is shown through the use of LM composites as soft, thermally conductive substrates than enable stretchable circuits and improved heat transfer efficiency for high powered LEDs.

My specific contributions include:

- Developed a new method that utilizes (3-Aminopropyl)triethoxysilane (APTES) to chemically anchor LM composites to diverse substrates. This method was shown to increase adhesion by up to 100x relative to untreated adherends.
- Studied the dependence of fracture energy on composite structure including LM droplet size and volume loading, which showed a decrease in fracture energy as LM volume fraction and mean droplet diameter are increased. Fracture energy was shown to have paired tunability with both composite modulus and thermal conductivity.
- Demonstrated the utility of the tough bonding method by bonding high powered LEDs to LM composites which improved heat transfer efficiency.

3. *Shape morphing mechanical metamaterials through reversible plasticity*

The goals described in *Research objective 3* were achieved by creating robots and machines capable of adapting their function through material-level shape change. These multi-functional machines are enabled by a shape morphing material that is capable of rapidly and reversibly morphing into complex, load-bearing shapes without the need for sustained power. The utility of this material is demonstrated through integration with power and onboard control to

create robots capable of morphing to change their transportation mechanism, and machines capable of deploying from a compact shape to a functional form factor.

My specific contributions include:

- A new multi-layered material system was developed that can rapidly and reversibly morph into load bearing structures. This material utilizes silicone elastomer encapsulation, LM as soft heating elements, LMPA for shape fixing and reversibility, and is structured with kirigami cuts to allow for large deformation.
- Developed a shape morphing, multi-model soft robot capable of land and air transport through material-level shape change and integration of on-board power and control.
- Developed a deployable underwater machine that can rapidly morph from a compact configuration to a functional form factor capable of underwater movement through water propulsion, buoyancy control through integrated pneumatic actuators, and object retrieval through a lower cargo bay.

4. *Mechanically cloaked multiphase magnetic elastomer soft composites for wearable wireless power transfer*

The goals described in *Research objective 4* were achieved by creating a new class of soft functional materials that consist of magnetic fluids dispersed as discrete droplets throughout an elastomer matrix. Magnetic fluids are created that consist of diverse magnetic particles in an immiscible carrier fluid to use as inclusions to elastomers. Significantly, upon dispersion of these fluids into an elastomer the droplets maintain their encapsulation of the rigid particles allowing for fluid like mechanical properties of the inclusions. A new hybrid composite material architecture is introduced that allows for high volume fractions of magnetic content while maintaining low stiffness and high extensibility. The utility of these materials is shown

through the use of these materials as magnetic backplanes to create soft wireless power transfer devices.

My specific contributions include:

- Provided a systematic study to quantify the zero-field mechanical properties and magnetic response of magnetic composites with unique architectures that utilize magnetic particles, magnetic fluids, and a combination of the two, which are introduced as hybrid composites.
- Introduced a method to disperse magnetic colloidal suspensions as discrete spherical droplets located throughout an elastomer matrix. By utilizing an Eshelby analysis, it is shown that the magnetic suspensions act as fluid inclusions under mechanical deformation. The carrier fluid was found to 'mechanically cloak' the dispersed solids allowing for a decrease in stiffness with an increase in magnetic permeability.
- Introduced hybrid composites that consisted of both magnetic powders and fluids to allow for high volume fractions of magnetic content while maintaining a soft mechanical response. These materials were utilized as magnetic backplanes for wearable wireless power transmitters.

5. *A unified understanding of magnetorheological elastomers for rapid and extreme stiffness tuning*

The goals described in *Research objective 5* were achieved by creating three classes of magnetic composites with rigid particles, magnetic fluids, and a combination of the two phases, and subjecting these materials to magneto-mechanical measurements to understand their active material properties. The materials are subjected to mechanical compression testing with zero-field applied and in the presence of a magnetic field of 280 kA m^{-1} to determine

the effect of microstructure on the stiffness tuning effect of these materials. In addition to different material structures, the stiffness of the silicone matrix of these materials is also varied to assess the effect of zero-field modulus on active stiffness tuning properties. A predictive model is determined that accurately unifies the stiffness tuning behavior of all three classes of MREs under a single predictive model. This new understanding is utilized to create magnetic elastomer composites with extreme changes in stiffness which we utilize to create a soft magnetic gripper capable of rapidly grasping and releasing objects of diverse geometries.

My specific contributions include:

- Provided a study of the stiffness tuning effects of magnetorheological elastomers with several material architectures including rigid particle composites, magnetorheological fluid composites, and hybrid magnetorheological composites. We introduce an MRE stiffness tuning model that accurate predicts the stiffness tuning effect of MREs of diverse structures.

- Quantified a fundamental trade-off between MR effect and zero field modulus that is observed across several material architectures and volume fractions. As the zero-field modulus of the composites increase, the magnitude of stiffness tuning decreases. As the zero-field modulus approaches 1 MPa, the MR enhancement factor approaches 1, signifying a negligible change in stiffness.

- Utilized the fundamental understanding quantified by our model to create MREs with rapid and extreme changes in stiffness (up to 70x). The utility of these materials is then demonstrated through the development of a soft adaptive gripper capable of rapidly grasping and releasing objects of diverse geometries.

7.2 Future work

In this work, we advance the field of multi-functional materials by creating liquid metal composites, morphing materials, and magnetic elastomer composites that enable the next generation of wearable electronics and soft machines. While significant progress has been achieved, the widespread implementation of these materials requires further work to address important scientific questions. With regards to liquid metal and low melting point alloy composites, one underlying question is how to manufacture and process these materials for large scale operations. Recently, LM composites have been begun to be produced through additive manufacturing approaches such as direct-ink write printing. The ability to manufacture these materials through automated processes is an important step forward for the success of these materials. However, manufacturing these materials through widely used methods such as heated extrusion from pellets utilizing single or multi-screw extruders, or fused filament fabrication for additive manufacturing would allow these materials to advance from the lab scale to feasible commercial success. The ability to process these materials through these material extrusion methods will require fundamental research to determine the answer to essential questions. Research to be considered includes a determination of the correct processing conditions for optimal processing of polymer composites with functional liquid (rather than solid) fillers. Additionally, it will be important to understand how the processing conditions can be utilized to effect the material structure, including the size and shape of liquid fillers, of the final composite.

With regards to magnetic elastomer composites, the understanding of processing discussed LMs and LMPA composites in the previous section is also applicable. However, perhaps more importantly for these materials is how they can be best integrated into engineered systems for real-world applications. MREs have long been studied for their potential use in vibrational damping for automotive applications, however limitations to their ability to

perform without the need for high-powered, bulky electromagnets, and under large applied loads presents challenges for the the implementation of these systems. While new material architectures of MREs with high stiffness tuning have recently been introduced, our work in Chapter 6 demonstrates that high-stiffness tuning magnetic elastomers require low zero-field moduli, which can limit their load-bearing capability. The utilization of these materials for automotive damping applications will likely require more efficiently designed load-transfer systems to integrate with MREs. Recent interest in soft machines such as adaptive grippers for manufacturing could allow for more feasible applications for these materials, where power requirements and space for bulky electromagnets may be less of a constraint. As research into soft robots continues to grow, it will be important to see what types of applications develop that take advantage of the rapid response, stiffness change, actuation properties, and shape memory effects of MREs.

Bibliography

[1] Young-Geun Park, Ga-Yeon Lee, Jiuk Jang, Su Min Yun, Enji Kim, and Jang-Ung Park. Liquid metal-based soft electronics for wearable healthcare. *Advanced Healthcare Materials*, 10(17):2002280, 2021.

[2] Hongbian Li, Jinfen Wang, and Ying Fang. Bioinspired flexible electronics for seamless neural interfacing and chronic recording. *Nanoscale Advances*, 2(8):3095–3102, 2020.

[3] George M Whitesides. Soft robotics. *Angewandte Chemie International Edition*, 57 (16):4258–4273, 2018.

[4] Sangbae Kim, Cecilia Laschi, and Barry Trimmer. Soft robotics: a bioinspired evolution in robotics. *Trends in biotechnology*, 31(5):287–294, 2013.

[5] Cecilia Laschi, Barbara Mazzolai, and Matteo Cianchetti. Soft robotics: Technologies and systems pushing the boundaries of robot abilities. *Science robotics*, 1(1):eaah3690, 2016.

[6] Panagiotis Polygerinos, Nikolaus Correll, Stephen A Morin, Bobak Mosadegh, Cagdas D Onal, Kirstin Petersen, Matteo Cianchetti, Michael T Tolley, and Robert F Shepherd. Soft robotics: Review of fluid-driven intrinsically soft devices; manufacturing, sensing, control, and applications in human-robot interaction. *Advanced Engineering Materials*, 19(12):1700016, 2017.

[7] Guanjun Bao, Hui Fang, Lingfeng Chen, Yuehua Wan, Fang Xu, Qinghua Yang, and Libin Zhang. Soft robotics: Academic insights and perspectives through bibliometric analysis. *Soft robotics*, 5(3):229–241, 2018.

[8] Michael D Bartlett, Michael D Dickey, and Carmel Majidi. Self-healing materials for soft-matter machines and electronics. *NPG Asia Materials*, 11(1):21, 2019.

[9] Eric J Markvicka, Michael D Bartlett, Xiaonan Huang, and Carmel Majidi. An autonomously electrically self-healing liquid metal–elastomer composite for robust soft-matter robotics and electronics. *Nature materials*, 17(7):618–624, 2018.

[10] Jiheong Kang, Jeffrey B-H Tok, and Zhenan Bao. Self-healing soft electronics. *Nature Electronics*, 2(4):144–150, 2019.

[11] John A Rogers, Takao Someya, and Yonggang Huang. Materials and mechanics for stretchable electronics. *science*, 327(5973):1603–1607, 2010.

[12] Michele Xiloyannis, Ryan Alicea, Anna-Maria Georgarakis, Florian L Haufe, Peter Wolf, Lorenzo Masia, and Robert Riener. Soft robotic suits: State of the art, core technologies, and open challenges. *IEEE Transactions on Robotics*, 38(3):1343–1362, 2021.

[13] Elliot W Hawkes, Carmel Majidi, and Michael T Tolley. Hard questions for soft robotics. *Science robotics*, 6(53):eabg6049, 2021.

[14] Michael D Dickey. Stretchable and soft electronics using liquid metals. *Advanced materials*, 29(27):1606425, 2017.

[15] Michael D Bartlett. Liquid assets for soft electronics. *Nature Materials*, 20(6):714–715, 2021.

[16] Dae-Hyeong Kim, Nanshu Lu, Rui Ma, Yun-Soung Kim, Rak-Hwan Kim, Shuodao Wang, Jian Wu, Sang Min Won, Hu Tao, Ahmad Islam, et al. Epidermal electronics. *science*, 333(6044):838–843, 2011.

[17] Yinji Ma, Kyung-In Jang, Liang Wang, Han Na Jung, Jean Won Kwak, Yeguang Xue, Hang Chen, Yiyuan Yang, Dawei Shi, Xue Feng, et al. Design of strain-limiting substrate materials for stretchable and flexible electronics. *Advanced functional materials*, 26(29):5345–5351, 2016.

[18] Alfred J Baca, Jong-Hyun Ahn, Yugang Sun, Matthew A Meitl, Etienne Menard, Hoon-Sik Kim, Won Mook Choi, Dae-Hyeong Kim, Young Huang, and John A Rogers. Semiconductor wires and ribbons for high-performance flexible electronics. *Angewandte Chemie International Edition*, 47(30):5524–5542, 2008.

[19] Marcos A Reyes-Martinez, Alfred J Crosby, and Alejandro L Briseno. Rubrene crystal field-effect mobility modulation via conducting channel wrinkling. *Nature communications*, 6(1):6948, 2015.

[20] Dae-Hyeong Kim, Jong-Hyun Ahn, Won Mook Choi, Hoon-Sik Kim, Tae-Ho Kim, Jizhou Song, Yonggang Y Huang, Zhuangjian Liu, Chun Lu, and John A Rogers. Stretchable and foldable silicon integrated circuits. *Science*, 320(5875):507–511, 2008.

[21] Dahl-Young Khang, Hanqing Jiang, Young Huang, and John A Rogers. A stretchable form of single-crystal silicon for high-performance electronics on rubber substrates. *Science*, 311(5758):208–212, 2006.

[22] Ned Bowden, Scott Brittain, Anthony G Evans, John W Hutchinson, and George M Whitesides. Spontaneous formation of ordered structures in thin films of metals supported on an elastomeric polymer. *nature*, 393(6681):146–149, 1998.

[23] Yeon Sik Choi, Yuan-Yu Hsueh, Jahyun Koo, Quansan Yang, Raudel Avila, Buwei Hu, Zhaoqian Xie, Geumbee Lee, Zheng Ning, Claire Liu, et al. Stretchable, dynamic covalent polymers for soft, long-lived bioresorbable electronic stimulators designed to facilitate neuromuscular regeneration. *Nature communications*, 11(1):5990, 2020.

[24] Jae-Woong Jeong, Woon-Hong Yeo, Aadeel Akhtar, James JS Norton, Young-Jin Kwack, Shuo Li, Sung-Young Jung, Yewang Su, Woosik Lee, Jing Xia, et al. Materials and optimized designs for human-machine interfaces via epidermal electronics. *Advanced Materials*, 25(47):6839–6846, 2013.

[25] Jonathan A Fan, Woon-Hong Yeo, Yewang Su, Yoshiaki Hattori, Woosik Lee, Sung-Young Jung, Yihui Zhang, Zhuangjian Liu, Huanyu Cheng, Leo Falgout, et al. Fractal design concepts for stretchable electronics. *Nature communications*, 5(1):3266, 2014.

[26] Phillip Won, Jung Jae Park, Taemin Lee, Inho Ha, Seonggeun Han, Mansoo Choi, Jinhwan Lee, Sukjoon Hong, Kyu-Jin Cho, and Seung Hwan Ko. Stretchable and transparent kirigami conductor of nanowire percolation network for electronic skin applications. *Nano letters*, 19(9):6087–6096, 2019.

[27] Zhuolei Zhang, Yun Yu, Yichao Tang, Ying-shi Guan, Yong Hu, Jie Yin, Katherine Willets, and Shenqiang Ren. Kirigami-inspired stretchable conjugated electronics. *Advanced Electronic Materials*, 6(1):1900929, 2020.

[28] Doh-Gyu Hwang and Michael D Bartlett. Tunable mechanical metamaterials through hybrid kirigami structures. *Scientific reports*, 8(1):3378, 2018.

[29] Braden M Li, Inhwan Kim, Ying Zhou, Amanda C Mills, Tashana J Flewwellin, and Jesse S Jur. Kirigami-inspired textile electronics: Kite. *Advanced Materials Technologies*, 4(11):1900511, 2019.

[30] Ahmad Rafsanjani, Yuerou Zhang, Bangyuan Liu, Shmuel M Rubinstein, and Katia Bertoldi. Kirigami skins make a simple soft actuator crawl. *Science Robotics*, 3(15): eaar7555, 2018.

[31] Yichao Tang, Yanbin Li, Yaoye Hong, Shu Yang, and Jie Yin. Programmable active

kirigami metasheets with more freedom of actuation. *Proceedings of the National Academy of Sciences*, 116(52):26407–26413, 2019.

[32] Yanbin Li, Qiuting Zhang, Yaoye Hong, and Jie Yin. 3d transformable modular kirigami based programmable metamaterials. *Advanced Functional Materials*, 31(43): 2105641, 2021.

[33] Takao Someya, Zhenan Bao, and George G Malliaras. The rise of plastic bioelectronics. *Nature*, 540(7633):379–385, 2016.

[34] Tarek Rafeedi and Darren J Lipomi. Multiple pathways to stretchable electronics. *Science*, 378(6625):1174–1175, 2022.

[35] Yuanwen Jiang, Zhitao Zhang, Yi-Xuan Wang, Deling Li, Charles-Théophile Coen, Ernie Hwaun, Gan Chen, Hung-Chin Wu, Donglai Zhong, Simiao Niu, et al. Topological supramolecular network enabled high-conductivity, stretchable organic bioelectronics. *Science*, 375(6587):1411–1417, 2022.

[36] Jie Xu, Sihong Wang, Ging-Ji Nathan Wang, Chenxin Zhu, Shaochuan Luo, Lihua Jin, Xiaodan Gu, Shucheng Chen, Vivian R Feig, John WF To, et al. Highly stretchable polymer semiconductor films through the nanoconfinement effect. *Science*, 355(6320): 59–64, 2017.

[37] Canhui Yang and Zhigang Suo. Hydrogel ionotronics. *Nature Reviews Materials*, 3(6): 125–142, 2018.

[38] Meixiang Wang, Pengyao Zhang, Mohammad Shamsi, Jacob L Thelen, Wen Qian, Vi Khanh Truong, Jinwoo Ma, Jian Hu, and Michael D Dickey. Tough and stretchable ionogels by in situ phase separation. *Nature materials*, 21(3):359–365, 2022.

[39] Yuanyuan Bai, Baohong Chen, Feng Xiang, Jinxiong Zhou, Hong Wang, and Zhigang Suo. Transparent hydrogel with enhanced water retention capacity by introducing highly hydratable salt. *Applied Physics Letters*, 105(15):151903, 2014.

[40] Julia A Carpenter, Thomas B Eberle, Simone Schuerle, Ahmad Rafsanjani, and André R Studart. Facile manufacturing route for magneto-responsive soft actuators. *Advanced Intelligent Systems*, 3(8):2000283, 2021.

[41] Jian-Ye Gao, Sen Chen, Tian-Ying Liu, Jiao Ye, and Jing Liu. Additive manufacture of low melting point metal porous materials: Capabilities, potential applications and challenges. *Materials Today*, 49:201–230, 2021.

[42] Nathan Lazarus, Chris D Meyer, Sarah S Bedair, Geoffrey A Slipher, and Iain M Kierzewski. Magnetic elastomers for stretchable inductors. *ACS applied materials & interfaces*, 7(19):10080–10084, 2015.

[43] Neha Sharma, Nitheesh M Nair, Garikapati Nagasarvari, Debdutta Ray, and Parasuraman Swaminathan. A review of silver nanowire-based composites for flexible electronic applications. *Flexible and Printed Electronics*, 2022.

[44] Steve Park, Michael Vosguerichian, and Zhenan Bao. A review of fabrication and applications of carbon nanotube film-based flexible electronics. *Nanoscale*, 5(5):1727–1752, 2013.

[45] Sushrut Bhanushali, Prakash Chandra Ghosh, George P Simon, and Wenlong Cheng. Copper nanowire-filled soft elastomer composites for applications as thermal interface materials. *Advanced Materials Interfaces*, 4(17):1700387, 2017.

[46] Sen Chen, Zhongshan Deng, and Jing Liu. High performance liquid metal thermal interface materials. *Nanotechnology*, 32(9):092001, 2020.

[47] Alexey Novikov, Josef Goding, Christopher Chapman, Estelle Cuttaz, and Rylie A Green. Stretchable bioelectronics: Mitigating the challenges of the percolation threshold in conductive elastomers. *APL Materials*, 8(10):101105, 2020.

[48] Hongye Sun, Zongyou Han, and Norbert Willenbacher. Ultrastretchable conductive elastomers with a low percolation threshold for printed soft electronics. *ACS applied materials & interfaces*, 11(41):38092–38102, 2019.

[49] Gagan Kaur, Raju Adhikari, Peter Cass, Mark Bown, and Pathiraja Gunatillake. Electrically conductive polymers and composites for biomedical applications. *Rsc Advances*, 5(47):37553–37567, 2015.

[50] Ravi Tutika, Shihuai H Zhou, Ralph E Napolitano, and Michael D Bartlett. Mechanical and functional tradeoffs in multiphase liquid metal, solid particle soft composites. *Advanced Functional Materials*, 28(45):1804336, 2018.

[51] Robert W Style, Ravi Tutika, Jin Young Kim, and Michael D Bartlett. Solid–liquid composites for soft multifunctional materials. *Advanced Functional Materials*, 31(1): 2005804, 2021.

[52] ABM Tahidul Haque, Ravi Tutika, Rachael L Byrum, and Michael D Bartlett. Programmable liquid metal microstructures for multifunctional soft thermal composites. *Advanced Functional Materials*, 30(25):2000832, 2020.

[53] Michael J Ford, Dinesh K Patel, Chengfeng Pan, Sarah Bergbreiter, and Carmel Majidi. Controlled assembly of liquid metal inclusions as a general approach for multifunctional composites. *Advanced Materials*, 32(46):2002929, 2020.

[54] Bryan E Schubert and Dario Floreano. Variable stiffness material based on rigid low-

melting-point-alloy microstructures embedded in soft poly (dimethylsiloxane)(pdms). *Rsc Advances*, 3(46):24671–24679, 2013.

[55] Siavash Sharifi, Amir Mohammadi Nasab, Pei-En Chen, Yiliang Liao, Yang Jiao, and Wanliang Shan. Robust bicontinuous elastomer–metal foam composites with highly tunable stiffness. *Advanced Engineering Materials*, 24(8):2101533, 2022.

[56] Edward J Barron III, Ray S Peterson, Nathan Lazarus, and Michael D Bartlett. Mechanically cloaked multiphase magnetic elastomer soft composites for wearable wireless power transfer. *ACS Applied Materials & Interfaces*, 12(45):50909–50917, 2020.

[57] Paolo Testa, Robert W Style, Jizhai Cui, Claire Donnelly, Elena Borisova, Peter M Derlet, Eric R Dufresne, and Laura J Heyderman. Magnetically addressable shape-memory and stiffening in a composite elastomer. *Advanced materials*, 31(29):1900561, 2019.

[58] AK Bastola, VT Hoang, and L Li. A novel hybrid magnetorheological elastomer developed by 3d printing. *Materials & Design*, 114:391–397, 2017.

[59] Michael D Bartlett, Navid Kazem, Matthew J Powell-Palm, Xiaonan Huang, Wenhuan Sun, Jonathan A Malen, and Carmel Majidi. High thermal conductivity in soft elastomers with elongated liquid metal inclusions. *Proceedings of the National Academy of Sciences*, 114(9):2143–2148, 2017.

[60] Dohgyu Hwang, Edward J Barron III, ABM Tahidul Haque, and Michael D Bartlett. Shape morphing mechanical metamaterials through reversible plasticity. *Science robotics*, 7(63):eabg2171, 2022.

[61] Seppe Terryn, Joost Brancart, Dirk Lefeber, Guy Van Assche, and Bram Vanderborght. Self-healing soft pneumatic robots. *Science Robotics*, 2(9):eaan4268, 2017.

[62] Alice Tonazzini, Stefano Mintchev, Bryan Schubert, Barbara Mazzolai, Jun Shintake, and Dario Floreano. Variable stiffness fiber with self-healing capability. *Advanced Materials*, 28(46):10142–10148, 2016.

[63] Edward J Barron III, Ella T Williams, Ravi Tutika, Nathan Lazarus, and Michael D Bartlett. A unified understanding of magnetorheological elastomers for rapid and extreme stiffness tuning. *RSC Applied Polymers*, 2023.

[64] Ashley H Chu, Tianyu Cheng, Arnold Muralt, and Cagdas D Onal. A passively conforming soft robotic gripper with three-dimensional negative bending stiffness fingers. *Soft Robotics*, 2023.

[65] Bertrand Tondu and Pierre Lopez. Modeling and control of mckibben artificial muscle robot actuators. *IEEE control systems Magazine*, 20(2):15–38, 2000.

[66] Koichi Suzumori, Shoichi Iikura, and Hirohisa Tanaka. Flexible microactuator for miniature robots. In *[1991] Proceedings. IEEE Micro Electro Mechanical Systems*, pages 204–209. IEEE, 1991.

[67] Koichi Suzumori, Shoichi Iikura, and Hiroshisa Tanaka. Applying a flexible microactuator to robotic mechanisms. *IEEE Control systems magazine*, 12(1):21–27, 1992.

[68] Toshiro Noritsugu, Mitsuhiko Kubota, and Sadaharu Yoshimatsu. Development of pneumatic rotary soft actuator made of silicone rubber. *Journal of Robotics and Mechatronics*, 13(1):17–22, 2001.

[69] Koichi Suzumori and Sameh Asaad. A novel pneumatic rubber actuator for mobile robot bases. In *Proceedings of IEEE/RSJ International Conference on Intelligent Robots and Systems. IROS'96*, volume 2, pages 1001–1006. IEEE, 1996.

[70] James Walker, Thomas Zidek, Cory Harbel, Sanghyun Yoon, F Sterling Strickland, Srinivas Kumar, and Minchul Shin. Soft robotics: A review of recent developments of pneumatic soft actuators. In *Actuators*, volume 9, page 3. MDPI, 2020.

[71] Wenkai Huang, Junlong Xiao, and Zhipeng Xu. A variable structure pneumatic soft robot. *Scientific Reports*, 10(1):18778, 2020.

[72] Shaohua Chen, Matthew Wei Ming Tan, Xuefei Gong, and Pooi See Lee. Low-voltage soft actuators for interactive human–machine interfaces. *Advanced Intelligent Systems*, 4(2):2100075, 2022.

[73] Hyun-Joong Chung, Andrew M Parsons, and Lelin Zheng. Magnetically controlled soft robotics utilizing elastomers and gels in actuation: A review. *Advanced Intelligent Systems*, 3(3):2000186, 2021.

[74] Liyu Wang, Yang Yang, Yonghua Chen, Carmel Majidi, Fumiya Iida, Erin Askounis, and Qibing Pei. Controllable and reversible tuning of material rigidity for robot applications. *Materials Today*, 21(5):563–576, 2018.

[75] Torben Daeneke, Khashayar Khoshmanesh, Nasir Mahmood, Isabela Alves De Castro, Dorna Esrafilzadeh, SJ Barrow, MD Dickey, and K Kalantar-Zadeh. Liquid metals: fundamentals and applications in chemistry. *Chemical Society Reviews*, 47(11):4073–4111, 2018.

[76] Edward Neville Da Costa Andrade and ER Dobbs. The viscosities of liquid lithium, rubidium and caesium. *Proceedings of the Royal Society of London. Series A. Mathematical and Physical Sciences*, 211(1104):12–30, 1952.

[77] GV Samsonov. The role of stable electron configurations in the origin of the properties

of chemical elements and compounds. *Soviet Powder Metallurgy and Metal Ceramics*, 5(12):955–963, 1966.

[78] Michael D Dickey. Emerging applications of liquid metals featuring surface oxides. *ACS applied materials & interfaces*, 6(21):18369–18379, 2014.

[79] Neeti Rustagi and Ritesh Singh. Mercury and health care. *Indian journal of occupational and environmental medicine*, 14(2):45, 2010.

[80] NJ Shanks, A Lambourne, C Morton, and JR Sanford. Comparison of accuracy of digital and standard mercury thermometers. *British Medical Journal (Clinical research ed.)*, 287(6401):1263, 1983.

[81] Huan Liu, Yang Yu, Wei Wang, Ying Liu, Yonghui An, Qian Wang, and Jing Liu. Novel contrast media based on the liquid metal gallium for in vivo digestive tract radiography: a feasibility study. *Biometals*, 32:795–801, 2019.

[82] Shi Cheng and Zhigang Wu. Microfluidic electronics. *Lab on a Chip*, 12(16):2782–2791, 2012.

[83] Seungho Yu and Massoud Kaviany. Electrical, thermal, and species transport properties of liquid eutectic ga-in and ga-in-sn from first principles. *The Journal of chemical physics*, 140(6):064303, 2014.

[84] Jiu Yang Zhu, Shi-Yang Tang, Khashayar Khoshmanesh, and Kamran Ghorbani. An integrated liquid cooling system based on galinstan liquid metal droplets. *ACS applied materials & interfaces*, 8(3):2173–2180, 2016.

[85] Zachary J Farrell and Christopher Tabor. Control of gallium oxide growth on liquid metal eutectic gallium/indium nanoparticles via thiolation. *Langmuir*, 34(1):234–240, 2018.

[86] Taylor V Neumann, Berra Kara, Yasaman Sargolzaeiaval, Sooik Im, Jinwoo Ma, Jiayi Yang, Mehmet C Ozturk, and Michael D Dickey. Aerosol spray deposition of liquid metal and elastomer coatings for rapid processing of stretchable electronics. *Micromachines*, 12(2):146, 2021.

[87] Yiliang Lin, Olivia Gordon, M Rashed Khan, Neyanel Vasquez, Jan Genzer, and Michael D Dickey. Vacuum filling of complex microchannels with liquid metal. *Lab on a Chip*, 17(18):3043–3050, 2017.

[88] Kyuyoung Kim, Junseong Ahn, Yongrok Jeong, Jungrak Choi, Osman Gul, and Inkyu Park. All-soft multiaxial force sensor based on liquid metal for electronic skin. *Micro and Nano Systems Letters*, 9(1):1–8, 2021.

[89] Collin Ladd, Ju-Hee So, John Muth, and Michael D Dickey. 3d printing of free standing liquid metal microstructures. *Advanced Materials*, 25(36):5081–5085, 2013.

[90] Michael D Bartlett, Andrew Fassler, Navid Kazem, Eric J Markvicka, Pratiti Mandal, and Carmel Majidi. Stretchable, high-k dielectric elastomers through liquid-metal inclusions. *Advanced Materials*, 28(19):3726–3731, 2016.

[91] Navid Kazem, Tess Hellebrekers, and Carmel Majidi. Soft multifunctional composites and emulsions with liquid metals. *Advanced Materials*, 29(27):1605985, 2017.

[92] Ethan J Krings, Haipeng Zhang, Suchit Sarin, Jeffery E Shield, Sangjin Ryu, and Eric J Markvicka. Lightweight, thermally conductive liquid metal elastomer composite with independently controllable thermal conductivity and density. *Small*, 17(52):2104762, 2021.

[93] Ravi Tutika, Steven Kmiec, ABM Tahidul Haque, Steve W Martin, and Michael D Bartlett. Liquid metal–elastomer soft composites with independently controllable and

highly tunable droplet size and volume loading. *ACS applied materials & interfaces*, 11(19):17873–17883, 2019.

[94] Michael J Ford, Maduran Palaniswamy, Cedric P Ambulo, Taylor H Ware, and Carmel Majidi. Size of liquid metal particles influences actuation properties of a liquid crystal elastomer composite. *Soft Matter*, 16(25):5878–5885, 2020.

[95] Mohammad H Malakooti, Michael R Bockstaller, Krzysztof Matyjaszewski, and Carmel Majidi. Liquid metal nanocomposites. *Nanoscale Advances*, 2(7):2668–2677, 2020.

[96] Sumin Moon, Hanul Kim, Kyoungmun Lee, Jinwon Park, Yunho Kim, and Siyoung Q Choi. 3d printable concentrated liquid metal composite with high thermal conductivity. *Iscience*, 24(10):103183, 2021.

[97] Tyler A Pozarycki, Dohgyu Hwang, Edward J Barron III, Brittan T Wilcox, Ravi Tutika, and Michael D Bartlett. Tough bonding of liquid metal-elastomer composites for multifunctional adhesives. *Small*, 18(41):2203700, 2022.

[98] Aaron Haake, Ravi Tutika, Gwyneth M Schloer, Michael D Bartlett, and Eric J Markvicka. On-demand programming of liquid metal-composite microstructures through direct ink write 3d printing. *Advanced Materials*, 34(20):2200182, 2022.

[99] Ravi Tutika, ABM Tahidul Haque, and Michael D Bartlett. Self-healing liquid metal composite for reconfigurable and recyclable soft electronics. *Communications Materials*, 2(1):64, 2021.

[100] Nanying Ning, Wei Huang, Suting Liu, Qi Zhao, Hua Zou, Bing Yu, Ming Tian, and Liqun Zhang. Highly stretchable liquid metal/polyurethane sponge conductors with

excellent electrical conductivity stability and good mechanical properties. *Composites Part B: Engineering*, 179:107492, 2019.

[101] John William Boley, Edward L White, and Rebecca K Kramer. Mechanically sintered gallium–indium nanoparticles. *Advanced Materials*, 27(14):2355–2360, 2015.

[102] Carl J Thrasher, Zachary J Farrell, Nicholas J Morris, Carson L Willey, and Christopher E Tabor. Mechanoresponsive polymerized liquid metal networks. *Advanced Materials*, 31(40):1903864, 2019.

[103] J William Boley, Wim M Van Rees, Charles Lissandrello, Mark N Horenstein, Ryan L Truby, Arda Kotikian, Jennifer A Lewis, and L Mahadevan. Shape-shifting structured lattices via multimaterial 4d printing. *Proceedings of the National Academy of Sciences*, 116(42):20856–20862, 2019.

[104] Eric J Markvicka, Ravi Tutika, Michael D Bartlett, and Carmel Majidi. Soft electronic skin for multi-site damage detection and localization. *Advanced Functional Materials*, 29(29):1900160, 2019.

[105] Seoyeon Kim, Sihyun Kim, Kyeongmin Hong, Michael D Dickey, and Sungjune Park. Liquid-metal-coated magnetic particles toward writable, nonwettable, stretchable circuit boards, and directly assembled liquid metal-elastomer conductors. *ACS Applied Materials & Interfaces*, 14(32):37110–37119, 2022.

[106] Bin Yao, Wei Hong, Tianwu Chen, Zhubing Han, Xinwei Xu, Renchao Hu, Jianyu Hao, Changhao Li, He Li, Steven E Perini, et al. Highly stretchable polymer composite with strain-enhanced electromagnetic interference shielding effectiveness. *Advanced Materials*, 32(14):1907499, 2020.

[107] Suqing Liang, Yaoyao Li, Yuzhen Chen, Jinbin Yang, Taipeng Zhu, Deyong Zhu,

Chuanxin He, Yizhen Liu, Stephan Handschuh-Wang, and Xuechang Zhou. Liquid metal sponges for mechanically durable, all-soft, electrical conductors. *Journal of Materials Chemistry C*, 5(7):1586–1590, 2017.

[108] Wuzhou Zu, Yunsik Ohm, Manuel Reis Carneiro, Michael Vinciguerra, Mahmoud Tavakoli, and Carmel Majidi. A comparative study of silver microflakes in digitally printable liquid metal embedded elastomer inks for stretchable electronics. *Advanced Materials Technologies*, 7(12):2200534, 2022.

[109] Gun-Hee Lee, Heejin Woo, Chanwoong Yoon, Congqi Yang, Jae-Young Bae, Wonsik Kim, Do Hoon Lee, Heemin Kang, Seungmin Han, Seung-Kyun Kang, et al. A personalized electronic tattoo for healthcare realized by on-the-spot assembly of an intrinsically conductive and durable liquid-metal composite. *Advanced Materials*, 34 (32):2204159, 2022.

[110] Lifei Zhu, Ben Wang, Stephan Handschuh-Wang, and Xuechang Zhou. Liquid metal–based soft microfluidics. *Small*, 16(9):1903841, 2020.

[111] Hyunwoo Bark, Matthew Wei Ming Tan, Gurunathan Thangavel, and Pooi See Lee. Deformable high loading liquid metal nanoparticles composites for thermal energy management. *Advanced Energy Materials*, 11(35):2101387, 2021.

[112] Matthew I Ralphs, Nicholas Kemme, Prathamesh B Vartak, Emil Joseph, Sujal Tipnis, Scott Turnage, Kiran N Solanki, Robert Y Wang, and Konrad Rykaczewski. In situ alloying of thermally conductive polymer composites by combining liquid and solid metal microadditives. *ACS applied materials & interfaces*, 10(2):2083–2092, 2018.

[113] Aastha Uppal, Wilson Kong, Ashish Rana, Jae Sang Lee, Matthew D Green, Konrad Rykaczewski, and Robert Y Wang. Precuring matrix viscosity controls thermal

conductivity of elastomeric composites with compression-activated liquid and solid metallic filler networks. *Advanced Materials Interfaces*, 10(9):2201875, 2023.

[114] Phillip Won, Seongmin Jeong, Carmel Majidi, and Seung Hwan Ko. Recent advances in liquid-metal-based wearable electronics and materials. *Iscience*, 24(7), 2021.

[115] Trung Thien Hoang, Phuoc Thien Phan, Mai Thanh Thai, James Davies, Chi Cong Nguyen, Hoang-Phuong Phan, Nigel Hamilton Lovell, and Thanh Nho Do. Magnetically engineered conductivity of soft liquid metal composites for robotic, wearable electronic, and medical applications. *Advanced Intelligent Systems*, 4(12):2200282, 2022.

[116] Phillip Won, Connor S Valentine, Mason Zadan, Chengfeng Pan, Michael Vinciguerra, Dinesh K Patel, Seung Hwan Ko, Lynn M Walker, and Carmel Majidi. 3d printing of liquid metal embedded elastomers for soft thermal and electrical materials. *ACS Applied Materials & Interfaces*, 14(49):55028–55038, 2022.

[117] Chengfeng Pan, Dongye Liu, Michael J Ford, and Carmel Majidi. Ultrastretchable, wearable triboelectric nanogenerator based on sedimented liquid metal elastomer composite. *Advanced Materials Technologies*, 5(11):2000754, 2020.

[118] Lifei Zhu, Yuzhen Chen, Wenhui Shang, Stephan Handschuh-Wang, Xiaohu Zhou, Tiansheng Gan, Qixing Wu, Yizhen Liu, and Xuechang Zhou. Anisotropic liquid metal–elastomer composites. *Journal of Materials Chemistry C*, 7(33):10166–10172, 2019.

[119] Etienne Palleau, Stephen Reece, Sharvil C Desai, Michael E Smith, and Michael D Dickey. Self-healing stretchable wires for reconfigurable circuit wiring and 3d microfluidics. *Advanced Materials*, 25(11):1589–1592, 2013.

[120] Febby Krisnadi, Linh Lan Nguyen, Ankit, Jinwoo Ma, Mohit Rameshchandra Kulkarni, Nripan Mathews, and Michael D Dickey. Directed assembly of liquid metal–elastomer conductors for stretchable and self-healing electronics. *Advanced Materials*, 32(30):2001642, 2020.

[121] Yangtai Hao, Jianye Gao, Yonggang Lv, and Jing Liu. Low melting point alloys enabled stiffness tunable advanced materials. *Advanced Functional Materials*, 32(25):2201942, 2022.

[122] Trevor L Buckner, Michelle C Yuen, Sang Yup Kim, and Rebecca Kramer-Bottiglio. Enhanced variable stiffness and variable stretchability enabled by phase-changing particulate additives. *Advanced Functional Materials*, 29(50):1903368, 2019.

[123] Adam Lipchitz, Glenn Harvel, and Takeyoshi Sunagawa. Thermophysical characteristics of liquid metal in-bi-sn eutectic (field's metal) as a similarity coolant. *Journal of Nuclear Engineering and Radiation Science*, 8(3):031301, 2022.

[124] Tianyu Yang, Jin Gu Kang, Patricia B Weisensee, Beomjin Kwon, Paul V Braun, Nenad Miljkovic, and William P King. A composite phase change material thermal buffer based on porous metal foam and low-melting-temperature metal alloy. *Applied Physics Letters*, 116(7):071901, 2020.

[125] B Brunetti, D Gozzi, M Iervolino, V Piacente, G Zanicchi, N Parodi, and G Borzone. Bismuth activity in lead-free solder bi–in–sn alloys. *Calphad*, 30(4):431–442, 2006.

[126] Boyang Yu, Linna Liu, Bingyang Liu, Xinyan Zhao, and Weiwei Deng. Printing of low-melting-point alloy as top electrode for organic solar cells. *Advanced Optical Materials*, 11(2):2201977, 2023.

[127] Wanliang Shan, Tong Lu, and Carmel Majidi. Soft-matter composites with electrically tunable elastic rigidity. *Smart Materials and Structures*, 22(8):085005, 2013.

[128] Amir Mohammadi Nasab, Trevor L Buckner, Bilige Yang, and Rebecca Kramer-Bottiglio. Effect of filler aspect ratio on stiffness and conductivity in phase-changing particulate composites. *Advanced Materials Technologies*, 7(5):2100920, 2022.

[129] Trevor L Buckner, Michelle C Yuen, and Rebecca Kramer-Bottiglio. Shape memory silicone using phase-changing inclusions. In *2020 3rd IEEE International Conference on Soft Robotics (RoboSoft)*, pages 259–265. IEEE, 2020.

[130] Nidhi Pashine, Amir Mohammadi Nasab, and Rebecca Kramer-Bottiglio. Reprogrammable allosteric metamaterials from disordered networks. *Soft Matter*, 19(8): 1617–1623, 2023.

[131] Emily A Allen and John P Swensen. Directional stiffness control through geometric patterning and localized heating of field's metal lattice embedded in silicone. In *Actuators*, volume 7, page 80. MDPI, 2018.

[132] Priyanuj Bhuyan, Yuwen Wei, Dongho Sin, Jaesang Yu, Changwoon Nah, Kwang-Un Jeong, Michael D Dickey, and Sungjune Park. Soft and stretchable liquid metal composites with shape memory and healable conductivity. *ACS Applied Materials & Interfaces*, 13(24):28916–28924, 2021.

[133] Riku Takahashi, Tao Lin Sun, Yoshiyuki Saruwatari, Takayuki Kurokawa, Daniel R King, and Jian Ping Gong. Creating stiff, tough, and functional hydrogel composites with low-melting-point alloys. *Advanced Materials*, 30(16):1706885, 2018.

[134] Dinara Zhalmuratova and Hyun-Joong Chung. Reinforced gels and elastomers for

biomedical and soft robotics applications. *ACS Applied Polymer Materials*, 2(3):1073–1091, 2020.

[135] Fanghang Deng, Quang-Kha Nguyen, and Pu Zhang. Multifunctional liquid metal lattice materials through hybrid design and manufacturing. *Additive Manufacturing*, 33:101117, 2020.

[136] Fei Long, Yingchun Shao, Zihui Zhao, Mingquan Fang, Zhiyu Zhang, Jianjun Guo, Aihua Sun, Yong Ren, Yuchuan Cheng, and Gaojie Xu. Printable multi-stage variable stiffness material enabled by low melting point particle additives. *Journal of Materials Chemistry C*, 2023.

[137] Ilse M Van Meerbeek, Benjamin C Mac Murray, Jae Woo Kim, Sanlin S Robinson, Perry X Zou, Meredith N Silberstein, and Robert F Shepherd. Morphing metal and elastomer bicontinuous foams for reversible stiffness, shape memory, and self-healing soft machines. *Advanced Materials*, 28(14):2801–2806, 2016.

[138] Ian D Tevis, Lucas B Newcomb, and Martin Thuo. Synthesis of liquid core–shell particles and solid patchy multicomponent particles by shearing liquids into complex particles (slice). *Langmuir*, 30(47):14308–14313, 2014.

[139] Shuhada A Idrus-Saidi, Jianbo Tang, Mohammad B Ghasemian, Jiong Yang, Jialuo Han, Nitu Syed, Torben Daeneke, Roozbeh Abbasi, Pramod Koshy, Anthony P O'Mullane, et al. Liquid metal core–shell structures functionalised via mechanical agitation: the example of field's metal. *Journal of Materials Chemistry A*, 7(30): 17876–17887, 2019.

[140] ZH Han, B Yang, Y Qi, and J Cumings. Synthesis of low-melting-point metallic nanoparticles with an ultrasonic nanoemulsion method. *Ultrasonics*, 51(4):485–488, 2011.

[141] Boyce S Chang, Ravi Tutika, Joel Cutinho, Stephanie Oyola-Reynoso, Jiahao Chen, Michael D Bartlett, and Martin M Thuo. Mechanically triggered composite stiffness tuning through thermodynamic relaxation (st3r). *Materials Horizons*, 5(3):416–422, 2018.

[142] Sungjune Park, Neil Baugh, Hardil K Shah, Dishit P Parekh, Ishan D Joshipura, and Michael D Dickey. Ultrastretchable elastic shape memory fibers with electrical conductivity. *Advanced Science*, 6(21):1901579, 2019.

[143] Jan Peters, Erin Nolan, Mats Wiese, Mark Miodownik, Sarah Spurgeon, Alberto Arezzo, Annika Raatz, and Helge A Wurdemann. Actuation and stiffening in fluid-driven soft robots using low-melting-point material. In *2019 IEEE/RSJ International Conference on Intelligent Robots and Systems (IROS)*, pages 4692–4698. IEEE, 2019.

[144] Yaopengxiao Xu, Pei-En Chen, Hechao Li, Wenxiang Xu, Yi Ren, Wanliang Shan, and Yang Jiao. Correlation-function-based microstructure design of alloy-polymer composites for dynamic dry adhesion tuning in soft gripping. *Journal of Applied Physics*, 131 (11), 2022.

[145] Amir Mohammadi Nasab, Patrick Stampfli, Siavash Sharifi, Aoyi Luo, Kevin T Turner, and Wanliang Shan. Dynamically tunable dry adhesion through a subsurface thin layer with tunable stiffness. *Advanced Materials Interfaces*, 9(7):2102080, 2022.

[146] Yiwei Han and Jingyan Dong. Electrohydrodynamic (ehd) printing of molten metal ink for flexible and stretchable conductor with self-healing capability. *Advanced Materials Technologies*, 3(3):1700268, 2018.

[147] Juan De Vicente, Daniel J Klingenberg, and Roque Hidalgo-Alvarez. Magnetorheological fluids: a review. *Soft matter*, 7(8):3701–3710, 2011.

[148] Georges Bossis, Sandris Lacis, Alain Meunier, and O Volkova. Magnetorheological fluids. *Journal of magnetism and magnetic materials*, 252:224–228, 2002.

[149] M Ashtiani, SH Hashemabadi, and A Ghaffari. A review on the magnetorheological fluid preparation and stabilization. *Journal of magnetism and Magnetic Materials*, 374:716–730, 2015.

[150] Xiaocong Zhu, Xingjian Jing, and Li Cheng. Magnetorheological fluid dampers: a review on structure design and analysis. *Journal of intelligent material systems and structures*, 23(8):839–873, 2012.

[151] Chun Yu Lai and Wei-Hsin Liao. Vibration control of a suspension system via a magnetorheological fluid damper. *Journal of Vibration and Control*, 8(4):527–547, 2002.

[152] Daniel J Klingenberg. Magnetorheology: Applications and challenges. *American Institute of Chemical Engineers. AIChE Journal*, 47(2):246, 2001.

[153] Donald Wilbur Felt, M Hagenbuchle, J Liu, and J Richard. Rheology of a magnetorheological fluid. *Journal of Intelligent Material Systems and Structures*, 7(5):589–593, 1996.

[154] N Lazarus and SS Bedair. Improved power transfer to wearable systems through stretchable magnetic composites. *Applied Physics A*, 122:1–7, 2016.

[155] JA Silva, C Gouveia, G Dinis, AM Pinto, and AM Pereira. Giant magnetostriction in low-concentration magnetorheological elastomers. *Composites Part B: Engineering*, 243:110125, 2022.

[156] Muhamad Amirul Sunni Rohim, Nurhazimah Nazmi, Irfan Bahiuddin, Saiful Amri Mazlan, and Nur Azmah Nordin. A mini review on modeling magnetostriction behavior

of magnetorheological solid materials. In *2022 IEEE 12th Symposium on Computer Applications & Industrial Electronics (ISCAIE)*, pages 133–138. IEEE, 2022.

[157] WH Li and XZ Zhang. A study of the magnetorheological effect of bimodal particle based magnetorheological elastomers. *Smart Materials and Structures*, 19(3):035002, 2010.

[158] Anna Boczkowska, Stefan F Awietjan, and Rafal Wroblewski. Microstructure–property relationships of urethane magnetorheological elastomers. *Smart Materials and Structures*, 16(5):1924, 2007.

[159] Shunta Kashima, Fumikazu Miyasaka, and Katsuhiro Hirata. Novel soft actuator using magnetorheological elastomer. *IEEE Transactions on magnetics*, 48(4):1649–1652, 2012.

[160] Holger Böse, Raman Rabindranath, and Johannes Ehrlich. Soft magnetorheological elastomers as new actuators for valves. *Journal of Intelligent Material Systems and Structures*, 23(9):989–994, 2012.

[161] SS Sun, Jian Yang, WH Li, Haiping Du, Gursel Alici, TH Yan, and Masami Nakano. Development of an isolator working with magnetorheological elastomers and fluids. *Mechanical Systems and Signal Processing*, 83:371–384, 2017.

[162] GJ Liao, XL Gong, SH Xuan, CJ Kang, and LH Zong. Development of a real-time tunable stiffness and damping vibration isolator based on magnetorheological elastomer. *Journal of Intelligent Material Systems and Structures*, 23(1):25–33, 2012.

[163] J David Carlson and Mark R Jolly. Mr fluid, foam and elastomer devices. *mechatronics*, 10(4-5):555–569, 2000.

[164] H Böse and R Röder. Magnetorheological elastomers with high variability of their mechanical properties. In *Journal of physics: Conference series*, volume 149, page 012090. IOP Publishing, 2009.

[165] Yu Tong, Xufeng Dong, and Min Qi. Improved tunable range of the field-induced storage modulus by using flower-like particles as the active phase of magnetorheological elastomers. *Soft Matter*, 14(18):3504–3509, 2018.

[166] John M Ginder, Mark E Nichols, Larry D Elie, and Janice L Tardiff. Magnetorheological elastomers: properties and applications. In *Smart Structures and Materials 1999: Smart Materials Technologies*, volume 3675, pages 131–138. SPIE, 1999.

[167] Mariangela Manti, Vito Cacucciolo, and Matteo Cianchetti. Stiffening in soft robotics: A review of the state of the art. *IEEE Robotics & Automation Magazine*, 23(3):93–106, 2016.

[168] John M Ginder, Mark E Nichols, Larry D Elie, and Seamus M Clark. Controllable-stiffness components based on magnetorheological elastomers. In *Smart structures and materials 2000: smart structures and integrated systems*, volume 3985, pages 418–425. SPIE, 2000.

[169] Yancheng Li, Jianchun Li, Weihua Li, and Haiping Du. A state-of-the-art review on magnetorheological elastomer devices. *Smart materials and structures*, 23(12):123001, 2014.

[170] Sung Soon Kang, Kisuk Choi, Jae-Do Nam, and Hyoung Jin Choi. Magnetorheological elastomers: Fabrication, characteristics, and applications. *Materials*, 13(20):4597, 2020.

[171] Raa Khimi Shuib, Kim Louise Pickering, and Brian Richard Mace. Dynamic properties

of magnetorheological elastomers based on iron sand and natural rubber. *Journal of Applied Polymer Science*, 132(8), 2015.

[172] Miao Yu, Pingan Yang, Jie Fu, Shuzhi Liu, and Song Qi. Study on the characteristics of magneto-sensitive electromagnetic wave-absorbing properties of magnetorheological elastomers. *Smart Materials and Structures*, 25(8):085046, 2016.

[173] Yonghong Wang, Xinru Zhang, Jaeeung Oh, and Kyungho Chung. Fabrication and properties of magnetorheological elastomers based on cr/enr self-crosslinking blends. *Smart materials and structures*, 24(9):095006, 2015.

[174] Ludovico Cestarollo, Shane Smolenski, and Amal El-Ghazaly. Nanoparticle-based magnetorheological elastomers with enhanced mechanical deflection for haptic displays. *ACS Applied Materials & Interfaces*, 14(16):19002–19011, 2022.

[175] Alla Dobroserdova, Malte Schümann, Dmitry Borin, Ekaterina Novak, Stefan Odenbach, and Sofia Kantorovich. Magneto-elastic coupling as a key to microstructural response of magnetic elastomers with flake-like particles. *Soft Matter*, 18(3):496–506, 2022.

[176] Bartłomiej Dyniewicz, Jacek M Bajkowski, and Czesław I Bajer. Semi-active control of a sandwich beam partially filled with magnetorheological elastomer. *Mechanical Systems and Signal Processing*, 60:695–705, 2015.

[177] Yanfen Zhou, Stephen Jerrams, Anthony Betts, Gerald Farrell, and Lin Chen. The influence of particle content on the equi-biaxial fatigue behaviour of magnetorheological elastomers. *Materials & Design*, 67:398–404, 2015.

[178] Jiangtao Zhang, Yanliang Qiao, Mei Zhang, and Pengcheng Zhai. Magnetorheological behavior of isotropic silicone rubber-based magnetorheological elastomers under cou-

pled static–dynamic compressive loads. *Smart Materials and Structures*, 31(9):095010, 2022.

[179] Marke Kallio, Tomi Lindroos, Samu Aalto, Erkki Järvinen, Tuomo Kärnä, and Tor Meinander. Dynamic compression testing of a tunable spring element consisting of a magnetorheological elastomer. *Smart Materials and Structures*, 16(2):506, 2007.

[180] Anil K Bastola, Milan Paudel, and Lin Li. Magnetic circuit analysis to obtain the magnetic permeability of magnetorheological elastomers. *Journal of Intelligent Material Systems and Structures*, 29(14):2946–2953, 2018.

[181] Lin Chen, XL Gong, and WH Li. Microstructures and viscoelastic properties of anisotropic magnetorheological elastomers. *Smart materials and structures*, 16(6): 2645, 2007.

[182] A Boczkowska, SF Awietjan, T Wejrzanowski, and KJ Kurzydłowski. Image analysis of the microstructure of magnetorheological elastomers. *Journal of Materials Science*, 44:3135–3140, 2009.

[183] Hossein Vatandoost, Ramin Sedaghati, and Subhash Rakheja. Development of new phenomenological models for predicting magnetic permeability of isotropic and anisotropic magneto-rheological elastomers. *IEEE Transactions on Instrumentation and Measurement*, 71:1–10, 2022.

[184] Anil Kumar Bastola, Lin Li, and Milan Paudel. A hybrid magnetorheological elastomer developed by encapsulation of magnetorheological fluid. *Journal of materials science*, 53:7004–7016, 2018.

[185] Paolo Testa, Benoît Chappuis, Sabrina Kistler, Robert W Style, Laura J Heyderman,

and Eric R Dufresne. Switchable adhesion of soft composites induced by a magnetic field. *Soft Matter*, 16(25):5806–5811, 2020.

[186] A.H. Sihvola and Institution of Electrical Engineers. *Electromagnetic Mixing Formulas and Applications*. IEE electromagnetic waves series. Institution of Electrical Engineers, 1999. ISBN 9780852967720. URL https://books.google.com/books?id=uIHSNwxBxjgC.

[187] Hiroshi Waki, Hajime Igarashi, and Toshihisa Honma. Estimation of effective permeability of magnetic composite materials. *IEEE transactions on magnetics*, 41(5): 1520–1523, 2005.

[188] Robert W Style, Rostislav Boltyanskiy, Benjamin Allen, Katharine E Jensen, Henry P Foote, John S Wettlaufer, and Eric R Dufresne. Stiffening solids with liquid inclusions. *Nature Physics*, 11(1):82–87, 2015.

[189] Nicholas Bira, Pallavi Dhagat, and Joseph R Davidson. A review of magnetic elastomers and their role in soft robotics. *Frontiers in Robotics and AI*, 7:588391, 2020.

[190] Dezheng Hua, Xinhua Liu, Shuaishuai Sun, Miguel Angel Sotelo, Zhixiong Li, and Weihua Li. A magnetorheological fluid-filled soft crawling robot with magnetic actuation. *IEEE/ASME Transactions on Mechatronics*, 25(6):2700–2710, 2020.

[191] Song Qi, Hengyu Guo, Jie Fu, Yuanpeng Xie, Mi Zhu, and Miao Yu. 3d printed shape-programmable magneto-active soft matter for biomimetic applications. *Composites Science and Technology*, 188:107973, 2020.

[192] Jiyun Kim, Su Eun Chung, Sung-Eun Choi, Howon Lee, Junhoi Kim, and Sunghoon Kwon. Programming magnetic anisotropy in polymeric microactuators. *Nature materials*, 10(10):747–752, 2011.

[193] Mengmeng Sun, Chenyao Tian, Liyang Mao, Xianghe Meng, Xingjian Shen, Bo Hao, Xin Wang, Hui Xie, and Li Zhang. Reconfigurable magnetic slime robot: deformation, adaptability, and multifunction. *Advanced Functional Materials*, 32(26):2112508, 2022.

[194] Vivek Ramachandran, Michael D Bartlett, James Wissman, and Carmel Majidi. Elastic instabilities of a ferroelastomer beam for soft reconfigurable electronics. *Extreme Mechanics Letters*, 9:282–290, 2016.

[195] Andrew B Croll, Nasibeh Hosseini, and Michael D Bartlett. Switchable adhesives for multifunctional interfaces. *Advanced Materials Technologies*, 4(8):1900193, 2019.

[196] Sanghee Lee, Changyong Yim, Wuseok Kim, and Sangmin Jeon. Magnetorheological elastomer films with tunable wetting and adhesion properties. *ACS applied materials & interfaces*, 7(35):19853–19856, 2015.

[197] Alexander Kovalev, Inna A Belyaeva, Christian von Hofen, Stanislav Gorb, and Mikhail Shamonin. Magnetically switchable adhesion and friction of soft magnetoactive elastomers. *Advanced Engineering Materials*, 24(10):2200372, 2022.

[198] Dong-Soo Choi, Tae-Hoon Kim, Seok-Han Lee, Changhyun Pang, Jin Woo Bae, and Sang-Youn Kim. Beyond human hand: shape-adaptive and reversible magnetorheological elastomer-based robot gripper skin. *ACS Applied Materials & Interfaces*, 12 (39):44147–44155, 2020.

[199] Nicholas Bira, Pallavi Dhagat, and Joseph R Davidson. Tuning the grasping strength of soft actuators with magnetic elastomer fingertips. *Smart Materials and Structures*, 31(4):045013, 2022.

[200] Wenqi Hu, Guo Zhan Lum, Massimo Mastrangeli, and Metin Sitti. Small-scale soft-bodied robot with multimodal locomotion. *Nature*, 554(7690):81–85, 2018.

[201] Yoonho Kim, Hyunwoo Yuk, Ruike Zhao, Shawn A Chester, and Xuanhe Zhao. Printing ferromagnetic domains for untethered fast-transforming soft materials. *Nature*, 558 (7709):274–279, 2018.

[202] Yoonho Kim, German A Parada, Shengduo Liu, and Xuanhe Zhao. Ferromagnetic soft continuum robots. *Science Robotics*, 4(33):eaax7329, 2019.

[203] Guolin Yun, Shi-Yang Tang, Qianbin Zhao, Yuxin Zhang, Hongda Lu, Dan Yuan, Shuaishuai Sun, Lei Deng, Michael D Dickey, and Weihua Li. Liquid metal composites with anisotropic and unconventional piezoconductivity. *Matter*, 3(3):824–841, 2020.

[204] Mingkui Zhang, Xuanhan Chen, Yongwei Sun, Minfeng Gan, Maze Liu, Shi-Yang Tang, Shiwu Zhang, Xiangpeng Li, Weihua Li, and Lining Sun. A magnetically and thermally controlled liquid metal variable stiffness material. *Advanced Engineering Materials*, 25(6):2201296, 2023.

[205] Trevor L Buckner, R Adam Bilodeau, Sang Yup Kim, and Rebecca Kramer-Bottiglio. Roboticizing fabric by integrating functional fibers. *Proceedings of the National Academy of Sciences*, 117(41):25360–25369, 2020.

[206] Joran W Booth, Olivier Cyr-Choiniere, Jennifer C Case, Dylan Shah, Michelle C Yuen, and Rebecca Kramer-Bottiglio. Surface actuation and sensing of a tensegrity structure using robotic skins. *Soft Robotics*, 8(5):531–541, 2021.

[207] Dylan S Shah, Joran W Booth, Robert L Baines, Kun Wang, Massimo Vespignani, Kostas Bekris, and Rebecca Kramer-Bottiglio. Tensegrity robotics. *Soft robotics*, 9(4): 639–656, 2022.

[208] Qingyuan Wang, Chengfeng Pan, Yuanxi Zhang, Lelun Peng, Zhipeng Chen, Carmel

Majidi, and Lelun Jiang. Magnetoactive liquid-solid phase transitional matter. *Matter*, 6(3):855–872, 2023.

[209] Yuhao Liu, Matt Pharr, and Giovanni Antonio Salvatore. Lab-on-Skin: A Review of Flexible and Stretchable Electronics for Wearable Health Monitoring. *ACS Nano*, 11 (10):9614–9635, oct 2017. doi: 10.1021/ACSNANO.7B04898. URL https://pubs.acs.org/doi/full/10.1021/acsnano.7b04898.

[210] Xuewen Wang, Zheng Liu, and Ting Zhang. Flexible Sensing Electronics for Wearable/Attachable Health Monitoring. *Small*, 13(25):1602790, jul 2017. ISSN 1613-6829. doi: 10.1002/SMLL.201602790. URL https://onlinelibrary.wiley.com/doi/full/10.1002/smll.201602790https://onlinelibrary.wiley.com/doi/abs/10.1002/smll.201602790https://onlinelibrary.wiley.com/doi/10.1002/smll.201602790.

[211] Laurent Dejace, Haotian Chen, Ivan Furfaro, Giuseppe Schiavone, and Stéphanie P Lacour. Microscale liquid metal conductors for stretchable and transparent electronics. *Advanced Materials Technologies*, 6(11):2100690, 2021.

[212] Haotian Chen, Laurent Dejace, and Stéphanie P Lacour. Electronic skins for healthcare monitoring and smart prostheses. *Annual Review of Control, Robotics, and Autonomous Systems*, 4:629–650, 2021.

[213] Mary M Rodgers, Vinay M Pai, and Richard S Conroy. Recent advances in wearable sensors for health monitoring. *IEEE Sensors Journal*, 15(6):3119–3126, 2014.

[214] Md Abdulla Al Mamun and Mehmet Rasit Yuce. Sensors and Systems for Wearable Environmental Monitoring Toward IoT-Enabled Applications: A Review. *IEEE Sensors Journal*, 19(18):7771–7788, sep 2019. doi: 10.1109/JSEN.2019.2919352.

[215] Veena Misra, Alper Bozkurt, Benton Calhoun, Thomas Jackson, Jesse S Jur, John Lach, Bongmook Lee, John Muth, Ömer Oralkan, Mehmet Öztürk, et al. Flexible technologies for self-powered wearable health and environmental sensing. *Proceedings of the IEEE*, 103(4):665–681, 2015.

[216] Akihito Noda and Hiroyuki Shinoda. Frequency-division-multiplexed signal and power transfer for wearable devices networked via conductive embroideries on a cloth. *IEEE MTT-S International Microwave Symposium Digest*, pages 537–540, oct 2017. doi: 10.1109/MWSYM.2017.8058619.

[217] III Edward J. Barron, Ray S. Peterson, Nathan Lazarus, and Michael D. Bartlett. Mechanically Cloaked Multiphase Magnetic Elastomer Soft Composites for Wearable Wireless Power Transfer. *ACS Applied Materials Interfaces*, 12(45):50909–50917, nov 2020. doi: 10.1021/ACSAMI.0C15909. URL https://pubs.acs.org/doi/full/10.1021/acsami.0c15909.

[218] Sheng Xu, Yihui Zhang, Jiung Cho, Juhwan Lee, Xian Huang, Lin Jia, Jonathan A Fan, Yewang Su, Jessica Su, Huigang Zhang, et al. Stretchable batteries with self-similar serpentine interconnects and integrated wireless recharging systems. *Nature communications*, 4(1):1543, 2013.

[219] C Majidi, R Kramer, and R J Wood. A non-differential elastomer curvature sensor for softer-than-skin electronics. *Smart Materials and Structures*, 20(10): 105017, aug 2011. ISSN 0964-1726. doi: 10.1088/0964-1726/20/10/105017. URL https://iopscience.iop.org/article/10.1088/0964-1726/20/10/105017https://iopscience.iop.org/article/10.1088/0964-1726/20/10/105017/meta.

[220] Sanming Hu, Zhijun Shi, Weiwei Zhao, Li Wang, and Guang Yang. Multifunctional piezoelectric elastomer composites for smart biomedical or wearable electron-

ics. *Composites Part B: Engineering*, 160:595–604, mar 2019. ISSN 1359-8368. doi: 10.1016/J.COMPOSITESB.2018.12.077.

[221] Robert Thomson and John Lynn. The benefits of using head mounted displays and wearable computers in a military maintenance environment. *ICEMT 2010 - 2010 International Conference on Education and Management Technology, Proceedings*, pages 560–564, 2010. doi: 10.1109/ICEMT.2010.5657592.

[222] Yunyun Wu, Sara S. Mechael, Cecilia Lerma, R. Stephen Carmichael, and Tricia Breen Carmichael. Stretchable Ultrasheer Fabrics as Semitransparent Electrodes for Wearable Light-Emitting e-Textiles with Changeable Display Patterns. *Matter*, 2(4):882–895, apr 2020. ISSN 2590-2385. doi: 10.1016/J.MATT.2020.01.017.

[223] Seonil Kwon, Hyuncheol Kim, Seungyeop Choi, Eun Gyo Jeong, Dohong Kim, Somin Lee, Ho Seung Lee, Young Cheol Seo, and Kyung Cheol Choi. Weavable and highly efficient organic light-emitting fibers for wearable electronics: a scalable, low-temperature process. *Nano letters*, 18(1):347–356, 2018.

[224] Han Eol Lee, Daewon Lee, Tae-Ik Lee, Jung Ho Shin, Gwang-Mun Choi, Cheolgyu Kim, Seung Hyung Lee, Jae Hee Lee, Yong Ho Kim, Seung-Mo Kang, et al. Wireless powered wearable micro light-emitting diodes. *Nano Energy*, 55:454–462, 2019.

[225] Yusuf A. Bhagat, Patrick Vcrdon, Sai Avuthu, Daniel Parsons, Mark Sussman, Girish Wable, and Ralph Hugeneck. Like Kleenex for Wearables: A soft, strong and disposable ECG monitoring system. *2018 IEEE Biomedical Circuits and Systems Conference, BioCAS 2018 - Proceedings*, dec 2018. doi: 10.1109/BIOCAS.2018.8584778.

[226] Yasser Khan, Aminy E Ostfeld, Claire M Lochner, Adrien Pierre, and Ana C Arias. Monitoring of vital signs with flexible and wearable medical devices. *Advanced materials*, 28(22):4373–4395, 2016.

[227] Jihong Liu, Meilin Liu, Yu Bai, Jiahao Zhang, Hongwei Liu, and Wenbin Zhu. Recent progress in flexible wearable sensors for vital sign monitoring. *Sensors*, 20(14):4009, 2020.

[228] Yi Li, Andres Villada, Shao-Hao Lu, He Sun, Jianliang Xiao, and Xueju Wang. Soft, flexible pressure sensors for pressure monitoring under large hydrostatic pressure and harsh ocean environments. *Soft Matter*, 19(30):5772–5780, 2023.

[229] Guorui Li, Xiangping Chen, Fanghao Zhou, Yiming Liang, Youhua Xiao, Xunuo Cao, Zhen Zhang, Mingqi Zhang, Baosheng Wu, Shunyu Yin, et al. Self-powered soft robot in the mariana trench. *Nature*, 591(7848):66–71, 2021.

[230] Mahmoud Tavakoli, Mohammad H Malakooti, Hugo Paisana, Yunsik Ohm, Daniel Green Marques, Pedro Alhais Lopes, Ana P Piedade, Anibal T de Almeida, and Carmel Majidi. Egain-assisted room-temperature sintering of silver nanoparticles for stretchable, inkjet-printed, thin-film electronics. *Advanced Materials*, 30(29):1801852, 2018.

[231] Brad L Cumby, Gerard J Hayes, Michael D Dickey, Ryan S Justice, Christopher E Tabor, and Jason C Heikenfeld. Reconfigurable liquid metal circuits by laplace pressure shaping. *Applied Physics Letters*, 101(17):174102, 2012.

[232] Mohammad AH Khondoker, Adam Ostashek, and Dan Sameoto. Direct 3d printing of stretchable circuits via liquid metal co-extrusion within thermoplastic filaments. *Advanced Engineering Materials*, 21(7):1900060, 2019.

[233] Sen Chen, Hong-Zhang Wang, Rui-Qi Zhao, Wei Rao, and Jing Liu. Liquid metal composites. *Matter*, 2(6):1446–1480, 2020.

[234] Taylor V. Neumann, Berra Kara, Yasaman Sargolzaeiaval, Sooik Im, Jinwoo Ma, Jiayi Yang, Mehmet C. Ozturk, and Michael D. Dickey. Aerosol Spray Deposition

of Liquid Metal and Elastomer Coatings for Rapid Processing of Stretchable Electronics. *Micromachines 2021, Vol. 12, Page 146*, 12(2):146, feb 2021. doi: 10.3390/MI12020146. URL https://www.mdpi.com/2072-666X/12/2/146/htmhttps://www.mdpi.com/2072-666X/12/2/146.

[235] Yiliang Lin, Olivia Gordon, M. Rashed Khan, Neyanel Vasquez, Jan Genzer, and Michael D. Dickey. Vacuum filling of complex microchannels with liquid metal. *Lab on a Chip*, 17(18):3043–3050, sep 2017. doi: 10.1039/C7LC00426E. URL https://pubs.rsc.org/en/content/articlehtml/2017/lc/c7lc00426ehttps://pubs.rsc.org/en/content/articlelanding/2017/lc/c7lc00426e.

[236] Khashayar Khoshmanesh, Shi-Yang Tang, Jiu Yang Zhu, Samira Schaefer, Arnan Mitchell, Kourosh Kalantar-Zadeh, and Michael D Dickey. Liquid metal enabled microfluidics. *Lab on a Chip*, 17(6):974–993, 2017.

[237] Jinpyo Jeon, Jeong-Bong Lee, Sang Kug Chung, and Daeyoung Kim. On-demand magnetic manipulation of liquid metal in microfluidic channels for electrical switching applications. *Lab on a Chip*, 17(1):128–133, 2017.

[238] Gerard J Hayes, Ju-Hee So, Amit Qusba, Michael D Dickey, and Gianluca Lazzi. Flexible liquid metal alloy (egain) microstrip patch antenna. *IEEE transactions on Antennas and Propagation*, 60(5):2151–2156, 2012.

[239] Chengfeng Pan, Eric J Markvicka, Mohammad H Malakooti, Jiajun Yan, Leiming Hu, Krzysztof Matyjaszewski, and Carmel Majidi. A liquid-metal–elastomer nanocomposite for stretchable dielectric materials. *Advanced Materials*, 31(23):1900663, 2019.

[240] P Fan, Z Sun, Y Wang, H Chang, P Zhang, S Yao, C Lu, W Rao, and J Liu. Nano liquid metal for the preparation of a thermally conductive and electrically insulating material with high stability. *RSC advances*, 8(29):16232–16242, 2018.

[241] Yiliang Lin, Christopher Cooper, Meng Wang, Jacob J Adams, Jan Genzer, and Michael D Dickey. Handwritten, soft circuit boards and antennas using liquid metal nanoparticles. *Small*, 11(48):6397–6403, 2015.

[242] Jiao Ye, Yu-Chen Yao, Jian-Ye Gao, Sen Chen, Pan Zhang, Lei Sheng, and Jing Liu. Lm-jelly: Liquid metal enabled biomimetic robotic jellyfish. *Soft Robotics*, 9(6):1098–1107, 2022.

[243] Xiangjun Qi, Hongtao Zhao, Lihong Wang, Fengqiang Sun, Xiaorui Ye, Xueji Zhang, Mingwei Tian, and Lijun Qu. Underwater sensing and warming e-textiles with reversible liquid metal electronics. *Chemical Engineering Journal*, 437:135382, 2022.

[244] Hongda Lu, Guolin Yun, Tim Cole, Yiming Ouyang, Hongtai Ren, Jian Shu, Yuxin Zhang, Shiwu Zhang, Michael D Dickey, Weihua Li, et al. Reversible underwater adhesion for soft robotic feet by leveraging electrochemically tunable liquid metal interfaces. *ACS Applied Materials & Interfaces*, 13(31):37904–37914, 2021.

[245] A. Bele, G. Stiubianu, S. Vlad, C. Tugui, C. D. Varganici, L. Matricala, D. Ionita, D. Timpu, and M. Cazacu. Aging behavior of the silicone dielectric elastomers in a simulated marine environment. *RSC Advances*, 6(11):8941–8955, jan 2016. doi: 10.1039/C5RA22780A. URL https://pubs.rsc.org/en/content/articlehtml/2016/ra/c5ra22780ahttps://pubs.rsc.org/en/content/articlelanding/2016/ra/c5ra22780a.

[246] Wanru Miao. *The Mechanism of Accelerated Hydrolytic Aging on Silicone Adhesive*. Michigan State University, 2020.

[247] D. Oldfield and T. Symes. Long term natural ageing of silicone elastomers. *Polymer Testing*, 15(2):115–128, jan 1996. ISSN 0142-9418. doi: 10.1016/0142-9418(95)00018-6.

[248] Ramesh Keshavaraj and Richard W. Tock. Modeling of Crosslinking Mechanism When Structural Silicone Sealants Are Subjected to Moisture. *Polymer-Plastics Technology and Engineering*, 32(6):579–593, nov 1993. doi: 10.1080/03602559308021023. URL https://www.tandfonline.com/doi/abs/10.1080/03602559308021023.

[249] Ramesh Keshavaraj, Richard W. Tock, and C. V.G. Vallabhan. Effects of moisture on structural silicone rubber sealants used in window glazing applications. *Construction and Building Materials*, 8(4):227–232, dec 1994. ISSN 0950-0618. doi: 10.1016/S0950-0618(09)90006-X.

[250] Sun-Tak Hwang, Thomas ES Tang, and Karl Kammermeyer. Transport of dissolved oxygen through silicone rubber membrane. *Journal of Macromolecular Science, Part B: Physics*, 5(1):1–10, 1971.

[251] Li Cheng, Yunfan Liu, Rongxin Chen, Sida Zhang, Ruijin Liao, Lijun Yang, and Tingting Wang. Method for predicting the water absorption of external insulating silicone rubber. *IEEE Transactions on Dielectrics and Electrical Insulation*, 29(4): 1242–1250, 2022.

[252] Monika Bleszynski and Maciej Kumosa. Silicone rubber RTV-1 aging in the presence of aqueous salt. *IEEE Transactions on Dielectrics and Electrical Insulation*, 23(5): 2822–2829, oct 2016. ISSN 10709878. doi: 10.1109/TDEI.2016.7736842.

[253] Sungjune Park, Kunal Mondal, Robert M Treadway III, Vikash Kumar, Siyuan Ma, James D Holbery, and Michael D Dickey. Silicones for stretchable and durable soft devices: Beyond sylgard-184. *ACS applied materials & interfaces*, 10(13):11261–11268, 2018.

[254] Cerwyn Chiew and Mohammad H Malakooti. A double inclusion model for liquid metal polymer composites. *Composites Science and Technology*, 208:108752, 2021.

[255] Shuo Wang, Xiangyu Zhao, Jie Luo, Lulu Zhuang, and Deqiu Zou. Liquid metal (lm) and its composites in thermal management. *Composites Part A: Applied Science and Manufacturing*, 163:107216.

[256] Huang Lin, GS Frankel, and WH Abbott. Analysis of ag corrosion products. *Journal of the Electrochemical Society*, 160(8):C345, 2013.

[257] El-Sayed M Sherif. Corrosion and corrosion inhibition of aluminum in arabian gulf seawater and sodium chloride solutions by 3-amino-5-mercapto-1, 2, 4-triazole. *International Journal of Electrochemical Science*, 6(5):1479–1492, 2011.

[258] El-Sayed M Sherif, RM Erasmus, and JD Comins. Corrosion of copper in aerated synthetic sea water solutions and its inhibition by 3-amino-1, 2, 4-triazole. *Journal of colloid and interface science*, 309(2):470–477, 2007.

[259] L Nunez, E Reguera, F Corvo, E Gonzalez, and C Vazquez. Corrosion of copper in seawater and its aerosols in a tropical island. *Corrosion Science*, 47(2):461–484, 2005.

[260] H Otmačić, J Telegdi, K Papp, and E Stupnišek-Lisac. Protective properties of an inhibitor layer formed on copper in neutral chloride solution. *Journal of Applied Electrochemistry*, 34:545–550, 2004.

[261] EL Holder, RN Conmey, and AD Venosa. Comparative laboratory-scale testing of dispersant effectiveness of 23 crude oils using four different testing protocols. *Journal of colloid and interface science*, 6(6):628–639, 2015.

[262] Robert F Shepherd, Filip Ilievski, Wonjae Choi, Stephen A Morin, Adam A Stokes, Aaron D Mazzeo, Xin Chen, Michael Wang, and George M Whitesides. Multigait soft robot. *Proceedings of the national academy of sciences*, 108(51):20400–20403, 2011.

[263] Daniela Rus and Michael T Tolley. Design, fabrication and control of soft robots. *Nature*, 521(7553):467–475, 2015.

[264] Zachary J Farrell, Carl J Thrasher, Alex E Flynn, and Christopher E Tabor. Silanized liquid-metal nanoparticles for responsive electronics. *ACS Applied Nano Materials*, 3 (7):6297–6303, 2020.

[265] Gregory G Guymon and Mohammad H Malakooti. Multifunctional liquid metal polymer composites. *Journal of Polymer Science*, 60(8):1300–1327, 2022.

[266] Carmel Majidi, Kaveh Alizadeh, Yunsik Ohm, Andre Silva, and Mahmoud Tavakoli. Liquid metal polymer composites: from printed stretchable circuits to soft actuators. *Flexible and Printed Electronics*, 7(1):013002, 2022.

[267] Lei Mou, Jie Qi, Lixue Tang, Ruihua Dong, Yong Xia, Yuan Gao, and Xingyu Jiang. Highly stretchable and biocompatible liquid metal-elastomer conductors for self-healing electronics. *Small*, 16(51):2005336, 2020.

[268] Shay Goff Wallace, Nathan P Bradshaw, Nicholas X Williams, Justin H Qian, Karl W Putz, Christopher E Tabor, and Mark C Hersam. Combustion-assisted photonic sintering of printed liquid metal nanoparticle films. *Advanced Materials Technologies*, page 2101178, 2021.

[269] Nikola Pekas, Qing Zhang, and David Juncker. Electrostatic actuator with liquid metal–elastomer compliant electrodes used for on-chip microvalving. *Journal of Micromechanics and Microengineering*, 22(9):097001, 2012.

[270] Pedro Alhais Lopes, Daniel Félix Fernandes, André F Silva, Daniel Green Marques, Aníbal T de Almeida, Carmel Majidi, and Mahmoud Tavakoli. Bi-phasic ag–in–ga-

embedded elastomer inks for digitally printed, ultra-stretchable, multi-layer electronics. *ACS Applied Materials & Interfaces*, 13(12):14552–14561, 2021.

[271] Abdollah Hajalilou, André F Silva, Pedro Alhais Lopes, Elahe Parvini, Carmel Majidi, and Mahmoud Tavakoli. Biphasic liquid metal composites for sinter-free printed stretchable electronics. *Advanced Materials Interfaces*, 9(5):2101913, 2022.

[272] Andrew Fassler and Carmel Majidi. Liquid-phase metal inclusions for a conductive polymer composite. *Advanced Materials*, 27(11):1928–1932, 2015.

[273] Shanliangzi Liu, Sang Yup Kim, Kristen E Henry, Dylan S Shah, and Rebecca Kramer-Bottiglio. Printed and laser-activated liquid metal-elastomer conductors enabled by ethanol/pdms/liquid metal double emulsions. *ACS Applied Materials & Interfaces*, 13 (24):28729–28736, 2021.

[274] Wilson Kong, Zhongyong Wang, Meng Wang, Kenneth C Manning, Aastha Uppal, Matthew D Green, Robert Y Wang, and Konrad Rykaczewski. Oxide-mediated formation of chemically stable tungsten–liquid metal mixtures for enhanced thermal interfaces. *Advanced Materials*, 31(44):1904309, 2019.

[275] Xiaohong Wang, Chennan Lu, and Wei Rao. Liquid metal-based thermal interface materials with a high thermal conductivity for electronic cooling and bioheat-transfer applications. *Applied Thermal Engineering*, 192:116937, 2021.

[276] Han Wang, Wenkui Xing, Shen Chen, Chengyi Song, Michael D Dickey, and Tao Deng. Liquid metal composites with enhanced thermal conductivity and stability using molecular thermal linker. *Advanced Materials*, 33(43):2103104, 2021.

[277] Pengcheng Wu, Jianzhong Fu, Yuetong Xu, and Yong He. Liquid metal microgels

for three-dimensional printing of smart electronic clothes. *ACS Applied Materials & Interfaces*, 14(11):13458–13467, 2022.

[278] Jan Roth, Victoria Albrecht, Mirko Nitschke, Cornelia Bellmann, Frank Simon, Stefan Zschoche, Stefan Michel, Claudia Luhmann, Karina Grundke, and Brigitte Voit. Surface functionalization of silicone rubber for permanent adhesion improvement. *Langmuir*, 24(21):12603–12611, 2008.

[279] DM Brewis and D Briggs. Adhesion to polyethylene and polypropylene. *Polymer*, 22 (1):7–16, 1981.

[280] Dong Zhang, Qin Sun, and Larry C Wadsworth. Mechanism of corona treatment on polyolefin films. *Polymer Engineering & Science*, 38(6):965–970, 1998.

[281] Amber M Hubbard, Wei Cui, Yiwan Huang, Riku Takahashi, Michael D Dickey, Jan Genzer, Daniel R King, and Jian Ping Gong. Hydrogel/elastomer laminates bonded via fabric interphases for stimuli-responsive actuators. *Matter*, 1(3):674–689, 2019.

[282] Lars Rossing, Rob BN Scharff, Bryan Chömpff, Charlie CL Wang, and Eugeni L Doubrovski. Bonding between silicones and thermoplastics using 3d printed mechanical interlocking. *Materials & Design*, 186:108254, 2020.

[283] Liangcai Xiong, Peng Chen, and Quansheng Zhou. Adhesion promotion between pdms and glass by oxygen plasma pre-treatment. *Journal of Adhesion Science and Technology*, 28(11):1046–1054, 2014.

[284] Shantanu Bhattacharya, Arindom Datta, Jordan M Berg, and Shubhra Gangopadhyay. Studies on surface wettability of poly (dimethyl) siloxane (pdms) and glass under oxygen-plasma treatment and correlation with bond strength. *Journal of microelectromechanical systems*, 14(3):590–597, 2005.

[285] Louis A Bloomfield. Primer system for bonding conventional adhesives and coatings to silicone rubber. *International Journal of Adhesion and Adhesives*, 68:239–247, 2016.

[286] Jiyue Yang and Andrew Garton. Primers for adhesive bonding to polyolefins. *Journal of applied polymer science*, 48(2):359–370, 1993.

[287] Tenghao Yin, Guogao Zhang, Shaoxing Qu, and Zhigang Suo. Peel of elastomers of various thicknesses and widths. *Extreme Mechanics Letters*, 46:101325, 2021.

[288] Joseph W Krumpfer and Thomas J McCarthy. Rediscovering silicones:"unreactive" silicones react with inorganic surfaces. *Langmuir*, 27(18):11514–11519, 2011.

[289] Hyunwoo Yuk, Teng Zhang, German Alberto Parada, Xinyue Liu, and Xuanhe Zhao. Skin-inspired hydrogel–elastomer hybrids with robust interfaces and functional microstructures. *Nature communications*, 7(1):1–11, 2016.

[290] Jay M Taylor, Karla Perez-Toralla, Ruby Aispuro, and Stephen A Morin. Covalent bonding of thermoplastics to rubbers for printable, reel-to-reel processing in soft robotics and microfluidics. *Advanced Materials*, 30(7):1705333, 2018.

[291] Tiance An, Shu Gong, Yunzhi Ling, Dashen Dong, Yunmeng Zhao, and Wenlong Cheng. Dynamically functioning and highly stretchable epidermal supercapacitor based on vertically aligned gold nanowire skins. *EcoMat*, 2(2):e12022, 2020.

[292] Tao Shen, Yong Liu, Yan Zhu, De-Quan Yang, and Edward Sacher. Improved adhesion of ag nps to the polyethylene terephthalate surface via atmospheric plasma treatment and surface functionalization. *Applied Surface Science*, 411:411–418, 2017.

[293] Alexander Y Fadeev and Thomas J McCarthy. Surface modification of poly (ethylene terephthalate) to prepare surfaces with silica-like reactivity. *Langmuir*, 14(19):5586–5593, 1998.

[294] Edwin P. Plueddemann. *Silane Coupling Agents*. Springer US, 1982. doi: 10.1007/978-1-4899-0342-6.

[295] AN Gent and RH Tobias. Effect of interfacial bonding on the strength of adhesion of elastomers. iii. interlinking by molecular entanglements. *Journal of Polymer Science: Polymer Physics Edition*, 22(8):1483–1490, 1984.

[296] JA Gohl, TC Thiele-Sardina, ML Rencheck, KA Erk, and CS Davis. A modular peel fixture for tape peel tests on immovable substrates. *Experimental Mechanics*, 61(7): 1209–1213, 2021.

[297] Navid Kazem, Michael D Bartlett, and Carmel Majidi. Extreme toughening of soft materials with liquid metal. *Advanced Materials*, 30(22):1706594, 2018.

[298] Seunghyun Lee and Matt Pharr. Sideways and stable crack propagation in a silicone elastomer. *Proceedings of the National Academy of Sciences*, 116(19):9251–9256, 2019.

[299] Buo Chen and David A Dillard. The effect of the t-stress on crack path selection in adhesively bonded joints. *International journal of adhesion and adhesives*, 21(5): 357–368, 2001.

[300] Seung Hee Jeong, Si Chen, Jinxing Huo, Erik Kristofer Gamstedt, Johan Liu, Shi-Li Zhang, Zhi-Bin Zhang, Klas Hjort, and Zhigang Wu. Mechanically stretchable and electrically insulating thermal elastomer composite by liquid alloy droplet embedment. *Scientific reports*, 5(1):1–10, 2015.

[301] Yunxia Gao and Jing Liu. Gallium-based thermal interface material with high compliance and wettability. *Applied Physics A*, 107(3):701–708, 2012.

[302] Shengfu Mei, Yunxia Gao, Zhongshan Deng, and Jing Liu. Thermally conductive and highly electrically resistive grease through homogeneously dispersing liquid metal

droplets inside methyl silicone oil. *Journal of Electronic Packaging*, 136(1):011009, 2014.

[303] Dae-Hyeong Kim, Jizhou Song, Won Mook Choi, Hoon-Sik Kim, Rak-Hwan Kim, Zhuangjian Liu, Yonggang Y Huang, Keh-Chih Hwang, Yong-wei Zhang, and John A Rogers. Materials and noncoplanar mesh designs for integrated circuits with linear elastic responses to extreme mechanical deformations. *Proceedings of the National Academy of Sciences*, 105(48):18675–18680, 2008.

[304] Nicholas W. Bartlett, Michael T. Tolley, Johannes T. B. Overvelde, James C. Weaver, Bobak Mosadegh, Katia Bertoldi, G. M.Whitesides, and Robert J. Wood. A 3D-printed, functionally graded soft robot powered by combustion. *Science*, 349(6244): 161–166, 2015.

[305] Bobak Mosadegh, Panagiotis Polygerinos, Christoph Keplinger, Sophia Wennstedt, Robert F. Shepherd, Unmukt Gupta, Jongmin Shim, Katia Bertoldi, Conor J. Walsh, and George M. Whitesides. Pneumatic networks for soft robotics that actuate rapidly. *Adv. Funct. Mater.*, 24(15):2163–2170, 2014. ISSN 16163028. doi: 10.1002/adfm.201303288.

[306] Alice Tonazzini, Stefano Mintchev, Bryan Schubert, Barbara Mazzolai, Jun Shintake, and Dario Floreano. Variable Stiffness Fiber with Self-Healing Capability. *Adv. Mater.*, 28(46):10142–10148, 2016. ISSN 15214095. doi: 10.1002/adma.201602580.

[307] Terry C. Shyu, Pablo F. Damasceno, Paul M. Dodd, Aaron Lamoureux, Lizhi Xu, Matthew Shlian, Max Shtein, Sharon C. Glotzer, and Nicholas A. Kotov. A kirigami approach to engineering elasticity in nanocomposites through patterned defects. *Nat. Mater.*, 14(8):785–789, 2015. ISSN 1476-1122. doi: 10.1038/nmat4327. URL http://www.nature.com/doifinder/10.1038/nmat4327.

[308] E Hawkes, B An, N M Benbernou, H Tanaka, S Kim, E D Demaine, D Rus, and R J Wood. Programmable matter by folding. *Proc. Natl. Acad. Sci.*, 107(28):12441 – 12445, 2010. doi: 10.1073/pnas.0914069107. URL http://www.pnas.org/content/107/28/12441.abstract.

[309] Zhenishbek Zhakypov, Kazuaki Mori, Koh Hosoda, and Jamie Paik. Designing minimal and scalable insect-inspired multi-locomotion millirobots. *Nature*, 571(7765):381–386, 2019. ISSN 1476-4687. doi: 10.1038/s41586-019-1388-8. URL https://doi.org/10.1038/s41586-019-1388-8.

[310] Evgueni T. Filipov, Tomohiro Tachi, Glaucio H. Paulino, and David A. Weitz. Origami tubes assembled into stiff, yet reconfigurable structures and metamaterials. *Proc. Natl. Acad. Sci. U. S. A.*, 112(40):12321–12326, 2015. ISSN 10916490. doi: 10.1073/pnas.1509465112.

[311] Mina Konakovic, Keenan Crane, Bailin Deng, Sofien Bouaziz, Daniel Piker, and Mark Pauly. Beyond Developable: Computational Design and Fabrication with Auxetic Materials. *ACM Trans. Graph.*, 35(4):89, 2016. ISSN 07300301. doi: 10.1145/2897824.2925944. URL http://dl.acm.org/citation.cfm?doid=2897824.2925944.

[312] Doh Gyu Hwang and Michael D. Bartlett. Tunable Mechanical Metamaterials through Hybrid Kirigami Structures. *Sci. Rep.*, 8(3378), 2018. ISSN 20452322. doi: 10.1038/s41598-018-21479-7. URL http://dx.doi.org/10.1038/s41598-018-21479-7.

[313] Douglas P. Holmes. Elasticity and Stability of Shape Changing Structures. *Curr. Opin. Colloid Interface Sci.*, 40:118–137, 2018. URL http://arxiv.org/abs/1809.04620.

[314] Ahmad Rafsanjani and Damiano Pasini. Bistable auxetic mechanical metamaterials inspired by ancient geometric motifs. *Extrem. Mech. Lett.*, 9:291–296, 2016.

ISSN 2352-4316. doi: https://doi.org/10.1016/j.eml.2016.09.001. URL https://www.sciencedirect.com/science/article/pii/S2352431616301298.

[315] H. Yasuda and J. Yang. Reentrant origami-based metamaterials with negative Poisson's ratio and bistability. *Phys. Rev. Lett.*, 114(18):1–5, 2015. ISSN 10797114. doi: 10.1103/PhysRevLett.114.185502.

[316] Marcelo A Dias, Michael P McCarron, Daniel Rayneau-Kirkhope, Paul Z Hanakata, David K Campbell, Harold S Park, and Douglas P Holmes. Kirigami actuators. *Soft matter*, 13(48):9087–9092, 2017.

[317] Ahmad Rafsanjani, Yuerou Zhang, Bangyuan Liu, Shmuel M Rubinstein, and Katia Bertoldi. Kirigami skins make a simple soft actuator crawl. *Sci. Robot.*, 3(15):eaar7555, 2018. ISSN 2470-9476. doi: 10.1126/scirobotics.aar7555. URL http://robotics.sciencemag.org/lookup/doi/10.1126/scirobotics.aar7555.

[318] Audrey Sedal, Amirhossein H. Memar, Tianshu Liu, Yigit Menguc, and Nick Corson. Design of Deployable Soft Robots through Plastic Deformation of Kirigami Structures. *IEEE Robot. Autom. Lett.*, 5(2):2272–2279, 2020. ISSN 23773766. doi: 10.1109/LRA.2020.2970943.

[319] Gary P.T. Choi, Levi H. Dudte, and L. Mahadevan. Programming shape using kirigami tessellations. *Nat. Mater.*, 18(9):999–1004, 2019. ISSN 14764660. doi: 10.1038/s41563-019-0452-y. URL http://dx.doi.org/10.1038/s41563-019-0452-y.

[320] Zirui Zhai, Yong Wang, and Hanqing Jiang. Origami-inspired, on-demand deployable and collapsible mechanical metamaterials with tunable stiffness. *Proc. Natl. Acad. Sci. U. S. A.*, 115(9):2032–2037, 2018. ISSN 10916490. doi: 10.1073/pnas.1720171115.

[321] Liyu Wang, Yang Yang, Yonghua Chen, Carmel Majidi, Fumiya Iida, Erin Askounis,

and Qibing Pei. Controllable and reversible tuning of material rigidity for robot applications. *Mater. Today*, 21(5):563–576, 2018. ISSN 18734103. doi: 10.1016/j.mattod.2017.10.010. URL https://doi.org/10.1016/j.mattod.2017.10.010.

[322] Zoey S Davidson, Hamed Shahsavan, Amirreza Aghakhani, Yubing Guo, Lindsey Hines, Yu Xia, Shu Yang, and Metin Sitti. Monolithic shape-programmable dielectric liquid crystal elastomer actuators. *Sci. Adv.*, 5(11):eaay0855, 2019. URL https://arxiv.org/pdf/1904.09606.pdf.

[323] A. Sydney Gladman, Elisabetta A. Matsumoto, Ralph G. Nuzzo, L. Mahadevan, and Jennifer A. Lewis. Biomimetic 4D printing. *Nat. Mater.*, 15(4):413–418, 2016. ISSN 14764660. doi: 10.1038/nmat4544.

[324] J H Pikul, S Li, H Bai, R T Hanlon, I Cohen, and R F Shepherd. Stretchable surfaces with programmable 3D texture morphing for synthetic camouflaging skins. *Science*, 358(6360):210–214, 2017.

[325] Jungwook Kim, James A Hanna, Myunghwan Byun, Christian D Santangelo, and Ryan C Hayward. Designing Responsive Buckled Surfaces by Halftone Gel Lithography. *Science*, 335(6073):1201–1205, 2012.

[326] Douglas P. Holmes, Matthieu Roché, Tarun Sinha, and Howard A. Stone. Bending and twisting of soft materials by non-homogenous swelling. *Soft Matter*, 7(11):5188–5193, 2011. ISSN 1744683X. doi: 10.1039/c0sm01492c.

[327] Emmanuel Siéfert, Etienne Reyssat, José Bico, and Benoît Roman. Bio-inspired pneumatic shape-morphing elastomers. *Nat. Mater.*, 18(1):24–28, 2019. ISSN 1476-4660. doi: 10.1038/s41563-018-0219-x.

[328] Hillel Aharoni, Yu Xia, Xinyue Zhang, Randall D Kamien, and Shu Yang. Universal

inverse design of surfaces with thin nematic elastomer sheets. *Proc. Natl. Acad. Sci.*, 115(28):7206 – 7211, 2018. doi: 10.1073/pnas.1804702115. URL http://www.pnas.org/content/115/28/7206.abstract.

[329] Qiguang He, Zhijian Wang, Yang Wang, Adriane Minori, Michael T Tolley, and Shengqiang Cai. Electrically controlled liquid crystal elastomer-based soft tubular actuator with multimodal actuation. *Sci. Adv.*, 5(10):eaax5746, 2019. ISSN 23752548. doi: 10.1126/sciadv.aax5746.

[330] Yoonho Kim, Hyunwoo Yuk, Ruike Zhao, Shawn A Chester, and Xuanhe Zhao. Printing ferromagnetic domains for untethered fast-transforming soft materials. *Nat. Lett.*, 558:274–279, 2018. ISSN 03704793. doi: https://doi.org/10.1038/s41586-018-0185-0.

[331] Ilse M. Van Meerbeek, Benjamin C. Mac Murray, Jae Woo Kim, Sanlin S. Robinson, Perry X. Zou, Meredith N. Silberstein, and Robert F. Shepherd. Morphing Metal and Elastomer Bicontinuous Foams for Reversible Stiffness, Shape Memory, and Self-Healing Soft Machines. *Adv. Mater.*, 28(14):2801–2806, 2016. ISSN 15214095. doi: 10.1002/adma.201505991.

[332] Kai Yu, Qi Ge, and H Jerry Qi. Reduced time as a unified parameter determining fixity and free recovery of shape memory polymers. *Nat. Commun.*, 5(3066), 2014. doi: 10.1038/ncomms4066.

[333] Trevor L. Buckner, Michelle C. Yuen, Sang Yup Kim, and Rebecca Kramer-Bottiglio. Enhanced Variable Stiffness and Variable Stretchability Enabled by Phase-Changing Particulate Additives. *Adv. Funct. Mater.*, 29(50):1903368, 2019. ISSN 16163028. doi: 10.1002/adfm.201903368.

[334] Fanghang Deng, Quang Kha Nguyen, and Pu Zhang. Multifunctional liquid metal lattice materials through hybrid design and manufacturing. *Addit. Manuf.*, 33:101117,

2020. ISSN 22148604. doi: 10.1016/j.addma.2020.101117. URL https://doi.org/10.1016/j.addma.2020.101117.

[335] Davide Zappetti, Seung Hee Jeong, Jun Shintake, and Dario Floreano. Phase Changing Materials-Based Variable-Stiffness Tensegrity Structures. *Soft Robot.*, 7(3):362–369, 2020. ISSN 21695180. doi: 10.1089/soro.2019.0091.

[336] Yufei Hao, Tianmiao Wang, Xi Fang, Kang Yang, Ling Mao, Juan Guan, and Li Wen. A variable stiffness soft robotic gripper with low-melting-point alloy. *Chinese Control Conf. CCC*, pages 6781–6786, 2017. ISSN 21612927. doi: 10.23919/ChiCC.2017.8028427.

[337] Jun Shintake, Bryan Schubert, Samuel Rosset, Herbert Shea, and Dario Floreano. Variable stiffness actuator for soft robotics using dielectric elastomer and low-melting-point alloy. *2015 IEEE/RSJ Int. Conf. Intell. Robot. Syst.*, pages 1097–1102, 2015. ISSN 21530866. doi: 10.1109/IROS.2015.7353507.

[338] Yi Yang, Marcelo A. Dias, and Douglas P. Holmes. Multistable kirigami for tunable architected materials. *Phys. Rev. Mater.*, 2(11):110601, 2018. ISSN 24759953. doi: 10.1103/PhysRevMaterials.2.110601. URL https://doi.org/10.1103/PhysRevMaterials.2.110601.

[339] Yanjun Li, Tsung-chow Su, and Bing Ouyang. Design and Deployment Analysis of Subsea Deployable Structures. *27th Int. Ocean Polar Eng. Conf.*, pages ISOPE–I–17–216, 2017.

[340] Thibaut Paschal, Jun Shintake, Stefano Mintchev, and Dario Floreano. Development of bio-inspired underwater robot with adaptive morphology capable of multiple swimming modes. *2017 IEEE/RSJ Int. Conf. Intell. Robot. Syst.*, pages 4197–4202, 2017. ISSN 21530866. doi: 10.1109/IROS.2017.8206281.

[341] Giacomo Picardi, Helmut Hauser, Cecilia Laschi, and Marcello Calisti. Morphologically induced stability on an underwater legged robot with a deformable body. *Int. J. Rob. Res.*, 40(1):435–448, 2021. ISSN 17413176. doi: 10.1177/0278364919840426.

[342] Francesco Giorgio-Serchi, Andrea Arienti, and Cecilia Laschi. Underwater soft-bodied pulsed-jet thrusters: Actuator modeling and performance profiling. *Int. J. Rob. Res.*, 35(11):1395–1416, 2016. ISSN 17413176. doi: 10.1177/0278364915622569.

[343] F. Giorgio-Serchi, A. Arienti, F. Corucci, M. Giorelli, and C. Laschi. Hybrid parameter identification of a multi-modal underwater soft robot. *Bioinspiration and Biomimetics*, 12(2), 2017. ISSN 17483190. doi: 10.1088/1748-3190/aa5ccc.

[344] Jun Shintake, Herbert Shea, and Dario Floreano. Biomimetic underwater robots based on dielectric elastomer actuators. *IEEE Int. Conf. Intell. Robot. Syst.*, pages 4957–4962, 2016. ISSN 21530866. doi: 10.1109/IROS.2016.7759728.

[345] Guorui Li, Xiangping Chen, Fanghao Zhou, Yiming Liang, Youhua Xiao, Xunuo Cao, Zhen Zhang, Mingqi Zhang, Baosheng Wu, Shunyu Yin, Yi Xu, Hongbo Fan, Zheng Chen, Wei Song, Wenjing Yang, Binbin Pan, Jiaoyi Hou, Weifeng Zou, Shunping He, Xuxu Yang, Guoyong Mao, Zheng Jia, Haofei Zhou, Tiefeng Li, Shaoxing Qu, Zhongbin Xu, Zhilong Huang, Yingwu Luo, Tao Xie, Jason Gu, Shiqiang Zhu, and Wei Yang. Self-powered soft robot in the Mariana Trench. *Nature*, 591(7848):66–71, 2021. ISSN 14764687. doi: 10.1038/s41586-020-03153-z.

[346] Wei Wang, Nam Geuk Kim, Hugo Rodrigue, and Sung Hoon Ahn. Modular assembly of soft deployable structures and robots. *Mater. Horizons*, 4(3):367–376, 2017. ISSN 20516355. doi: 10.1039/c6mh00550k.

[347] Andrew D. Marchese, Cagdas D. Onal, and Daniela Rus. Autonomous Soft Robotic

Fish Capable of Escape Maneuvers Using Fluidic Elastomer Actuators. *Soft Robot.*, 1 (1):75–87, 2014. ISSN 21695180. doi: 10.1089/soro.2013.0009.

[348] Qiguang He, Zhijian Wang, Yang Wang, Zijun Wang, Chenghai Li, Raja Annapooranan, Jian Zeng, Renkun Chen, and Shengqiang Cai. Electrospun liquid crystal elastomer microfiber actuator. *Science Robotics*, 6(57):eabi9704, 2021.

[349] Qiguang He, Zhijian Wang, Yang Wang, Adriane Minori, Michael T Tolley, and Shengqiang Cai. Electrically controlled liquid crystal elastomer–based soft tubular actuator with multimodal actuation. *Science advances*, 5(10):eaax5746, 2019.

[350] Hetao Chu, Xinghao Hu, Zhong Wang, Jiuke Mu, Na Li, Xiaoshuang Zhou, Shaoli Fang, Carter S Haines, Jong Woo Park, Si Qin, et al. Unipolar stroke, electroosmotic pump carbon nanotube yarn muscles. *Science*, 371(6528):494–498, 2021.

[351] Federico Renda, Matteo Cianchetti, Michele Giorelli, Andrea Arienti, and Cecilia Laschi. A 3d steady-state model of a tendon-driven continuum soft manipulator inspired by the octopus arm. *Bioinspiration & biomimetics*, 7(2):025006, 2012.

[352] Taylor H Ware, Michael E McConney, Jeong Jae Wie, Vincent P Tondiglia, and Timothy J White. Voxelated liquid crystal elastomers. *Science*, 347(6225):982–984, 2015.

[353] Davide Falanga, Kevin Kleber, Stefano Mintchev, Dario Floreano, and Davide Scaramuzza. The foldable drone: A morphing quadrotor that can squeeze and fly. *IEEE Robotics and Automation Letters*, 4(2):209–216, 2018.

[354] Barbara Mazzolai, Alessio Mondini, Francesca Tramacere, Gianluca Riccomi, Ali Sadeghi, Goffredo Giordano, Emanuela Del Dottore, Massimiliano Scaccia, Massimo Zampato, and Stefano Carminati. Octopus-inspired soft arm with suction cups for

enhanced grasping tasks in confined environments. *Advanced Intelligent Systems*, 1(6): 1900041, 2019.

[355] O H Yeoh. Some forms of the strain energy function for rubber. *Rubber Chem. Technol.*, 66(5):754–771, 1993. ISSN 00359475. doi: 10.5254/1.3538343.

[356] Xiao-Yong Jia, Jin-Feng Mei, Jian-Cheng Lai, Cheng-Hui Li, and Xiao-Zeng You. A Highly Stretchable Polymer that Can Be Thermally Healed at Mild Temperature. *Macromolecular Rapid Communications*, 37(12):952–956, jun 2016. ISSN 10221336. doi: 10.1002/marc.201600142. URL http://doi.wiley.com/10.1002/marc.201600142.

[357] Zeming Song, Xu Wang, Cheng Lv, Yonghao An, Mengbing Liang, Teng Ma, David He, Ying Jie Zheng, Shi Qing Huang, Hongyu Yu, and Hanqing Jiang. Kirigami-based Stretchable Lithium-ion Batteries. *Scientific Reports*, 5(1):1–9, jun 2015. ISSN 20452322. doi: 10.1038/srep10988. URL https://www.nature.com/articles/srep10988.

[358] Changsheng Wu, Xin Wang, Long Lin, Hengyu Guo, and Zhong Lin Wang. Paper-Based Triboelectric Nanogenerators Made of Stretchable Interlocking Kirigami Patterns. *ACS Nano*, 10(4):4652–4659, apr 2016. ISSN 1936086X. doi: 10.1021/acsnano.6b00949. URL https://pubs.acs.org/doi/abs/10.1021/acsnano.6b00949.

[359] Renxiao Xu, Anton Zverev, Aaron Hung, Caiwei Shen, Lauren Irie, Geoffrey Ding, Michael Whitmeyer, Liangjie Ren, Brandon Griffin, Jack Melcher, Lily Zheng, Xining Zang, Mohan Sanghadasa, and Liwei Lin. Kirigami-inspired, Highly Stretchable Micro-supercapacitor Patches Fabricated by Laser Conversion and Cutting. *Microsystems and Nanoengineering*, 4(1):1–10, dec 2018. ISSN 20557434. doi: 10.1038/s41378-018-0036-z. URL https://www.nature.com/articles/s41378-018-0036-z.

[360] Nam Su Jang, Kang Hyun Kim, Sung Hun Ha, Soo Ho Jung, Hye Moon Lee, and Jong Man Kim. Simple Approach to High-Performance Stretchable Heaters Based on Kirigami Patterning of Conductive Paper for Wearable Thermotherapy Applications. *ACS Applied Materials and Interfaces*, 9(23):19612–19621, jun 2017. ISSN 19448252. doi: 10.1021/acsami.7b03474. URL https://pubs.acs.org/doi/abs/10.1021/acsami.7b03474.

[361] Li Peng, Zhen Xu, Zheng Liu, Yan Guo, Peng Li, and Chao Gao. Ultrahigh Thermal Conductive yet Superflexible Graphene Films. *Advanced Materials*, 29(27), jul 2017. ISSN 15214095. doi: 10.1002/adma.201700589. URL https://onlinelibrary.wiley.com/doi/full/10.1002/adma.201700589https://onlinelibrary.wiley.com/doi/abs/10.1002/adma.201700589https://onlinelibrary.wiley.com/doi/10.1002/adma.201700589.

[362] Ye P. Mamunya, V. V. Davydenko, P. Pissis, and E. V. Lebedev. Electrical and Thermal Conductivity of Polymers Filled with Metal Powders. *European Polymer Journal*, 38(9):1887–1897, sep 2002. ISSN 00143057. doi: 10.1016/S0014-3057(02)00064-2.

[363] Haeleen Hong, Yei Hwan Jung, Ju Seung Lee, Chanho Jeong, Jong Uk Kim, Sori Lee, Hyewon Ryu, Heyn Kim, Zhenqiang Ma, and Tae-il Kim. Anisotropic Thermal Conductive Composite by the Guided Assembly of Boron Nitride Nanosheets for Flexible and Stretchable Electronics. *Advanced Functional Materials*, 29(37):1902575, sep 2019. ISSN 1616-301X. doi: 10.1002/adfm.201902575. URL https://onlinelibrary.wiley.com/doi/abs/10.1002/adfm.201902575.

[364] C. P. Wong and Raja S. Bollampally. Thermal Conductivity, Elastic Modulus, and Coefficient of Thermal Expansion of Polymer Composites Filled with Ceramic Particles for

Electronic Packaging. *Journal of Applied Polymer Science*, 74(14):3396–3403, dec 1999. ISSN 1097-4628. doi: 10.1002/(SICI)1097-4628(19991227)74:14<3396::AID-APP13>3.0.CO;2-3. URL https://onlinelibrary.wiley.com/doi/full/10.1002/{%}28SICI{%}291097-4628{%}2819991227{%}2974{%}3A14{%}3C3396{%}3A{%}3AAID-APP13{%}3E0.CO{%}3B2-3https://onlinelibrary.wiley.com/doi/abs/10.1002/{%}28SICI{%}291097-4628{%}2819991227{%}2974{%}3A14{%}3C3396{%}3A{%}3AAID-APP13{%}3E0.CO{%}3B2-3ht.

[365] R. C. Progelhof, J. L. Throne, and R. R. Ruetsch. Methods for Predicting the Thermal Conductivity of Composite Systems: A Review, 1976. ISSN 15482634.

[366] Thomas Steen Hansen, Keld West, Ole Hassager, and Niels B. Larsen. Highly Stretchable and Conductive Polymer Material made from Poly(3,4-ethylenedioxythiophene) and Polyurethane Elastomers. *Advanced Functional Materials*, 17(16):3069–3073, nov 2007. ISSN 1616301X. doi: 10.1002/adfm.200601243. URL https://onlinelibrary.wiley.com/doi/full/10.1002/adfm.200601243https://onlinelibrary.wiley.com/doi/abs/10.1002/adfm.200601243https://onlinelibrary.wiley.com/doi/10.1002/adfm.200601243.

[367] N C Das, T K Chaki, and D Khastgir. Effect of Axial Stretching on Electrical Resistivity of Short Carbon Fibre and Carbon Black Filled Conductive Rubber composites. *Polymer International*, 51(2):156–163, feb 2002. ISSN 0959-8103. doi: 10.1002/pi.811. URL http://doi.wiley.com/10.1002/pi.811.

[368] Wei Gao, Lanlan Wang, Xingzhe Wang, and Hongzhong Liu. Magnetic Driving Flowerlike Soft Platform: Biomimetic Fabrication and External Regulation. *ACS Applied Materials and Interfaces*, 8(22):14182–14189, jun 2016. ISSN 19448252. doi: 10.1021/acsami.6b03218.

[369] John M. Ginder, Mark E. Nichols, Larry D. Elie, and Janice L. Tardiff. Magnetorheological Elastomers: Properties and Applications. In Manfred R. Wuttig, editor, *Smart Structures and Materials 1999: Smart Materials Technologies*, volume 3675, pages 131–138. SPIE, jul 1999. doi: 10.1117/12.352787. URL http://proceedings.spiedigitallibrary.org/proceeding.aspx?articleid=983114.

[370] Jiaxing Li, Mengying Zhang, Limu Wang, Weihua Li, Ping Sheng, and Weijia Wen. Design and Fabrication of Microfluidic Mixer from Carbonyl Iron-PDMS Composite Membrane. *Microfluidics and Nanofluidics*, 10(4):919–925, apr 2011. ISSN 16134982. doi: 10.1007/s10404-010-0712-2.

[371] Nathan Lazarus, Chris D. Meyer, Sarah S. Bedair, Geoffrey A. Slipher, and Iain M. Kierzewski. Magnetic Elastomers for Stretchable Inductors. *ACS Applied Materials and Interfaces*, 2015. ISSN 19448252. doi: 10.1021/acsami.5b02189.

[372] N. Lazarus and S. S. Bedair. Improved Power Transfer to Wearable Systems through Stretchable Magnetic Composites. *Applied Physics A: Materials Science and Processing*, 122(5), may 2016. ISSN 14320630. doi: 10.1007/s00339-016-0067-y.

[373] Christian Gollwitzer, Alexander Turanov, Marina Krekhova, Günter Lattermann, Ingo Rehberg, and Reinhard Richter. Measuring the Deformation of a Ferrogel Sphere in a Homogeneous Magnetic Field. *Journal of Chemical Physics*, 128(16), jan 2008. ISSN 00219606. doi: 10.1063/1.2905212. URL http://arxiv.org/abs/0801.1244http://dx.doi.org/10.1063/1.2905212.

[374] Ravi Tutika, Shihuai H. Zhou, Ralph E. Napolitano, and Michael D. Bartlett. Mechanical and Functional Tradeoffs in Multiphase Liquid Metal, Solid Particle Soft Composites. *Advanced Functional Materials*, 28(45):1804336, nov 2018. ISSN 1616301X. doi: 10.1002/adfm.201804336. URL http://doi.wiley.com/10.1002/adfm.201804336.

[375] Robert W. Style, John S. Wettlaufer, and Eric R. Dufresne. Surface Tension and the Mechanics of Liquid Inclusions in Compliant Solids. *Soft Matter*, 11(4):672–679, jan 2015. ISSN 17446848. doi: 10.1039/c4sm02413c.

[376] Robert W. Style, Ravi Tutika, Jin Young Kim, and Michael D. Bartlett. Solid–Liquid Composites for Soft Multifunctional Materials. *Advanced Functional Materials*, page 2005804, 2020.

[377] Matthew I. Ralphs, Nicholas Kemme, Prathamesh B. Vartak, Emil Joseph, Sujal Tipnis, Scott Turnage, Kiran N. Solanki, Robert Y. Wang, and Konrad Rykaczewski. In Situ Alloying of Thermally Conductive Polymer Composites by Combining Liquid and Solid Metal Microadditives. *ACS Applied Materials and Interfaces*, 10(2):2083–2092, 2018. ISSN 19448252. doi: 10.1021/acsami.7b15814.

[378] Ravi Tutika, Steven Kmiec, A. B.M. Tahidul Haque, Steve W. Martin, and Michael D. Bartlett. Liquid Metal-Elastomer Soft Composites with Independently Controllable and Highly Tunable Droplet Size and Volume Loading. *ACS Applied Materials and Interfaces*, 11(19):17873–17883, may 2019. ISSN 19448252. doi: 10.1021/acsami.9b04569.

[379] P. Fan, Z. Sun, Y. Wang, H. Chang, P. Zhang, S. Yao, C. Lu, and W. Rao. Nano Liquid Metal for the Preparation of a Thermally Conductive and Electrically Insulating Material with High Stability. *RSC Advances*, 8(29):16232–16242, 2018. ISSN 2046-2069. doi: 10.1039/c8ra00262b.

[380] Michael D. Bartlett, Andrew Fassler, Navid Kazem, Eric J. Markvicka, Pratiti Mandal, and Carmel Majidi. Stretchable, High-k Dielectric Elastomers through Liquid-Metal Inclusions. *Advanced Materials*, 28(19):3726–3731, may 2016. ISSN 15214095. doi: 10.1002/adma.201506243.

[381] Michael D. Bartlett, Navid Kazem, Matthew J. Powell-Palm, Xiaonan Huang, Wenhuan Sun, Jonathan A. Malen, and Carmel Majidi. High Thermal Conductivity in Soft Elastomers with Elongated Liquid Metal Inclusions. *Proceedings of the National Academy of Sciences of the United States of America*, 114(9):2143–2148, feb 2017. ISSN 10916490. doi: 10.1073/pnas.1616377114.

[382] A. B. M. Tahidul Haque, Ravi Tutika, Rachael L. Byrum, and Michael D. Bartlett. Programmable Liquid Metal Microstructures for Multifunctional Soft Thermal Composites. *Advanced Functional Materials*, page 2000832, apr 2020. ISSN 1616-301X. doi: 10.1002/adfm.202000832. URL https://onlinelibrary.wiley.com/doi/abs/10.1002/adfm.202000832.

[383] Michael D. Dickey. Stretchable and Soft Electronics using Liquid Metals. *Advanced Materials*, 29(27):1606425, jul 2017. ISSN 09359648. doi: 10.1002/adma.201606425. URL http://doi.wiley.com/10.1002/adma.201606425.

[384] Eric J. Markvicka, Michael D. Bartlett, Xiaonan Huang, and Carmel Majidi. An Autonomously Electrically Self-healing Liquid Metal-Elastomer Composite for Robust Soft-matter Robotics and Electronics. *Nature Materials*, 17(7):618–624, jul 2018. ISSN 14764660. doi: 10.1038/s41563-018-0084-7.

[385] Titao Jing, Bingang Xu, and Yujue Yang. Liquid Doping Materials as Micro-carrier of Functional Molecules for Functionalization of Triboelectric Materials and Flexible Triboelectric Nanogenerators for Energy Harvesting and Gesture Detection. *Nano Energy*, 74:104856, aug 2020. ISSN 22112855. doi: 10.1016/j.nanoen.2020.104856.

[386] S. S. P. Parkin, K. P. Roche, M. G. Samant, P. M. Rice, R. B. Beyers, R. E. Scheuerlein, E. J. O'Sullivan, S. L. Brown, J. Bucchigano, D. W. Abraham, Yu Lu, M. Rooks, P. L. Trouilloud, R. A. Wanner, and W. J. Gallagher. Exchange-Biased Magnetic

Tunnel Junctions and Application to Nonvolatile Magnetic Random Access Memory (invited). *Journal of Applied Physics*, 85(8):5828–5833, apr 1999. ISSN 0021-8979. doi: 10.1063/1.369932. URL http://aip.scitation.org/doi/10.1063/1.369932.

[387] H S Wong, S K He, H J Chung, M S Zhang, Kelvin Cher, Melvin Low, T J Zhou, Y Yang, and S K Wong. Reduction of Magnetic Damping and Isotropic Coercivity and Increase of Saturation Magnetization in Rh-incorporated CoIr System. *Nanotechnology*, 27(45), oct 2016. doi: 10.1088/0957-4484/27/45/455705. URL https://iopscience.iop.org/article/10.1088/0957-4484/27/45/455705/pdf.

[388] Matthew J. Bauer, Andrew Thomas, Bridget Isenberg, John Varela, Andrea Faria, David P. Arnold, and Jennifer S. Andrew. Ultra-Low-Power Current Sensor Utilizing Magnetoelectric Nanowires. *IEEE Sensors Journal*, 20(10):5139–5145, may 2020. ISSN 15581748. doi: 10.1109/JSEN.2020.2968224.

[389] Hsing Yu Chen and Andrew T. Conn. A Stretchable Inductor with Integrated Strain Sensing and Wireless Signal Transfer. *IEEE Sensors Journal*, 20(13):7384–7391, jul 2020. ISSN 15581748. doi: 10.1109/JSEN.2020.2979076.

[390] Anthony P. Taylor, Camilo Velez Cuervo, David P. Arnold, and Luis Fernando Velasquez-Garcia. Fully 3D-printed, Monolithic, Mini Magnetic Actuators for Low-cost, Compact Systems. *Journal of Microelectromechanical Systems*, 28(3):481–493, jun 2019. ISSN 19410158. doi: 10.1109/JMEMS.2019.2910215.

[391] In Gon Lee, Nam Kim, In Kui Cho, and Ic Pyo Hong. Design of a Patterned Soft Magnetic Structure to Reduce Magnetic Flux Leakage of Magnetic Induction Wireless Power Transfer Systems. *IEEE Transactions on Electromagnetic Compatibility*, 59(6): 1856–1863, dec 2017. ISSN 00189375. doi: 10.1109/TEMC.2017.2690967.

[392] Tommaso Campi, Silvano Cruciani, and Mauro Feliziani. Magnetic Shielding of Wireless Power Transfer Systems - IEEE Conference Publication. In *2014 International Symposium on Electromagnetic Compatibility, Tokyo*, Tokyo, may 2014. IEEE. URL https://ieeexplore.ieee.org/abstract/document/6997187.

[393] Stasiu Chyczewski, Seahee Hwangbo, Yong Kyu Yoon, and David P. Arnold. Experimental Demonstration of Multi-watt Wireless Power Transmission to Ferrite-core Receivers at 6.78 MHz. *Wireless Power Transfer*, 6(1):17–25, mar 2019. ISSN 20528418. doi: 10.1017/wpt.2018.6.

[394] Mark R. Jolly, J. David Carlson, Beth C. Muñoz, and Todd A. Bullions. The Magnetoviscoelastic Response of Elastomer Composites Consisting of Ferrous Particles Embedded in a Polymer Matrix. *Journal of Intelligent Material Systems and Structures*, 7(6):613–622, 1996. ISSN 1045389X. doi: 10.1177/1045389X9600700601.

[395] A. V. Chertovich, G. V. Stepanov, E. Yu Kramarenko, and A. R. Khokhlov. New Composite Elastomers with Giant Magnetic Response. *Macromolecular Materials and Engineering*, 295(4):336–341, apr 2010. ISSN 14387492. doi: 10.1002/mame.200900301.

[396] J. David Carlson and Mark R. Jolly. MR Fluid, Foam and Elastomer Devices. *Mechatronics*, 10(4):555–569, jun 2000. ISSN 09574158. doi: 10.1016/S0957-4158(99)00064-1.

[397] Yancheng Li, Jianchun Li, Tongfei Tian, and Weihua Li. A Highly Adjustable Magnetorheological Elastomer Base Isolator for Applications of Real-time Adaptive Control. *Smart Materials and Structures*, 22(9):095020, aug 2013. ISSN 0964-1726. doi: 10.1088/0964-1726/22/9/095020.

[398] Yi Han, Wei Hong, and Leann E. Faidley. Field-stiffening Effect of Magneto-rheological Elastomers. *International Journal of Solids and Structures*, 50(14-15):2281–2288, jul 2013. ISSN 00207683. doi: 10.1016/j.ijsolstr.2013.03.030.

[399] Hua-xia Deng, Xing-long Gong, and Lian-hua Wang. Development of an Adaptive Tuned Vibration Absorber with Magnetorheological Elastomer. *Smart Materials and Structures*, 15(5):N111, aug 2006. ISSN 0964-1726. doi: 10.1088/0964-1726/15/5/N02.

[400] N Hoang, N Zhang, and H Du. An Adaptive Tunable Vibration Absorber using a New Magnetorheological Elastomer for Vehicular Powertrain Transient Vibration Reduction. *Smart Materials and Structures*, 20(1):015019, dec 2011. ISSN 0964-1726. doi: 10.1088/0964-1726/20/1/015019.

[401] N Hoang, N Zhang, W H Li, and H Du. Development of a Torsional Dynamic Absorber using a Magnetorheological Elastomer for Vibration Reduction of a Powertrain Test Rig. *Journal of Intelligent Material Systems and Structures*, 24(16):2036–2044, nov 2013. ISSN 1045-389X. doi: 10.1177/1045389X13489361. URL http://journals.sagepub.com/doi/10.1177/1045389X13489361.

[402] David York, Xiaojie Wang, and Faramarz Gordaninejad. A New MR Fluid-Elastomer Vibration Isolator. *Journal of Intelligent Material Systems and Structures*, 18(12): 1221–1225, dec 2007. ISSN 1045-389X. doi: 10.1177/1045389X07083622. URL http://journals.sagepub.com/doi/10.1177/1045389X07083622.

[403] A. K. Bastola, V. T. Hoang, and L. Li. A Novel Hybrid Magnetorheological Elastomer developed by 3D Printing. *Materials and Design*, 114:391–397, jan 2017. ISSN 18734197. doi: 10.1016/j.matdes.2016.11.006.

[404] A. K. Bastola, L. Li, and M. Paudel. A Hybrid Magnetorheological Elastomer developed by Encapsulation of Magnetorheological Fluid. *Journal of Materials Science*, 53 (9):7004–7016, may 2018. ISSN 15734803. doi: 10.1007/s10853-018-2012-2.

[405] Xiaojie Wang and Faramarz Gordaninejad. A New Magnetorheological Fluid-elastomer Mount: Phenomenological Modeling and Experimental Study. *Smart Materials and*

Structures, 18(9):095045, aug 2009. doi: 10.1088/0964-1726/18/9/095045. URL https://iopscience.iop.org/article/10.1088/0964-1726/18/9/095045https://iopscience.iop.org/article/10.1088/0964-1726/18/9/095045/meta.

[406] Paolo Testa, Robert W. Style, Jizhai Cui, Claire Donnelly, Elena Borisova, Peter M. Derlet, Eric R. Dufresne, and Laura J. Heyderman. Magnetically Addressable Shape-Memory and Stiffening in a Composite Elastomer. *Advanced Materials*, 31(29):1900561, jul 2019. ISSN 0935-9648. doi: 10.1002/adma.201900561. URL https://onlinelibrary.wiley.com/doi/abs/10.1002/adma.201900561.

[407] Jin Bae Lee, Hae Jin Kim, Janez Ludnik, Andreja Jelen, Damir Pajit, Magdalena Wencka, Zvonko Jagliiit, Anton Meden, and Janez Dolinšek. Synthesis and Magnetic Properties of Hematite Particles in a "Nanomedusa" Morphology. 2014. doi: 10.1155/2014/902968. URL http://dx.doi.org/10.1155/2014/902968.

[408] L. R. Bickford, J. Pappis, and J. L. Stull. Magnetostriction and Permeability of Magnetite and Cobalt-Substituted Magnetite. *Physical Review*, 99(4):1210–1214, aug 1955. ISSN 0031899X. doi: 10.1103/PhysRev.99.1210.

[409] Kozo Iwauchi, Yasuo Kita, and Naokazu Koizumi. Magnetic and Dielectric Properties of Fe3O4. *Journal of the Physical Society of Japan*, 49(4):1328–1335, nov 1980. ISSN 13474073. doi: 10.1143/JPSJ.49.1328.

[410] T. D. Yensen. What is the Magnetic Permeability of Iron? *Journal of the Franklin Institute*, 206(4):503–510, oct 1928. ISSN 00160032. doi: 10.1016/S0016-0032(28)90558-X.

[411] H. H. Helms and Edmond Adams. Sendust Sheet-processing Techniques and Magnetic Properties. *Journal of Applied Physics*, 35(3):871–872, mar 1964. ISSN 00218979. doi: 10.1063/1.1713515. URL http://aip.scitation.org/doi/10.1063/1.1713515.

[412] C. A. Grant, P. C. Twigg, and D. J. Tobin. Static and dynamic nanomechanical properties of human skin tissue using atomic force microscopy: Effect of scarring in the upper dermis. *Acta Biomaterialia*, 8(11):4123–4129, nov 2012. ISSN 18787568. doi: 10.1016/j.actbio.2012.06.042.

[413] Mingchao Zhang, Chunya Wang, Huimin Wang, Muqiang Jian, Xiangyang Hao, and Yingying Zhang. Carbonized Cotton Fabric for High-Performance Wearable Strain Sensors. *Advanced Functional Materials*, 27 (2), jan 2017. ISSN 16163028. doi: 10.1002/adfm.201604795. URL https://onlinelibrary.wiley.com/doi/full/10.1002/adfm.201604795https://onlinelibrary.wiley.com/doi/abs/10.1002/adfm.201604795https://onlinelibrary.wiley.com/doi/10.1002/adfm.201604795.

[414] Amir Mohammadi Nasab, Siavash Sharifi, Shuai Chen, Yang Jiao, and Wanliang Shan. Robust three-component elastomer–particle–fiber composites with tunable properties for soft robotics. *Advanced Intelligent Systems*, 3(2):2000166, 2021.

[415] Mohammad Amin Karimi, Vahid Alizadehyazdi, Bruno-Pier Busque, Heinrich M Jaeger, and Matthew Spenko. A boundary-constrained swarm robot with granular jamming. In *2020 3rd IEEE International Conference on Soft Robotics (RoboSoft)*, pages 291–296. IEEE, 2020.

[416] Yongkang Jiang, Diansheng Chen, Che Liu, and Jian Li. Chain-like granular jamming: a novel stiffness-programmable mechanism for soft robotics. *Soft robotics*, 6(1):118–132, 2019.

[417] Alexander L Evenchik, Alexander Q Kane, EunBi Oh, and Ryan L Truby. Electrically controllable materials for soft, bioinspired machines. *Annual Review of Materials Research*, 53, 2023.

[418] Tomas Amadeo, Daniel Van Lewen, Taylor Janke, Tommaso Ranzani, Anand Devaiah, Urvashi Upadhyay, and Sheila Russo. Soft robotic deployable origami actuators for neurosurgical brain retraction. *Frontiers in Robotics and AI*, 8:731010, 2022.

[419] Zhenpeng Xu, Ryan Hensleigh, Nikhil JRK Gerard, Huachen Cui, Mourad Oudich, Wentao Chen, Yun Jing, and Xiaoyu Rayne Zheng. Vat photopolymerization of fly-like, complex micro-architectures with dissolvable supports. *Additive Manufacturing*, 47:102321, 2021.

[420] Leah T Gaeta, Kevin J McDonald, Lorenzo Kinnicutt, Megan Le, Sidney Wilkinson-Flicker, Yixiao Jiang, Taylan Atakuru, Evren Samur, and Tommaso Ranzani. Magnetically induced stiffening for soft robotics. *Soft Matter*, 19(14):2623–2636, 2023.

[421] Hua Dong and Glenn M Walker. Adjustable stiffness tubes via thermal modulation of a low melting point polymer. *Smart materials and structures*, 21(4):042001, 2012.

[422] Iris De Falco, Giada Gerboni, Matteo Cianchetti, and Arianna Menciassi. Design and fabrication of an elastomeric unit for soft modular robots in minimally invasive surgery. *Journal of visualized experiments: JoVE*, (105), 2015.

[423] Allen Jiang, Tommaso Ranzani, Giada Gerboni, Laura Lekstutyte, Kaspar Althoefer, Prokar Dasgupta, and Thrishantha Nanayakkara. Robotic granular jamming: Does the membrane matter? *Soft Robotics*, 1(3):192–201, 2014.

[424] Vincent Wall, Raphael Deimel, and Oliver Brock. Selective stiffening of soft actuators based on jamming. In *2015 IEEE International Conference on Robotics and Automation (ICRA)*, pages 252–257. IEEE, 2015.

[425] Mark R Jolly, J David Carlson, Beth C Muñoz, and Todd A Bullions. The magneto-viscoelastic response of elastomer composites consisting of ferrous particles embedded

in a polymer matrix. *Journal of Intelligent Material Systems and Structures*, 7(6): 613–622, 1996.

[426] MA Moreno, Jorge Gonzalez-Rico, ML Lopez-Donaire, Angel Arias, and D Garcia-Gonzalez. New experimental insights into magneto-mechanical rate dependences of magnetorheological elastomers. *Composites Part B: Engineering*, 224:109148, 2021.

[427] Cole B Haverkamp, Dohgyu Hwang, Chanhong Lee, and Michael D Bartlett. Deterministic control of adhesive crack propagation through jamming based switchable adhesives. *Soft Matter*, 17(7):1731–1737, 2021.

[428] Holger Böse, Thomas Gerlach, and Johannes Ehrlich. Magnetorheological elastomers—an underestimated class of soft actuator materials. *Journal of Intelligent Material Systems and Structures*, 32(14):1550–1564, 2021.

[429] Anil K Bastola and Mokarram Hossain. A review on magneto-mechanical characterizations of magnetorheological elastomers. *Composites Part B: Engineering*, 200:108348, 2020.

[430] Kyeongmin Hong, Minjae Choe, Seoyeon Kim, Hye-Min Lee, Byung-Joo Kim, and Sungjune Park. An ultrastretchable electrical switch fiber with a magnetic liquid metal core for remote magnetic actuation. *Polymers*, 13(15):2407, 2021.

[431] Matthew Ralphs, Wilson Kong, Robert Y Wang, and Konrad Rykaczewski. Thermal conductivity enhancement of soft polymer composites through magnetically induced percolation and particle–particle contact engineering. *Advanced Materials Interfaces*, 6(6):1801857, 2019.

[432] Xiao-Min Dong, YU Miao, Chang-Rong Liao, and Wei-Min Chen. A new variable

stiffness absorber based on magneto-rheological elastomer. *Transactions of Nonferrous Metals Society of China*, 19:s611–s615, 2009.

[433] John M Ginder, William F Schlotter, and Mark E Nichols. Magnetorheological elastomers in tunable vibration absorbers. In *Smart structures and materials 2001: damping and isolation*, volume 4331, pages 103–110. SPIE, 2001.

[434] Jakub Bernat, Piotr Gajewski, Rafał Kapela, Agnieszka Marcinkowska, and Paulina Superczyńska. Design, fabrication and analysis of magnetorheological soft gripper. *Sensors*, 22(7):2757, 2022.

[435] Yusuke Tsugami, Thibault Barbié, Kenjiro Tadakuma, and Takeshi Nishida. Development of universal parallel gripper using reformed magnetorheological fluid. In *2017 11th Asian control conference (ASCC)*, pages 778–783. IEEE, 2017.

[436] Piotr Zając, Jerzy Kaleta, Daniel Lewandowski, and Aleksandra Gasperowicz. Isotropic magnetorheological elastomers with thermoplastic matrices: structure, damping properties and testing. *Smart Materials and Structures*, 19(4):045014, 2010.

[437] S Raa Khimi and Kim L Pickering. Comparison of dynamic properties of magnetorheological elastomers with existing antivibration rubbers. *Composites Part B: Engineering*, 83:175–183, 2015.

[438] I Bica, EM Anitas, and LME Averis. Tensions and deformations in composites based on polyurethane elastomer and magnetorheological suspension: Effects of the magnetic field. *Journal of Industrial and Engineering Chemistry*, 28:86–90, 2015.

[439] Miao Yu, Song Qi, Jie Fu, PA Yang, and Mi Zhu. Preparation and characterization of a novel magnetorheological elastomer based on polyurethane/epoxy resin ipns matrix. *Smart Materials and Structures*, 24(4):045009, 2015.

[440] Toshihiko Komatsuzaki and Yoshio Iwata. Design of a real-time adaptively tuned dynamic vibration absorber with a variable stiffness property using magnetorheological elastomer. *Shock and Vibration*, 2015, 2015.

[441] Xiuying Qiao, Xiushou Lu, Xinglong Gong, Tao Yang, Kang Sun, and Xiaodong Chen. Effect of carbonyl iron concentration and processing conditions on the structure and properties of the thermoplastic magnetorheological elastomer composites based on poly (styrene-b-ethylene-co-butylene-b-styrene)(sebs). *Polymer Testing*, 47:51–58, 2015.

[442] Yu Tong, Xufeng Dong, and Min Qi. High performance magnetorheological fluids with flower-like cobalt particles. *Smart Materials and Structures*, 26(2):025023, 2017.

[443] A Boczkowska and SF Awietjan. Effect of the elastomer stiffness and coupling agents on rheological properties of magnetorheological elastomers. *WIT Trans. Eng. Sci.*, 72: 263–274, 2011.

[444] Zsolt Varga, Genovéva Filipcsei, and Miklós Zrínyi. Magnetic field sensitive functional elastomers with tuneable elastic modulus. *Polymer*, 47(1):227–233, 2006.

Appendices

Appendix A

Chapter 2 Supporting Information

Thermal and electrical conductivity analysis

For the thermal conductivity specimens in Figure 2.4, "n" is the number of THW testing runs performed on each composite sample: n = 5 for all data points. The number of composite samples on which THW analysis was performed is "m". The sample size was limited by the testing conditions, which would cause corrosion of the copper contacts or cause the platinum wire to break.

Composite	**Ambient**	**Freshwater**	**Saltwater**	**Con. Saltwater**
Ecoflex ϕ=0%	m = 2	m = 3	m = 2 (day 1) m = 3 (week 1-3) m = 2 (week4)	m=3
Ecoflex ϕ=40%	m = 3	m = 3	m = 4 (day 1 - week 2) m=3 (week 3-4)	m = 4 (day 1 - week 2) m = 3 (week 3-4)
Ecoflex ϕ=80%	m = 1	m = 1	m = 1	m = 1

Table A.1: Thermal conductivity measurement sample sizes.

For the electrical conductivity specimens in Figure 2.5, n denotes the number of composite samples tested. Three measurements at lenghts of 10, 20, and 30 mm were taken to create a linear fit for each sample.

Composite	**Ambient**	**Freshwater**	**Saltwater**	**Con. Saltwater**
Sylgard ϕ=40%	n = 4	n = 4	n = 4	n = 4 (day 0 - week 2) n = 3 (week 3-4)
Sylgard ϕ=80%	n = 4	n = 4	n = 4	n = 4 (day 0 - week 3) n = 3 (week 4)

Table A.2: Electrical conductivity measurement sample sizes.

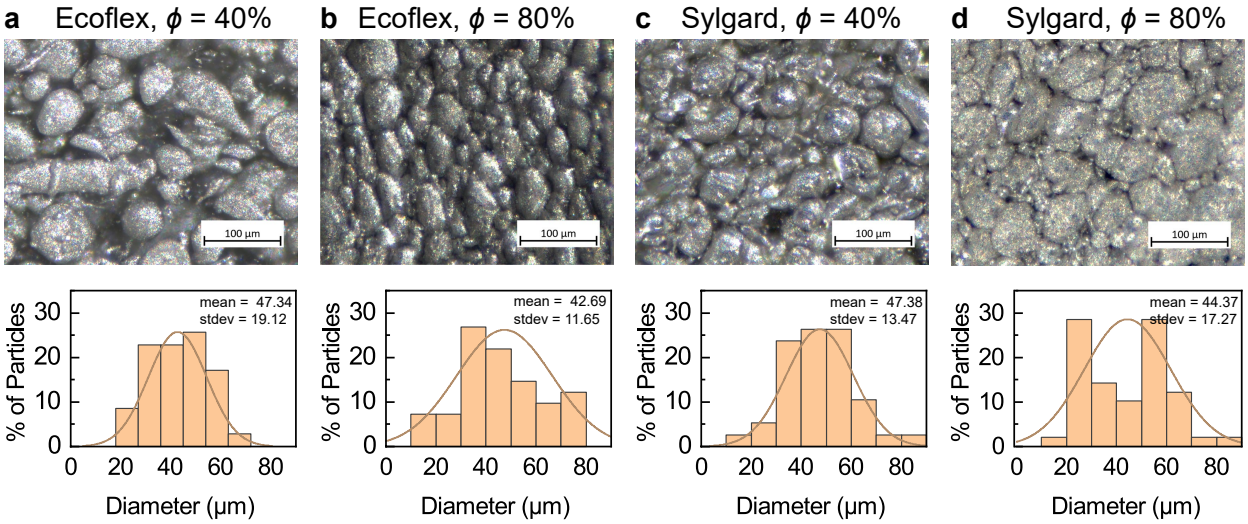


Figure A.1: Micrographs and associated particle size distributions for a) Ecoflex $\phi = 40\%$ (n = 42 droplets) b) Ecoflex $\phi = 80\%$ (n = 35) c) Sylgard $\phi = 40\%$ (n = 38) and d) Sylgard $\phi = 80\%$ samples (n = 49).

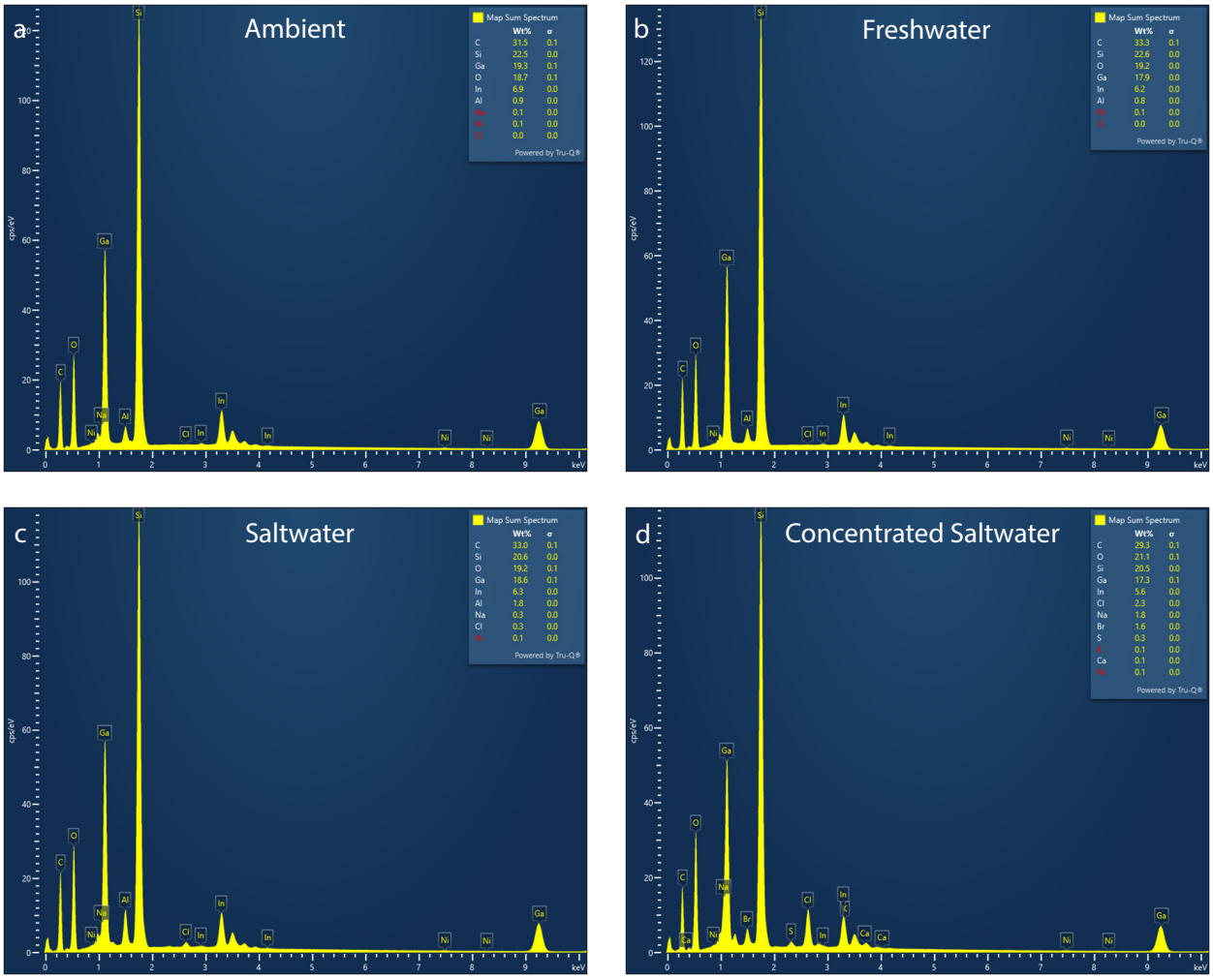


Figure A.2: Energy disperse X-ray spectroscopy spectra of Ecoflex $\phi = 80\%$ aged for two weeks in **a)** ambient, **b)** freshwater, **c)** saltwater, **d)** concentrated saltwater environments.

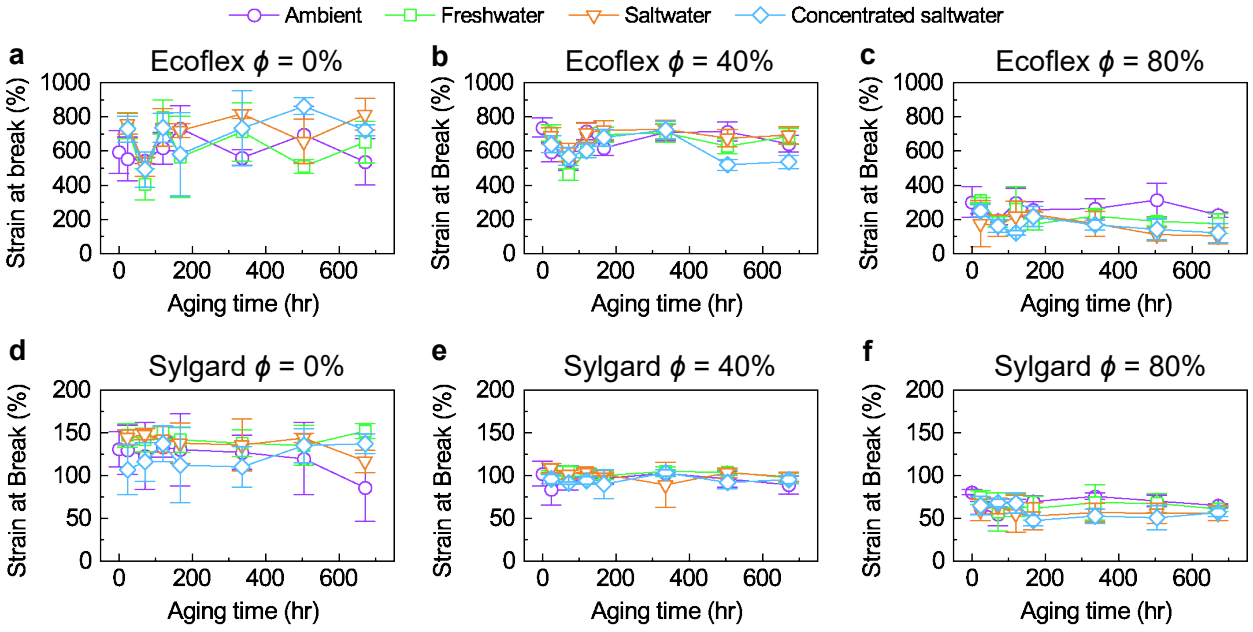


Figure A.3: Strain at break of Ecoflex LM composites and d-f) Sylgard composites. Error bars represent standard deviation for n = 3.

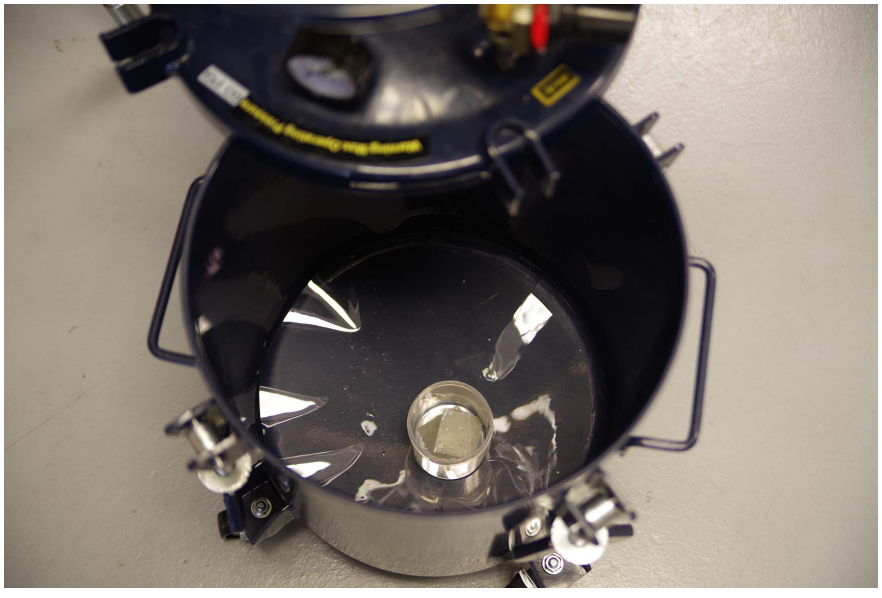


Figure A.4: Pressure pot setup for hydrostatic testing.



Figure A.5: $\phi = 40\%$ remains nonconductive after 1 hour at 3 atm in a pressure pot.



Figure A.6: $\phi = 80\%$ remains nonconductive after 1 hour at 3 atm in a pressure pot.

Appendix B

Chapter 3 Supporting Information

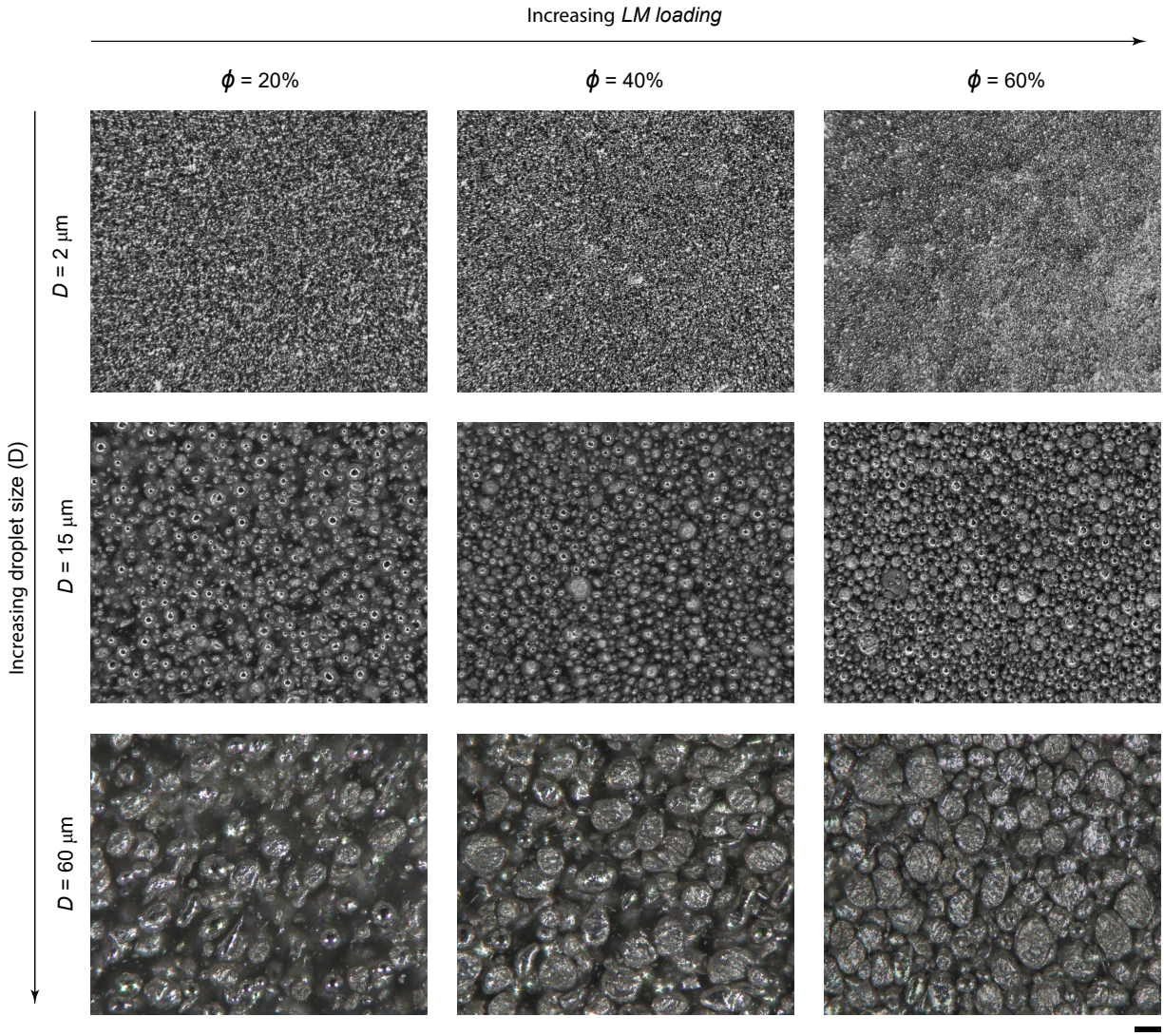


Figure B.1: **Liquid metal droplet micrographs.** Rows show different LM volume loadings (ϕ = 20, 40, 60%) and columns show different LM droplet sizes (d = 2, 15, 60 µm). Scale bar is 50 µm.

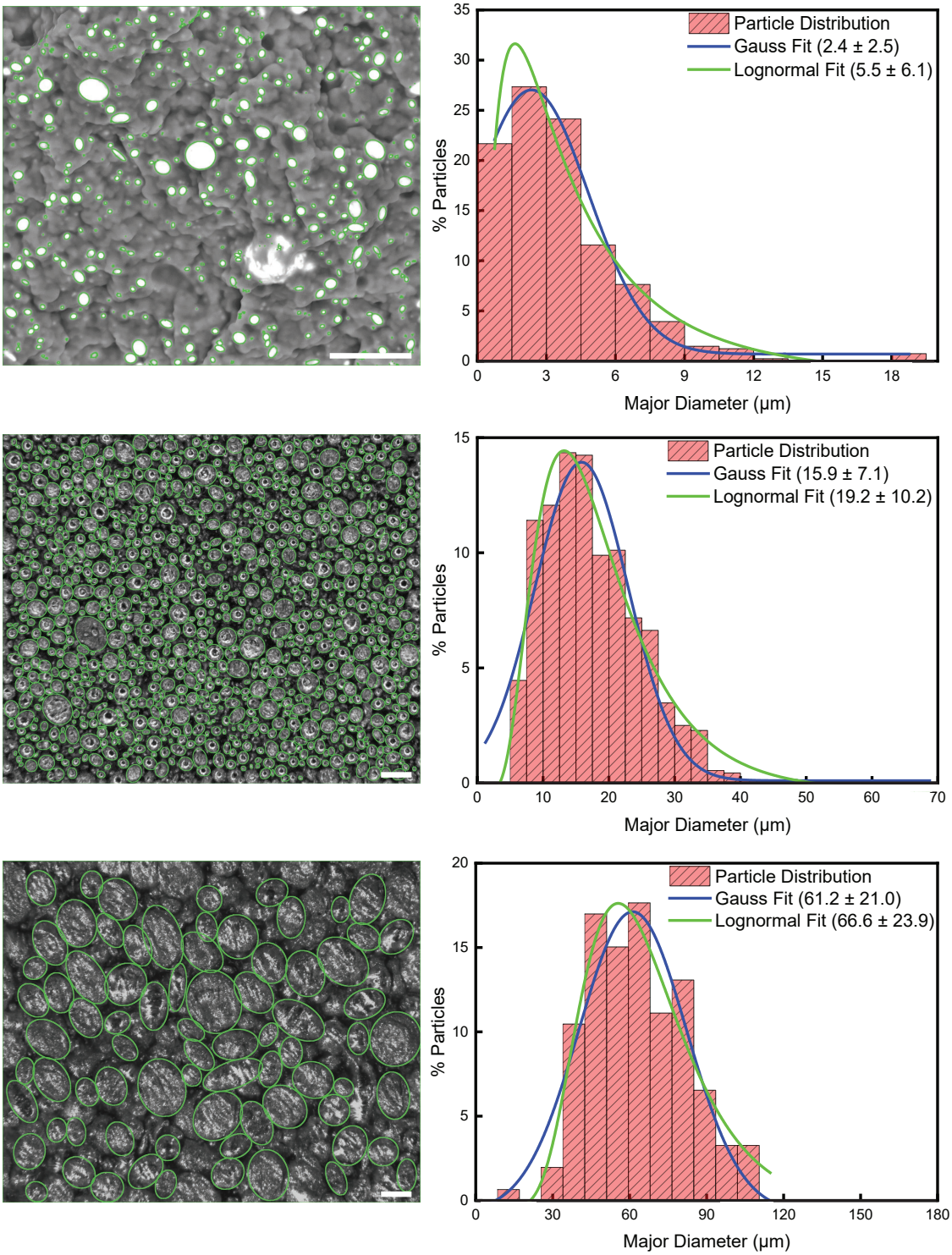


Figure B.2: **LM composite particle analysis.** From top to bottom: Analyzed SEM image of composite with smallest particles ($\phi = 20\%$), analyzed micrograph of composite with medium-sized particles ($\phi = 60\%$), analyzed micrograph of composite with large particles ($\phi = 60\%$), with associated major droplet diameter histograms with Gauss and lognormal fits. All scale bars are 50 μm.

Appendix C

Chapter 4 Supporting Information

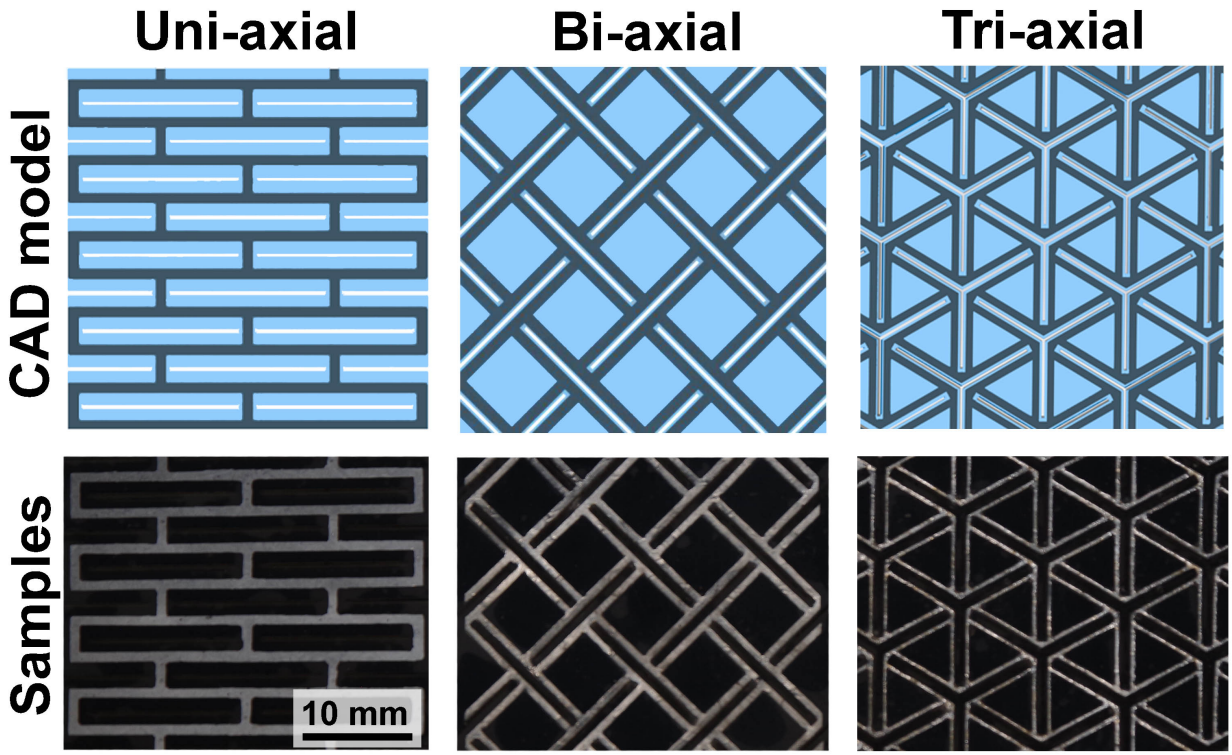


Figure C.1: **Modeled and fabricated samples.** CAD models and fabricated sample images of three different kirigami configurations including uni-axial, bi-axial, and tri-axial designs.

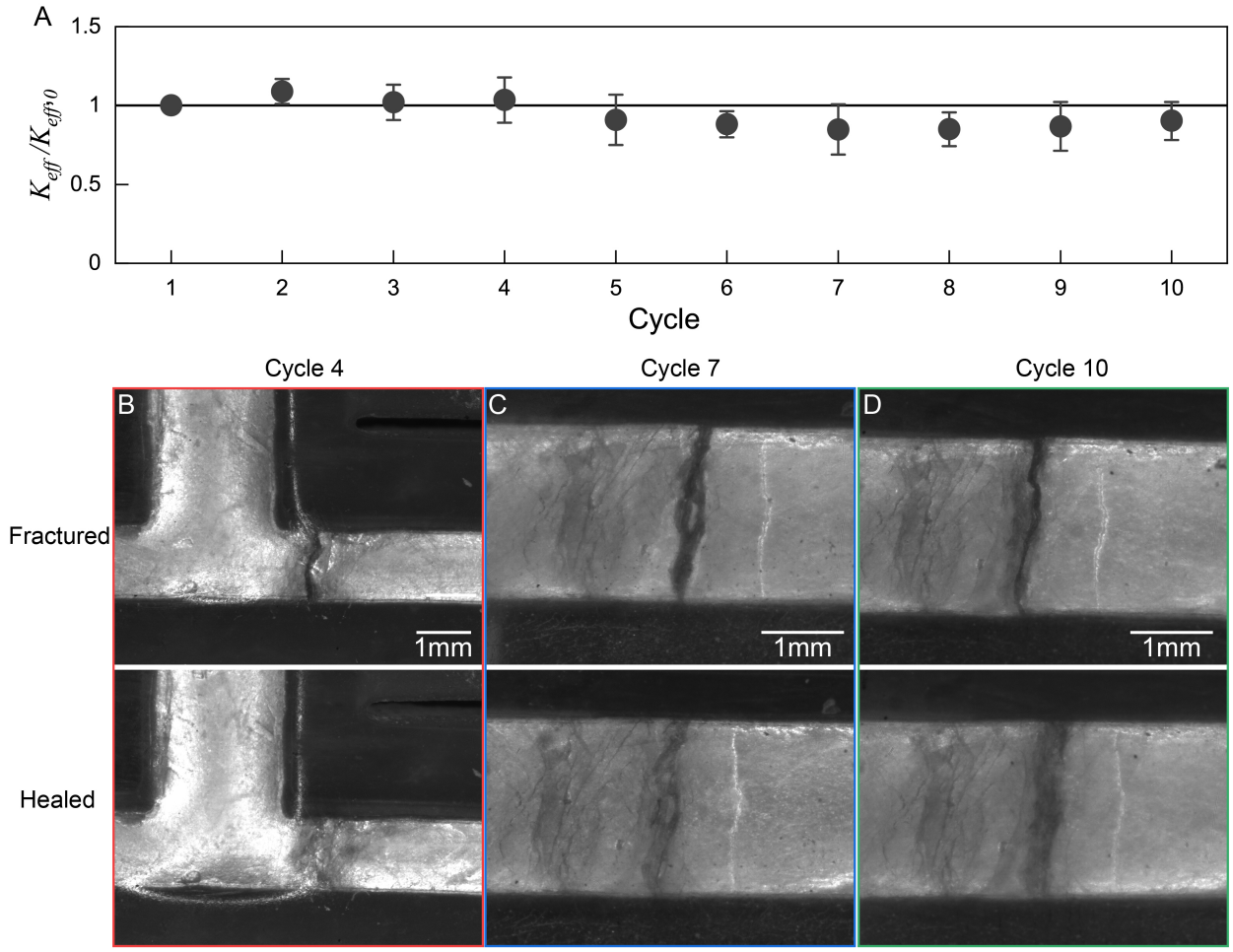


Figure C.2: **Self-healing evaluation through cyclic fracture/healing testing.** (**A**) Normalized stiffness as a function of cycle number. The average normalized stiffness value of three composites is included for each cycle. We intentionally break then heal the endoskeleton by vacuum-assisted thermal healing before each cycle. Error bars represent the standard deviation for $n = 3$. (**B**) Microscopic images of a fractured then healed point before cycle 4, (**C**) before cycle 7, and (**D**) before cycle 10.

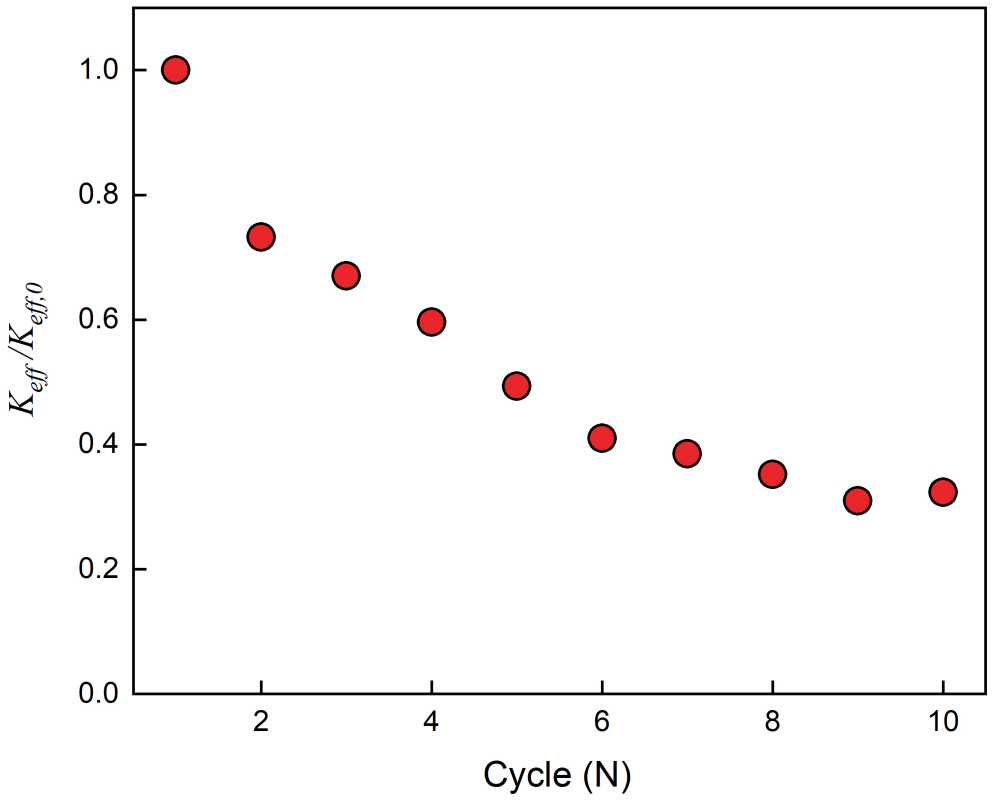


Figure C.3: **Cyclic loading test of unpressurized kirigami composite.** The normalized effective stiffness of an unpressurized kirigami composite as a function of loading cycle.

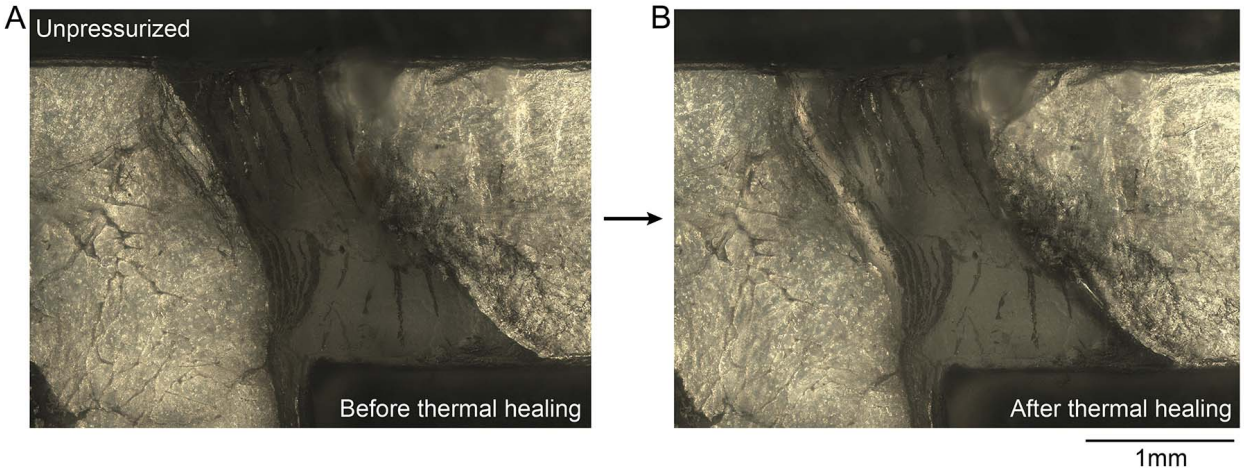


Figure C.4: **Poor crack healing of an unpressurized system.** Optical micrographs of a LMPA endoskeleton beam in an unpressurized kirigami composite (**a**) before and (**b**) after thermal healing. The composite is tested under uni-axial loading 10 cycles before taking micrographs. The large void is created due to interfacial phenomena (*e.g.*, oxide formation).

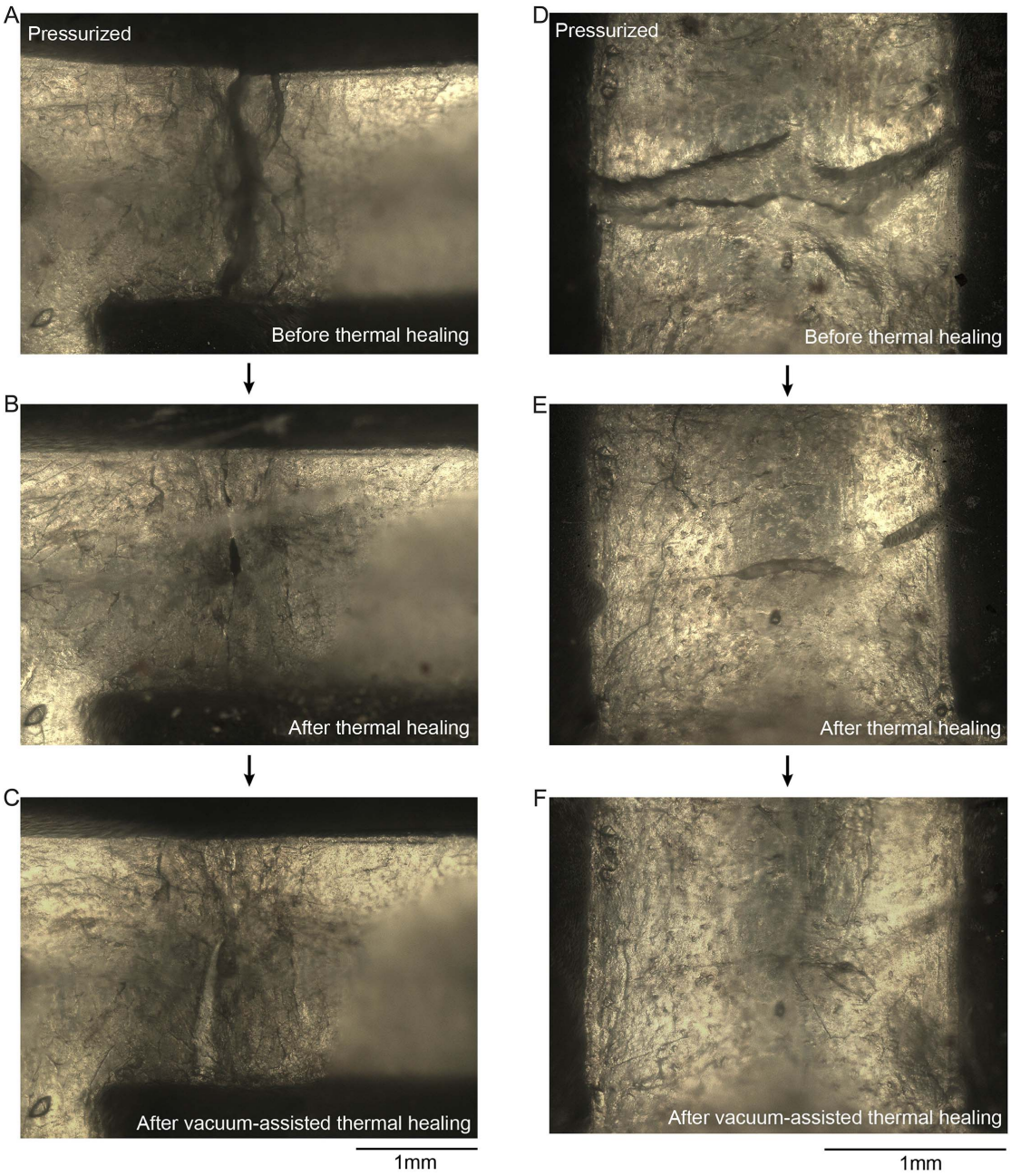


Figure C.5: **Excellent crack healing of a pressurized system.** Optical micrographs of two LMPA endoskeleton beams in a pressurized kirigami composite. The composite is tested under uni-axial loading 10 cycles and shown to have no substantial fractures and voids. (**a-b**) We intentionally fracture two beams and characterized thermal healing capability. (**c-d**) After the thermal healing process, the cracks are effectively recovered. (**e-f**) Through a vacuum-assisted thermal healing process, the cracks are fully recovered.

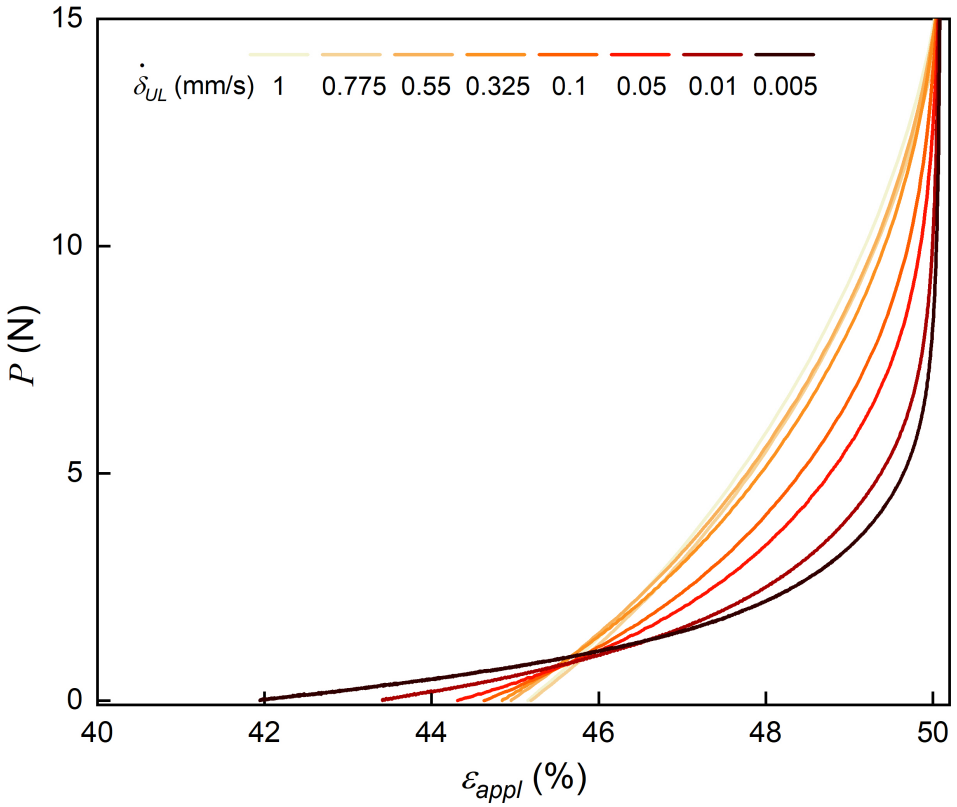


Figure C.6: **Tensile loading test.** Plot of load as a function of applied strain. After ε_{appl} = 50 % is applied to the composite, the sample is unloaded at different rates $\dot{\delta}_{UL}$ = 0.005, 0.01, 0.05, 0.1, 0.325, 0.55, 0.775, and 1 mm s^{-1}.

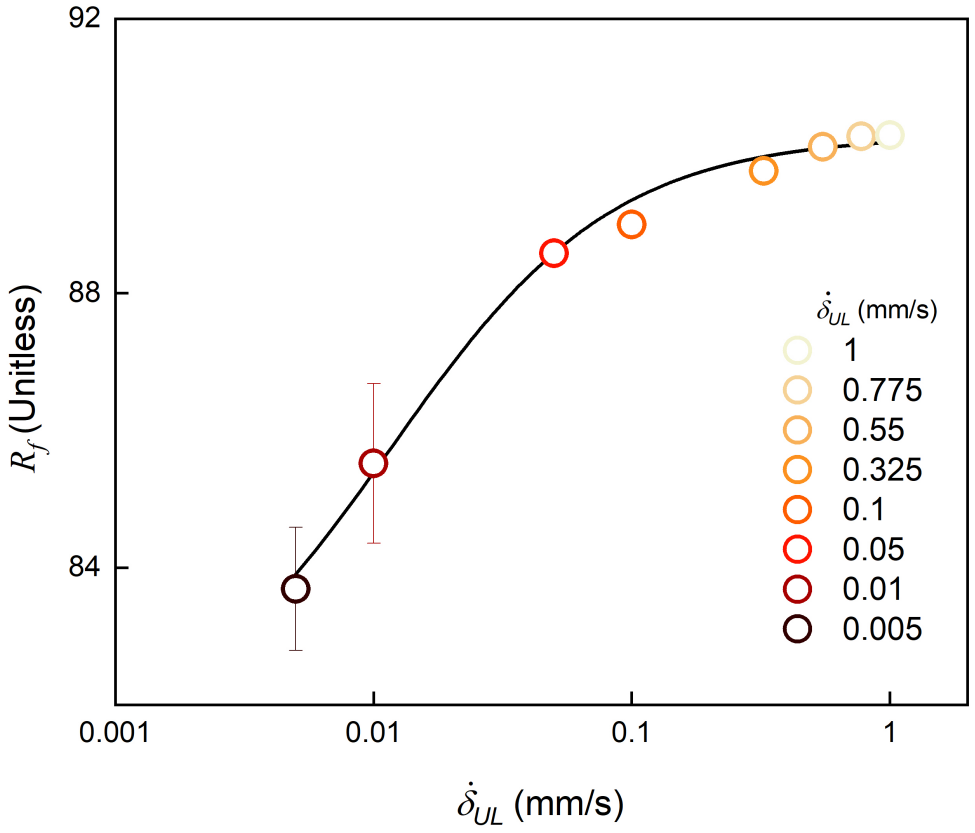


Figure C.7: **Shape-fixing capability.** Plot of shape-fixity ratio as a function of unloading rates for $\varepsilon_{appl} = 50$ %. The data is obtained from Fig. C.6, and the fixity ratio is calculated using Equation 2. Error bars represent the standard deviation for $n = 3$.

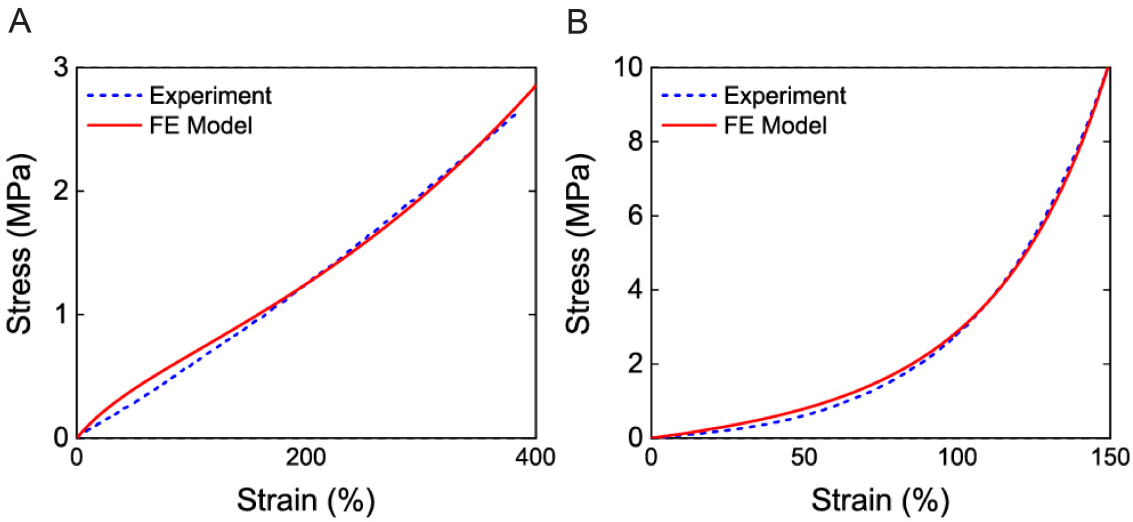


Figure C.8: **Material calibration of elastomer.** Comparison of experimental and FE model of elastomeric material of kirigami in (a) engineering and (b) true stress-strain frameworks.

Appendix D

Chapter 5 Supporting Information

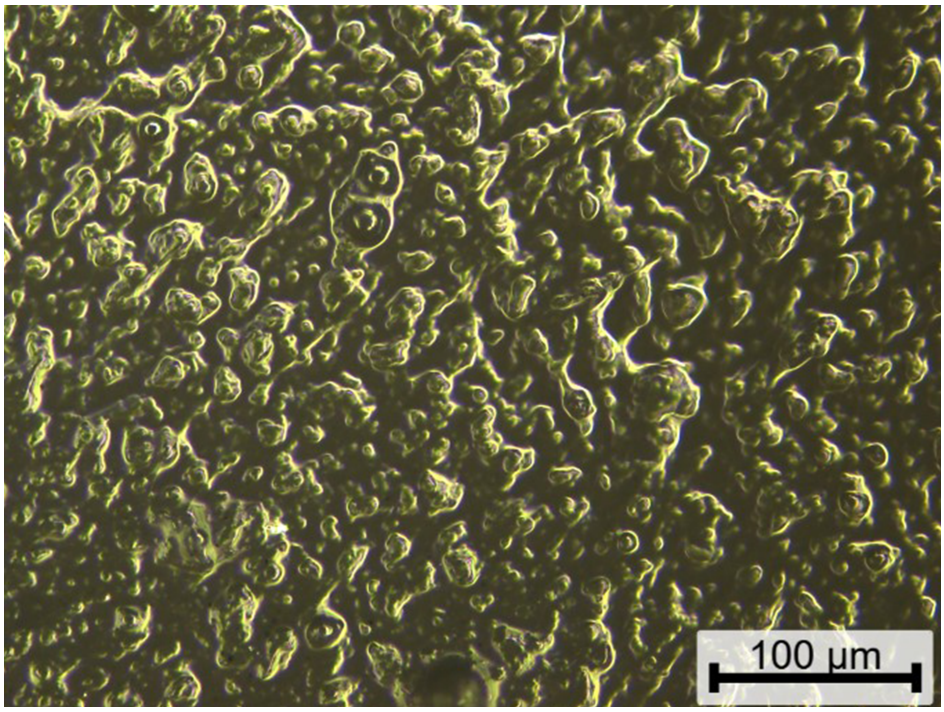


Figure D.1: Micrograph of a 33 % by volume propylene glycol in Ecoflex composite demonstrating immiscibility.

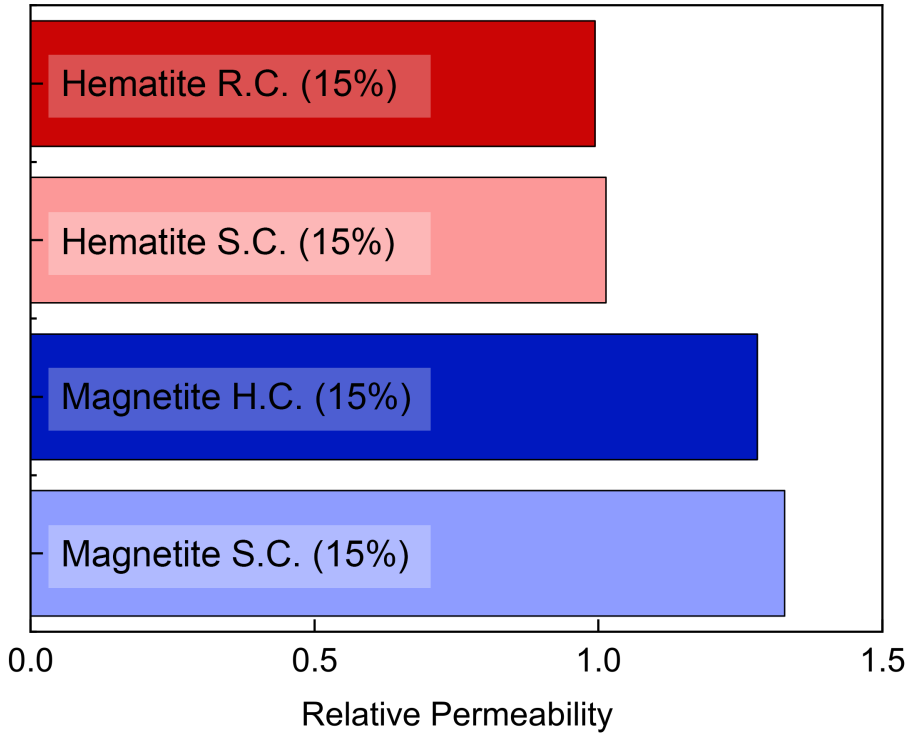


Figure D.2: Magnetic comparison between rigid particle composites (R.C.) and suspension composites (S.C.) at the same $\Omega_{composite} = 15$ %. The rigid particle and suspension composites were found to have similar permeabilities at the same rigid particle volume fractions of $\Omega_{composite} = 15$ %.

Appendix E

Chapter 6 Supporting Information

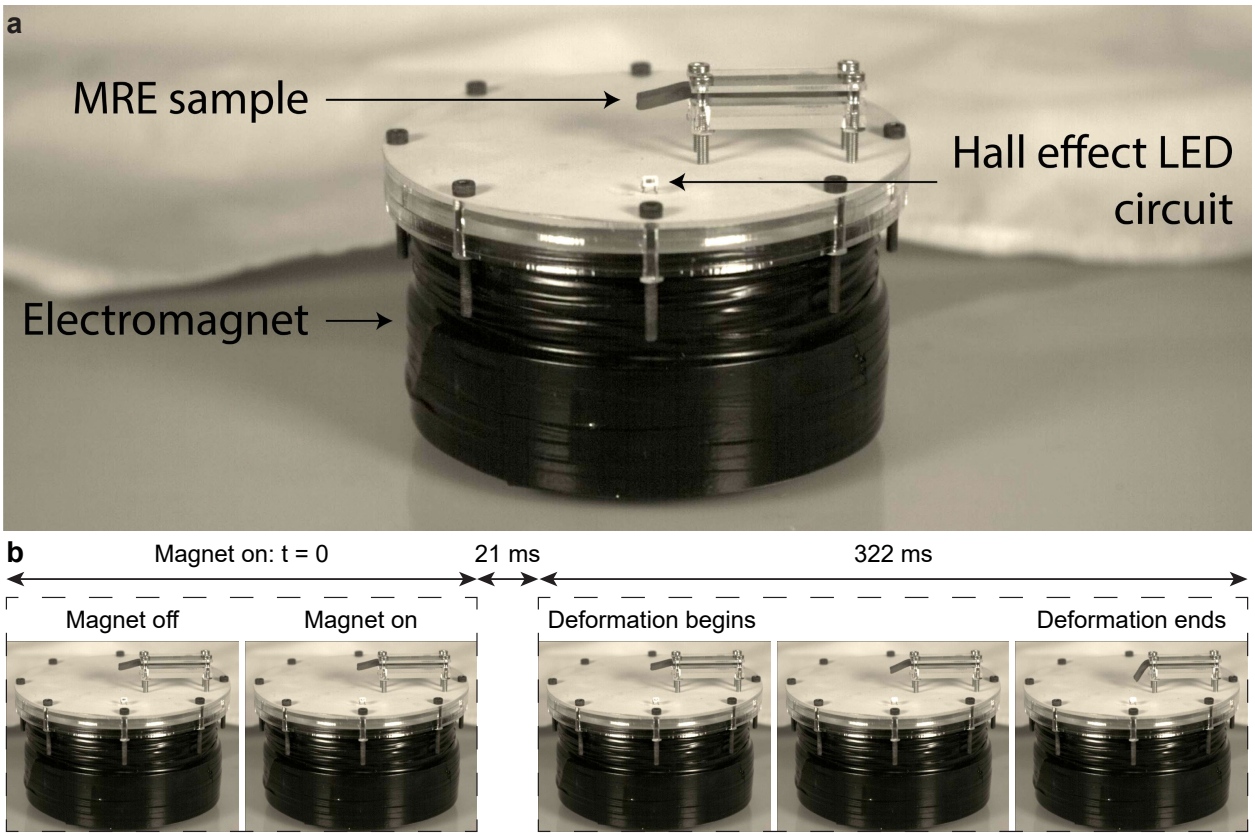


Figure E.1: **MRE response time. a)** Schematic of magneto-response testing fixture. Hall effect circuit activates LED in response to a magnetic field from the electromagnet. **b)** Measured response of MRE to applied magnetic field. MRE begins to respond within 21 ms of magnetic field activation. Full actuation of the MRE is measured to be 322 ms.

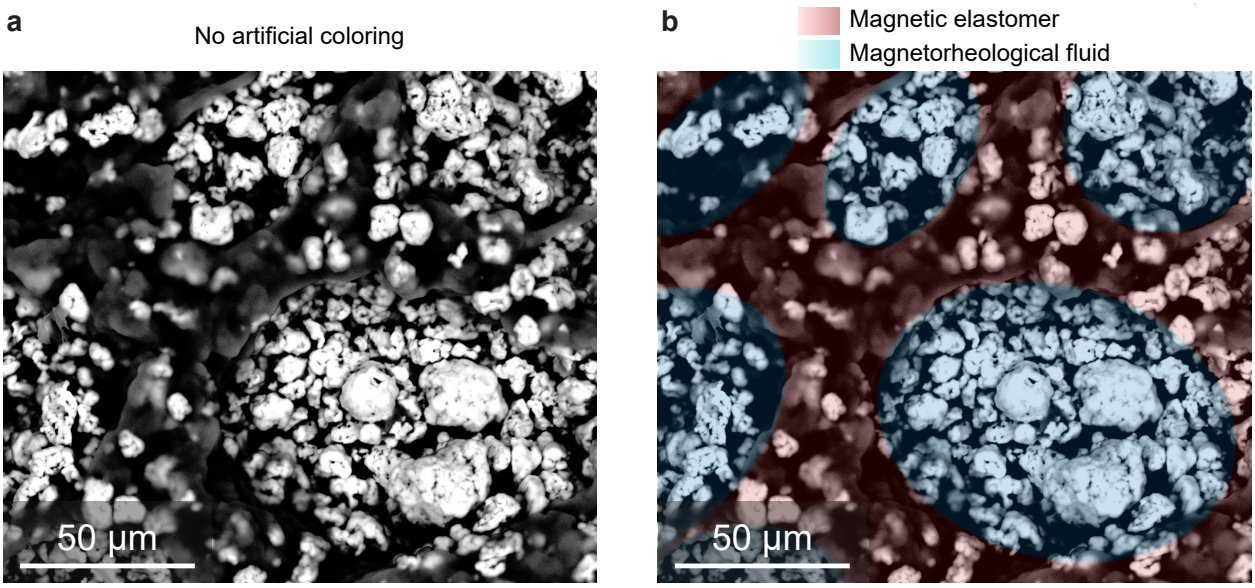


Figure E.2: **Hybrid composite MRE microstructure.** Scanning electron microscopy (SEM) of hybrid composite MRE cross-section. **a)** Uncolored SEM. **b)** Artificially colored hybrid composite MRE from Figure 1g. The magnetorheological fluid droplets are determined as the regions where elastomer is not visible on the surface.

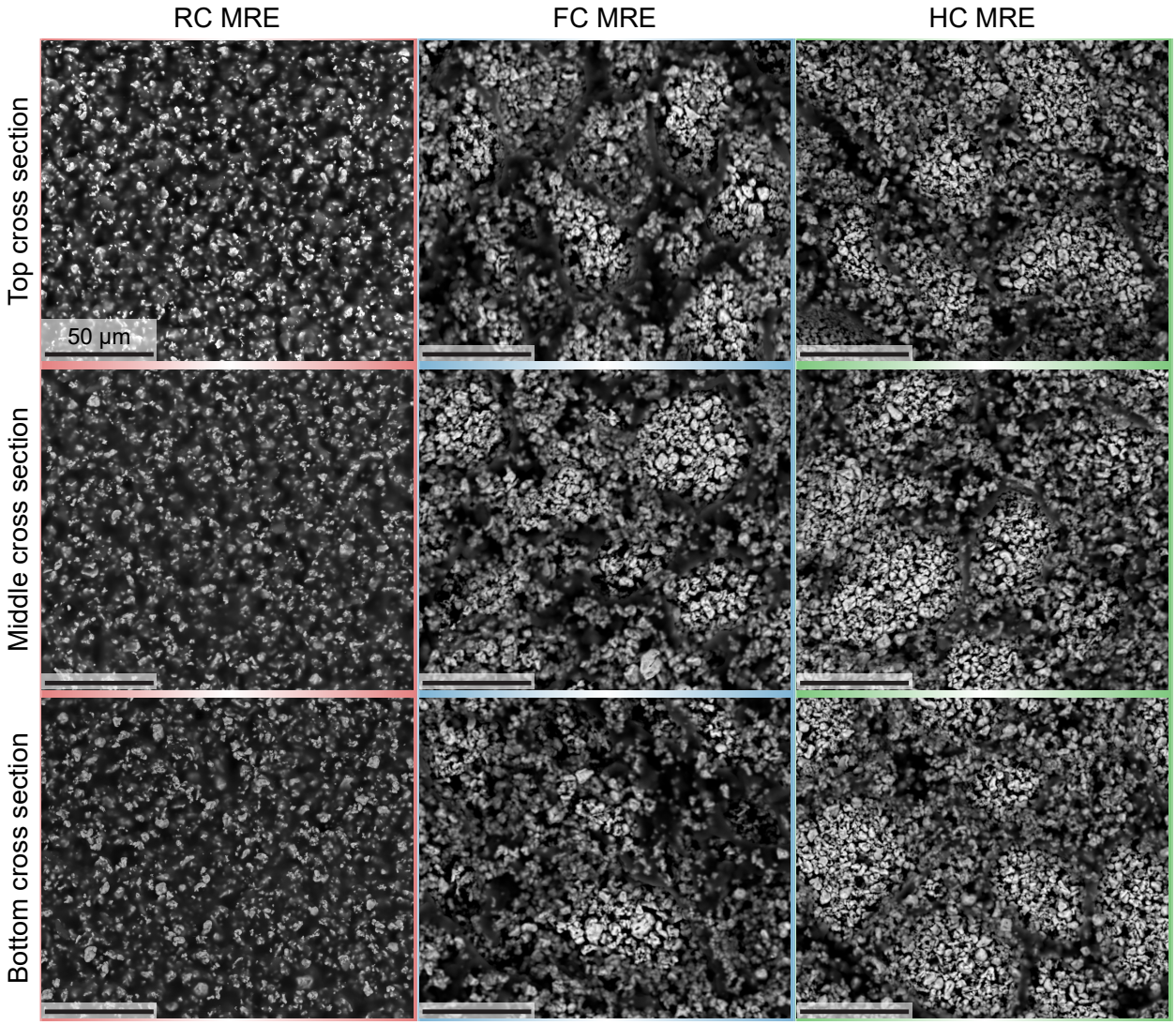


Figure E.3: **MREs with diverse microstructure.** SEM images of RC, FC, and HC MREs at different depths of the material (magnification = 1500x).

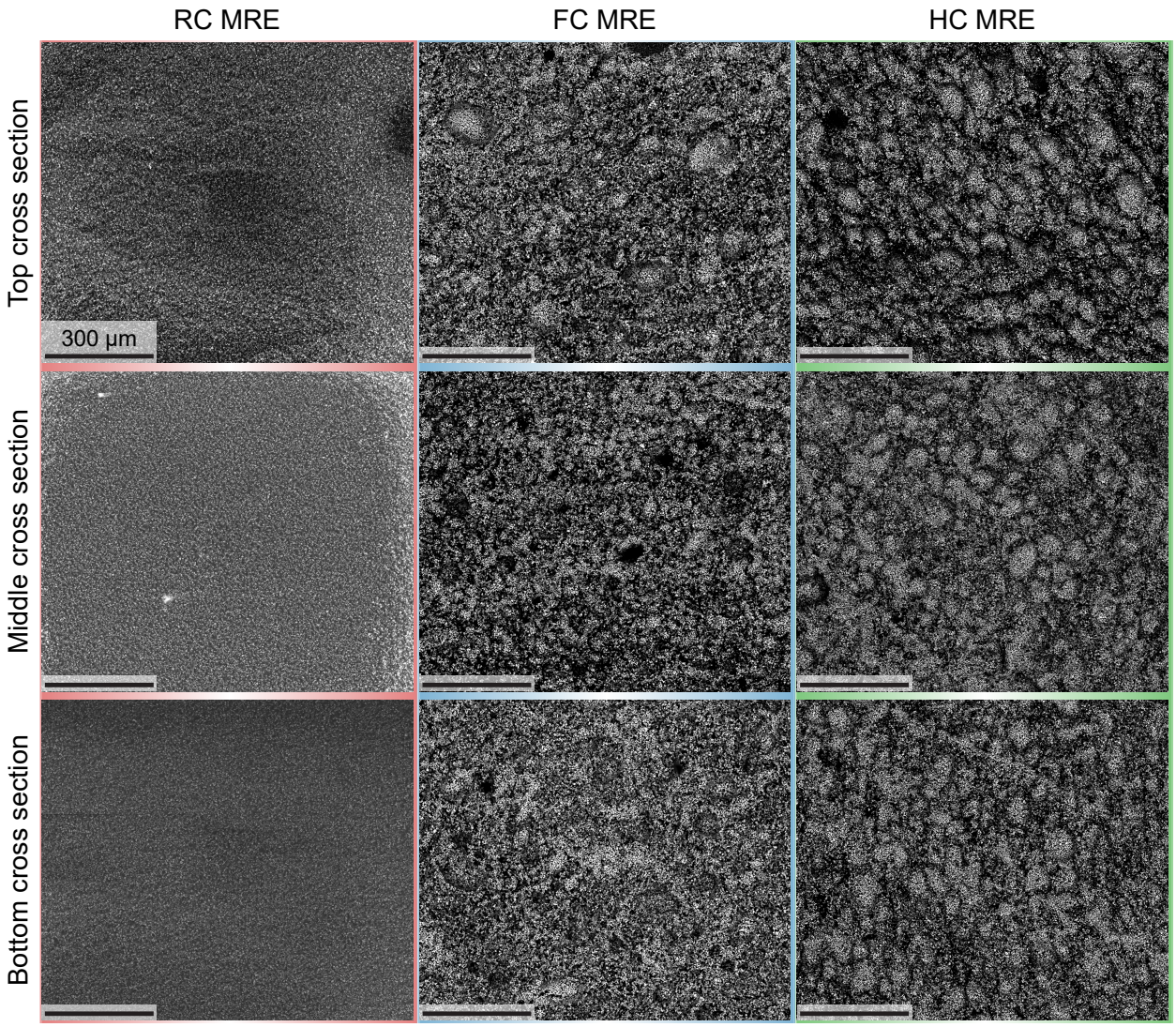


Figure E.4: **Microstructural imaging at lower magnification.** SEM images of RC, FC, and HC MREs at different depths of the material (magnification = 250x).

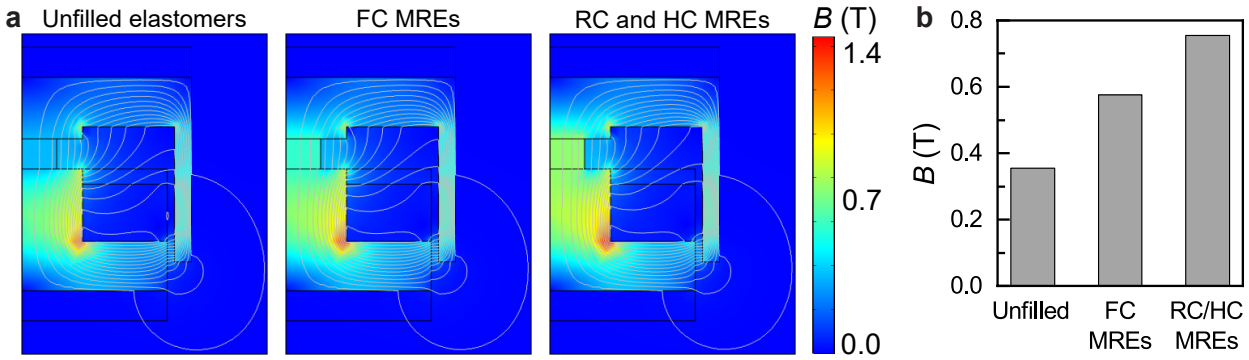


Figure E.5: **Magnetic flux density through MRE samples. a)** Finite element analysis of MRE testing fixture. **b)** Average magnetic flux density through compression testing specimens.

	Sylgard weight ratio		Ecoflex weight ratio		Total (wt%)	
(kPa)	Base	Curing agent	Part A	Part B	Sylgard	Ecoflex
8	60	1	0	0	100%	0%
60	45	1	0	0	100%	0%
200	0	0	1	1	0%	100%
900	10	1	1	1	50%	50%
3000	10	1	0	0	100%	0%

Table E.1: **Silicone elastomer compositions for control of matrix modulus.**

	Elastomer phase (vol%)		MR fluid phase (vol%)		Total (vol%)		
	Iron powder	Elastomer	Iron powder	Propylene glycol	Elastomer phase	MR fluid phase	Magnetic content
RC MRE	25%	75%	0%	0%	100%	0%	25%
FC MRE	0%	100%	35%	65%	50%	50%	17.5%
HC MRE	15%	85%	35%	65%	50%	50%	25%

Table E.2: **MRE component volume fractions.**